

Influence of asymmetric tooth profile and manufacturing process on the bending strength of polymer spur gears

A thesis submitted in partial fulfillment of the requirements

for the degree of

DOCTOR OF PHILOSOPHY

by

A. Karthik Pandian

(156103042)



**Department of Mechanical Engineering
Indian Institute of Technology Guwahati**

Guwahati, Assam – 781309, India

November 2022



CERTIFICATE

It is certified that the work contained in the thesis entitled **Influence of asymmetric tooth profile and manufacturing process on the bending strength of polymer spur gears** by **A. Karthik Pandian**, a student in the Department of Mechanical engineering, Indian Institute of Technology Guwahati, Guwahati, India, for the award of the degree of **Doctor of Philosophy** has been carried out under our supervision and this work has not been submitted elsewhere for the degree.

Dr. S. Senthilvelan

Professor

Department of Mechanical Engineering

Indian Institute of Technology Guwahati

Guwahati, Assam – 781039, India.

Dr. Sachin Singh Gautam

Associate Professor

Department of Mechanical Engineering

Indian Institute of Technology Guwahati

Guwahati, Assam – 781039, India.



Dedicated to

My father

Mr. V. Arumugam

(1958 - 2020)





Acknowledgment

“We learned about gratitude and humility – that so many people had a hand in our success...” – **Michelle Obama**

True to any significant endeavour, doctoral research requires the support of several people for its successful completion. I owe a great deal of gratitude to so many people who made this journey possible. The occurrence of the devastating COVID-19 pandemic in the midst of this journey was a rude awakening. I realized the importance of the support I receive from the community every day, and the need to practice gratitude.

First of all, I am eternally grateful to **Prof. Calvin Sophistus King**, who instructed me during my undergraduate study at Dr. Mahalingam college of engineering and technology, for inspiring me to pursue higher studies. Also, I am deeply obliged to **Dr. Solai Murugan** for instilling the belief that I could successfully complete a research program. I would like to extend my sincere thanks to the **Faculty of Mechanical engineering, IIT Guwahati** for offering me an opportunity to pursue doctoral research.

I am, forever, indebted to my supervisors **Prof. S. Senthivelan** and **Dr. Sachin Singh Gautam** for their expert guidance and immense patience during the program. They spared no effort to ensure that I develop as a competent researcher. Their unique – yet contrasting – working styles, and wide-ranging perspectives have shaped my research attitude. Prof. S. Senthivelan’s principle of *treating every problem as an opportunity to learn* has inspired me to adopt a tenacious and indefatigable approach towards life. My conversations with Dr. Sachin Singh Gautam have enabled me to develop a holistic outlook towards research, which is congruent with the rapidly evolving world. Working under these gentlemen has been a real education.

I would like to express my gratitude to the members of my Doctoral committee, **Prof. Uday S. Dixit**, **Prof. S. Kanagaraj**, and **Prof. Hemant B. Kaushik** for their constructive criticism and valuable suggestions, which greatly improved my work. I very much appreciate the support rendered by **Mr. Jiten Basumatary** and other technical superintendents. I gratefully acknowledge the assistance of **Mr. Bhaskar** and other instrument operators of *Central Instruments Facility*, IIT Guwahati for supporting microscopy studies. Many thanks to **Mr. B.R. Singh** of *Oka Basu’s Metal technologies Pvt. Ltd.*, **Mr. Joshy** of *Just Preci Comps Pvt. Ltd.*, **Mr. Prashanth** of *Perfect Gears Pvt. Ltd.*, and PSG TIFAC CORE for their assistance.

I had great pleasure working alongside **Mrs. Sarita Bharti** and **Mr. Shiv Sahaya Shukla**, whose friendship and unwavering support made this arduous journey less lonely. I thank my seniors **Dr. M. Kodeeswaran**, **Dr. A. Johnney Mertens**, **Dr. R. Vignesh Babu**, **Dr. N. Bala Subramani** and **Dr. Mirzaul Karim Hussain** for their guidance and helpful advice at various junctures. Special thanks to my lab colleagues **Ms. Arnika Verma**, **Mr. Adithya Kumar**, **Mr. Subrata Debnath**, **Mr. Ayan Islam**, **Mr. Shahidul Islam**, and **Mr. Ganesh Kumar** for extending a great deal of assistance over the years.

Many thanks to **Mr. Vaibhav Jaiswal**, **Mr. Kishore Kumar**, **Mr. Anirban Basumatary**, **Mr. Arnab Sharma** and other members of the *Biomedical devices and biomaterials laboratory* for their continuous support throughout the program. Also, I would like to acknowledge the indispensable support rendered by my colleagues, **Dr. Ajith Kumar Sahoo**, **Dr. Dhananjay Kumar**, **Dr. Mashruddin Sheikh**, **Mr. Raktim Biswas**, **Mr. Sagar Mohan**, **Mr. Saptarshi Dutta**, and **Mr. Vivekananda Haldar**. I am deeply grateful to **Mr. Karunakaran**, **Dr. Veluchamy** and **Mr. Rama Krishnan** for their support during the admission process.

My father, **Mr. V. Arumugam** – a great believer in my abilities and a perpetual source of wisdom and positivity – was instrumental in shoring up my confidence during adversities and failures. I thank my mother **Mrs. P. Subbulakshmi** for her endless love, remarkable patience, and deep understanding during my long absence. I am greatly indebted to my brother **Mr. A. Vairaprahash** who, despite numerous personal difficulties, adeptly managed the challenges at home enabling me to continue my work. I would also like to thank my grandmother **Mrs. Sankaravadivu**, my aunt **Mrs. Soundaravalli**, and my uncle **Mr. Eswaran** for their constant encouragement and moral support throughout the program. I owe a great deal of gratitude to my friends back home, **Mr. S. Abinav**, **Mr. M. Karthick**, **Mr. N. Kathiravan**, **Mr. A. Pradeep**, and **Mr. A. Sethupathy**, for their steadfast support over the years.

This is an extensive, but by no means, an exhaustive list of people who assisted me during this long journey. Regretfully, several persons to whom I owe my gratitude could not be mentioned here due to space constraints. Though unspoken, their valuable assistance is deeply appreciated. Last, but not the least, a heartfelt thanks to the **Ministry of Education, Government of India**, for granting monthly financial assistance to research scholars, enabling numerous students to pursue research.

17 November 2022

IIT Guwahati

Karthik Pandian

Abstract

The usage of polymer gears has increased significantly due to the improvements in design practices, material properties and manufacturing accuracy. In polymer gear drives, asymmetric tooth profile and polymer mating gear exert significant influence on bending fatigue strength and stiffness behavior. Additive manufacturing of polymer gears such as by selective laser sintering process – advantageous for prototyping and low-volume manufacturing – confer properties that depend on the build configuration.

In this work, the bending fatigue behavior of injection-molded Nylon 66 symmetric ($20^\circ/20^\circ$) and asymmetric ($34^\circ/20^\circ$ and $20^\circ/34^\circ$) gears, and selective laser sintered Nylon 12 symmetric gears built in 'flat' and 'on-edge' configurations were evaluated. The effects of asymmetric tooth and polymer mating gear on the deflection and load sharing characteristics were investigated. The bending fatigue performance was evaluated experimentally through load-controlled, pulsator tests in a custom-built test rig. Experimental determination of mesh deflection was carried out using an in-house developed static tooth deflection test rig. Quasi-static numerical simulations were performed in ABAQUS® to predict root bending stress, load share ratio, and tooth and mesh deflections.

The bending fatigue performance of metal – polymer pairs was dominated by root bending stress, whereas operating temperature determined the performance of polymer – polymer pairs. The bending fatigue life of $34^\circ/20^\circ$ configuration was the highest among metal – polymer pairs, whereas in polymer – polymer pairs, the life of $20^\circ/34^\circ$ configuration was greater than other configurations. The form factor exerted a decisive influence on the magnitude of bending stress compared to the stress correction factor. The deflection-induced load sharing occurred in $20^\circ/20^\circ$ and $20^\circ/34^\circ$ configurations.

The peak mesh deflection and peak-to-valley amplitude in a cycle were lowest in the $20^\circ/34^\circ$ configuration. In the $34^\circ/20^\circ$ configuration, the increase in the single tooth contact period caused by a higher drive side pressure angle resulted in greater peak mesh deflection and peak-to-valley amplitude. The negligible tooth compliance of metal gear caused unsymmetrical load sharing in metal- polymer pairs' double tooth contact zones.

The bending fatigue strength of selective laser sintered Nylon 12 gears built in a 'flat' configuration was greater than that of injection-molded Nylon 66 gears. The layered structure of the selective laser sintered gears impeded the crack propagation, as the crack front extended

across all the layers along the face width direction. The bending fatigue life of selective laser sintered 40° and 160° configurations were lower than injection-molded Nylon 66 gears. The cross-laminar mode of crack propagation in SLS 40° lead to greater fatigue life. However, the crack path in SLS 160° was along the interlayer region, which expedited the crack propagation.

Keywords: polymer gear; bending fatigue; tooth deflection; asymmetric tooth profile; injection molding; selective laser sintering; build orientation



Contents

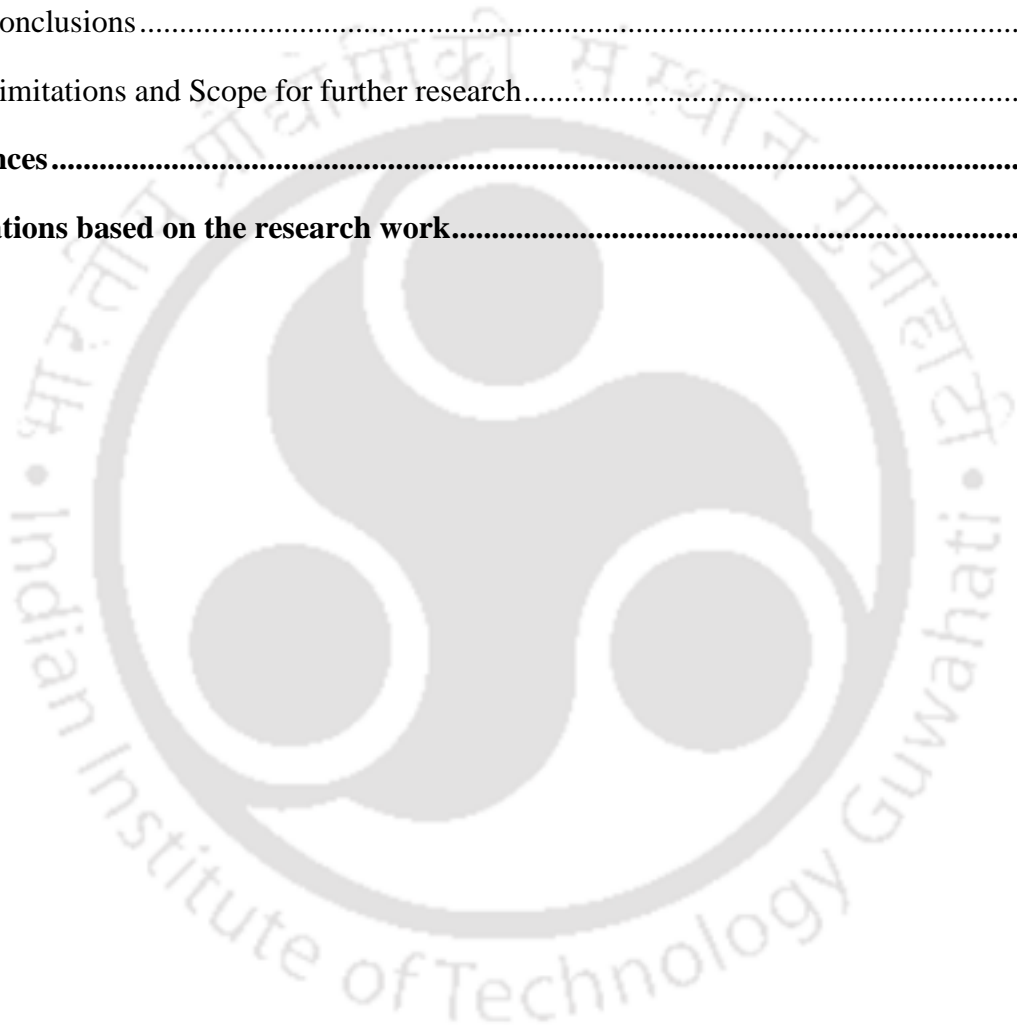
Acknowledgment	i
Abstract	iii
List of Figures	xi
List of Tables	xvii
List of Equations	xix
Abbreviations	xxi
Notations	xxiii
Chapter 1 Introduction	1
1.1 Polymer gears – Current usage and challenges in deployment.....	1
1.2 Asymmetric gears – Potential in polymer gearing.....	3
1.3 Additive manufacturing and the resurgence of customized designs.....	4
1.4 Gear tooth breakage – Importance of the design against bending fatigue.....	6
1.5 Gear tooth deflection – Transmission error, noise and vibrations.....	8
1.6 Research motivation.....	9
1.7 Aims of research	10
1.7.1 Research method.....	10
1.8 Organization of the thesis	11
Chapter 2 Literature survey	13
2.1 Performance of injection-molded polymer gears.....	13
2.1.1 Influence of mating gear material on the performance of polymer gear	14
2.1.2 Tooth deflection and transmission error in polymer gears	15
2.2 Performance of asymmetric gears.....	17
2.2.1 Bending strength of asymmetric gears – Evaluation of bending stress and influence of gear geometry parameters.....	17
2.2.2 Analytical determination of bending stress in asymmetric gears	18

2.2.3 Bending stress reduction through geometric modifications.....	19
2.2.4 Fatigue behavior of asymmetric gears	19
2.2.5 Stiffness and transmission error characteristics of asymmetric gears	20
2.3 Mechanical behavior of additively manufactured parts.....	21
2.3.1 Effect of build configuration on the mechanical properties of selective laser sintered specimens.....	22
2.3.2 Comparison of mechanical properties of injection-molded and selective laser sintered specimens	25
2.3.3 Additive manufacturing in gear prototyping.....	26
2.3.4 Fatigue performance of additively manufactured polymer gears	27
2.4 Summary of literature review and research gaps	28
Chapter 3 Materials and methods.....	31
3.1 Gear design and fabrication	32
3.1.1 Injection-molded gears.....	33
3.1.2 Selective laser sintered gears	35
3.2 Experimental study	38
3.2.1 In-house bending fatigue test rig.....	39
3.2.2 Bending fatigue test details.....	41
3.2.3 In-house static tooth deflection test rig.....	44
3.2.4 Static tooth deflection test details	45
3.2.5 Material characterization	47
3.3 Root bending stress in polymer gears – Influence of load sharing	48
3.3.1 Analytical determination of root bending stress	49
3.3.2 Calculation of load sharing ratio.....	52
3.4 Finite element analysis.....	52
3.4.1 Finite element model description.....	52
3.4.2 Boundary conditions	53
3.4.3 Model discretization and mesh convergence study	54

3.4.4 Material behavior	56
3.5 Summary	58
Chapter 4 Influence of asymmetric tooth profile on the bending fatigue behavior of polymer gears	59
4.1 Analysis of root bending stress in symmetric and asymmetric gears	59
4.1.1 Bending stress variation in a mesh cycle	60
4.1.2 Determination of form and stress correction factors.....	62
4.1.3 Sample ISO method calculation.....	66
4.1.4 Sample finite element method-based calculation	67
4.1.5 Analytical method vs. Finite element method	68
4.1.6 Symmetric vs. Asymmetric.....	69
4.2 Bending fatigue life of symmetric and asymmetric gears	70
4.2.1 Influence of load sharing on the bending fatigue strength.....	73
4.3 Gear surface temperature	76
4.4 Failure modes under bending fatigue.....	79
4.5 Summary	82
Chapter 5 Effect of polymer mating gear on the bending fatigue performance of asymmetric polymer gears	85
5.1 Root bending stress and load sharing behavior.....	85
5.2 Influence of mating gear material on the bending fatigue life.....	89
5.3 Analysis of deflection behavior	92
5.4 Analysis of hysteresis behavior	95
5.5 Failure modes in metal - polymer and polymer - polymer pairs.....	99
5.6 Summary	101
Chapter 6 Tooth deflection characteristics of asymmetric polymer gears.....	103
6.1 Details of numerical simulations	103
6.2 Mesh deflection in symmetric and asymmetric gear pairs.....	105
6.2.1 Phases in a mesh cycle.....	105

6.2.2 Mesh cycle duration.....	106
6.2.3 Load sharing pattern	107
6.2.4 Mesh deflection variation in a cycle	110
6.3 Tooth deflection variation in a cycle	112
6.4 Magnitude of mesh deflection	116
6.4.1 Peak mesh deflection in a cycle	116
6.4.2 Amplitude of mesh deflection in a cycle	117
6.5 Magnitude of tooth deflection in driven gears	118
6.5.1 Peak tooth deflection.....	118
6.5.2 Amplitude of tooth deflection in a cycle.....	119
6.6 Path of contact.....	120
6.7 Comparison of experimental and simulation values	122
6.8 Design implications	125
6.8.1 Tooth asymmetry	125
6.8.2 Mating gear material	126
6.9 Summary	127
Chapter 7 Bending fatigue performance of selective laser sintered polymer gears built in ‘flat’ configuration.....	129
7.1 Bending fatigue life of selective laser sintered gears.....	129
7.2 Thermal behavior of gears during testing	131
7.3 Investigation of failure mode	135
7.3.1 Crack propagation in additively manufactured parts	135
7.3.2 Failure morphology of selective laser sintered and injection-molded gears.....	137
7.4 Summary	139
Chapter 8 Effect of ‘on-edge’ build configuration on the bending fatigue behavior of selective laser sintered polymer gears	141
8.1 Effect of layer orientation on the bending fatigue strength	141
8.2 S-N curves of injection-molded and selective laser sintered gears.....	142

8.3 Surface temperature of gears	144
8.4 Crack propagation in gears	150
8.4.1 Examination of failure zone morphology	151
8.4.2 Fractography	154
8.5 Summary	156
Chapter 9 Conclusion and Scope for future work	157
9.1 Conclusions	158
9.2 Limitations and Scope for further research.....	158
References	161
Publications based on the research work.....	178





List of Figures

<i>Figure number</i>	<i>Title</i>	<i>Page number</i>
1.1	Polymer gears (unreinforced and reinforced).	2
1.2	Symmetric and asymmetric tooth configurations.	4
1.3	Standard build configurations in additive manufacturing.	6
1.4	Schematic illustration of single tooth bending fatigue test.	8
1.5	Sources of transmission error.	9
3.1	(a) Schematic representation of the gear geometry and (b) Symmetric and asymmetric teeth.	33
3.2	(a) Symmetric and asymmetric master and test gears and (b) Tensile specimen used in monotonic tests and flexure specimen used in DMA.	34
3.3	(a) Windsor GT-50 injection-molding machine and (b) Sinterstation 2500 selective laser sintering machine.	36
3.4	(a) Selective laser sintered and injection-molded gears and (b) Schematic representation of gear build configuration during selective laser sintering process.	37
3.5	Layer orientation in selective laser sintered gears built in ‘on-edge’ configuration.	38
3.6	(a) Bending fatigue test rig developed in-house, (b) Schematic illustration of the test rig, (c) Human-machine interface module, and (d) Servo drive inside the HMI.	40
3.7	(a) Typical loading waveform applied during the test and (b) Evolution of tooth deflection of a selective laser sintered gear tooth subjected to 5 Nm.	42
3.8	(a) Schematic representation of the meshing gears indicating the region of temperature measurement, (b) Close-up view of the teeth mesh, (c) Infrared thermal imager, and (d) a sample infrared image of the teeth mesh.	43

3.9 Experimental test rig used to measure static tooth deflection in polymer gears.....	45
3.10 Typical plots of experimental data: (a) Applied torque values in a test and (b) mesh deflection variation during a test.....	46
3.11 Material characterization data of Nylon 66: (a) Tensile stress-strain curve and (b) Frequency-dependent storage and loss moduli obtained from DMA.	48
3.12 Critical section parameters used in bending stress determination.	50
3.13 Gear pair model 1 of symmetric gear: (a) Kinematic model indicating boundary conditions, (b) Discretization, and (c, d) Element density in root and flank contact region. ...	55
3.14 Gear pair model 2 of asymmetric gear: (a) Kinematic model, (b) Discretization in teeth, and (c, d) Element density in root and flank regions.	55
3.15 Mesh convergence study: (a) Root bending stress and computational time corresponding to various element sizes, (b) Principal stress distribution in the gear teeth for the fillet element size of 3 μm , and (c) bending stress distribution in the root region.	56
4.1 (a) Bending stress variation across mesh cycle for symmetric and asymmetric configurations, (b, c) Principal stress in symmetric gear, (d, e) Principal stress in asymmetric gear configuration $20^\circ/34^\circ$, and (f, g) Principal stress in asymmetric gear configuration $34^\circ/20^\circ$	61
4.2 Critical section parameters of symmetric and asymmetric configurations based on ISO and FEM: (a, b) $20^\circ/20^\circ$, (c, d) $20^\circ/34^\circ$, and (e, f) $34^\circ/20^\circ$ (all dimensions are in mm).....	63
4.3 ISO- and FEM-based values of form factor, stress correction factor, and fillet stress factor.	69
4.4 (a) ISO- and FEM-based bending stresses of symmetric and asymmetric gears, (b, c) bending stress in symmetric gear, (d, e) bending stress in asymmetric configuration $20^\circ/34^\circ$, and (f, g) bending stress in asymmetric configuration $34^\circ/20^\circ$	71
4.5 Bending fatigue life distribution of symmetric and asymmetric gears.	72
4.6 Tooth deflections of symmetric and asymmetric gears.	73

4.7 (a) Maximum root bending stresses of symmetric and asymmetric gears, (b, c) bending stress distribution in symmetric gear, (d, e) bending stress distribution in asymmetric configuration 20°/34°, and (f, g) bending stress distribution in asymmetric configuration 34°/20°.....	74
4.8 von Mises stress distributions in symmetric and asymmetric gears subjected to 8 and 12 Nm: (a, b) 20°/20°, (c, d) 20°/34°, and (e, f) 34°/20° configurations.	75
4.9 Thermal behavior of 34°/20° configuration: (a) Typical surface temperature evolution during testing and (b, c, d, and e) IR thermographs of tooth at various stages.....	77
4.10 (a) Average surface temperature during testing and (b, c) IR thermograph of 34°/20° and 20°/34° configurations at 20000 s.....	78
4.11 Stereomicroscopic images of the bending fatigue failure in symmetric and asymmetric gear teeth: (a, b) 20°/20°, (c, d) 20°/34°, and (e, f) 34°/20° configurations. Multiple cracks on the drive side fillet and coast side cracks are indicated.	79
4.12 FESEM images of symmetric and asymmetric gear teeth: (a, b) 20°/20°, (c, d) 20°/34°, and (e, f) 34°/20° configurations.....	80
4.13 Magnified view of crack tips of symmetric and asymmetric gear teeth: (a, b) 20°/20°, (c, d) 20°/34°, and (e, f) 34°/20° configurations.	81
5.1 Bending stress in metal - polymer (M-P) and polymer - polymer (P-P) pairs of symmetric and asymmetric configurations: (a) Maximum root bending stress, (b, c) Principal stress distribution in 20°/20° configuration, (d, e) Principal stress distribution in 20°/34° configuration, and (f, g) Principal stress distribution in 34°/20° configuration.	87
5.2 Load sharing in metal - polymer (left) and polymer - polymer gear pairs (right): (a) LSR corresponding to 8, 10, and 12 Nm, (b, c) von Mises stress distribution in 20°/20° configuration subjected to 8 Nm, (d, e) von Mises stress distribution in 20°/34° configuration subjected to 8 Nm, and (f, g) von Mises stress distribution in 34°/20° configuration subjected to 8 Nm.....	88
5.3 Bending fatigue life of metal-polymer and polymer-polymer gear pairs.	90

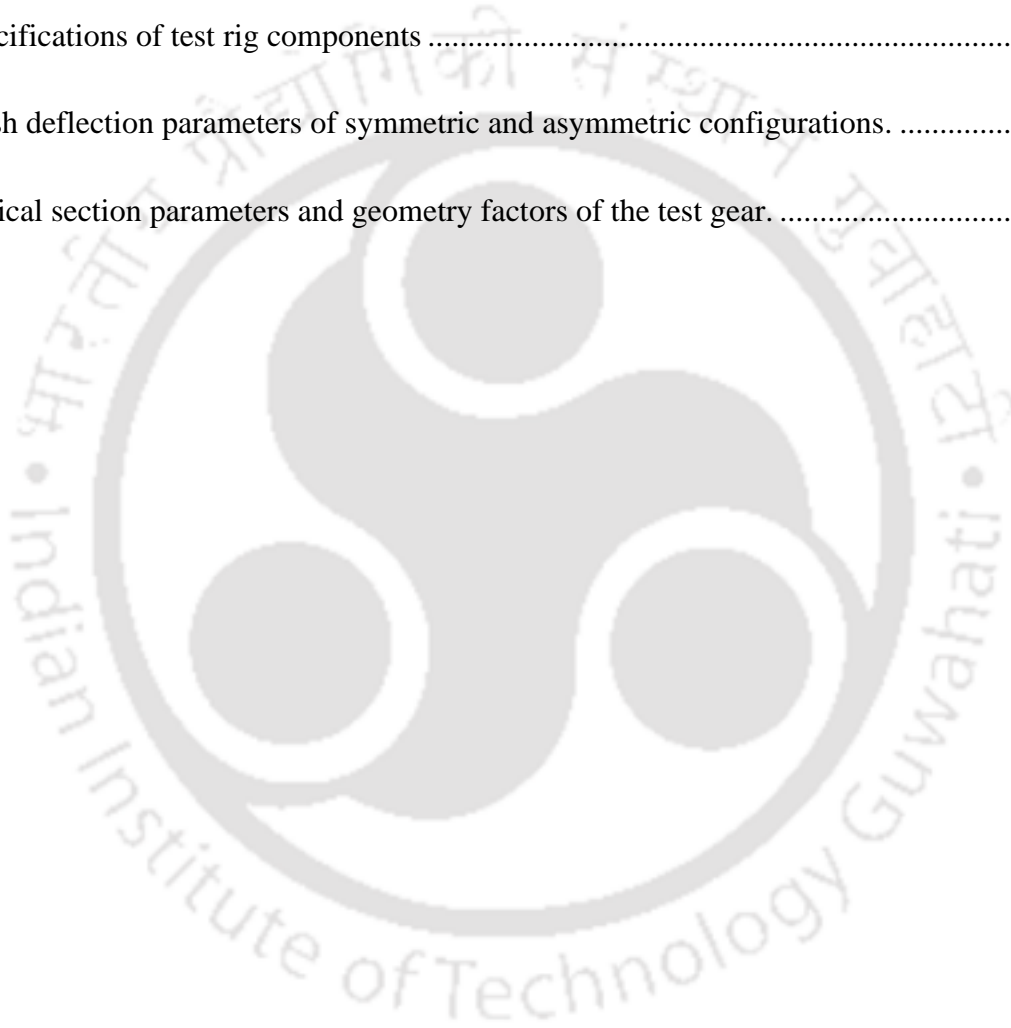
5.4 Thermal behavior of gears: (a) Average surface temperatures of metal - polymer and polymer - polymer gear pairs and (b, c) Temperature distribution at cycle 10000 in 34°/20° and 20°/34° configurations subjected to 10 Nm.	91
5.5 Tooth deflections of asymmetric gear teeth subjected to 8 and 12 Nm: (a) Metal – Polymer pairs, (b) Polymer - Polymer asymmetric pairs, (c, d) Tooth deflection variation in metal - polymer pairs, and (e, f) Tooth deflection variation in polymer - polymer pairs.	93
5.6 Hysteresis loops of metal - polymer pairs corresponding to 12 Nm: (a) comparison of 34°/20° and 20°/34° configurations at cycle 10000 and (b) evolution of loops with progression of cycles.	96
5.7 Hysteresis behavior of metal - polymer and polymer - polymer pairs subjected to 12 Nm: (a) hysteresis loops of 34°/20° configuration at cycle 50 and (b) hysteresis loop areas of asymmetric configurations at cycle 10000.	97
5.8 Failed teeth of symmetric and asymmetric configurations: (a, c, e) metal-polymer pairs and (b, d, f) polymer-polymer pairs.	98
5.9 FESEM images of 20°/20°, 34°/20° and 20°/34° test gears (top to bottom): (a, c, e) metal-polymer pairs and (b, d, f) polymer-polymer pairs.	99
5.10 Magnified view of crack tips of 20°/20°, 34°/20° and 20°/34° configurations (top to bottom): (a, c, e) metal-polymer pairs and (b, d, f) polymer-polymer pairs.	100
6.1 (a) Path of measurement along the tooth depth, (b) Rotation of driver gear during loading, and (c) Typical driver gear rotation at the end of analysis.	104
6.2 (a) Single tooth contact and (b) double tooth contact.	105
6.3 Typical mesh deflection curves of symmetric gear pairs subjected to 1 Nm. The extents of handover zones are indicated.	106
6.4 Predicted mesh deflections of symmetric and asymmetric gear pairs during a cycle for: (a) 1 Nm and (b) 1.5 Nm.	107
6.5 Load sharing ratio of symmetric and asymmetric gears for: (a) 1 Nm and (b) 1.5 Nm. ..	108
6.6 Tooth deflection variation in a mesh cycle for: (a) 1 Nm and (b) 1.5 Nm.	113

6.7 Tooth deflection variation in driven gear subjected to 1 Nm at the pitch point: (a, b) 20°/20°, (c, d) 20°/34°, and (e, f) 34°/20° configuration.	115
6.8 Peak mesh deflection values of metal - polymer and polymer - polymer gear pairs.....	116
6.9 Mesh deflection amplitude of symmetric and asymmetric configurations.....	117
6.10 Maximum tooth deflection values of symmetric and asymmetric configurations.....	118
6.11 Amplitude of tooth deflection in symmetric and asymmetric gears.....	119
6.12 Theoretical path of contact.....	120
6.13 Predicted contact path of metal - polymer and polymer - polymer gear pairs subjected to 1 and 1.5 Nm: (a) 20°/20°, (b) 34°/20°, and (c) 20°/34°.	121
6.14 Mesh deflection values determined from experiments: (a) 1 Nm and (b) 1.5 Nm.	123
6.15 Deviations between experimental and simulation values: (a) 20°/20°, (b) 34°/20°, and (c) 20°/34° configuration.....	124
7.1 Stress-life curves of injection-molded and selective laser sintered gears.....	130
7.2 Average surface temperature of the test gears at various loads.	132
7.3 IR thermal images of injection-molded (left) and selective laser sintered (right) gears subjected to 6 and 8 Nm: (a - d) 2500 cycle and (e - h) 50000 cycle.	134
7.4 Surface temperature evolution in selective laser sintered and injection-molded gears subjected to 6 and 8 Nm.....	135
7.5 (a) The three standard build configurations of additively manufactured compact tension specimens and (b) Bending fatigue crack in selective laser sintered gear built in 'flat' configuration.....	136
7.6 Failure zone images of test gears loaded at 8 Nm: (a, c, e, g) selective laser sintered gear built in 'flat' configuration and (b, d, f, h) injection-molded gear.....	138
8.1 Bending fatigue life of selective laser sintered gear teeth subjected to 5 Nm.	142

8.2 S-N curves of injection-molded and selective laser sintered gears.....	143
8.3 Infrared thermal images at 50, 75, and 100% of the lifetime corresponding to the load of 6 Nm: (a, b, c) injection-molded gear, (d, e, f) selective laser sintered gear 40° configuration, and (g, h, i) selective laser sintered gear 160° configuration.....	145
8.4 Average surface temperature of test gears as a function of the applied torque.	146
8.5 Surfaces of injection-molded gear tooth (a, c, e) and selective laser sintered gear tooth (b, d, f) in the fillet region. Broad and close-up views of the surfaces are presented.	147
8.6 Orientation of layer planes in selective laser sintered gears.	148
8.7 Bending fatigue cracks in test gears observed under stereomicroscope (a, c, e) and FESEM (b, d, f). (a, b) Injection-molded gear, (c, d) Selective laser sintered gear tooth 40° configuration and (e, f) Selective laser sintered gear tooth 160° configuration.	151
8.8 Magnified view of the bending fatigue cracks as observed under FESEM: (a, b) Injection-molded gear, (c, d) Selective laser sintered gear tooth 40° configuration and (e, f) Selective laser sintered gear tooth 160° configuration.	152
8.9 Crack propagation in injection-molded and selective laser sintered gear teeth.....	153
8.10 Fracture surfaces of test gears viewed under FESEM. (a, b) Injection-molded gear, (c, d) Selective laser sintered gear tooth 40° configuration and (e, f) Selective laser sintered gear tooth 160° configuration.	155

List of Tables

<i>Table number</i>	<i>Title</i>	<i>Page number</i>
3.1	Gear geometry parameters	32
3.2	SLS process parameters	36
3.3	Specifications of test rig components	41
6.1	Mesh deflection parameters of symmetric and asymmetric configurations.	126
7.1	Critical section parameters and geometry factors of the test gear.	130

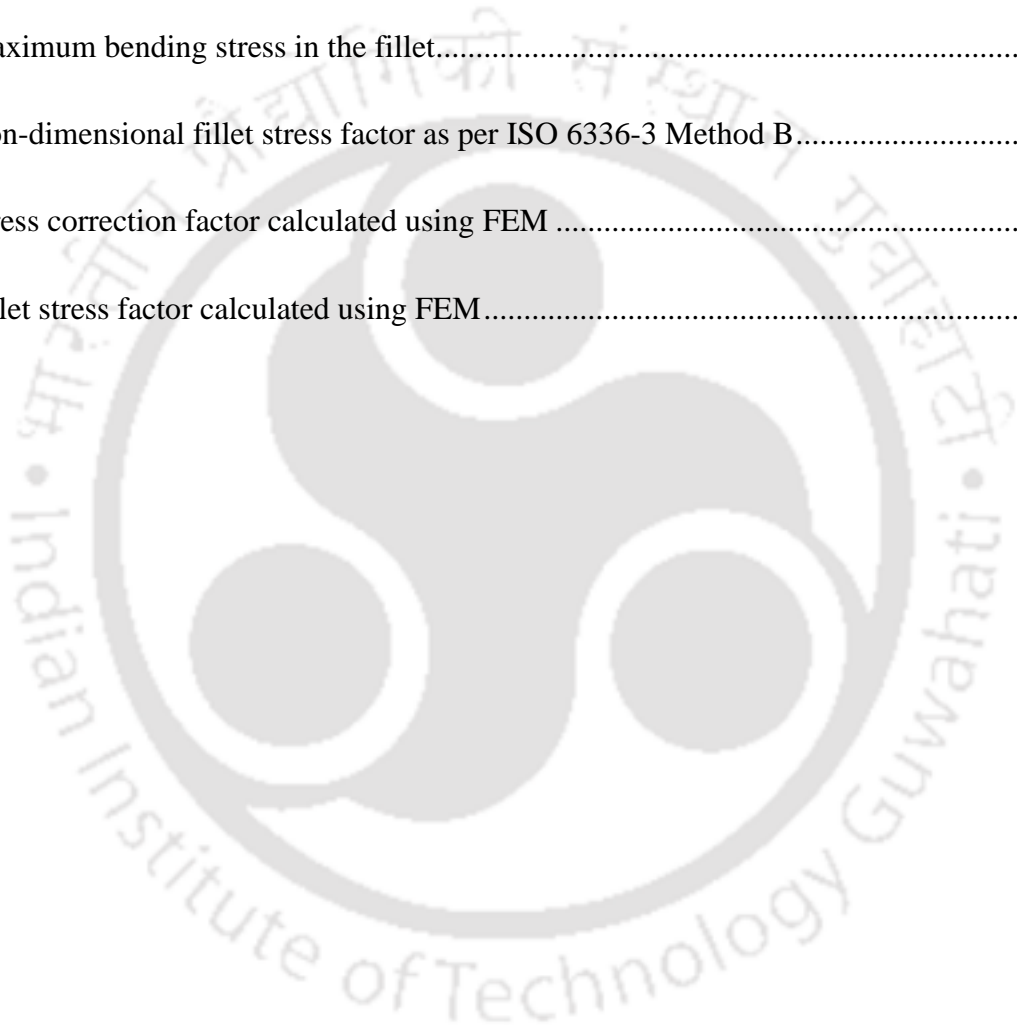




List of Equations

<i>Equation number</i>	<i>Title</i>	<i>Page number</i>
3.1	Maximum tensile stress at the root as per ISO 6336-3 Method B	51
3.2	Nominal root bending stress as per ISO 6336-3 Method B	51
3.3	Form factor expression as per ISO 6336-3 Method B	51
3.4	Stress correction factor expression as per ISO 6336-3 Method B	51
3.5	Non-dimensional parameter L of stress correction factor formulation	51
3.6	Non-dimensional parameter q_s of stress correction factor formulation	51
3.7	Non-dimensional parameter a of stress correction factor formulation	51
3.8	Load share ratio of the leading contact pair	52
4.1	Angle of tangent on the coast side root fillet	62
4.2	Radius of the highest point of single tooth contact	62
4.3	Radius of base circle	63
4.4	Length of the line of action	64
4.5	Base pitch	64
4.6	Load angle at the highest point of single tooth contact	64
4.7	Pressure angle at the highest point of single tooth contact	64
4.8	Parameter θ used for calculating load angle at the highest point of single tooth contact ..	64
4.9	Tip angle	64
4.10	Involute function of tip angle	64
4.11	Involute function of the angle at the highest point of single tooth contact	64

4.12 Form factor expression including compressive stress	65
4.13 Stress correction factor expression	65
4.14 Non-dimensional parameter L of stress correction factor formulation	65
4.15 Non-dimensional parameter q_s of stress correction factor formulation	65
4.16 Non-dimensional parameter a of stress correction factor formulation	65
4.17 Maximum bending stress in the fillet.....	65
4.18 Non-dimensional fillet stress factor as per ISO 6336-3 Method B.....	65
4.19 Stress correction factor calculated using FEM	66
4.20 Fillet stress factor calculated using FEM.....	66



Abbreviations

ABS	Acrylonitrile Butadiene Styrene
AGMA	American Gear Manufacturers Association
AISI	American Iron and Steel Institute
AM	Additive Manufacturing
ASTM	American Society for Testing and Materials
BEV	Battery Electric Vehicle
CT	Compact Tension specimen
DIN	Deutsches Institut für Normung e.V.
DMA	Dynamic Mechanical Analysis
DTC	Double Tooth Contact
FDM	Fused Deposition Modeling
FEM	Finite Element Method
FESEM	Field Emission Scanning Electron Microscope
FFF	Fused Filament Fabrication
HCF	High Cycle Fatigue
HCR	High Contact Ratio
HMI	Human Machine Interface
HPSTC	Highest Point of Single Tooth Contact
IM	Injection Molding
ISO	International Organization for Standardization
IR	Infrared
LCF	Low Cycle Fatigue

LPSTC	Lowest Point of Single Tooth Contact
LSR	Load Sharing Ratio
MPCM	Multi Pair Contact Model
MPLM	Multi Point Load Model
NCR	Normal Contact Ratio
PBT	Poly(Butylene Terephthalate)
PEEK	Polyether Ether Ketone
PEI	Poly Ether Imide
POM	Polyoxymethylene
RM	Rapid Manufacturing
RP	Rapid Prototyping
SAE	Society of Automotive Engineers
SAP	Start of Active Profile
SLA	Stereolithography
SLS	Selective Laser Sintering
SS	Stainless Steel
STBFT	Single Tooth Bending Fatigue Test
STC	Single Tooth Contact
STE	Static Transmission Error
TE	Transmission Error
VDI	Verein Deutscher Ingenieure

Notations

Latin symbols

a	Dimensionless parameter in stress correction factor formula
b	Face width (mm)
c	Center distance between axes (mm)
E	Young's modulus (GPa)
F_n	Normal force acting on the tooth (N)
F_t	Tangential force acting on the tooth (N)
h_f	Bending moment arm (mm)
K_A	Application factor
K_v	Dynamic factor
L	Dimensionless parameter in stress correction factor formula
m	Module (mm)
p	Base pitch (mm)
q_s	Dimensionless parameter in stress correction factor formula
r	Radius of the circle (mm)
s_f	Critical section thickness (mm)
T	Torque (Nm)
Y_B	Rim thickness factor
Y_{DT}	Deep tooth factor
Y_F	Form factor
Y_S	Stress correction factor

Greek symbols

α	Pressure angle ($^{\circ}$)
ε	Contact ratio
ν	Poisson's ratio
ρ	Material density (kg/m^3)
ψ	Angle of tangent at critical section ($^{\circ}$)
θ	Difference between the pressure angle at HPSTC and load angle
ν	Tip angle

Mixed symbols

σ_F	Maximum root bending stress (MPa) (Chapter 3), Fillet stress factor (Chapter 4)
σ_{F0}	Nominal bending stress (MPa)
α_{Load}	Load angle ($^{\circ}$)
ρ_f	Radius of fillet at the critical section (mm)
$K_{F\alpha}$	Transverse load factor
$K_{F\beta}$	Face load factor
Y_{β}	Helix angle factor
Y_{ε}	Contact ratio factor

Subscripts

a	Addendum circle
b	Base circle
c	Coast side of tooth
d	Drive side of tooth
FEM	Value attained from finite element method

<i>g</i>	Gear
<i>HPSTC</i>	Highest point of single tooth contact
<i>ISO</i>	Value attained from ISO method
<i>max</i>	Maximum value
<i>o</i>	Pitch circle
<i>p</i>	Pinion
<i>tip</i>	Tip circle
<i>w</i>	Working circle





Chapter 1

Introduction

Gear is a mechanical component that transmits power and motion by progressive engagement of projections called teeth (Maitra, 1994). Gear drives are optimal for efficiently converting torque and speed within a wide power range in a cost-effective manner. Gear drives have been in use for a long time, with the earliest recorded application dating back to 2600 BC (Dudley and Radzevich, 2012). While early gear designs focused more on reliable transmission than efficiency, the requisite gear performance has increased steadily over time. Modern transmission systems demand gears with greater load-carrying capacity, higher operational velocities, lesser noise and vibrations, lighter weight, and cheaper production and operating costs.

The endeavor to decrease the mass of components has prompted engineers to devise innovative and disruptive solutions for increasing the power density of vehicle powertrains. The construction of light-weight structures entails alternate materials, topology optimization, and an integrated design approach. Consequently, in gear design, plastics enable the realization of low weight and cost-effective designs. In addition, the digitalization of the design process – three-dimensional geometric modeling and simulations to predict the gear behavior – is essential for attaining high-performance designs. The rapidly advancing additive manufacturing (AM) technologies facilitate one-off and low-volume productions of gears at acceptable costs. Thus, plastic materials, digitalized design, and additive manufacturing are integral for responding to the ever-rising challenges in the gear industry.

1.1 Polymer gears – Current usage and challenges in deployment

Historically, polymers have elicited significant interest in gear designers due to low material density and cheaper material costs. Other advantages include lower friction that enables operation without lubrication and the capacity to dampen noise and vibrations (Kapelevich, 2019b). Despite the operational and cost advantages with respect to metal gears, certain inherent limitations hinder the adoption of polymer gears. The primary disadvantages are inadequate flexural strength and surface durability, which limits the load-carrying capacity of

gears. Also, the influence of temperature and humidity on material properties, greater tooth deflection caused by the low modulus of elasticity, and inferior geometric accuracy associated with the injection molding (IM) process complicate the design process. As a result, early use of polymer gears was restricted to lightly-loaded motion transmission applications. Figure 1.1 depicts an assortment of unreinforced and reinforced polymer gears.

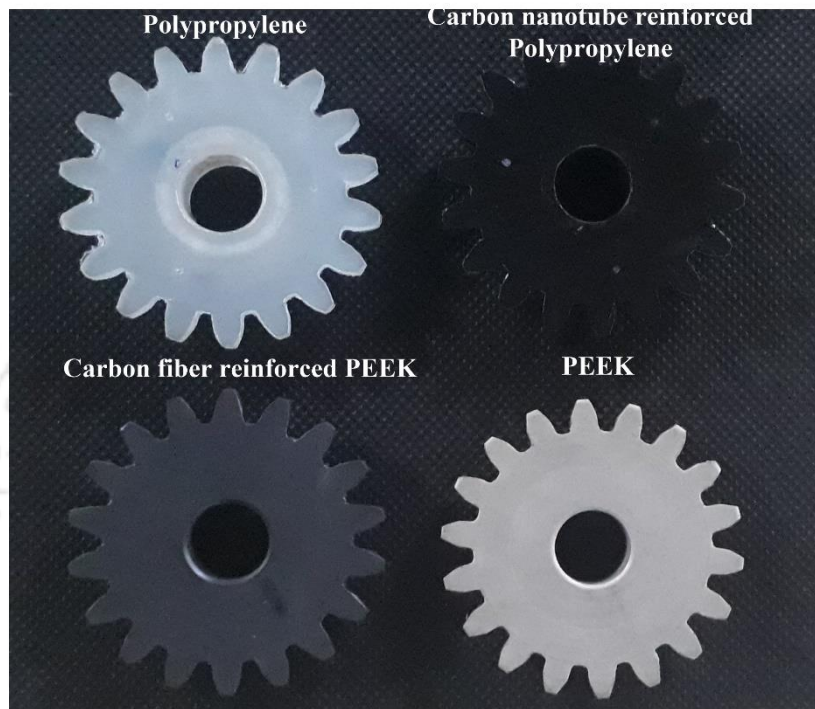


Fig. 1.1 Polymer gears (unreinforced and reinforced).

In recent years, the development of polymer resins with superior and consistent material properties has significantly improved the load-carrying capacity of polymer gears (Smith and Ulrich, 2012). Also, fiber reinforcements and anti-friction additives offset insufficient flexural strength and wear resistance. Advancements in the injection molding process have resulted in greater control over the accuracy of polymer gears. Consequently, various moderate load applications such as cameras, printers, washing machines, medical pumps, and robotic actuators increasingly use polymer gears (Kapelevich, 2019b). In automobiles, polymer gear usage includes actuators for window lifting, door locking, light adjustment, and electric power steering (Fink *et al.*, 2019).

The material of the mating gear influences multiple parameters of polymer gear performance, such as fatigue life, operating temperature, and failure mode (Mao *et al.*, 2009). Polymer gears are operated in two types of material engagements: metal - polymer and polymer - polymer material pairs. Each type of engagement offers specific advantages with respect to operational

performance and cost. Depending on the function, a polymer - polymer gear pair can be more advantageous than a metal - polymer gear pair in terms of weight reduction and cost savings. Also, using materials with similar stiffness for driver and driven gears averts the stiffness mismatch observed in metal - polymer gear pairs.

Greater tooth size and higher safety factors are essential in polymer gear designs. The principles of metal gear design are not necessarily appropriate for polymer gears. Polymer gears with optimized tooth geometry operating in conjunction with metal gears under oil-lubricated conditions can transmit the power needed to propel smaller passenger cars (Götz and Stahl, 2019). Although advanced polymer resins, fiber reinforcements, wear-resistant additives, and oil lubrication enhance the load-carrying capacity, tooth geometry optimization is necessary to realize the peak performance potential of a polymer gear design. In this regard, a tooth geometry that is particularly beneficial to polymer gears is the asymmetric tooth form.

1.2 Asymmetric gears – Potential in polymer gearing

Asymmetric gears consist of teeth with dissimilar pressure angles on the drive side and coast side flanks (Figure 1.2). Asymmetric gears are appropriate for unidirectional drives in which the coast side flank is unloaded or moderately loaded. Typically, metal gear applications with demanding performance requirements employ asymmetric gears in case non-standard symmetric gears with optimal geometry are unable to deliver the desired performance. Some of the modern applications of asymmetric gears include gearboxes of aircraft engines such as gas turbine engines and turboprop engines (Kapelevich, 2019a). The independent selection of pressure angles for drive and coast flanks in asymmetric gears permits the designer to optimize the strength and stiffness of the tooth.

Asymmetric gears offer two configurations based on the magnitude of pressure angle on the drive flank: pressure angle on the drive flank (α_{drive}) greater than that of the coast flank and pressure angle on the coast flank (α_{coast}) greater than that of the drive flank. The configuration with a greater pressure angle on the coast flank, also called the 'buttress tooth,' provides greater tooth stiffness. On the other hand, the configuration with a greater pressure angle on the drive flank enhances the surface durability by decreasing contact stress. Both configurations reduce the bending stress in the root region. The asymmetric gears are not widely used despite the significant advantages conferred by the asymmetric tooth form. The aversion to using asymmetric gears is attributable to the increased costs of developing customized tooling for machining different pressure angles on each flank.

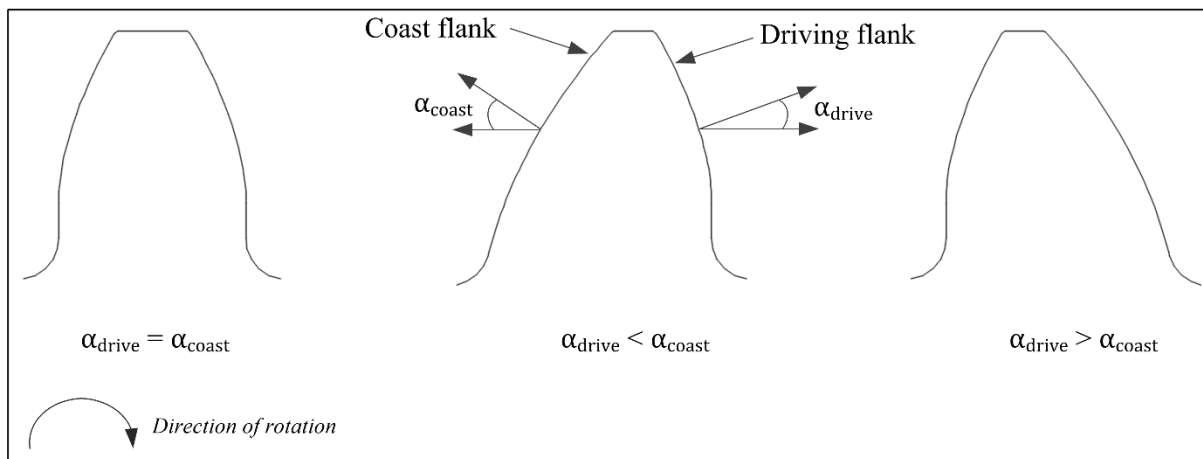


Fig. 1.2 Symmetric and asymmetric tooth configurations.

Although cost variation is insignificant in cases of mass production, the increased costs can be prohibitive in low-volume productions. Also, unlike the relatively simple design process in symmetric gears, selecting pressure angles and other geometric parameters of asymmetric gears require detailed analysis. Moreover, customization of pressure angles reduces interchangeability. Therefore, asymmetric gears are considered only if the enhanced performance of the design justifies the increase in costs and efforts.

The forming processes such as injection molding are not affected by the issues related to custom tooling. As each unique design requires a separate mold, the tooling costs of symmetric and asymmetric gears are comparable. For polymer gear fabrication, injection molding is generally preferred over machining as it facilitates design flexibility and a higher production rate, resulting in cost-effectiveness (Kapelevich, 2019b). Hence, utilizing an asymmetric tooth profile could enhance the performance of polymer gears without incurring any significant increase in manufacturing costs. Although tooling costs are similar for symmetric and asymmetric gears in injection molding, tooling cost is inevitable. In low-volume and one-off productions, such as the gears developed as functional prototypes during the design process, additive manufacturing can further decrease costs by eliminating tooling.

1.3 Additive manufacturing and the resurgence of customized designs

Additive manufacturing is a freeform fabrication technique that builds parts by sequentially depositing the material in multiple layers. In contrast to conventional processes, AM presents numerous advantages such as shorter design cycle time, greater freedom for increasing the geometric complexity, customization of products, and economical manufacturing of parts in lower volumes (Goodridge, Tuck and Hague, 2012). Over the years, significant progress has

transformed AM from a tool of Rapid prototyping (RP) to Rapid Manufacturing (RM). From the inception of AM technologies, the research and development of gear transmissions involved rapid prototyping techniques such as stereolithography to accelerate the implementation of new gear designs.

As mentioned earlier, polymer gears require customized geometry to enhance fatigue performance. AM permits the designer to explore the usage of customized, high-performance tooth geometries, which otherwise are infeasible to fabricate using conventional manufacturing methods economically. Traditionally, gear design parameters such as geometry, dimensions, material, and manufacturing method were selected based on the application's demands. However, industrial standardization and the compulsions of mass manufacturing have led to an indirect design process in which the gear geometry and dimensions are determined based on the parameters of a standardized rack. But, such standardized gears are slowly losing relevance in an increasingly dynamic market where customized, high-performance products are necessary to meet consumer demand. Hence, manufacturers must complement conventional manufacturing practices with AM to deliver solutions at competitive prices.

Among AM processes, selective laser sintering (SLS) presents considerable advantages over other processes in one-off as well as low-volume manufacturing of performance parts. Selective laser sintering is a powder bed fusion process in which thin layers of powdered material are deposited consecutively and sintered using laser power to form the end part. Unlike the Fused Deposition Modeling (FDM) process, which is limited by the material's melting point (Carneiro, Silva and Gomes, 2015), SLS can process a diverse class of materials such as polymer, metals, ceramics, and composites (Goodridge, Tuck and Hague, 2012). Hence, durable polymers with a higher melting point can be considered for design. Also, SLS supports the simultaneous printing of multiple parts on the build platform, which is essential for producing parts in significant numbers. Hence, SLS could be utilized for additive manufacturing of high-performance polymer gears.

In AM, the build configuration of a part during the layer deposition affects the layer orientation, influencing the performance of the part. Theoretically, AM allows for a part to be built in multiple configurations. For example, the standard build configurations of tensile test specimens are: flat, on-edge, and upright (Munguia and Dalgarno, 2014). Figure 1.3 illustrates the three standard build configurations of a tensile specimen. Among the three, the 'upright' configuration can accommodate more specimens on the build platform as the space occupied

by each specimen is lesser. In cylindrical components such as gears, 'on-edge' and 'upright' build configurations yield end parts with identical layer orientation. The 'flat' configuration imparts a uniform layer pattern in all gear teeth. On the other hand, 'on-edge' and 'upright' configurations produce gears in which layer orientation is different in each tooth. Generally, the build configuration that accommodates the highest number of parts in the build platform is desirable, as it increases the production volume.



Fig. 1.3 Standard build configurations in additive manufacturing.

The operational performance is the foremost factor that determines the deployment of a particular gear design. Accordingly, the additively manufactured polymer gears must deliver the requisite performance demanded by an application, irrespective of the design and manufacturing advantages. As injection molded gears are the incumbents in polymer gear transmissions, the load-carrying capacity of AM gears in terms of bending fatigue strength and surface durability must be comparable with injection-molded gears.

1.4 Gear tooth breakage – Importance of the design against bending fatigue

The gear tooth breakage caused by bending fatigue is a standard failure mode in gears under continuous operation (Fernandes, 1996). The normal component of the force transmitted by a gear tooth applies a bending moment, inducing bending stress. Bending fatigue is the progressive reduction of bending strength of a gear tooth caused by cyclic bending stress.

Bending fatigue initiates cracks in the root fillet region that is subjected to tensile stress. Bending fatigue failure comprises three stages: crack initiation, crack propagation, and fracture. The crack initiation and propagation phases consume a significant part of the gear life. Once the crack propagates to a critical length, uncontrolled propagation commences, resulting in fracture. Bending fatigue failures are usually caused by high cycle fatigue (HCF), in which the maximum cyclic bending stress is below the material yield strength. Low cycle fatigue (LCF) failures, in which a gear tooth fails within 10,000 cycles, are quite rare and occur if the gear tooth is overloaded (ANSI/AGMA 1010-F14, 2014).

Although gears undergo various other failures such as wear, Hertzian fatigue, scuffing, plastic deformation, etc., the bending fatigue induced tooth breakage is particularly undesirable owing to the potential damage it can cause. The onset of bending fatigue crack in one tooth usually triggers a sequence of failures involving adjacent teeth. As the crack propagates in one tooth, the load sustained by adjacent teeth increases, inducing bending fatigue failures in those teeth. Tooth breakage can disengage the drive from the power source in certain instances, immediately halting the power transmission. In industries, such sudden malfunctioning imposes unscheduled maintenance breaks, disrupting the production activities. Moreover, tooth breakage in critical applications like helicopter gearboxes can be catastrophic (Lewicki and Ballarini, 1997), causing fatalities and material damage. Thus, bending fatigue strength is a crucial aspect of a gear design.

Generally, the load-carrying capacity of polymer gears is evaluated by dynamic testing, in which a gear pair rotates continuously against each other until failure (AGMA 946-A21, 2021). The dynamic testing must be conducted in conditions simulating the actual service environment to obtain a realistic assessment. Such full-scale dynamic tests are costly and time-consuming. The bending fatigue strength of gears, on the other hand, is evaluated by means of non-rotating pulsator tests. The test gear remains stationary in pulsator tests, and load is repeatedly applied on a single tooth until failure.

The single tooth bending fatigue test (STBFT) is a pulsator test used for evaluating the effect of design variables such as material, geometry, and processing parameters on the bending fatigue strength of gears (SAE J1619, 2017). Figure 1.4 depicts a schematic representation of the single tooth bending fatigue test. Polymer gears, in general, experience both bending fatigue and contact fatigue failures as external lubrication is not common. However, to use polymer gears in high-performance applications, external lubrication such as oil lubrication is necessary

to reduce wear and dissipate heat (Smith and Ulrich, 2012). As bending fatigue failure is the usual failure mode in gears operating under oil lubrication, bending fatigue could be the predominant cause of failure in future polymer gear applications.

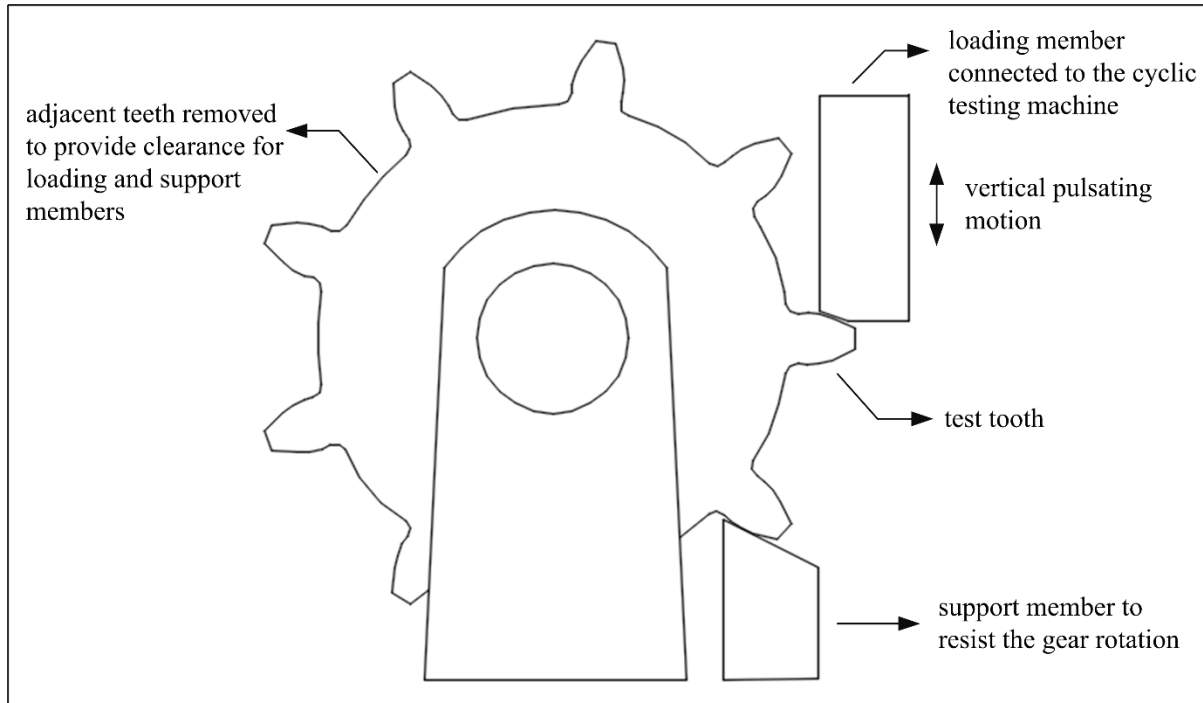


Fig. 1.4 Schematic illustration of single tooth bending fatigue test.

1.5 Gear tooth deflection – Transmission error, noise and vibrations

Vibrations in mechanical systems affect component performance, and noise adversely impacts human comfort. Therefore, considerable effort is expended to reduce the noise and vibrations emanating from the transmission system. The mesh stiffness of a gear pair has significant implications for a system's noise and vibration behavior. Theoretical kinematic calculations assume an ideal gear tooth to be rigid with infinite stiffness. However, gear teeth undergo considerable deflection during loading due to material elasticity. The gear tooth deflection comprises deflections due to bending, shear, Hertzian loads, and the tooth rotation with respect to the root (Wang and Howard, 2005).

The inaccuracies in tooth geometry and elastic deflections affect the conjugate motion, resulting in transmission error. The transmission error (TE), which is the deviation between the ideal and actual position of the gear tooth, acts as the primary source of vibration in gear systems (Smith, 2003). The magnitude of transmission error in metal gears is dominated by factors related to geometric inaccuracy. Conversely, stiffness factors determine the magnitude

of TE in polymer gears, as lesser material stiffness leads to significantly larger tooth deflection (Meuleman *et al.*, 2007). Figure 1.5 shows the various factors that contribute to the gear transmission error. Although the superior damping capacity of polymers moderates the vibrations and noise, higher tooth deflection induces contact outside the theoretical line of action, causing interference and accelerated wear in the flank region (Walton *et al.*, 1995). Also, polymer gears are extensively used in precision motion applications, which demand tighter control over tooth deflections. As the mesh stiffness crucially influences kinematic and fatigue performances in polymer gears, developing a gear design with appropriate mesh stiffness is essential.

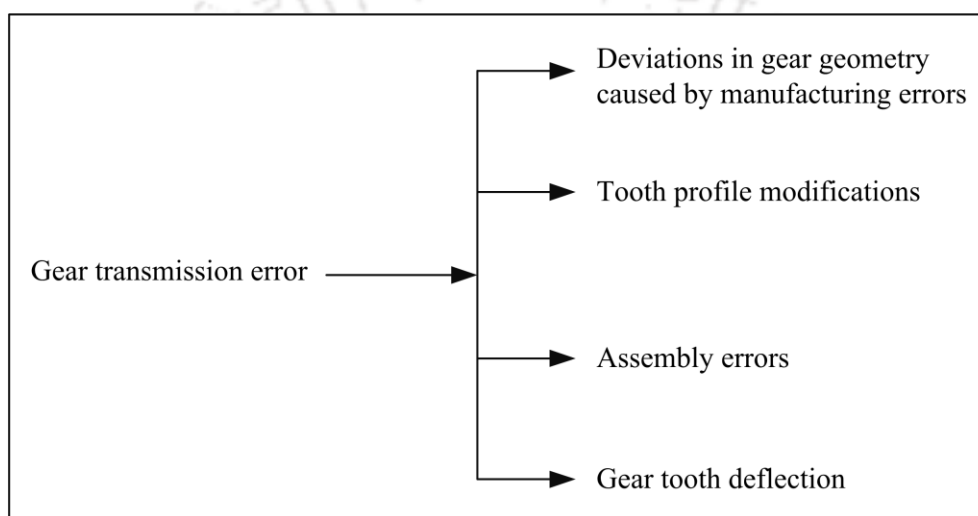


Fig. 1.5 Sources of transmission error.

1.6 Research motivation

The asymmetric tooth form can increase the load-carrying capacity of injection-molded polymer gears without additional costs. Preliminary investigations (Kumar, Kommogi and Senthilvelan, 2009; Mohan and Senthilvelan, 2014) have demonstrated the potential of the asymmetric tooth form to improve the fatigue performance of polymer gears. As the bending fatigue strength determines tooth breakage, a detailed study on the bending fatigue behavior of asymmetric polymer gears is warranted.

The performance of a polymer gear is significantly affected by the mating gear material. The operation of a polymer - polymer gear pair is advantageous owing to lesser inertia, balanced mesh stiffness, reduced weight, and lower manufacturing costs. These advantages motivate the designer to operate asymmetric polymer gears in polymer - polymer engagement.

Consequently, it is necessary to investigate the bending fatigue behavior of asymmetric polymer gear mated with another polymer gear.

The mesh stiffness significantly influences the accuracy of motion in polymer gears and affects the gear performance in both precision gearing and power gearing applications. The asymmetric tooth form has higher tooth stiffness and can decrease noise and vibrations (Kapelevich, 2013). These potential advantages motivate an evaluation of the tooth deflection characteristics of asymmetric polymer gears. As materials of the gear pair affect the mesh stiffness, the deflection behavior of both metal - polymer and polymer - polymer gear pairs must be investigated.

The additive manufacturing process of selective laser sintering is preferable for economical manufacturing of one-off and low-volume orders of polymer gears with greater tooth strength. Polymer gears manufactured by the fused deposition modeling process exhibit satisfactory performance compared to injection-molded gears (Zhang, Purssell, *et al.*, 2020). Similarly, the monotonic and fatigue performance of selective laser sintered tensile specimens was comparable to that of injection-molded specimens (Van Hooreweder *et al.*, 2013). These encouraging results merit a comparative evaluation of the bending fatigue behavior of polymer gears manufactured by selective laser sintering and injection molding. As the build configuration influences the mechanical properties, a study on the bending fatigue behavior of selective laser sintered gears built in other configurations is essential. This research endeavors to address the aforementioned issues related to polymer spur gears.

1.7 Aims of research

The current research aims to:

- Study the influence of asymmetric tooth profile and polymer mating gear on the bending fatigue behavior and tooth deflection behavior of injection-molded polymer spur gears.
- Investigate the effect of the selective laser sintering manufacturing method and build configuration on the bending fatigue behavior of polymer spur gears.

1.7.1 Research method

The above research aims were realized through the following steps:

- Experimental determination of the bending fatigue life of injection-molded symmetric and asymmetric polymer gears mated with metal gears using bending fatigue tests.

- Experimental determination of the bending fatigue life of injection-molded symmetric and asymmetric polymer gears mated with polymer gears using bending fatigue tests.
- Numerical prediction of the static tooth and mesh deflections of symmetric and asymmetric polymer gears mated with metal and polymer gears using finite element analysis.
- Experimental determination of the static mesh deflections of symmetric and asymmetric polymer gears mated with metal and polymer gears by static load tests.
- Experimental determination of the bending fatigue life of selective laser sintered polymer gears built in 'flat' and 'on-edge' build configurations using bending fatigue tests.

1.8 Organization of the thesis

The thesis is structured into nine chapters. The motivation for the current research, research aims, review of the relevant literature, and the methods adopted to achieve the research objectives are covered in Chapters 1-3. The results obtained from the present work are reported in Chapters 4-8. Chapter 9 discusses the significant outcomes of the research and outlines the scope for future works. A concise overview of the contents of each chapter is given below:

Chapter 1 describes the current state of polymer gear usage in the industry and signifies the potential of asymmetric tooth form and additive manufacturing in the development of polymer gears for high-performance applications. The factors motivating the current research have been discussed. The aims and objectives of the research are outlined at the end of the chapter.

Chapter 2 extensively reviews the literature related to the topics of interest and concisely describes the methods adopted and results obtained in those works. Previous works dealing with the strength and stiffness behavior of asymmetric gears, the influence of metal and polymer mating gears on the behavior of polymer gears, and the stiffness and transmission error characteristics of polymer gears have been discussed. The review also includes a survey of works that investigated the performance of additively manufactured gears. Specimen-level studies that evaluated the influence of layer orientation on the mechanical properties of additively manufactured specimens are also discussed.

Chapter 3 describes the various aspects of analytical calculations, experimental gear tests, and numerical simulations carried out during research. The analytical calculation procedures utilized to compute bending stress and load sharing ratio are described. Comprehensive descriptions of gear fabrication, test rigs, and test procedures are given. Also, a detailed account of the finite element models is included.

Chapter 4 deals with the bending fatigue performance of symmetric and asymmetric polymer gears mated with metal gears. The bending fatigue strength and failure morphology of the gears are reported. A detailed discussion on the test gears' bending stress, form factor, and stress correction factor is presented.

Chapter 5 discusses the impact of the polymer mating gear on load sharing, bending fatigue life, operating temperature, and failure morphology of symmetric and asymmetric polymer gears. The tooth deflection of asymmetric gear and its effect on the hysteresis behavior is analyzed.

Chapter 6 is devoted to the study of tooth and mesh deflection characteristics of asymmetric polymer gears. The study involves an analysis of the predictions obtained from viscoelastic simulations and experimentally determined values.

Chapter 7 compares the bending fatigue performances of injection-molded gears and selective laser sintered gears built in a 'flat' configuration. The influence of layered structure on the bending fatigue strength, thermal behavior, and crack propagation behavior has been discussed.

Chapter 8 deals with the bending fatigue behavior of selective laser sintered gears built in an 'on-edge' configuration. The impact of varying layer orientation on the bending fatigue strength of each tooth has been discussed. Also, it includes a study of the crack morphology to understand the effect of layer orientation on crack propagation.

Chapter 9 summarizes the research outcomes and outlines the scope for further extension of the work

Chapter 2

Literature survey

The wide-scale implementation of polymer gears in high-performance applications requires designs that deliver greater load-carrying capacity, lesser noise during operation, reduced weight, and flexibility in manufacturing volumes. The load-carrying capacity of polymer gears can be enhanced by asymmetric tooth profiles. The operation of driver and driven gears made of polymer material has the potential to minimize the system noise and weight. Gear designs with complex geometry can be realized at competitive costs by means of additive manufacturing. To accomplish the stated research aims, it is necessary to review the current state-of-the-art to understand the research areas under consideration. Also, the appropriate methods to be adopted during the research must be identified.

Accordingly, a comprehensive review of the literature encompassing the areas of asymmetric gears, polymer gears, and additively manufactured parts was undertaken. This chapter presents the review of the relevant literature in three major sections. The fatigue and stiffness behavior of injection-molded polymer gears is described in the first section. The second section examines the performance of asymmetric gears in terms of bending strength, fatigue behavior, and mesh stiffness. The third section discusses specimen-based studies on the relative performance of selective laser sintered and injection molded parts, and the effect of layer orientation on the monotonic and fatigue strengths. In addition, the fatigue behavior of additively manufactured gears and their other functional characteristics, such as dimensional accuracy, have been presented. The final section summarizes the significant findings of the review relevant to the stated research aims, along with details of the research gaps identified during the review.

2.1 Performance of injection-molded polymer gears

The performance of polymer gears is influenced by a multitude of factors such as material, geometry, reinforcements, lubrication, etc. As a result, the literature pertaining to the performance of polymer gears is quite broad, with wide-ranging investigations on fatigue behavior, stiffness behavior, failure characteristics, and evaluation of operating variables such

as stress, temperature, etc. The current review only includes studies related to the fatigue performance of polymer gears mated with polymer gears and investigations studying the stiffness and transmission error behavior. This section deals with works on symmetric gears only. The performance of asymmetric polymer gears is discussed in the next section.

2.1.1 Influence of mating gear material on the performance of polymer gear

Several studies investigating the performance of polymer gears have utilized polymer mating gears. The wear and durability of unreinforced and glass-fiber reinforced Polyoxymethylene (POM) gears were evaluated by Mao *et al.* (2019) under polymer - polymer engagement. Similarly, Soudmand and Shelesh-Nezhad (2020) examined the wear characteristics of gears made of nanocomposites based on poly(butylene terephthalate) (PBT) by running the test gears against mating gears made of the same material. Zorko (2021) evaluated the high cycle bending fatigue behavior of gear pairs with a curved path of contact by running Nylon 66 gears against POM gears. The same material engagement was adopted by Trobentar *et al.* (2022) in a recent study, in which the acoustic characteristics of POM - Nylon 66 pairs of S-gears were investigated.

The material of the mating gear prominently influences the fatigue performance of polymer gears. Yamaguchi (1990) compared the efficiency and failure life of steel - polymer and polymer - polymer pairs of various materials such as Acrylonitrile butadiene styrene (ABS) and POM. Walton *et al.* (2002) evaluated the gear pair efficiency of various materials such as Polyoxymethylene, Nylon 66, Polyether ether ketone, and glass-fiber reinforced Nylon 66. Significant variation was observed between the efficiencies of different material pairs. In a study carried out by Mao *et al.* (2009), the performance of similar and dissimilar gear pairs of Polyoxymethylene and Nylon 66 were investigated. The fatigue life of dissimilar pairs depended on the material of the driving gear, as POM - Nylon 66 pairs exhibited higher life compared to Nylon 66 - POM pairs. The wear behavior was different for POM and Nylon 66 gears.

Wood, Williams and Weidig (2012) evaluated the fatigue life of lubricated steel-polymer and polymer - polymer combinations of PEEK, Nylon 46, and carbon-fiber reinforced PEEK. Zorko *et al.* (2017) evaluated the fatigue strength and thermal behavior of POM - POM and POM - Nylon 66 pairs of involute and S-gears. From these studies, it can be inferred that the fatigue behavior of polymer-polymer gear pairs, such as wear and failure mechanisms, varies with respect to the material of driven as well as driving gear.

In several investigations, the effect of metal and polymer driver gears on the operational characteristics of the gear pair has been evaluated. Yelle and Burns (1981) analytically calculated the actual contact ratio of POM-POM and steel-POM gear pairs to estimate the influence of material on the load shared by the loaded tooth. Dearn, Hoskins, Petrov, *et al.* (2013) studied the performance of uncoated and coated Nylon 66, PEEK, and carbon-fiber reinforced PEEK gears. The surface temperature and weight loss of different combinations such as steel - uncoated, steel - coated, uncoated - uncoated, coated - uncoated, and coated - coated were compared. In another investigation by Dearn, Hoskins, Andrei, *et al.* (2013), the lubrication regimes of steel - polymer and polymer - polymer pairs of PEEK gears were determined based on oil film thickness and efficiency. Koide *et al.* (2017) evaluated the transmission efficiency and surface temperature of steel - polymer and polymer - polymer combinations of sine and involute POM gears.

These studies conducted experimental investigations using conventional rotational tests, which simulate the actual operation. The study of tribological performance is necessary, as the driver and driven gear materials affect contact stress, which, in turn, influences the wear and frictional heating. Nonetheless, the evaluation of bending fatigue strength is essential since tooth breakage due to bending fatigue occurs in polymer gears (Senthilvelan and Gnanamoorthy, 2006; Pogačnik and Tavčar, 2015; Hasl *et al.*, 2018).

2.1.2 Tooth deflection and transmission error in polymer gears

Studies dealing with the transmission error in polymer gears have evaluated the mesh stiffness, as tooth deflection is the primary source of transmission error in polymer gears. Although few works have adopted analytical and experimental approaches, FEM has been the preferred tool of investigation in most studies. Numerical prediction of stiffness behavior by means of different material models has been the primary focus of research.

Using an analytical approach, Yelle and Burns (1981) investigated the deflection characteristics of steel - acetal and acetal - acetal pairs. The actual contact ratio, load sharing pattern, and compliance of each pair were evaluated. Tsai and Tsai (1997) adopted the deflection-based approach to predict the static transmission error (STE) of Nylon 66 gears paired with metal and polymer gears. Du, Randall and Kelly (1998) presented a modified model for the prediction of gear TE in cases where the stiffness component has greater influence. Simulation and experimental analyses of steel and nylon gears indicated that the effect of misalignment on mesh stiffness was pronounced in nylon gears. Meuleman *et al.* (2007)

predicted the TE caused by tooth deflection in acetal gears. Mesh deflections and stiffnesses were calculated by means of a beam model and compared with results from numerical simulations and experiments. Letzelter *et al.* (2009) formulated a computational model to predict the load sharing and TE in Nylon 66 gears. The linear viscoelastic behavior of material was incorporated in the model, along with the influence of temperature and speed. In a subsequent effort, Cathelin *et al.* (2013) validated the previously proposed transmission error model (Letzelter *et al.* (2009)) using experimental measurements of transmission error. The correlation between simulation and experimental results was acceptable.

Karimpour, Dearn and Walton (2010) investigated the kinematic behavior of polymer gears by numerical simulations and assessed the impact of large deflection on the bending and contact stress, load sharing, and path of contact. In addition, the influence of other critical variables such as applied loads, temperature, and friction was evaluated. Wood, Williams and Weidig (2012) experimentally investigated the transmission error behavior of PEEK and Nylon 46 materials under similar and dissimilar engagements. The torque and transmission error variation was lower in pairs of similar materials. The authors concluded that the relative stiffness of the pair has a more significant influence over variation than individual stiffnesses of gear materials.

Trobenar, Glodež and Zafošnik (2015) investigated the impact of the material model, loading approach, contact type, and element type on predicting tooth deflection values. The deflections predicted using Marlow's hyper-elastic model were greater than that of the linear elastic model. Kodeeswaran, Suresh and Senthilvelan (2016) conducted a numerical and experimental study to determine the static transmission error and bending stiffness of Nylon 66 gears paired with steel gears. As part of the experimental study, a test rig was developed in-house to measure the mesh deflection of gear pairs subjected to static torques. The difference between the numerical prediction and experimental measurements was considerable.

In a subsequent effort, Kodeeswaran, Suresh and Senthilvelan (2019) studied the effect of loading rate on the predicted values of bending stress and static transmission error of Nylon 66 gears by employing a non-linear, elastic-plastic model. As the loading rate increased, the difference between numerically predicted and experimentally measured values of STE at pitch point decreased. Chakroun *et al.* (2021) conducted a numerical study to predict the mesh stiffness of Nylon 66 spur gears. The generalized Maxwell model approximated the material response to quasi-static loads.

2.2 Performance of asymmetric gears

The load-carrying capacity and operational life of gears depend on gear teeth' bending strength and surface durability. As the focus of the current study is bending strength, the literature review included numerical and analytical investigations that have evaluated the influence of asymmetric tooth form on the bending strength of asymmetric gears, emphasizing bending stress evaluation and methods to minimize bending stress. The survey also considered experimental investigations dealing with the fatigue behavior of metal and polymer asymmetric gears. Finally, works investigating the factors that affect gear performance, such as mesh stiffness and transmission error characteristics, were reviewed.

2.2.1 Bending strength of asymmetric gears – Evaluation of bending stress and influence of gear geometry parameters

A general framework for designing asymmetric gears based on the theory of generalized parameters was presented by Kapelevich (2000). The asymmetric gears with a larger drive side pressure angle designed according to that procedure demonstrated reduced bending stress and vibration levels compared to standard gears. The numerical stress analysis performed by Litvin, Lian and Kapelevich (2000) confirmed the ability of asymmetric gears with higher drive side pressure angles to reduce bending as well as contact stress. The bending stress in asymmetric configurations with higher coast side pressure angle was investigated by Deng, Nakanishi and Inoue (2003). Numerical evaluation of such configurations revealed that the maximum root bending stress decreases as the coast side pressure angle increases. Cavdar, Karpat and Babalik (2005) developed a program to compute the optimum drive side pressure angle to achieve maximum bending stress reduction in asymmetric gears. The influence of tooth number and drive side pressure angle on contact ratio was investigated.

Another investigation assessing the effects of asymmetric tooth configurations on the bending and contact stresses was conducted by Fuentes *et al.* (2013) using the Integrated Gear Design software. The results were in alignment with the findings of previous studies. The load-carrying capacity of normal contact ratio gears designed using the Direct gear design[®] procedure was investigated by Marimuthu and Muthuveerappan (2016a). Non-dimensional bending stress and the influence of parameters such as pressure angles on the drive side and coast side flanks, gear ratio, coefficient of asymmetry, contact ratio, and teeth number were evaluated using the Finite element method. In a subsequent effort (Marimuthu and Muthuveerappan, 2016b), the non-dimensional bending and contact stresses of high contact ratio asymmetric gears designed using

the Direct gear design[®] procedure were estimated. The gears attained from the Direct gear design[®] – both normal contact ratio and high contact ratio – exhibited enhanced load carrying capacity compared to gears designed using a conventional procedure.

2.2.2 Analytical determination of bending stress in asymmetric gears

The bending stress in symmetric gears can be calculated by following established procedures in standards outlined by organizations such as International Organization for Standardization (ISO 6336-3, 2006) and American Gear Manufacturers Association (ANSI/AGMA 2101-D04, 2004). The Finite Element Method (FEM) has been the commonly employed tool for predicting bending stress in asymmetric gears. The non-standardized tooth geometry of asymmetric gear persuades the use of FEM in spite of the considerable time and effort required for the development of numerical models. However, the inherent simplicity and robustness of analytical calculations have encouraged researchers to develop analytical solutions for bending stress in asymmetric gears.

In the investigation by Cavdar, Karpat and Babalik (2005), the work by Pedrero, Rueda and Fuentes (1999) was adopted to compute the critical section parameters of the asymmetric tooth along with the form factor and stress correction factors. Moya *et al.* (2010) presented an algorithm to compute the Lewis form factor of polymer asymmetric spur gears. The profile asymmetry was incorporated into the calculation by using the asymmetry coefficient. Regression equations comprising asymmetry coefficient and the number of teeth as independent variables were generated to calculate the form factor. Sekar and Muthuveerappan (2015) formulated a modified framework for determining the form and stress correction factors of asymmetric gears based on ISO 6336 Method B. A comparative analysis of the critical section parameters such as angle of tangents, tooth thickness, the radius of curvature, and bending moment arm calculated using the analytical method and FEM was performed.

Thomas *et al.* (2018) introduced a new analytical approach based on the search method to estimate the bending stress of asymmetric gears. In the proposed method, the location of the critical section was not assumed, and the stress in the root fillet profile was evaluated at multiple locations. Using the proposed search method, the bending stress predicted was more accurate than the bending stress determined using the ISO method. Mo, Ma and Jin (2019) defined a composite formula incorporating friction, shear stress, and compressive stress to calculate the bending stress in asymmetric gears. The effect of friction was described by a new factor called friction stress factor.

2.2.3 Bending stress reduction through geometric modifications

Multiple studies have explored the optimization of tooth geometry and tool geometry as a method to reduce bending stress in asymmetric gears. Muni, Kumar and Muthuveerappan (2007) minimized the bending stress of asymmetric gear by optimizing the profile shift of the non-standard rack cutter. Multiple non-standard rack cutters with different profile shifts were considered based on various combinations of gear and pinion addendum pressure angles obtained for a constant contact ratio. The rack cutters that generate the gear pair with equal and minimum bending stress are considered to be optimum. Costopoulos and Spitas (2009) proposed an innovative asymmetric tooth with an involute profile on the driving flank and a non-involute straight-line profile on the coast flank. In addition, the standard trochoidal fillet on the driving side was replaced with a circular fillet to decrease the bending stress further. The analysis of the non-dimensional model of the proposed design indicated a maximum bending stress reduction of 28% with respect to standard symmetric gear with a 20° pressure angle.

A fillet optimization technique for decreasing the bending stress in asymmetric gears was proffered by Kapelevich and Shekhtman (2009). The process included an approximation of the fillet profile using a trigonometric function and the selection of the optimal coefficients of the function using a search method. The selection of coefficients was guided by the bending stress predicted using FEM. Pedersen (2010) suggested bending stress reduction in asymmetric gears by optimizing the cutting tool shape to modify the shape and thickness of the tooth root. The analysis concluded with the proposal of a new standard rack cutter for asymmetric configuration with higher drive side pressure angle and configuration with higher coast side pressure angle.

2.2.4 Fatigue behavior of asymmetric gears

Using experimental methods, few works have demonstrated the enhanced bending fatigue strength of asymmetric metal gears. Brown *et al.* (2011) conducted Single tooth bending fatigue tests investigate the bending fatigue strength of asymmetric gear designs used in main helicopter drive. The bending fatigue strength of asymmetric gears with circular root was greater than that of baseline symmetric gears with circular and optimized root forms. Sanders *et al.* (2011) evaluated the effect of an asymmetric tooth and the fillet geometry on the fatigue life of gears. Gears that had a fillet with an elliptical geometry exhibited a significantly higher fatigue life than those with a circular fillet. Demet and Ersoyoğlu (2021) evaluated the bending

fatigue strength of AISI 4140 steel gears by STBFT. The asymmetric gears exhibited a statistically significant increase in bending strength compared to the symmetric gears.

The influence of asymmetric teeth on the bending strength of injection-molded polymer gears has been evaluated by Mohan and Senthilvelan (2014). The performances of unreinforced and glass fiber reinforced polypropylene gears with symmetric and asymmetric tooth profiles were assessed experimentally. Bending fatigue tests were conducted under a strain-controlled mode using an in-house designed test fixture coupled to a servo-hydraulic testing machine. Fiber reinforcement and asymmetric tooth increased the load-carrying capacity of gears. The fatigue life was higher for asymmetric gears with a higher drive side pressure angle.

Regarding durability, studies on metal gears indicate that asymmetric tooth profile may increase the resistance to wear. Scuffing tests conducted by Brown *et al.* (2011) revealed that the mean scuffing load of asymmetric gears was 25% greater than that of symmetric gears. Sekar (2019) performed a comprehensive numerical study to predict the wear performance of asymmetric gears using Archard's wear model. A decrease in wear depth and an increase in mechanical efficiency were observed, indicating the potential for durability improvement. As the drive side pressure angle increased from 30° to 35°, the maximum contact pressure decreased despite the increase in contact force caused by a greater pressure angle.

Studies evaluating the durability of injection-molded asymmetric polymer gears by dynamic testing have reported interesting findings. Kumar, Kommogi and Senthilvelan (2009) observed that in asymmetric polypropylene gears, a higher drive side pressure angle enhanced the transmission efficiency and reduced the temperature. However, further investigation on the durability of polypropylene gears by Mertens and Senthilvelan (2016) revealed that the fatigue life of asymmetric gears was lesser than that of symmetric gears. In a separate study, Mertens, Kumar and Senthilvelan (2016) evaluated the effect of surface roughness of the steel mating gear on the wear, thermal, and failure characteristics of asymmetric polypropylene gears. As anticipated, the surface temperature and wear increased due to the greater friction caused by the increase in surface roughness of the steel gear tooth.

2.2.5 Stiffness and transmission error characteristics of asymmetric gears

In literature, investigations concerning the stiffness behavior and transmission error characteristics are less and limited to the study of metal gears. Typically, studies have evaluated the influence of drive side and coast side pressure angles on the tooth deflection and transmission error using numerical methods. In addition, geometry modifications have been

proposed to alter the transmission error characteristics, as transmission errors occurring during gear operation can be used as input for early diagnosis of anomalies in the system.

Litvin, Lian and Kapelevich (2000) reduced transmission error and noise in asymmetric gears by introducing profile and longitudinal crowning to localize tooth contact. Apart from reducing the magnitude of transmission error, the modifications also transformed the shape of the transmission error function. The bending stiffness of asymmetric teeth with higher coast side pressure angle was evaluated by Deng, Nakanishi and Inoue (2003) using a numerical method. The bending stiffness increased with an increase in the coast side pressure angle. A dynamic analysis was performed by Karpat *et al.* (2008) to study the static transmission error of symmetric gears and asymmetric gears with higher pressure angles on the loading flank. The increase in addendum length reduced the amplitude of static transmission error in asymmetric gears. Deng, Hua and Han (2015) proposed changes in the pressure angle of the rack-cutter to improve the transmission characteristics of asymmetric gears.

Using the finite element method, Masuyama and Miyazaki (2016) evaluated the tooth deflection and bending stress of asymmetric gears. The bending stress decreased, and bending stiffness increased in gears with a greater pressure angle on the loading flank. Karpat *et al.* (2017) predicted the stiffness for four different cases of asymmetric gears using numerical analysis. The results from the numerical analysis were utilized to develop analytical equations for tooth stiffness. Doğan and Karpat (2019) investigated the effect of crack length on the single tooth and time-varying mesh stiffness of asymmetric gears. A dynamic model was proposed to compute the dynamic transmission error, which was used in fault detection. Karpat, Yuce and Doğan (2020) presented an experimental approach to determine the single tooth stiffness of asymmetric gears. A numerical analysis supplemented the experimental campaign to validate the results. The experimentally determined and numerically predicted values showed good agreement, confirming the efficacy of the experimental set-up and procedure.

2.3 Mechanical behavior of additively manufactured parts

The strength of additively manufactured parts is influenced by the orientation of layers, which is determined by the build configuration. Also, to replace a prevailing part with an additively manufactured part, the performance of the additively manufactured part must be equivalent to that of the existing part. To gain a broader understanding of these factors, specimen-level investigations were reviewed in addition to gear-based studies. Since injection molding is the

incumbent process for manufacturing polymer gears, studies comparing the performances of injection molded and additively manufactured parts were reviewed.

Although all additive manufacturing processes build parts layer-by-layer, the binding mechanism varies with each process and influences the properties of the part to a great extent. Selective laser sintering was the additive manufacturing process considered for this study. Accordingly, the review of specimen-level studies only considered investigations dealing with selective laser sintered polymer parts. However, the review of gear-based studies included a broader study of investigations involving other additive manufacturing processes, as the works related to additively manufactured gears are limited.

2.3.1 Effect of build configuration on the mechanical properties of selective laser sintered specimens

The build configuration determines the orientation of layers with respect to the load applied during the service. Studies that evaluated the mechanical properties of SLS specimens have observed anisotropic behavior. The influence of layer orientation on the monotonic properties of SLS specimens has been investigated extensively in several studies. Gibson and Shi (1997) evaluated the influence of position and orientation of specimens during selective laser sintering on the tensile strength of nylon specimens. Orientation that minimizes the length of the scan vector yielded better tensile strength as the temperature distribution was uniform across the scan vector. Also, orientation in which the applied load was perpendicular to the layer direction offered the least tensile strength. The cross-sectional area of the specimen influenced the part distortion during fabrication.

Ajoku *et al.* (2006) investigated the tensile, flexural, and compressive properties of laser-sintered Nylon 12 specimens. Significant differences were observed in the properties of specimens built in three different build configurations. Build orientation and end-of-vector effect affected the bonding between successive layers, thereby influencing the mechanical properties. Caulfield, McHugh and Lohfeld (2007) reported that the tensile properties such as Young's modulus, yield strength, and the fracture strength of selective laser sintered specimens built in the 'on-edge' configuration were higher than the specimens made in the 'upright' configuration. The energy density supplied during the sintering process affected the porosity and strength of specimens. Jain, Pandey and Rao (2008) studied the influence of parameters such as part bed temperature, layer thickness, refresh rate, and hatch pattern on the strength of tensile specimens manufactured by selective laser sintering. The hatch pattern, which refers to

the orientation of layers, affected the tensile strength considerably. The layer orientation along the long axis exhibited greater strength compared to the specimen with layer orientation perpendicular to the loading axis.

In a separate work by Jain, Pandey and Rao (2009), the impact of delay time on the tensile properties of selective laser sintered PA 2200 specimens was evaluated. As build configuration has considerable influence over the delay time, specimens fabricated with different orientations were tested to establish the relationship between build orientation, delay time, and tensile strength. An algorithm was developed to determine the optimum build orientation for the specimens. Majewski and Hopkinson (2011) investigated the effect of section thickness and build orientation on the tensile properties of laser-sintered Nylon12 specimens. The build orientation induced variations in tensile strength, modulus, and elongation at break, albeit the variation was not significant. Starr, Gornet and Usher (2011) studied the influence of processing conditions such as laser speed, laser power, scan spacing, and layer thickness on the tensile properties of laser-sintered Nylon 12 specimens. The influence of build orientation and build position was evaluated as well. The effect of build orientation on the yield stress was dependent on the laser power as anisotropy in yield stress values was negligible at higher laser power. In contrast, anisotropy was prominently evident at intermediate and lower laser power. Stichel *et al.* (2017) evaluated the influence of microstructural features such as porosity and residual particle on the mechanical properties of SLS Nylon 12 specimens. The ultimate tensile strength of the specimens decreased as the layer orientation along the loading axis increased from 0° to 90°.

The influence of build orientation on fatigue behavior of selective laser sintered specimens has been studied in several investigations. Van Hooreweder *et al.* (2013) investigated the uniaxial fatigue behavior of tensile specimens built in two mutually perpendicular build configurations. The fatigue behavior was generally isotropic, and the effect of building configuration was minimal. In a separate effort, Van Hooreweder and Kruth (2014) studied the influence of notch and notch manufacturing methods on the fatigue life of Nylon 12 SLS specimens. The notched specimens exhibited higher fatigue life compared to plain specimens. Specimens with in-built notches sustained a greater number of fatigue cycles than specimens with machined notches. Specimens with layer orientation parallel to the direction of loading exhibited marginally higher fatigue life than specimens with layers oriented perpendicular to the loading direction.

Munguia and Dalgarno (2014) evaluated the bending fatigue strength of Nylon 12 specimens built in ‘flat’ and ‘upright’ orientations using four-point rotating bending tests. In addition to bending fatigue tests, tensile specimens built in three standard configurations were also tested. The anisotropy in tensile properties was significant, whereas variations in bending fatigue strength were not prominent. However, a clear endurance limit for the material was observed regardless of the build orientation. In another study, Munguia and Dalgarno (2015) investigated the effect of loading mode on the bending fatigue strength of laser-sintered Nylon 12. Rotating bending and reversed bending fatigue tests were conducted with specimens built with different layer orientations. The authors observed no significant variations between the fatigue behavior of rotating bending and reversed bending specimens.

A few researchers have investigated the crack propagation behavior of selective laser sintered specimens built in different orientations. In the study by Blattmeier *et al.* (2012), the role of layer orientation on the fracture behavior of Nylon 12 was evaluated by fabricating compact tension specimens in two different orientations: 45° and 90°. The layer orientation influenced crack propagation direction as the crack extended along the layer direction. Thus, the crack extension was along the direction of the notch in 90° specimens whereas, in 45° specimens, the crack extension plane was inclined with respect to the notch plane. Brugo *et al.* (2016) investigated the crack propagation tendency of SLS parts using compact tension (CT) specimens prepared in three build configurations. The stress intensity factor and the maximum force sustained during loading were different for each specimen, confirming anisotropy. Specimens in which all layers contained the crack exhibited superior crack resistance. Cano, Salazar and Rodríguez (2018) evaluated the influence of temperature and glass reinforcement on the fracture behavior of SLS Nylon 12. Fracture parameters such as energy release rate and J-integral values were determined using compact tension specimens manufactured in two perpendicular orientations. Differences were observed between the fracture parameters of each orientation at every testing temperature. However, the variation between specimens with parallel and perpendicular layer orientations was maximum at 50°C, which was attributed to the viscous behavior of the material close to the glass transition temperature. In a subsequent study by Cano, Salazar and Rodríguez (2019), the fatigue crack growth in selective laser sintered Nylon 12 was investigated using the same specimens with perpendicular orientations. The fatigue crack resistance was better in specimens in which the layer orientation was perpendicular to the direction of crack growth. In specimens with layer orientation parallel to the crack path, the fracture surfaces were smoother as the resistance offered for crack

propagation was lesser. From these works, it can be inferred that the change in build configuration could induce anisotropy in properties, albeit the degree of anisotropy may vary.

2.3.2 Comparison of mechanical properties of injection-molded and selective laser sintered specimens

Several studies have compared the monotonic and fatigue behavior of specimens manufactured by selective laser sintering and injection molding. Athreya, Kalaitzidou and Das (2011) evaluated the tensile and flexural behavior of unreinforced and 4% carbon black reinforced Nylon 12 prepared by SLS and compared it with the performance of injection-molded specimens. The reinforced SLS specimens demonstrated inferior mechanical properties owing to the non-uniform dispersion of carbon black. Blattmeier *et al.* (2012) studied the influence of surface attributes on the crack propagation rate in SLS and IM Nylon 12 specimens. In laser sintered specimens, the greater resistance to crack initiation and lower crack propagation rates resulted in higher fracture toughness than injection-molded specimens. The fatigue life of Nylon 12 SLS and IM specimens subjected to a completely reversed load ($R = -1$) was estimated experimentally by Van Hooreweder *et al.* (2013). Also, the dimensional quality, surface roughness, density, microstructure, and the crystal structure of the specimens were assessed. Although variations were observed in these parameters, the general fatigue behavior was comparable for SLS and IM specimens.

Zhu *et al.* (2015) investigated the microstructural properties of selective laser sintered and injection molded polypropylene specimens. The degree of crystallinity was higher in SLS specimens due to the slower cooling rate. The mechanical properties such as tensile strength and tensile modulus were also superior for SLS specimens. The faster rate of cooling in IM impeded the growth of crystals. In the study by Arai *et al.* (2017), the injection-molded poly(butylene terephthalate) exhibited superior mechanical properties compared to selective laser sintered specimens, albeit elastic modulus was higher for SLS specimens. The porosity in SLS specimens influenced the mechanical properties significantly, with the lowest porosity values yielding enhanced properties. Wörz *et al.* (2018) studied the long-term degradation behavior of SLS and IM Nylon 12 specimens. Tensile specimens were conditioned at multiple temperatures for varying periods of storage. Density, surface roughness, mechanical properties, and morphology were evaluated to understand the effect of the production process. Compared to the IM specimens, the tensile properties of SLS specimens degraded quickly.

2.3.3 Additive manufacturing in gear prototyping

Typically, additive manufacturing processes are employed in the gear design cycle for developing prototypes based on computer-aided design (CAD) models. In studies related to additively manufactured plastic gears, parameters such as dimensional accuracy, kinematic precision of mating profiles, stress distribution, and the feasibility of rapid manufacturing have been evaluated. In a study by Sobolak and Budzik (2008), the kinematical precision of bevel gears made by the stereolithography (SLA) process was examined by determining the contact area on the tooth surface. SL-5170 resin was considered as gear material for the study as transparency was desired. In another study, the ability of SLA to manufacture high reduction gears was explored by Berger and Mäule (2009). The accuracy of miniaturized cycloid gears and harmonic drive gears built using the SLA process was comparable to injection molded gears. Sobolak and Jagiełowicz (2012) conducted a photo-elastic investigation to evaluate the stress and strain in SLA gears subjected to static load conditions. Also, the gears were utilized as prototypes for vacuum casting due to the higher degree of dimensional accuracy rendered by the SLA process.

Lieh, Wang and Badiru (2017) measured the surface roughness of Acrylonitrile Butadiene Styrene (ABS) gears fabricated by Fused deposition modeling and compared the observed readings with theoretical estimates. The Fused deposition modeling is a trademark of the Stratasys® and is commonly used for referring to the Fused filament fabrication (FFF) process. The geometrical dimensions such as outside diameter and tooth thickness of additively manufactured gears were compared with that of steel gears. The measurements of steel gears were closer to theoretical estimates than that of additively manufactured gears.

García-García and González-Palacios (2018) presented an algorithm to design bevel gears with exact spherical involute. The designed bevel gears were printed with polylactide filament using the FDM process. The efficacy of the proposed algorithm was evaluated by comparing the digital model and the model obtained by scanning the manufactured gear. The impact of printing direction on the geometric deviations of FDM fabricated ABS and Nylon gears was investigated by Mašović *et al.* (2019). Among the tested gears, the dimensional accuracy of ABS gears built in the horizontal orientation was better. Durakbasa *et al.* (2019) manufactured the gearbox components in miniaturized form using the selective laser sintering process and evaluated the functionality, surface quality, porosity, and geometric deviations of the elements. The measurements were obtained using tactile and optical methods.

2.3.4 Fatigue performance of additively manufactured polymer gears

Few researchers have evaluated the fatigue performance of additively manufactured gears. Since the SLA process offers higher geometrical accuracy, the SLA gears are appropriate to serve as geometrical models for further development. However, the SLA gears are disregarded for fatigue applications as the durability is inadequate (Sobolak and Jagiełowicz, 2012). Therefore, the FDM process was widely adopted in studies related to the fatigue behavior of AM gears. The forecast of service life of Nylon gears printed by the FDM process was carried out by Zhang, Mao, *et al.* (2020) using an artificial neural network-based model. The parameters of the FDM process were optimized, which enhanced the fatigue life by a factor of 3. In a subsequent study, (Zhang, Pursell, *et al.*, 2020) studied the operational behavior of five variants of Nylon FDM gears and presented a comparison with injection-molded Nylon 66 gears. Among the FDM gears, the Nylon 618 gears performed better than the injection-molded Nylon 66 gears.

Sobolak *et al.* (2020) prepared unfilled and reinforced ABS gears with involute and sinusoidal profiles using the FFF method. The operating temperature and noise levels of the gears during fatigue tests were compared. The reinforcement increased the noise intensity while decreasing the operating temperature in gears. Gbadeyan, Mohan and Kanny (2020) manufactured nanocomposite ABS gears reinforced with varying proportions of nano clay and characterized the tensile, flexural, and impact behavior of the gears. The mechanical properties were optimal for gears with a 2% weight proportion of nano clay. The durability of ABS, Polyetheretherketone and Polyetherimide (PEI) gears printed by the FFF process was evaluated by Pisula *et al.* (2021). The surface topography charts were analyzed, and the highest wear resistance was observed in the PEEK gears. Fekete (2021) performed multi-body simulations to study the effect of varying coefficients of friction and temperature on the wear behavior of polylactic acid gears.

2.4 Summary of literature review and research gaps

The fatigue performance of symmetric polymer gears has been studied in many works, whereas only a few investigations have reported the fatigue performance of asymmetric polymer gears. The fatigue life of asymmetric polymer gears, under dynamic testing, has been inferior compared to symmetric gears. Because gears undergo both bending fatigue and contact fatigue failures, the influence of asymmetric tooth form on each failure mode must be investigated separately. Hence, a comprehensive experimental study involving load-controlled bending fatigue tests is necessary to determine the effect of asymmetric configuration on the bending fatigue performance of polymer gears.

The influence of mating gear on fatigue performance has been assessed in terms of tribological parameters. However, the effect of polymer mating gear material on the bending fatigue strength of polymer gears has not been evaluated so far. Polymer driver gear increases the contact ratio, efficiency, and lubricant thickness while decreasing the variation in torque. However, the influence of mating gear material on the fatigue life and the operating temperature was dependent on the material combination. Hence, a focused investigation is needed to study the bending fatigue performance of metal-polymer and polymer-polymer pairs of asymmetric gears.

The tooth deflection and transmission error of symmetric polymer gears have been evaluated using analytical, numerical, and experimental methods. However, mesh and tooth stiffness of asymmetric polymer gears have not been investigated so far. The research related to the stiffness behavior of asymmetric gears has been limited and focused solely on metal gear pairs. The load sharing behavior of polymer gears distinctly differs from that of metal gear pairs, which underscores the need for a separate numerical and experimental investigation to study the stiffness characteristics of asymmetric gears made of polymers.

The investigations concerning the fatigue performance of additively manufactured polymer gears are limited. The fused deposition modeling process has been widely used, with several investigations evaluating the functional characteristics of FDM gears. On the contrary, the application of selective laser sintering for gear fabrication has been limited. The fatigue performance of SLS gears has not been evaluated so far, warranting a dedicated investigation.

Several works have demonstrated that the monotonic and fatigue properties of injection-molded and selective laser sintered specimens are comparable, indicating the efficacy of SLS parts. However, there is a distinct lack of knowledge regarding the relative fatigue performance

of injection molded and additively manufactured polymer gears. Apart from work by Zhang, Purssell, *et al.* (2020), which compared the fatigue performance of FDM gears with the literature data of IM gears, no other work has compared the fatigue performances of additively manufactured and injection molded gears. The fatigue performances of SLS and IM gears must be assessed to determine the utility of SLS gears.

The build configuration of a part induces anisotropy in mechanical properties. The effect of build configuration and layer orientation on the material properties of specimens has been investigated extensively. But there is a critical knowledge gap regarding the impact of layer orientation on the performance of additively manufactured gears. This necessitates the evaluation of fatigue performance of SLS gears built in different configurations such as 'flat' and 'on-edge' configurations.

The fatigue performance of additively manufactured polymer gears has been commonly evaluated by employing dynamic testing, which encompasses the effect of contact fatigue as well as bending fatigue. However, the individual effect of bending fatigue on the performance of additively manufactured polymer gears has not been studied so far. Thus, there is a necessity to evaluate the fatigue life, operating temperature, and failure morphology of selective laser sintered polymer gears subjected to pulsating bending fatigue loads.



Chapter 3

Materials and methods

The evaluation of bending fatigue performance includes the construction of S-N curves to determine the bending fatigue strength of gear and investigation of the failure morphology by fractography studies. In the case of polymer gears, fatigue loading causes hysteresis heating, which increases the gear temperature considerably. Hence, the effect of the design variable on the gear operating temperature during testing is also analyzed. The construction of S-N curves requires the determination of maximum bending stress in the root region of the gear tooth. The root bending stress is usually determined using analytical equations and the finite element method.

The investigation of mesh stiffness of a gear pair behavior requires the evaluation of tooth and mesh deflections. The FEM is widely adopted for predicting the deflections as non-linearities such as complex geometry, user-defined material model, and contact interactions can be included with relative ease in finite element models. In addition, the finite element model of a gear pair can estimate other factors such as bending stress, contact stress, and load sharing ratio. Experimental analysis, although challenging and time-consuming, has been employed regularly in studies as it measures the deflections under actual conditions. The finite element model, in contrast, is an ideal representation of the gear pair.

This chapter describes the experimental, numerical, and analytical methods adopted during the research work. The first section presents the details of gear design, such as gear geometry, material, and the fabrication of injection molded and selective laser sintered gears. The details of the experimental study, comprising descriptions of test rigs and test procedures for the determination of bending fatigue life and mesh deflection, are included in the second section. The third section describes the analytical formulation used for determining bending stress and load sharing ratio. Finally, details of the finite element models utilized in the study are presented in the fourth section.

3.1 Gear design and fabrication

This study considered symmetric and asymmetric spur gear pairs of unitary gear ratio and involute profile teeth. The geometric parameters of the gear are provided in Table 3.1. The symmetric gear adopted the standard 20° pressure angle for the tooth profiles, which has been widely used in other studies. Sekar and Muthuveerappan (2015) compared the asymmetric configurations 30°/20° and 25°/20° with the symmetric configuration 20°/20°. Sanders *et al.* (2011) compared the asymmetric configuration 20°/25° with the symmetric configuration 20°/20°. For the asymmetric gears, the design objective was to maximize the potential of an existing symmetric gear model. Thus, one flank of the tooth retained the pressure angle of 20°. The pressure angle of the other flank was optimized based on the 'peaking limit' of the tooth thickness at the tip. A pressure angle of 34° adhered to the peaking limit and provided the maximum bending stress reduction. Hence, a pressure angle of 34° was used for the other flank. In this work, each gear configuration is designated in the order of drive side pressure angle followed by coast side pressure angle (α_d / α_c). For example, the gear configuration 34°/20° indicates that the pressure angles on the drive and coast sides are 34° and 20°, respectively. Figure 3.1(a) indicates the geometric parameters. The pressure angle configurations of the symmetric and asymmetric gears used in this study are shown in Figure 3.1(b).

Table 3.1 Gear geometry parameters

Parameter	Symmetric gear	Asymmetric gear
Pressure angle (drive side / coast side)	$\alpha_d / \alpha_c - 20^\circ / 20^\circ$	Configuration 1: $\alpha_d / \alpha_c - 34^\circ / 20^\circ$ Configuration 2: $\alpha_d / \alpha_c - 20^\circ / 34^\circ$
Module (mm)	3	
Number of teeth	18	
Tip circle diameter (mm)	60	
Face width (mm)	8 (master gear) / 4 (test gear)	
Root fillet radius (mm)	1.14	

The 34°/20° and 20°/34° asymmetric configurations are referred to as those with 'higher drive side pressure angle' and 'higher coast side pressure angle,' respectively. The driving and driven gear are referred to as 'master gear' and 'test gear,' respectively. The design parameters of the

master and test gears are identical. However, the master gear was designed with a higher face width of 8 mm to prevent slip. The symmetric and asymmetric master gears, used in metal-polymer gear pairs, were prepared from the AISI SS 316 steel using the wire cut electric discharge process. The dimensions of the test gear were selected such that bending fatigue failure could be induced by loads that can be exerted by the test rig used in the study.

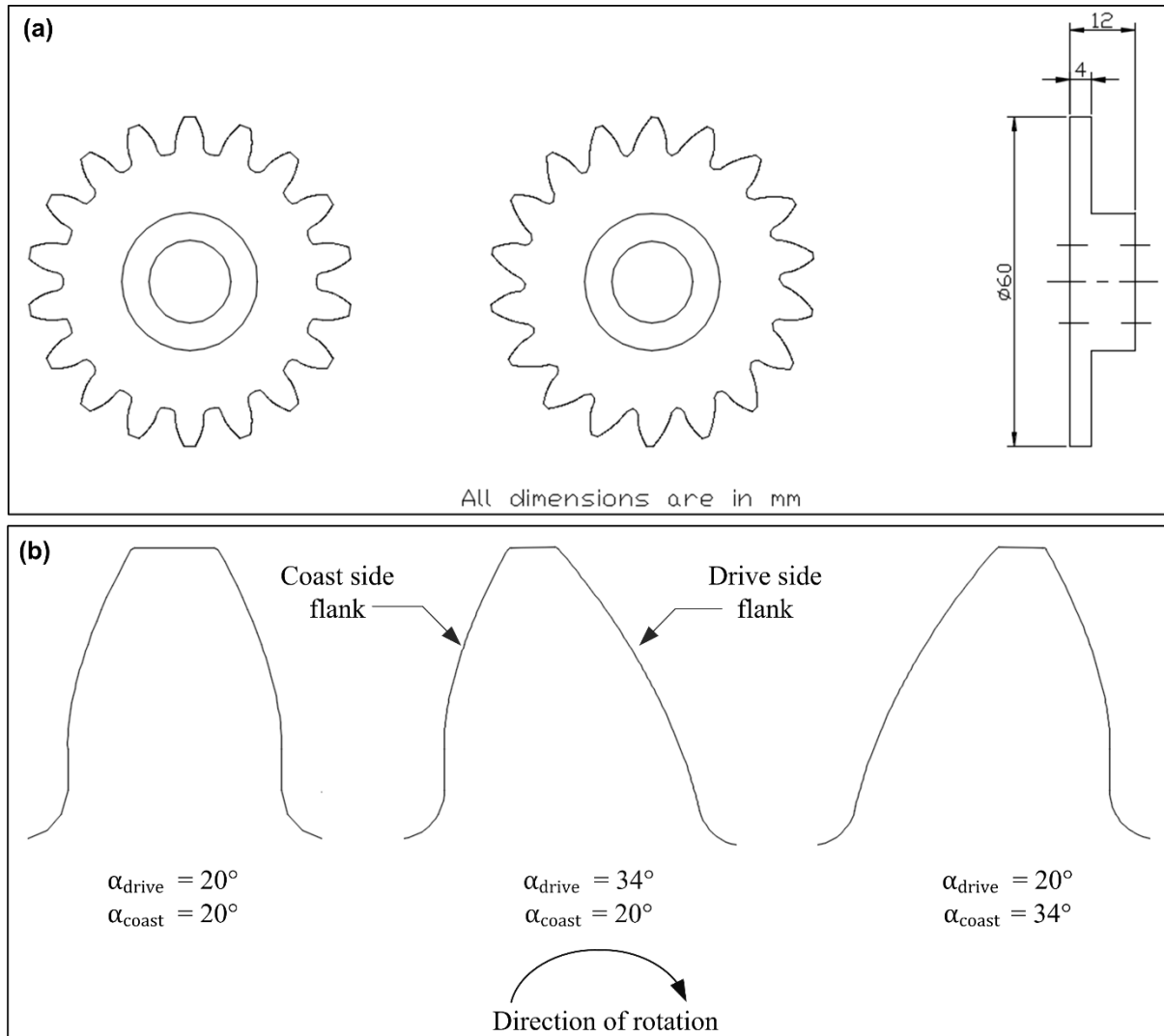


Fig. 3.1 (a) Schematic representation of the gear geometry and (b) Symmetric and asymmetric teeth.

3.1.1 Injection-molded gears

Nylon 66 (Polyamide 66) was chosen as the material for injection molded gears as it is one of the widely used materials for polymer gears. The injection molding of master and test gears was carried out at Just Preci Comps, Thiruvananthapuram, using the DGP Windsor ST-50 machine (Figure 3.3 (a)). Since polyamides are hygroscopic, it was imperative to remove the moisture entrapped by the pellets and store them in a moisture-free environment. Hence, the

molding was preceded by pre-heating pellets at 353 K for 4 hours and storing pellets in a desiccator before molding. During molding, the four heating zones in the barrel were maintained at temperatures of 558, 563, 568, and 573 K, respectively. The injection pressure and screw speed during the process were 7 MPa and 11.51 rad/s, respectively.



Fig. 3.2 (a) Symmetric and asymmetric master and test gears and (b) Tensile specimen used in monotonic tests and flexure specimen used in DMA.

After molding, the gears were preserved in a desiccator for stabilization and the prevention of moisture infiltration before testing. Since defects in injection molded components adversely impact the strength, it is essential to identify gears devoid of any noticeable defects. Hence, the molded gears were weighed in an analytical balance, and the gears with greater weight were

considered for testing. The selected gears were subjected to further visual examinations, and gears with visually detectable defects were discarded. The master and test gears are shown in Figure 3.2 (a). In addition to gear samples, specimens for material characterization tests such as tensile testing and dynamic mechanical analysis (DMA) were manufactured using injection molding. The tensile specimen dimensions conformed to the ASTM D638-14 (2014) Type I geometry, with a thickness of 3.2 mm. The dimensions of the DMA three-point bending specimen were $30 \times 7 \times 3.2$ mm. The tensile and DMA samples are shown in Figure 3.2 (b).

3.1.2 Selective laser sintered gears

In this study, Nylon 12 was the material considered for selective laser sintered gears. In the previous works, polymer gears manufactured by the FDM process were based on ABS, Nylon, PEEK, and PEI, whereas Nylon was the material for SLS gears. Nylon 12 is the predominant polymer build material in laser sintering and constitutes 95% of the market. Therefore, most of the investigations involving the SLS process have utilized Nylon 12, albeit other materials such as polypropylene and poly(butylene terephthalate) were also considered. Apart from the availability, the primary reason for the ubiquitous use of Nylon 12 is the wider processing temperature window. The window of processing temperature affects the crystallization rate, which influences the part shrinkage and distortion. The broad temperature window delays the crystallization and minimizes part distortion (Goodridge, Tuck and Hague, 2012). The Nylon 12 could be suitable for polymer gears, as shrinkage and distortion significantly affect the dimensional accuracy of gear teeth.

The selective laser sintering process was carried out at PSG TIFAC - CORE, Coimbatore, using the SLS Sinterstation 2500+ equipment (Figure 3.3 (b)). The feedstock materials were DuraForm[®] PA and HP 3D high reusability Nylon 12, commercial variants of Nylon 12, supplied by the 3D Systems[®] and *hp*[®], respectively. The coordinate system adopted for the SLS process was based on the ISO/ASTM 52921, which specifies the directions of x, y, and z-axes to be considered during the additive manufacturing process. According to ISO/ASTM 52921, the x-axis must lie parallel to the front edge of the build platform. The z-axis should be perpendicular to the build surface, along the surface normal. Accordingly, during the sintering of gears, the scanning direction was the x-axis, and the layer build direction was along the z-axis. The size of the powder was 60 μm . For the sintering process, the manufacturer recommended specifications were applied, and no optimization process was performed. The SLS process parameters are shown in Table 3.2.



Fig. 3.3 (a) Windsor GT-50 injection-molding machine and (b) Sinterstation 2500 selective laser sintering machine.

Table 3.2 SLS process parameters

Parameter	Value
<i>Laser power</i>	12.5 W
<i>Scanning speed</i>	5 m/s
<i>Layer thickness</i>	0.1 mm
<i>Laser beam diameter</i>	0.45 mm
<i>Powder bed temperature</i>	132 °C

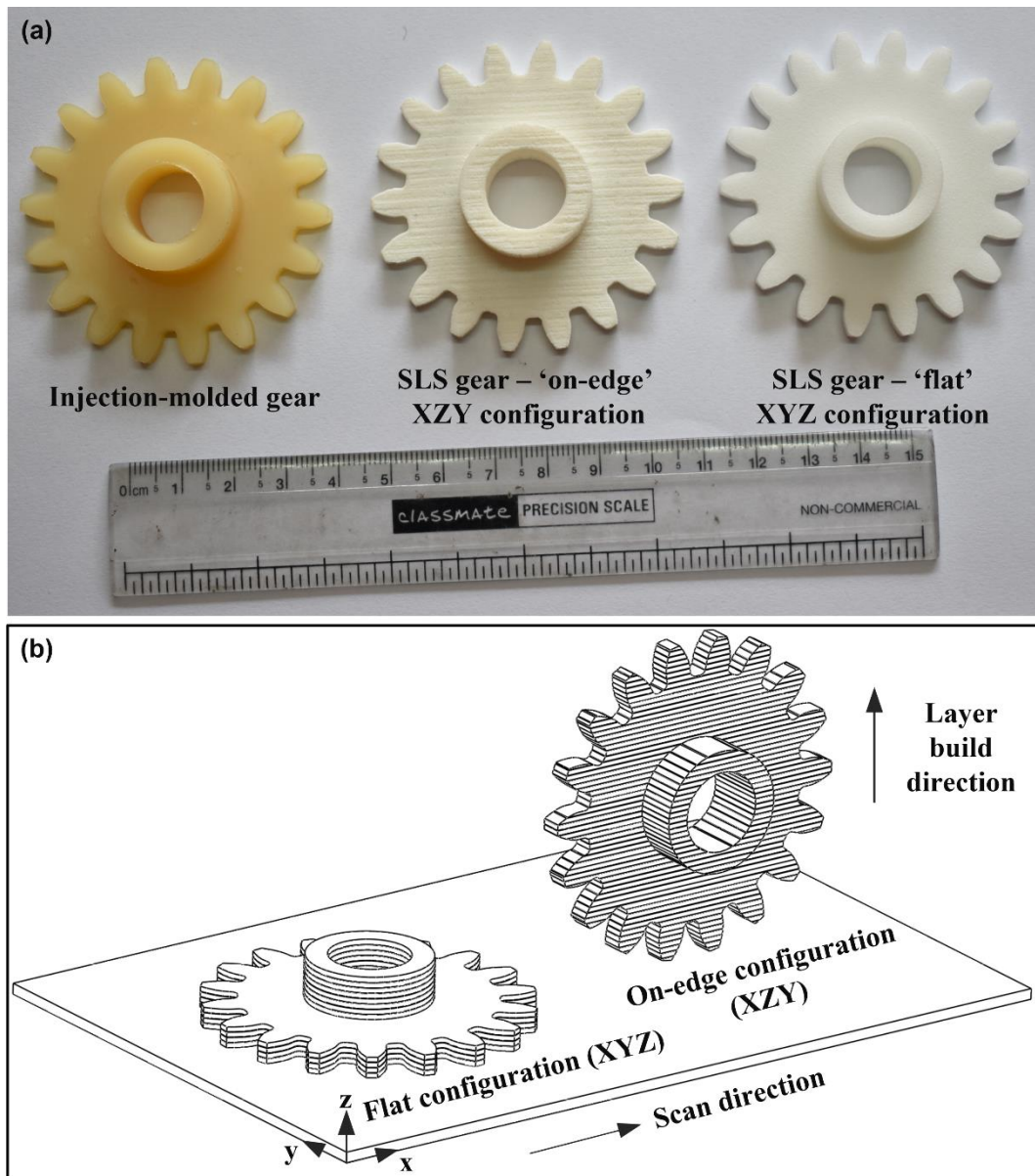


Fig. 3.4 (a) Selective laser sintered and injection-molded gears and (b) Schematic representation of gear build configuration during selective laser sintering process.

The ISO/ASTM 52921 specifies orthogonal orientation notation to define the build configuration of an additively manufactured part. This notation describes the initial build configuration by indicating the coordinate axis parallel to each dimension of the part in the descending order of length. Thus, the coordinate axis parallel to the longest dimension of the part is specified first, followed by the coordinate axes parallel to the second and third-longest dimensions. The schematic of SLS gears indicating the build configuration, direction of scanning, and direction of the build is shown in Figure 3.4 (b). In the first type of build configuration, the gear body is placed on the build platform, and layers are deposited along the face width direction. The gear rests on the teeth in the second build configuration type, and

layers are deposited along the diameter. The first configuration is commonly referred to as the 'flat' configuration, whereas the second configuration is designated as the 'on-edge' configuration. As per the ISO/ASTM 52921, the 'flat' configuration must be denoted by 'XYZ' or 'YXZ,' as the dimensions are equal along both the x and y axes. On the other hand, the 'on-edge' configuration must be denoted by 'XZY' or 'ZXY' as dimensions along the x and z axes are equal. The SLS gears employed in this investigation were built in the 'flat' and 'on-edge' configurations (Figure 3.4 (a)).

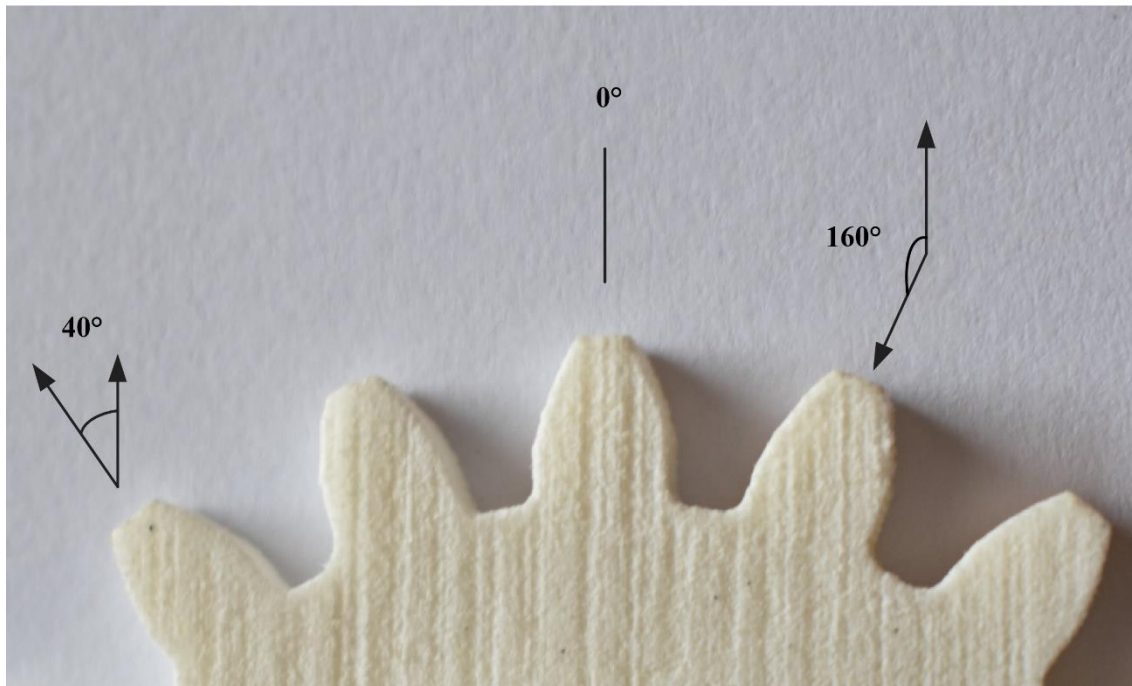


Fig. 3.5 Layer orientation in selective laser sintered gears built in 'on-edge' configuration.

The 'on-edge' build configuration causes variation in layer orientation with respect to the tooth center axis due to the circular geometry of gears. As a result, multiple tooth configurations with different layer orientations are obtained, and the number of unique configurations is determined by the number of teeth in gear. The teeth configurations are designated based on the angle subtended by the layer with respect to the tooth axis (Figure 3.5). The gear was built such that the tooth axes of two diametrically opposite teeth were parallel to the scanning direction (x-axis). The layer orientations obtained were between 0° and 160° at an interval of 20° . Due to the symmetry of the gear geometry, each type of layer orientation was present in two teeth.

3.2 Experimental study

This section discusses the components of the in-house built bending fatigue and static tooth deflection test rigs such as transducers, loading systems, data acquisition systems, etc.

Similarly, the specifics of testing protocols such as loading mode, the magnitude of loading, termination criteria, etc., are discussed as well. Finally, the details of material characterization tests conducted to determine the viscoelastic properties of Nylon 66 have been presented.

3.2.1 In-house bending fatigue test rig

An in-house, purpose-built test rig (Kodeeswaran *et al.*, 2016) was employed to conduct the bending fatigue tests. The SAE J1619 standard outlines the test fixture design, testing protocols, and calculations pertaining to the STBFT. The apparatus defined by the SAE J1619 standard for gear bending fatigue test presents specific challenges during the testing of polymer gears. In the SAE J1619 test fixture, the gear tooth is loaded by an upper anvil insert connected to a loading arm. The gear rotation is prevented by placing the lower adjacent tooth on the lower anvil insert. However, this arrangement is inapplicable for polymer gears, as the high tooth deflection of the lower support tooth can disrupt the stability of the gear during testing. In addition, loading by the upper anvil does not incorporate the load sharing effect. This issue is addressed in the in-house test rig by firmly locking the test gear on the shaft using a pin arrangement. The deflection-induced load sharing has a significant influence on the bending fatigue life in polymer gears (Walton *et al.*, 1994), but the anvil loading arrangement precludes the study of the effect of load sharing. On the other hand, the in-house developed rig was designed to incorporate these requirements. The test rig loads the test gear tooth using a master gear tooth and simulates realistic loading conditions. This arrangement allows the users to study the effect of load sharing on the bending fatigue strength.

Figure 3.6 shows the in-house developed polymer gear bending fatigue test rig. The test rig can apply unidirectional and bi-directional fatigue loads at a constant cycling frequency. The test rig is capable of applying a maximum torque of 14 Nm at a maximum cycling frequency of 20 Hz. The test gear and master gear are mounted on the respective gear shafts. The gear pair can mesh in any desired position along the line of action. The rotation of the driven gear shaft is arrested using a locking plate. Due to the non-rotation of the driven gear shaft, the alternate motion of the master gear exerts a bending fatigue load on the test gear.

The load is generated by a servo-motor located in the rear end of the setup. A servo drive (Motiflex) regulates load and cycling frequency, whereas the user input is transmitted through a Human-machine interface (HMI). The torque generated by the servo motor is measured by a torque sensor between the motor and the driver gear. The torque sensor is connected on both ends by bellow couplings to curtail the slippage between coupling and shaft.

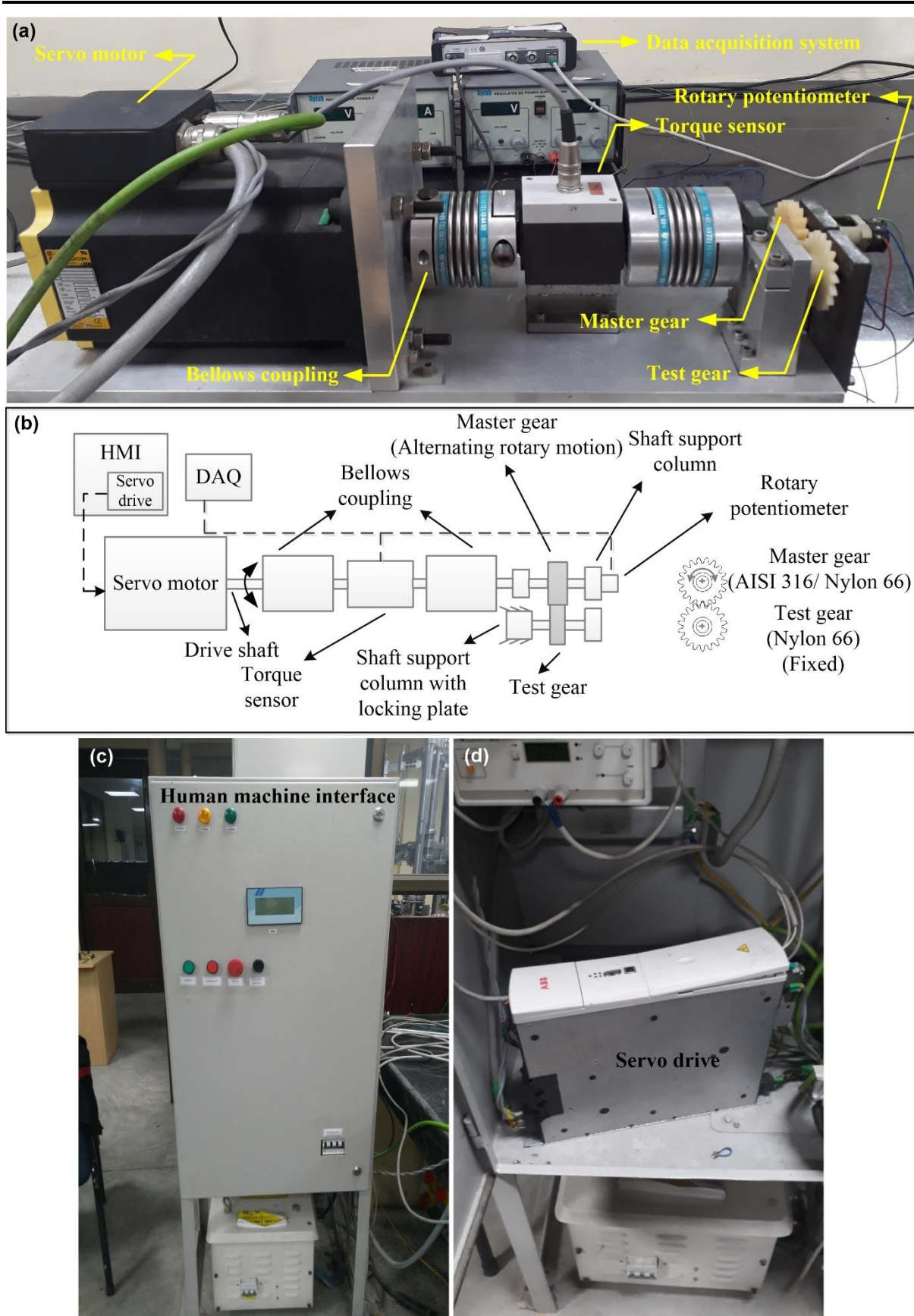


Fig. 3.6 (a) Bending fatigue test rig developed in-house, (b) Schematic illustration of the test rig, (c) Human-machine interface module, and (d) Servo drive inside the HMI.

A rotary displacement sensor, coupled to the driver gear shaft, measures the deflection of the tooth pair by measuring the angular displacement of the drive shaft. The data generated by the sensors are gathered by a Data acquisition system at a steady sampling rate of 300 Hz and actively monitored through a computer. During testing, the test gear undergoes an increase in the surface temperature, which is recorded using an Infrared (IR) thermal imaging camera. The major specifications of the primary and auxiliary systems of the test rig and the infrared thermal imager are indicated in Table 3.3.

Table 3.3 Specifications of test rig components

Component	Specifications
<i>Servo motor</i> BALDOR, BDM – 100C – 3250	Continuous stall torque, 14.2 Nm Rated speed, 1200 rpm
<i>Data acquisition system</i> HBM, QuantumX - MX840A	Data rate, 0.1 to 19200 Hz Operating temperature range, -20 °C to +65 °C
<i>Torque sensor</i> HBM, T20WN	Torque measurement range, 0 to 100 Nm Maximum measurable rotational speed, 3000 rpm
<i>Rotary potentiometer</i> MCB PR27M	Theoretical electrical travel, 0° to 345° Operating temperature range, -55 °C to +125 °C
<i>Bellow couplings</i> KBK, KB4C	Maximum torque, 1400 Nm Temperature range, -30 °C to +120 °C
<i>Infrared thermal imager</i> Testo, 870-1	Infrared Resolution, 160 × 120 pixels Temperature range, -20 °C to +280 °C

3.2.2 Bending fatigue test details

Load-controlled bending fatigue tests were carried out to assess the bending fatigue behavior of the test gears. Cyclic bending fatigue loads conforming to the sine wave pattern were applied. The cyclic loading was repeated in nature, with a stress ratio of $R = 0$, which agrees with the actual loading pattern in gears (Figure 3.7 (a)). Theoretically, contact between two gear teeth occurs along a line. However, in actual contact conditions, the contact occurs in an area. Hence, in the experiments, the gears were loaded in such a way that the contact occurred between the pitch point and the highest point of single tooth contact (HPSTC). The applied test loads were selected to study the performance of the test gears under the high cycle fatigue conditions (life $> 10^4$ cycles). The torque applied on the injection-molded symmetric and asymmetric gears ranged between 5 and 12 Nm. For selective laser sintered gears, the applied

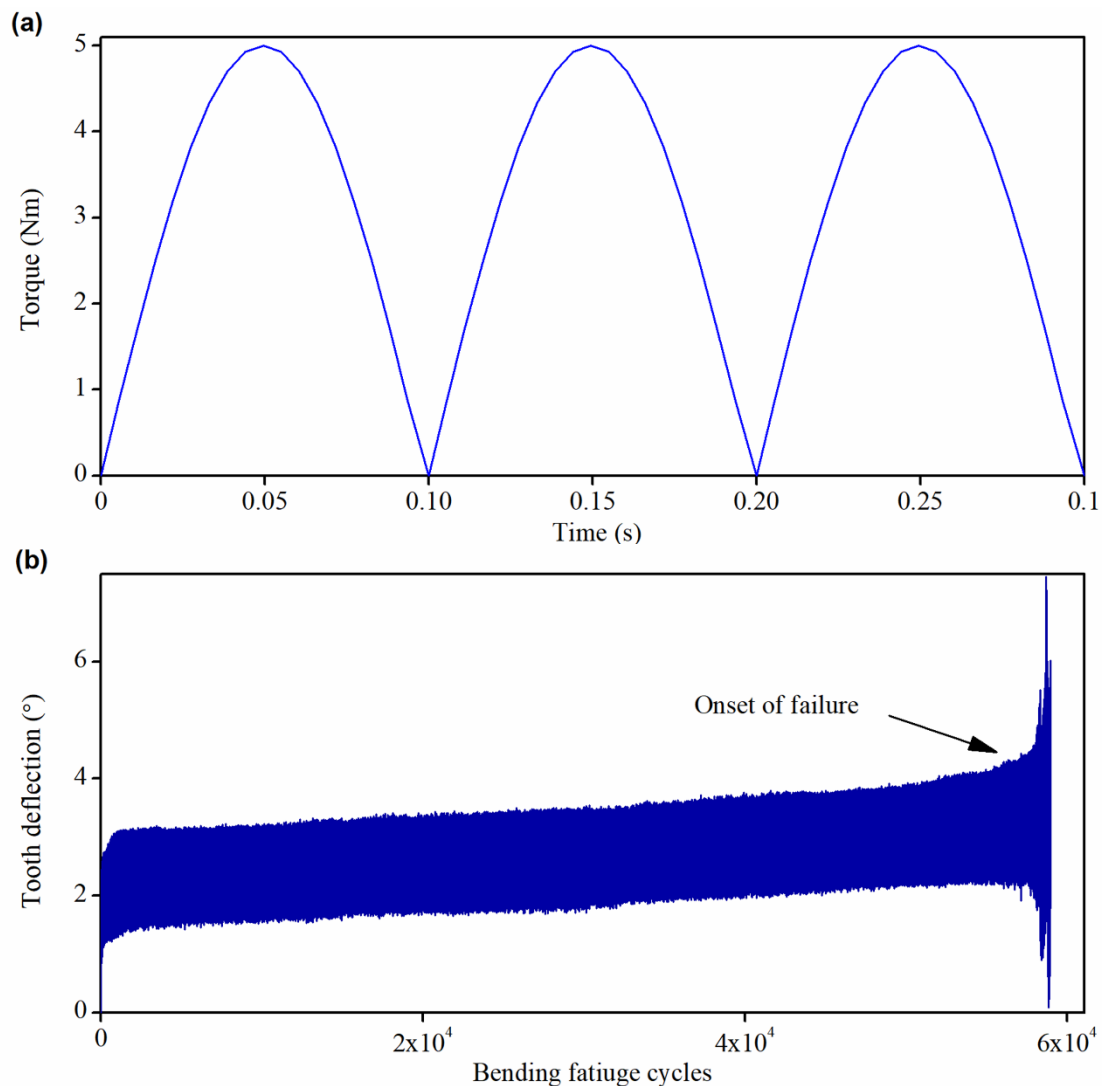


Fig. 3.7 (a) Typical loading waveform applied during the test and (b) Evolution of tooth deflection of a selective laser sintered gear tooth subjected to 5 Nm.

torque was in the range of 4 - 8 Nm. To obtain reliable test data, different gears were tested with the same load to account for the variation in properties among the gears in a batch. In SLS gears built in the 'flat' configuration, the layer arrangement is consistent across all teeth, and layers are not oriented with respect to the tooth axis. As a result of this identical layer pattern, the influence of layer arrangement on the tooth bending fatigue strength is similar in every tooth. However, in gears built in the 'on-edge' configuration, the bending fatigue strength of each tooth may vary from each other as the layer orientation is different in each tooth. The degree of anisotropy in bending fatigue strength could be determined by individually testing each tooth with different layer orientations and identifying the layer orientations with the highest and lowest fatigue life. The test gear comprises 18 teeth, with two sets of 9 unique tooth orientations ranging from 0° to 160° with an interval of 20° . Each configuration was tested at

one load level (5 Nm), and the configurations with the highest and lowest strength were subjected to further tests at various load levels. In the investigations concerning injection-molded symmetric and asymmetric gears, the influence of deflection-induced load sharing on the bending fatigue strength was evaluated. Hence, the teeth adjacent to the loaded tooth were not removed, as the adjacent tooth contact alters the stiffness of the pair. However, in the investigations of selective laser sintered gears, the individual strength of each orientation was determined. Hence, the adjacent teeth were removed in those experiments to prevent load sharing. In an effort to minimize the test duration, an accelerated life testing methodology was adopted, and a cycling frequency of 10 Hz was applied.

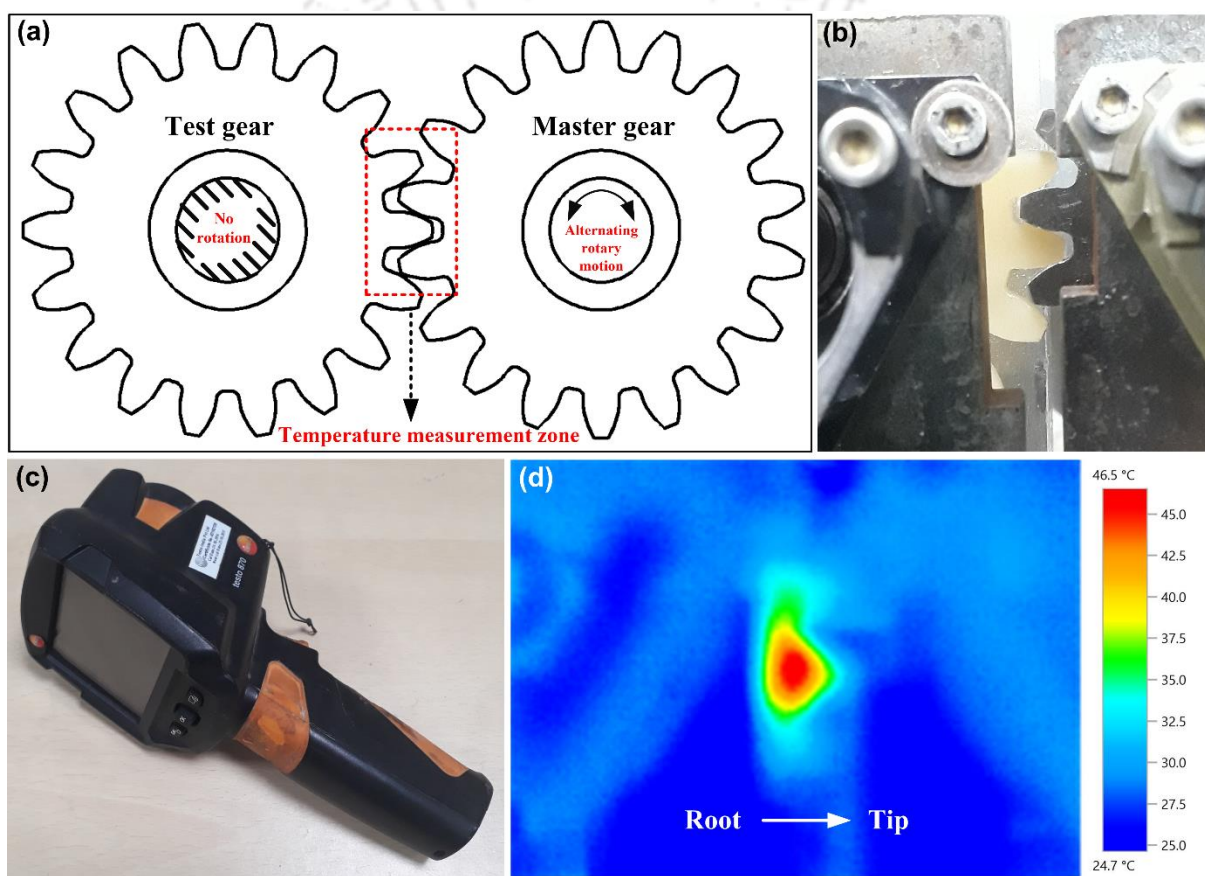


Fig. 3.8 (a) Schematic representation of the meshing gears indicating the region of temperature measurement, (b) Close-up view of the teeth mesh, (c) Infrared thermal imager, and (d) a sample infrared image of the teeth mesh.

Generally, higher cycling frequencies are not recommended for polymer testing, as the internal heat generation weakens the strength of the material (Rosato, Rosato and Rosato, 2001; Kodeeswaran *et al.*, 2019). However, for tests entailing considerably longer duration, accelerated testing is warranted. As bending fatigue tests are typically time-consuming, a

higher cycling frequency was deemed appropriate. During the course of the test, cracks occur in the drive side fillet region due to the prolonged bending fatigue loads. The tests were concluded after the crack propagated to a noticeable length. The tooth fracture was avoided in order to study the crack morphology on the gear surface. The crack propagation was detected by monitoring the output of the rotary displacement sensor, which measures the tooth deflection. Figure 3.7 (b) depicts the typical evolution of gear tooth deflection during testing. The sudden spike in the tooth deflection above 50000 cycles denotes the rapid crack propagation.

During cyclic loading, the hysteresis heating in polymer gears decreases the tooth stiffness. This leads to a steady rise in the minimum tooth deflection during a cycle. In the event of the non-occurrence of crack failure until 2 million cycles, the test was discontinued and declared to be a 'run-out.' Kalin and Kupec (2017) set 2 million as the limit for suspending the tests. Unlike rotational tests, the bending fatigue tests are limited by the maximum cycling frequency that can be applied. A lower cycling frequency increases the test duration significantly. Hence, it is essential to prescribe a 'run-out' limit in bending fatigue tests to conserve time.

The test environment temperature was around 25 ± 2 °C, whereas the relative humidity was $50\pm 5\%$ RH. The surface temperature of the test tooth was monitored and recorded by the IR camera at selected intervals. Since the temperature rise in bending fatigue tests is limited to the test tooth and its immediate vicinity, the thermal imager recorded the gear surface temperature in that region (Figure 3.8). The measurement was carried out to observe the temperature evolution and study the distribution in various tooth regions. In fatigue tests, the temperature rise is rapid in the initial phase, followed by a stable temperature rise, culminating in a sharp temperature rise during the failure phase. Hence, more data was collected during the initial and final stages. The gear temperature was not regulated by any external arrangements to remove the heat generated during the tests. The fatigue tests were followed by microscopy investigations using a stereomicroscope (Nikon, SMZ25) and a field emission scanning electron microscope (FESEM) (Zeiss, SIGMA 300). The gear tooth surface in the fillet region was examined to investigate the crack morphology. In certain cases, the fracture surfaces were inspected to analyze the path of the crack front.

3.2.3 In-house static tooth deflection test rig

The mesh deflections of gear pairs were measured using a custom-built test setup (Kodeeswaran, Suresh and Senthilvelan, 2016) (Figure 3.9). The driver (master gear) and

driven (test gear) gears were mounted on their respective shafts at a fixed center distance. The loading system comprised a loading hanger suspended from a pulley using a wire wound over it. The pulley was connected to the master gear shaft. Thus, adding weights to the hanger applied a static torque on the master gear shaft, which was measured by a torque sensor (HBM, T20WN). The master gear transmitted the torque to the driven gear. The test gear shaft was placed in a static condition using a locking plate. This arrangement permits the master and test gear teeth to mesh at any location along the tooth profile.

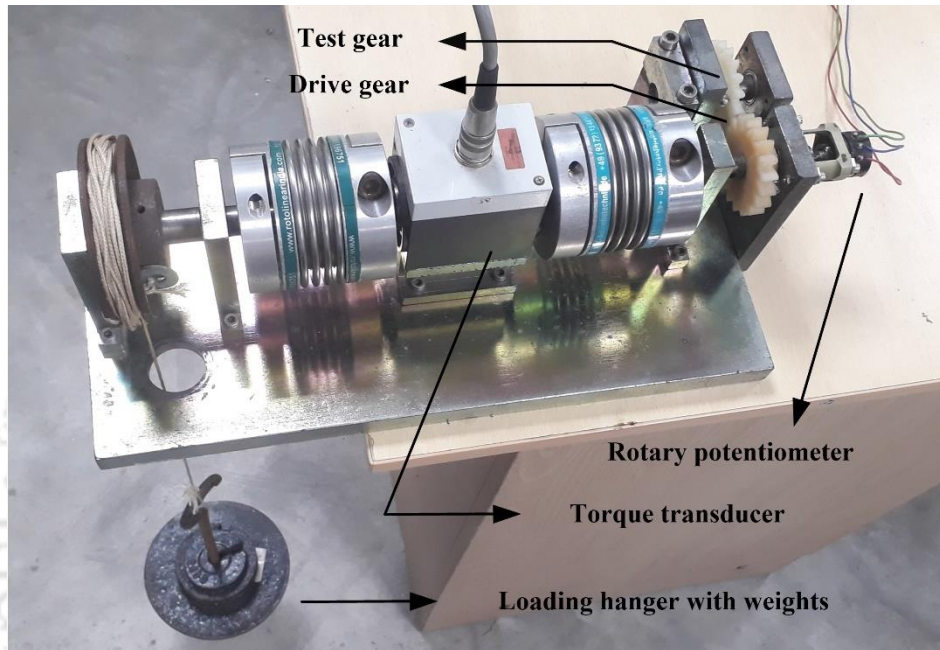


Fig. 3.9 Experimental test rig used to measure static tooth deflection in polymer gears.

A rotary potentiometer (MCB, PR27M) fixed to the driveshaft recorded the angular displacement of the driver gear during loading. The master gear rotation occurs due to the teeth deflection as the test gear is fixed. This rotation serves as an indicator of the torsional mesh deflection. Since the tooth deflection occurs on a minute scale, the measurements must be precise, and unnecessary errors caused by slippage must be avoided. Therefore, the pulley, torque sensor, and the master gear shaft were connected using bellows couplings (KBK, KB4C), which prevent interplay between the coupling and shaft. The test gear was attached to the shaft using a pin and nut locking arrangement. This prevented the relative rotation with respect to the shaft, resulting in deflection only in the tooth region.

3.2.4 Static tooth deflection test details

During testing, the ambient temperature and humidity levels were $25\pm 2^\circ\text{C}$ and $50\pm 5\%$ RH, respectively. The mesh deflections corresponding to two torque levels (1 and 1.5 Nm) were

measured. Torques of lower magnitude were applied to prevent plastic deformation. The measurement was carried out on the entire flank length to encompass the mesh cycle. The measurement was concluded when the test gear tooth disengaged completely from the driver gear tooth. The contact positions were identified in terms of roll angle. The roll angle indicates the angle of rotation of the gear pair to mesh at a particular location. The tooth tip was the reference position in the tests, indicated by a roll angle of 0° .

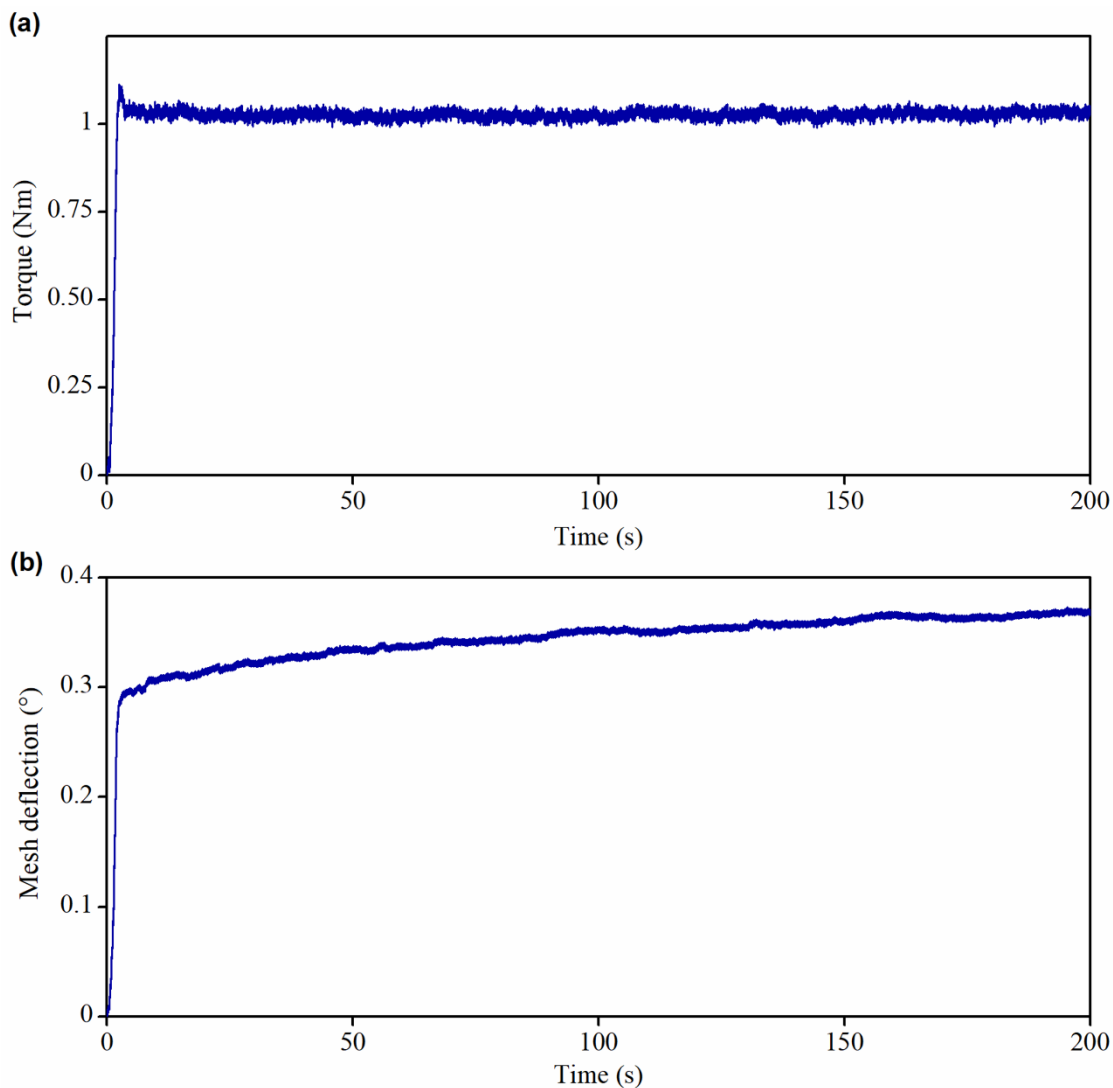


Fig. 3.10 Typical plots of experimental data: (a) Applied torque values in a test and (b) mesh deflection variation during a test.

Each mesh position was spaced at an interval of 2° from the previous position. The mesh deflection increased rapidly during the initial phase due to the sudden application of the load. For each mesh position, the load was applied for a duration of 200 s. Due to viscoelastic creep, the teeth deflected continuously during loading. The value of mesh deflection at 200 s was

considered for comparison. To obviate the effect of creep in subsequent measurements, a recovery period of 10 minutes was maintained after the completion of each test. The tooth regained its original undeformed position during this recovery period. Figure 3.10 shows the typical plots of applied torque and mesh deflection data acquired during experiments.

3.2.5 Material characterization

To acquire the material properties required for simulating the mechanical behavior of Nylon 66, material characterization tests such as tensile tests and dynamic mechanical analyses were carried out. Tensile tests were conducted using the INSTRON 8801 in displacement-controlled mode at a strain rate of 0.0003 s^{-1} to determine Young's modulus of Nylon 66 (Kodeeswaran, Suresh and Senthilvelan, 2019). Figure 3.11 (a) depicts the variation of tensile stress with respect to tensile strain during loading. Dynamic mechanical analysis was conducted using the analyzer Anton Parr MCR 702e MultiDrive. A frequency scan was carried out under flexural mode to obtain the frequency-dependent viscoelastic data.

Oscillating flexural strain was imposed on three-point bending specimens, while the cycling frequency was varied. The testing under the three-point bending mode is advantageous as it does not involve any clamping arrangement. Modulus error may occur in geometric arrangements involving clamping due to the difference between the stiffnesses of testing and clamping materials. Also, the geometric stiffness is lowest for three-point bending specimens, which minimizes the load required to strain the material (Duncan, 2008).

The cycling frequency ranged between 0.1 to 50 Hz. The DMA experiments were conducted in an environment similar to the conditions under which gear tests were performed. The ASTM D4065-20 (2020) stipulates that the maximum strain amplitude must be within 1%. Generally, this limit pertains to the linear viscoelastic range, in which the material response is independent of the applied strain. Accordingly, a strain amplitude of 0.25% was considered for the analysis. A pre-load of 0.1 N was maintained to sustain continuous contact during the test. Storage and loss moduli corresponding to various frequencies were obtained from the DMA experiments. The evolution of storage modulus and loss modulus as a function of cycling frequency is represented as a semi-log plot in Figure 3.11 (b).

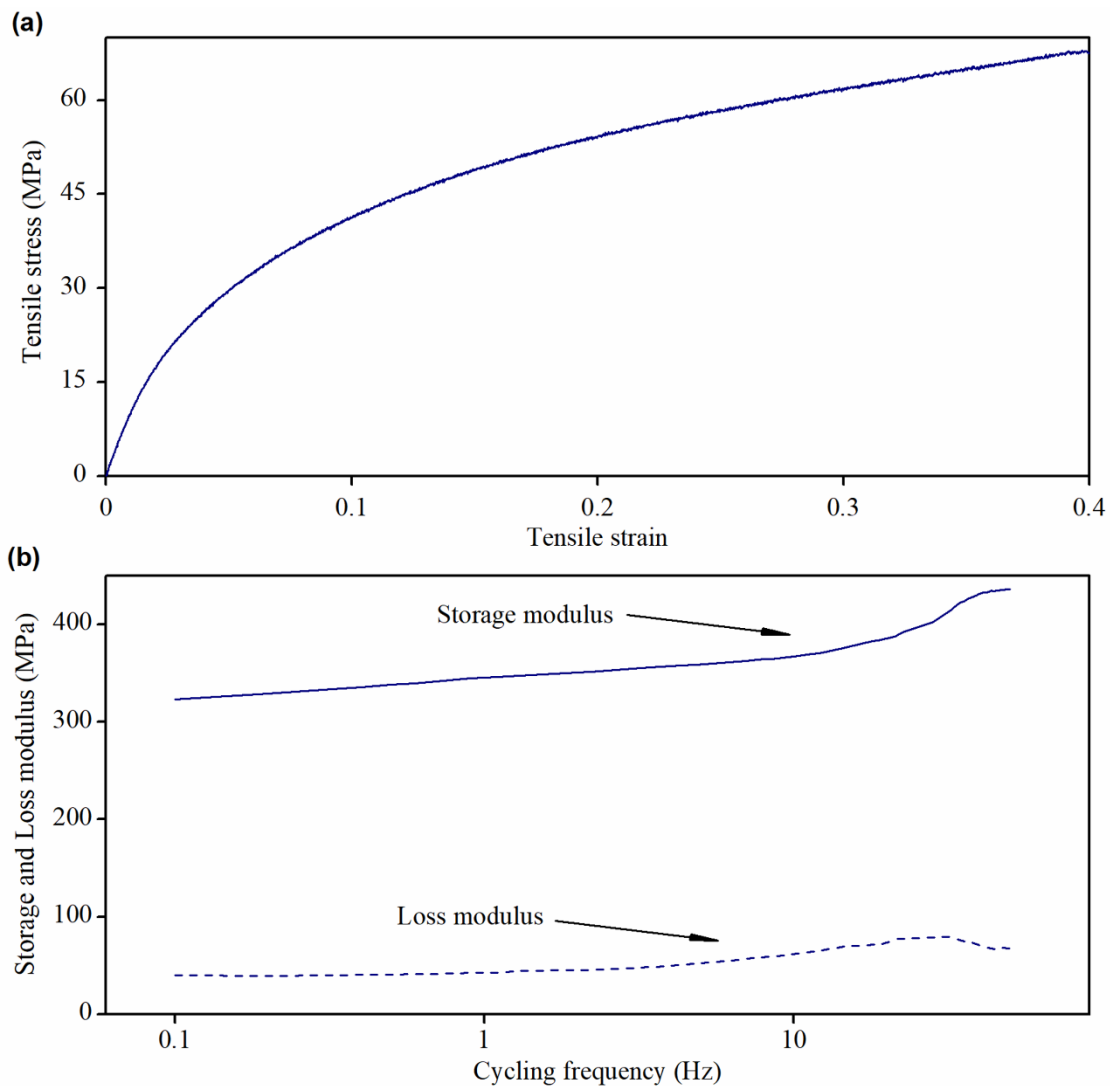


Fig. 3.11 Material characterization data of Nylon 66: (a) Tensile stress-strain curve and (b) Frequency-dependent storage and loss moduli obtained from DMA.

3.3 Root bending stress in polymer gears – Influence of load sharing

The evaluation of the maximum root bending stress is essential to comprehend the influence of tooth asymmetry and mating gear material on the fatigue performance of the gear pair. ISO 6336-3 defines the nominal bending stress as the maximum principal stress induced in the fillet when a geometrically ideal gear pair is subjected to a static torque. The maximum bending stress induced on the tooth fillet depends on the magnitude of the peak load experienced during the cycle. The load shared by the adjacent teeth alters the peak load and influences the maximum bending stress of a tooth. The actual contact ratio of a polymer gear is greater than the theoretical transverse contact ratio, which significantly enhances the load shared by the adjacent teeth (Walton *et al.*, 1994).

The actual contact ratio during operation is dependent on the stiffness of the material and applied load. The influence of these factors on the actual contact ratio is limited for metal gears, as the higher tooth stiffness minimizes the tooth deflection. On the contrary, the lower Young's modulus causes considerable tooth deflection in polymer gears, resulting in premature and extended contacts. Furthermore, the extent of load sharing in polymer gears increases with an increase in the magnitude of the applied load (Karimpour, Dearn and Walton, 2010; Hasl *et al.*, 2017).

Hence, estimation of bending stress without considering the effect of deflection-induced load sharing can result in unrealistically high bending stress values. The experimental results of Hasl *et al.* (2018) revealed that the load-carrying capacity of POM gears was significantly higher than the predicted values, as the effect of the increased contact ratio was disregarded by the VDI 2736 method. Thus, polymer gears need to consider the deflection-induced increase in load sharing during the calculation of maximum bending stress.

The analytical methods VDI 2736 Blatt 2:2014-06 (2014) and DIN 3990:1987-12 (1987) Method C incorporate the load sharing by means of the contact ratio factor (Y_ϵ), which is calculated using the transverse contact ratio (Hasl *et al.*, 2017). Few works (Fürstenberger, 2013; Hasl *et al.*, 2017) have employed analytical techniques wherein the effect of deflection-induced load sharing was considered during the calculation of the bending stress of metal - polymer gear pairs. Apart from analytical methods, the finite element method has been utilized to calculate the load sharing in polymer gears (Walton *et al.*, 1994; Van Melick, 2007; Karimpour, Dearn and Walton, 2010). The ISO 6336-3 Method A advocates the use of FEM for the calculation of bending stress. The finite element analysis can incorporate the effect of gear materials on load sharing and bending stress. In addition, FEM predicts bending stress with better accuracy compared to analytical methods (Lisle, Shaw and Frazer, 2017).

Hence, this study predicted the maximum bending stress in the root region of symmetric and asymmetric gears of metal - polymer and polymer - polymer material combinations using finite element analyses carried out in ABAQUS/Standard. In addition, the load sharing ratio was determined to quantify and analyze the effect of mating gear material on the load sharing behavior. The finite element model used in analyses is described in the next section.

3.3.1 Analytical determination of root bending stress

As mentioned earlier, the calculation of root bending stress is essential to construct S-N curves. In the case of selective laser sintered gears, load sharing was absent in the experimental study

owing to the removal of adjacent teeth. Hence, a numerical analysis was not adopted to determine the bending stress. The maximum bending stress in the fillet (σ_F) corresponding to each applied test load was determined analytically by following ISO 6336-3 Method B. As Method B is suitable for analyzing fatigue tests involving loading at a particular point, it was deemed appropriate for the current study. The nominal bending stress (σ_{F0}) was calculated, and modifying factors such as application factor (K_A), dynamic factor (K_v), face load factor ($K_{F\beta}$), and transverse load factor ($K_{F\alpha}$) were disregarded. In order to obtain a conservative estimate of the bending stress, the compressive stress was excluded. Equations (3.1) and (3.2) specify the expressions for the maximum and nominal bending stress at the root.

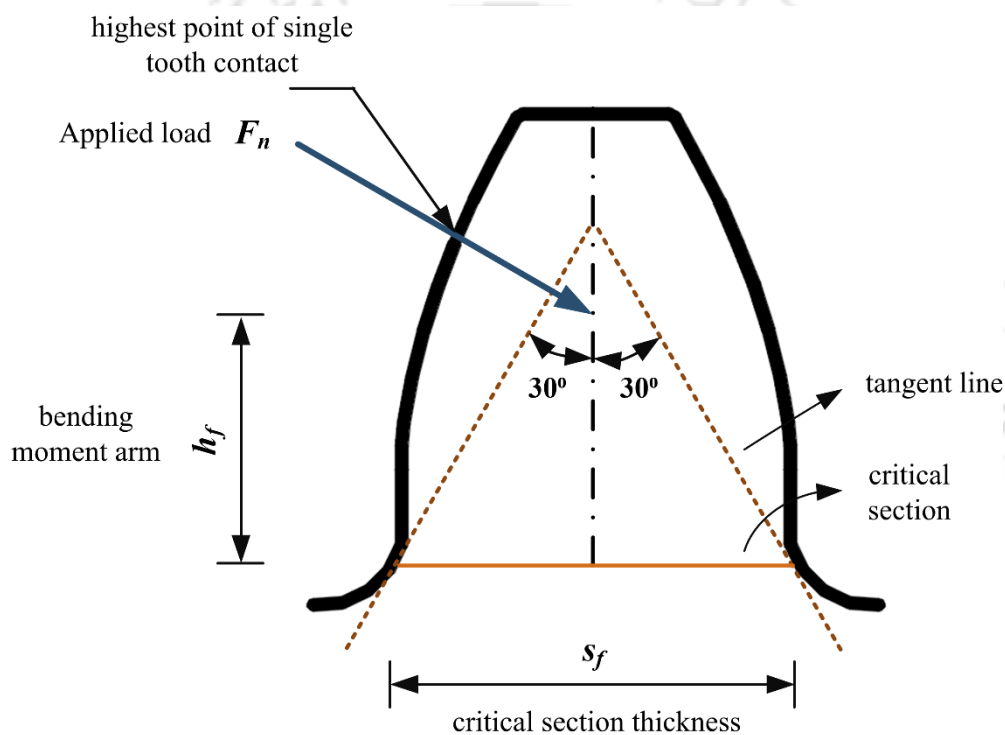


Fig. 3.12 Critical section parameters used in bending stress determination.

The determination of the form factor (Y_F) and stress correction factor (Y_S) involves the estimation of bending moment arm (h_f) and critical section thickness (s_f). The h_f and s_f depend on the location of the highest point of single tooth contact (Figure 3.12). In polymer gears, the deflection-induced load sharing can alter the HPSTC causing a divergence from the theoretical value. However, the theoretical estimate of the HPSTC was applied as load sharing was absent in SLS gears. The values of h_f and s_f of the test gear geometry were estimated graphically using the 30° tangent method.

In this method, two 30° lines were drawn tangent to the fillets to identify the critical section location. The bending moment arm was measured as the distance between the critical section and the point of intersection of the line of action and the tooth centerline. The s_f and h_f were utilized to determine the form and stress correction factors using equations (3.3) - (3.7). The theoretically estimated values of h_f , s_f , Y_F , and Y_S for the considered symmetric gear geometry are presented in the next chapter. The helix angle factor (Y_β), rim thickness factor (Y_B), and deep tooth factor (Y_{DT}) were assigned the value of 1.

The maximum tensile stress (σ_F) at the root is given by Eq. 3.1 as

$$\sigma_F = \sigma_{F0} K_A K_v K_{F\beta} K_{F\alpha} \quad (3.1)$$

The expression of nominal root stress (σ_{F0}) is given by Eq. 3.2 as

$$\sigma_{F0} = \frac{F_t}{bm} Y_F Y_S Y_\beta Y_B Y_{DT} \quad (3.2)$$

where F_t is the nominal tangential force acting on the tooth, b is the tooth face width, and m is the normal module.

The form factor expression is defined by Eq. 3.3 as

$$Y_F = \frac{6 \left(\frac{h_f}{m} \right) \cos \alpha_{Load,HPSTC}}{\left(\frac{s_f}{m} \right)^2 \cos \alpha} \quad (3.3)$$

where $\alpha_{Load,HPSTC}$ is the load angle at the highest point of single tooth contact and α is the pressure angle at the pitch cylinder. Eq. 3.4 provides the expression for the stress correction factor,

$$Y_S = (1.2 + 0.13L) q_s^a \quad (3.4)$$

The parameters L , q_s , and a are given in Eq. 3.5 - 3.7 as

$$L = \frac{s_f}{h_f} \quad (3.5)$$

$$q_s = \frac{s_f}{2\rho_f} \quad (3.6)$$

$$a = \frac{1}{1.21 + \frac{2.3}{L}} \quad (3.7)$$

where ρ_f is the radius of the root fillet at the critical section.

3.3.2 Calculation of load sharing ratio

The load sharing behavior of steel-polymer and polymer-polymer gear pairs was compared using the load sharing ratio (LSR). The load sharing ratio indicates the fraction of the total load applied on a contact pair. The loaded tooth is the leading contact pair, and the adjacent tooth is the trailing contact pair. The calculation of the load sharing ratio requires the contact force exerted on the flanks of leading and trailing teeth. The contact force on the flanks' during loading was obtained from numerical simulations. Typically, in a cycle, the LSR for a teeth pair reaches a maximum of 1 during the single tooth contact period and returns to zero as the tooth pair disengages completely. The formula used for calculating the LSR of the leading pair (Sekar and Muthuveerappan, 2015) is shown below:

$$LSR_{\text{Leading pair}} = \frac{\text{Contact force at leading Pair}}{\text{Contact force at leading pair} + \text{Contact force at trailing pair}} \quad (3.8)$$

3.4 Finite element analysis

This section describes the various aspects of the finite element models used in the study and the rationale behind the selection of each parameter. First, the geometric model of the gear pair and the relevant boundary conditions are presented. Following this, the details related to model discretization and material behavior approximation are discussed.

3.4.1 Finite element model description

As mentioned earlier, the maximum bending stress induced in the root region of a polymer gear tooth depends on the load shared by the adjacent tooth (Van Melick, 2007), which necessitates the inclusion of load sharing effects in the analysis. For considering the impact of adjacent tooth contact, multi-pair contact models (MPCM) and multi-point loaded models (MPLM) can be employed. The gear tooth deflection comprises three components: bending, contact, and shear. For accurate prediction of the bending stress, the numerical model of the gear pair must consider the three deflection components. In this regard, a multi-pair contact model is better than a multi-point loaded model as it incorporates the contact deflections precisely (Thirumurugan and Muthuveerappan, 2011). This, in turn, enables the MPCM to accurately calculate the load shared by the adjacent tooth under various conditions. On the contrary, the

use of MPLM requires pre-determination of the load shared by the teeth using analytical methods, which may lead to misestimation.

Generally, three-dimensional (3D) models are appropriate for representing the actual contact conditions, which may involve misalignments and edge contact caused by the inaccuracies of gear geometry and assembly elements. Non-uniform contact and load distribution along the facewidth significantly increase stress and transmission error, resulting in premature failure. However, simulations involving contact and large deformation are time-intensive, and consequently, the use of two-dimensional models (2D) is encouraged to reduce the computational effort. In quasi-static numerical analyses, the gear bending stress can be predicted using a three-teeth model with a minimum error of 1% compared to models of the complete gear (Lisle, Shaw and Frazer, 2017). Hence, a model with three teeth is preferable compared to a complete gear model. A three-teeth model is adequate to incorporate the double tooth contact as part of the mesh cycle. A full-rim body was considered over a sectoral body as gear models with a full rim suitably approximate the actual gear mounting conditions. The rigidity induced by the boundary conditions constrains the tooth deflection in the sector model, causing lesser deflection than in full-rim models (Thirumurugan and Muthuveerappan, 2010).

Accordingly, this study uses 2D, multipair contact models of symmetric and asymmetric gears with three teeth and full-rim. In the model, the driver and driven gears are positioned at the top and the bottom, respectively. The parts of symmetric and asymmetric gears were created and discretized in ABAQUS/Standard. An ideal involute curve was considered for the profile, and the profile deviations which occur during fabrication were disregarded. The involute profile for the teeth was generated using the coordinates determined using a MATLAB code.

3.4.2 Boundary conditions

In order to perform the quasi-static analysis, appropriate boundary conditions were applied on the driver and driven gears. In the case of driver gear, the displacement motions along the three directions were arrested, and rotation was allowed with respect to the z-axis. For driven gear, displacements and rotations were constrained completely. The rotation with respect to the center axis was allowed for master gear, as the rotation of master gear is necessary to exert load on the flanks of test gear. For the torque application, a reference node was created on the center axis of the driver gear (RP-1, RP-2).

A kinematic association was established between the center axis and the inner portion of the hub. The user-defined load was applied in the form of torque through the reference node RP-

2. The applied torque was transmitted to the gear by the kinematic coupling. Surface-to-surface contact interaction was specified. The contacting flanks of driven and driver gears were assigned as the master and slave surfaces, respectively. The non-linear option NLGEOM in ABAQUS was enabled during the analysis due to polymers' large deformation behavior and the inherent non-linear nature of the contact simulations. The analyses were performed under plane strain conditions.

3.4.3 Model discretization and mesh convergence study

The model was discretized with the 4-noded CPE4R, a bilinear, quadrilateral element applied for plane strain analyses. The model instances were meshed using the top-down technique. The mesh density was higher in the root fillet and drive side contact flanks of the teeth, whereas the mesh was coarser in the hub and rim portions. The model was discretized in two ways. In the first type, referred to as 'Gear pair model 1,' free meshing with the advancing front algorithm was employed. In order to extract the tooth deflection from various points along the tooth depth, the model was discretized in a different way. In the second type, referred to as 'Gear pair model 2,' the gear geometry was partitioned into various regions with a partition line in the middle of the tooth, extending from the tip to the root region. In the immediate vicinity of flanks and fillet, a region in the shape of a band was partitioned and meshed with finer element size using the structured mesh technique. On the other hand, the free mesh technique was used in the body region with a coarser element size.

Gear pair model 1 was used in the study investigating the influence of asymmetric teeth on the bending fatigue performance of steel-polymer gear pairs. Gear pair model 2 was utilized in the study investigating the effect of metal and polymer mating gears on the bending fatigue performance of asymmetric polymer gears. For investigating the deflection characteristics of asymmetric polymer gears, Gear pair model 2 was employed. Figures 3.13 and 3.14 show 'Gear pair model 1' of symmetric gears and 'Gear pair model 2' of asymmetric gears, respectively.

The mesh density in the fillet region was optimized to enhance the accuracy of the results. The h-method was adopted to study the convergence of the maximum bending stress in the fillet region of the symmetric gear. The element size was progressively reduced until the deviation in the stress value was less than 2%. The maximum principal stress was considered as the bending stress. The predicted stress results were compared with the analytically determined values to validate the finite element model. ISO 6336 Method B was used to estimate the theoretical bending stress. Figure 3.15 (a) shows the maximum root bending stress in a steel-

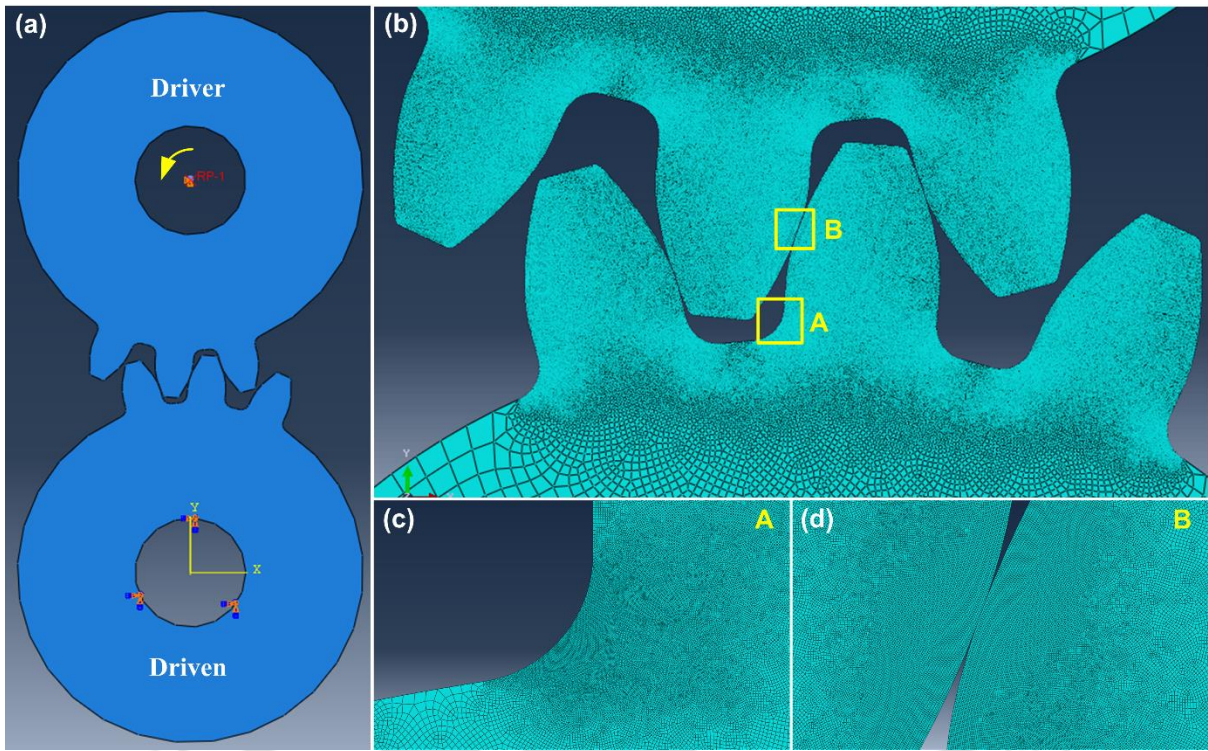


Fig. 3.13 Gear pair model 1 of symmetric gear: (a) Kinematic model indicating boundary conditions, (b) Discretization, and (c, d) Element density in root and flank contact region.

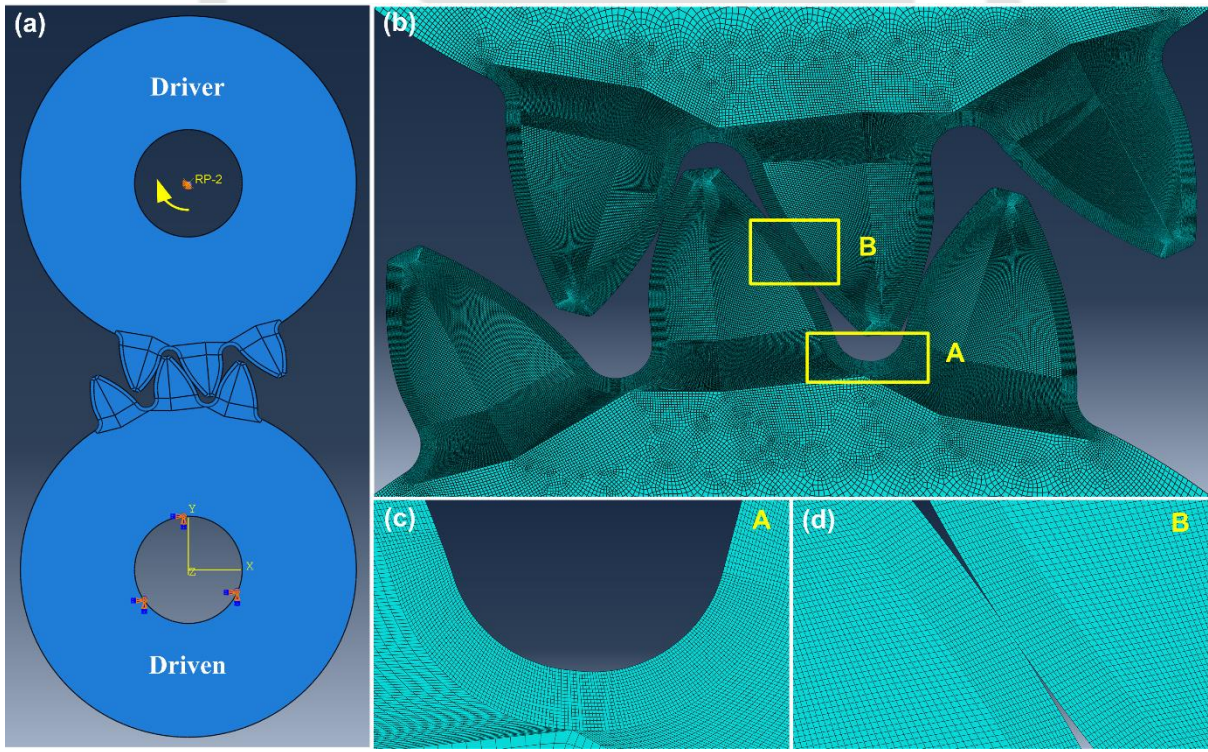


Fig. 3.14 Gear pair model 2 of asymmetric gear: (a) Kinematic model, (b) Discretization in teeth, and (c, d) Element density in root and flank regions.

steel symmetric gear pair for a reference load of 1 Nm. The bending stress distribution in the gear tooth is shown in Figure 3.15 (b and c). Below an element size of 10 μm , the deviation was negligible. However, the computational time increases significantly. Based on the results, the element size of 10 μm was considered optimum for the mesh in the fillet region. The element size in the flank region was 50 μm , whereas the element size in the coarse mesh region varied from 0.05 to 2.5 mm.

3.4.4 Material behavior

AISI 316 and Nylon 66 were considered for the driver gear material, whereas Nylon 66 was the driven gear material in both steel-polymer and polymer-polymer pairings. The behavior of AISI 316 steel was defined using a linear elastic model. Accordingly, Young's modulus ($E = 200 \text{ GPa}$), Poisson's ratio ($\nu = 0.3$), and density ($\rho = 7850 \text{ kg/m}^3$) were specified in the *Elastic* part of the ABAQUS material module. The material response of Nylon 66 was approximated using both linear elastic and viscoelastic models, depending on the application.

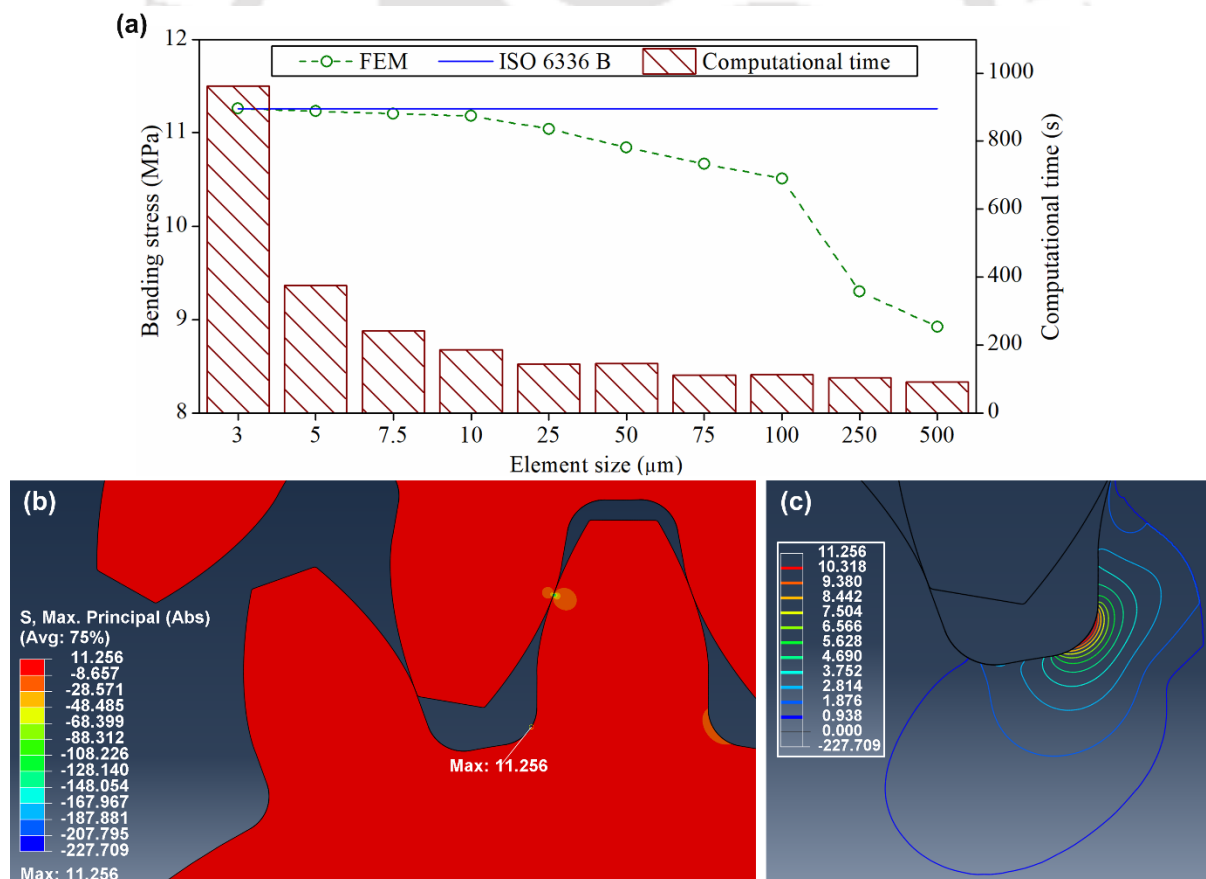


Fig. 3.15 Mesh convergence study: (a) Root bending stress and computational time corresponding to various element sizes, (b) Principal stress distribution in the gear teeth for the fillet element size of 3 μm , and (c) bending stress distribution in the root region.

In the study of the fatigue behavior of symmetric and asymmetric injection-molded gears, the FEM was used to predict bending stress and load sharing ratio. The Nylon 66 gears were assumed to exhibit linear elastic behavior and isotropic properties. The linear elastic assumption has been utilized to calculate polymer gears' bending stress in multiple works (Karimpour, Dearn and Walton, 2010; Hasl *et al.*, 2017). The Young's modulus ($E = 1.141$ GPa), Poisson's ratio ($\nu = 0.41$), and density ($\rho = 1140$ kg/ m³) of Nylon 66 were specified in the *Elastic* part of the ABAQUS material module. The specified material properties corresponded to the laboratory conditions. In the investigation of the stiffness behavior of injection-molded symmetric and asymmetric gears, the predicted mesh deflection values were compared with experimental values. The mesh deflection was measured continuously for 200 s in experiments. Since approximation of time-dependent response was required, a viscoelastic model was considered for Nylon 66 in that study. The linear elastic model was appropriate for stress analysis as the bending stress was predicted instantaneously.

In ABAQUS, the viscoelastic behavior of a material is modeled using a dimensionless relaxation modulus, which is defined by a Prony series expansion. ABAQUS provides multiple options to define the relaxation parameters of the Prony series. One option is to specify the frequency-dependent material response data obtained from experiments that apply oscillating load on the material (Simulia, 2014). The experimental values of storage and loss moduli were provided along with the cycling frequency as input in a tabular form to the *Viscoelastic* part of the ABAQUS model. The selection of the number of terms for the Prony series expansion of relaxation modulus depends on the range of test data. ABAQUS permits a maximum of 13 terms for the Prony series. Generally, it is preferable not to use a number of terms larger than the number of logarithmic decades required to span the entire test data. In our case, three parameters were considered for the model as the entire data range was within three logarithmic decades.

In numerical models of gears involving friction, the magnitude of bending stress decreases with an increase in friction on the contact surface (Li and Mao, 2013). The use of a frictionless contact surface in analysis results in a higher bending stress value, which is useful for a safer design. Therefore, frictionless contact was employed in stress analysis to predict the maximum bending stress. However, in actual contact conditions, friction exists between teeth surfaces and affects the performance considerably. Hence, a friction coefficient of 0.28 was considered in the study that compared the experimental and predicted mesh deflections.

3.5 Summary

This chapter described the details of the experimental and numerical methods employed in investigations, along with the analytical formulations. The following details were provided:

- The dimensions of gear geometry, material, and the parameters of injection molding and selective laser sintering processes.
- The components of the in-house built bending fatigue test rig and static gear tooth deflection test rigs such as loading system, control system, transducers, and fixtures for mounting the gears.
- The test procedure adopted during bending fatigue tests and static tooth deflection tests such as applied load range, loading mode, cycling frequency, termination criteria, etc.
- Details of material characterization tests such as tensile test and dynamic mechanical analysis.
- Analytical equations used for estimating the maximum root bending stress and load sharing ratio.
- The specifics of the finite element models of gear pairs used in the numerical simulations such as boundary conditions, discretization, mesh convergence analysis, and material models.

Chapter 4

Influence of asymmetric tooth profile on the bending fatigue behavior of polymer gears

Asymmetric tooth profile reduces the bending stress and increases the fatigue life of gears. The bending fatigue performances of injection-molded symmetric and asymmetric Nylon 66 gears are described in this chapter. Initially, the bending stress variation across a mesh cycle in symmetric ($20^\circ/20^\circ$) and asymmetric configurations ($34^\circ/20^\circ$ and $20^\circ/34^\circ$) has been compared to evaluate the influence of the asymmetric tooth on the bending strength. Following that, the form factor (Y_F) and stress correction factor (Y_S) of each configuration computed using an adapted ISO 6336 Method B approach have been analyzed to assess the cause behind the variation in bending stress.

After the stress analysis, the experimental results have been presented. The life of symmetric and asymmetric configurations subjected to load-controlled bending fatigue cycles and the influence of deflection-induced load sharing on the bending fatigue strength of asymmetric gear configurations have been discussed in detail. The thermal behavior exhibited by gears during testing and the post-failure morphology of gears are described in the end.

4.1 Analysis of root bending stress in symmetric and asymmetric gears

The maximum bending stress in the root fillet occurs during loading at the highest point of single tooth contact. In gear pairs comprising gear materials with lower stiffness, such as polymer, the location of the HPSTC is influenced by the deflection-induced load sharing. As mentioned previously, the low Young's modulus of the polymer gear increases the tooth deflection, leading to premature and extended contacts. Consequently, the single tooth contact zone (STC) diminishes, and the position of the HPSTC advances (Van Melick, 2007). Hence, for metal - polymer gear pairs, the theoretical HPSTC determined using the kinematic relations is unsuitable because it refers to a location in the double tooth contact zone (DTC).

Therefore, in order to identify the exact location of the HPSTC, the bending stress corresponding to every mesh position along the profile needs to be computed. Because Method

B of ISO 6336 does not account for the effect of load sharing, the use of FEM – as per ISO 6336 Method A – is pertinent for the bending stress determination. Accordingly, the bending stress variation across a mesh cycle was predicted using FEM to determine the HPSTC for the Steel – Nylon 66 gear pair. Also, FEM was employed to directly compare the bending strength of symmetric and asymmetric gears. The finite element analyses carried out as part of the study utilized ‘Gear pair model 1.’

4.1.1 Bending stress variation in a mesh cycle

The entire contact path in a tooth – between engagement and disengagement of a tooth pair – was simulated, with each position separated by a roll angle of 1° . The roll angle of 0° denotes the contact at the tooth tip, signifying the start of the engagement. Since the lower material stiffness of polymer gears advance and delay contacts, a deviation between the ideal and actual length of contact exists. Consequently, the number of simulations required to traverse the contact path is not pre-determined and depends on the tooth configuration and applied load. Figure 4.1 (a) shows the bending stress trends of symmetric and asymmetric configurations for an applied torque of 1 Nm.

The distribution of principal stress in each configuration is shown in Figure 4.1 (b) – (g). The asymmetric gear configurations ($34^\circ/20^\circ$ and $20^\circ/34^\circ$) exhibited lower bending stresses than the symmetric configuration ($20^\circ/20^\circ$). Compared to the $20^\circ/20^\circ$ configuration, the bending stress reductions in the $20^\circ/34^\circ$ and the $34^\circ/20^\circ$ configurations were 17% and 21%, respectively. Fuentes *et al.* (2013) reported that the bending stress of a $30^\circ/20^\circ$ asymmetric gear was lower than that of a $20^\circ/30^\circ$ asymmetric gear. Similarly, Sekar and Muthuveerappan (2015) observed that the minimum bending stress in asymmetric gear was found with a higher pressure angle on the drive side.

The use of a higher pressure angle increased the STC zone and decreased the mesh cycle period, resulting in a lower contact ratio. Figure 4.1 (a) indicates the significant increase in the STC zone and a decrease in the mesh cycle period for the $34^\circ/20^\circ$ configuration. The bending stress distributions in the DTC zones on either side of the STC zone were unequal. This was attributed to the different load sharing behavior observed in metal-polymer gear pairs. Unlike metal gear pairs, which exhibit symmetrical load sharing, the load sharing in a metal - polymer gear pair is skewed (Van Melick, 2007; Kirupasankar, Gurunathan and Gnanamoorthy, 2012). This causes unequal stress distributions in the DTC zones.

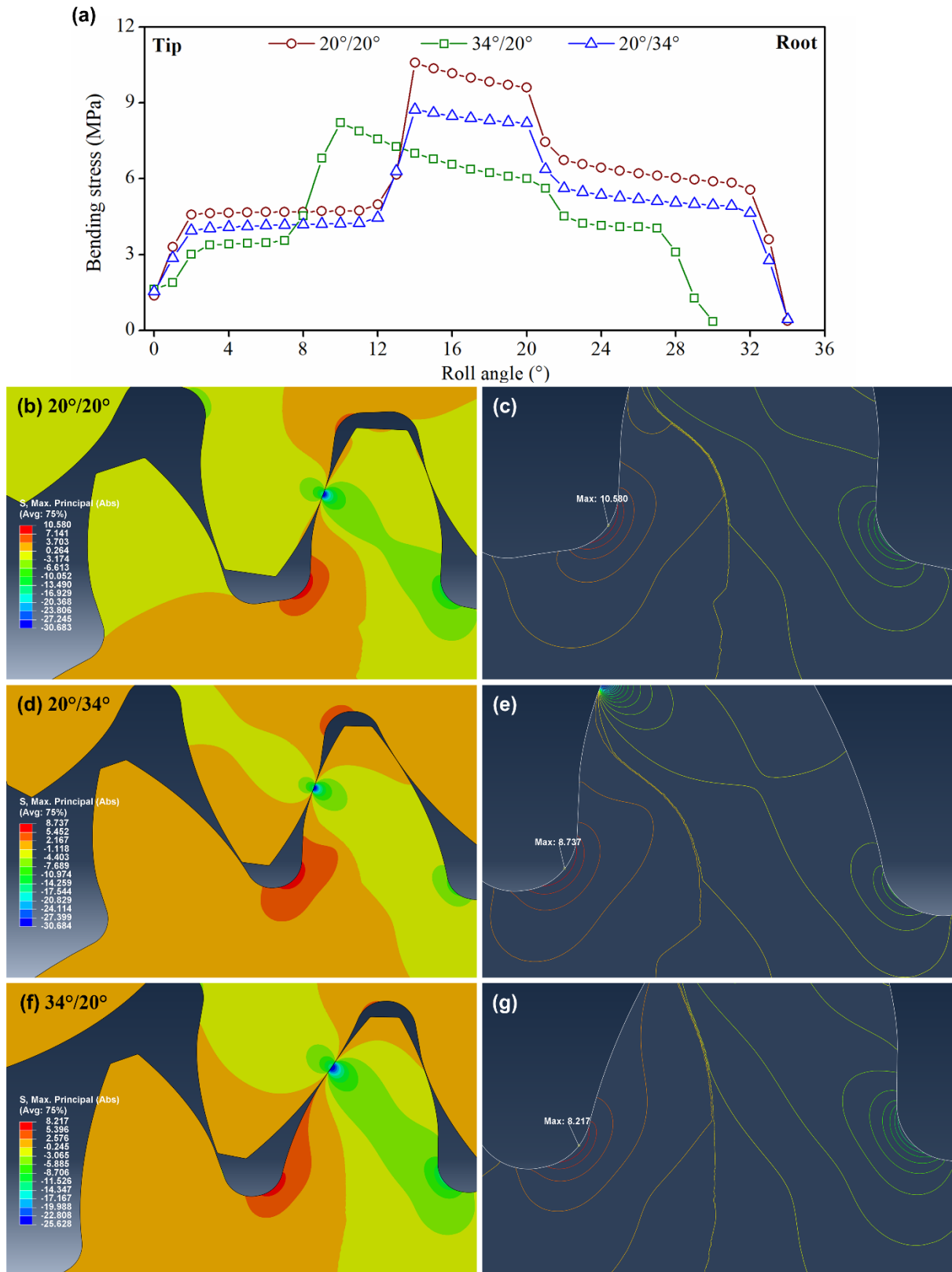


Fig. 4.1 (a) Bending stress variation across mesh cycle for symmetric and asymmetric configurations, (b, c) Principal stress in symmetric gear, (d, e) Principal stress in asymmetric gear configuration 20°/34°, and (f, g) Principal stress in asymmetric gear configuration 34°/20°.

4.1.2 Determination of form and stress correction factors

The finite element stress analysis established the considerable difference between the bending stresses of symmetric and asymmetric configurations. In order to comprehend this variation in bending stress, the effects of the drive and coast side pressure angles on the nominal bending stress needs to be quantified. The drive side pressure angle influences the location of the HPSTC, load angle, and length of the drive side fillet. These parameters determine the bending moment arm (h_f) and critical section thickness (s_f), which govern the bending stress in the fillet. The form factor (Y_F) and stress correction factor (Y_S) enclose h_f and s_f in ISO 6336-3 Method B. Hence, Y_F and Y_S can be regarded as a measure to elucidate the influence of the pressure angle on bending stress.

For asymmetric gears, Y_F and Y_S were determined based on the adapted ISO 6336-3 Method B framework presented by Sekar and Muthuveerappan (2015). To estimate Y_F and Y_S , the use of the h_f and s_f values determined by the FEM was deemed appropriate because the radius of the HPSTC predicted using an analytical expression does not conform to the actual HPSTC in metal – polymer gear pair. Nevertheless, Y_F and Y_S were determined both analytically and numerically to illustrate the relevance of each method.

In the analytical method, to determine the critical section thickness, the tangent line method was used to identify the maximum stress point on the fillet. The angle of tangent on the drive side (ψ_d) was assigned a value of 30° . The angle of tangent on the coast side (ψ_c) was determined using expression 4.1

$$\psi_c = 30 + \alpha_d - \alpha_c \quad (4.1)$$

Based on the values of ψ_c and ψ_d , s_f was estimated graphically (Figure 4.2 (a), (c), and (e)). To calculate h_f , the location of the highest point of single tooth contact and the load angle corresponding to HPSTC are required. The expression to calculate the radius at HPSTC (r_{HPSTC}) is given in Eq. 4.2

$$r_{HPSTC} = \sqrt{\left(r_{b,d,p}^2 + \left[p_{b,w,d} - AD + \sqrt{r_{a,d,p}^2 - r_{b,d,p}^2} \right]^2 \right)} \quad (4.2)$$

in which $r_{b,d,p}$ and $r_{a,d,p}$ are the base circle and addendum circle radii on the drive side of the pinion. The base circle on the drive side was calculated using Eq. 4.3

$$r_{b,d} = r_{o,d} \cos \alpha_{o,d} \quad (4.3)$$

wherein $r_{o,d}$ and $\alpha_{o,d}$ are the pitch circle radius and nominal pressure angle on the drive side of the tooth.

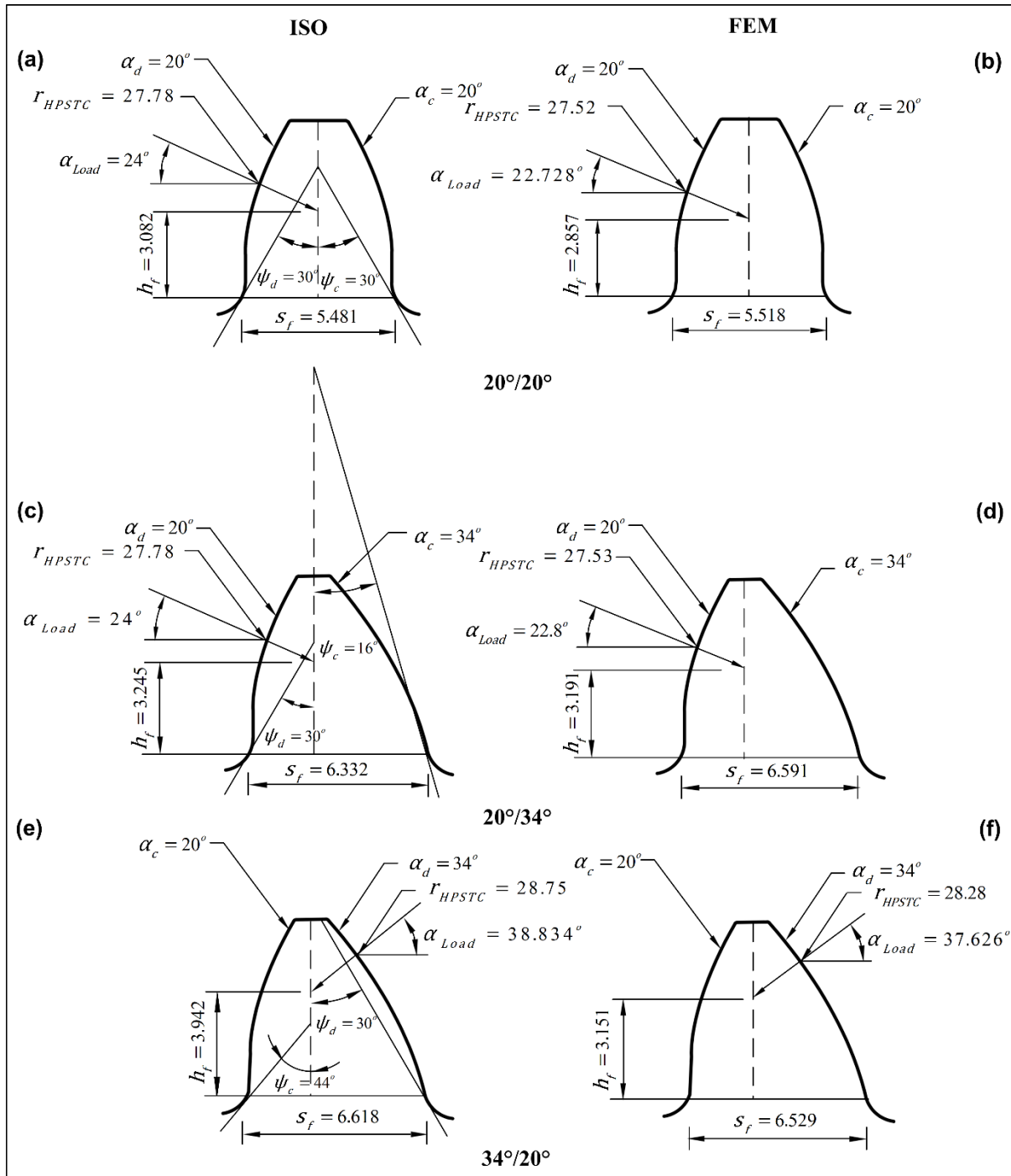


Fig. 4.2 Critical section parameters of symmetric and asymmetric configurations based on ISO and FEM: (a, b) 20°/20°, (c, d) 20°/34°, and (e, f) 34°/20° (all dimensions are in mm).

The length of the line of action, AD, in expression 4.2 was determined using Eq. 4.4

$$AD = \sqrt{r_{a,d,p}^2 - r_{b,d,p}^2} + \sqrt{r_{a,d,g}^2 - r_{b,d,g}^2} - (c_w \sin \alpha_{w,d}) \quad (4.4)$$

where c_w and $\alpha_{w,d}$ are the working center distance and pressure angle. In present case, the working center distance and pressure angle converge with theoretical values. Also, the addendum and base circle radii are the same for pinion and gear. The drive side base pitch $p_{b,w,d}$ was calculated using Eq. 4.5

$$p_{b,w,d} = \pi m \cos \alpha_{w,d} \quad (4.5)$$

The load angle at the HPSTC was calculated using the expression 4.6

$$\alpha_{Load,HPSTC} = \alpha_{HPSTC} - \theta \quad (4.6)$$

The α_{HPSTC} was determined using Eq. 4.7

$$\alpha_{HPSTC} = \cos^{-1} \left(\frac{r_{b,d}}{r_{HPSTC}} \right) \quad (4.7)$$

The parameter θ in equation (4.6) was computed using the expression 4.8

$$\theta = \text{inv } \nu_d - \text{inv } \nu_{HPSTC} \quad (4.8)$$

The computation of θ requires the tip angle ν_d , which was calculated using Eq. 4.9

$$\nu_d = \cos^{-1} \left(\frac{r_{b,d}}{r_{tip}} \right) \quad (4.9)$$

The involute function of ν_d was calculated through equation 4.10

$$\text{inv } \nu_d = \tan \nu_d - \nu_d \quad (4.10)$$

The involute function of ν_{HPSTC} was determined by using Eq. 4.11

$$\text{inv } \nu_{HPSTC} = \tan \alpha_{HPSTC} - \alpha_{HPSTC} \quad (4.11)$$

Using the r_{HPSTC} and α_{HPSTC} , the value of h_f was determined graphically. In the bending stress calculation, the exclusion of the compressive stress caused by the radial component can induce significant errors for gears with high pressure angles (Lisle, Shaw and Frazer, 2017). Hence, the compressive stress component was included in the form factor expression. The form factor (Y_F) and the stress correction factor (Y_S) were estimated using relations (4.12) – (4.16).

$$Y_{F,ISO} = \underbrace{\frac{6(h_f m) \cos \alpha_{Load,HPSTC}}{(s_f)^2}}_{\text{Tensile (I)}} - \underbrace{\frac{m \sin \alpha_{Load,HPSTC}}{s_f}}_{\text{Compressive (II)}} \quad (4.12)$$

$$Y_{S,ISO} = (1.2 + 0.13L)q_s^a \quad (4.13)$$

where

$$L = \frac{s_f}{h_f} \quad (4.14)$$

$$q_s = \frac{s_f}{2\rho_f} \quad (4.15)$$

$$a = \frac{1}{1.21 + \frac{2.3}{L}} \quad (4.16)$$

The maximum tensile stress at the drive side fillet is calculated by the ISO 6336 Method B (Eq. 4.17) as follows:

$$\sigma_{ISO,max} = \frac{F_n}{bm} Y_{F,ISO} Y_{S,ISO} \quad (4.17)$$

where F_n is the normal force, b is the face width, and m is the module. From this relation, a normalized, non-dimensional factor called the fillet stress factor ($\sigma_{F,ISO}$) was defined (Eq. 4.18) to compare the stresses of the different configurations.

$$\sigma_{F,ISO} = \frac{\sigma_{ISO,max}}{\frac{F_n}{bm}} = Y_{F,ISO} Y_{S,ISO} \quad (4.18)$$

In the finite element method, the torque was selected to apply equal normal forces on the symmetric and asymmetric gears. The normal force acting on the 20°/20° configuration for a torque of 1 Nm was selected as a baseline, and the torque on the 34°/20° configuration was calculated according to the following expression: $T = F_n \times r_b$. The critical stress locations on the drive and the coast side fillets were extracted from the nodal coordinates during post-processing. The h_f , s_f and $\alpha_{Load,HPSTC}$ values corresponding to the metal - polymer gear pairs are depicted in Figure 4.2 (b), (d), and (f). The form factor ($Y_{F,FEM}$) was calculated by substituting h_f and s_f in the expression for $Y_{F,ISO}$ (Eq. 4.12).

The stress correction factor ($Y_{S,FEM}$) was calculated using the inverse relation (Eq. 4.19) as follows:

$$Y_{S,FEM} = \frac{\sigma_{F,FEM}}{Y_{F,FEM}} \quad (4.19)$$

where $\sigma_{F,FEM}$ is the fillet stress factor calculated using the FEM. $\sigma_{F,FEM}$ was estimated using the expression 4.20

$$\sigma_{F,FEM} = \frac{\sigma_{FEM,max}}{\frac{F_n}{bm}} \quad (4.20)$$

To illustrate the procedure, a sample calculation has been presented. All the parameters corresponding to the 20°/34° configuration have been calculated using both ISO and FEM procedures.

4.1.3 Sample ISO method calculation

The angle of tangent on the coast side of the 20°/34° configuration is,

$$\psi_c = 30 + \alpha_d - \alpha_c = 30 + 20 - 34 = 16^\circ$$

For the angles of tangent 30° and 16°, the critical section thickness was 6.332. The next step involves the calculation of base circle radius, base pitch, and the length of the line of action (AD) to compute the radius of HPSTC. These values are given by:

$$r_{b,d} = r_{o,d} \cos \alpha_{o,d} = 27 \times \cos 20^\circ = 25.37 \text{ mm}$$

$$\begin{aligned} AD &= \sqrt{r_{a,d,p}^2 - r_{b,d,p}^2} + \sqrt{r_{a,d,g}^2 - r_{b,d,g}^2} - (c_w \sin \alpha_{w,d}) = \\ &= \sqrt{30^2 - 25.37^2} + \sqrt{30^2 - 25.37^2} - (54 \times \sin 20^\circ) = 13.55 \text{ mm} \end{aligned}$$

$$p_{b,w,d} = \pi m \cos \alpha_{w,d} = \pi \times 3 \times \cos 20^\circ = 8.86 \text{ mm}$$

$$r_{HPSTC} = \sqrt{\left(25.37^2 + \left[8.86 - 13.55 + \sqrt{30^2 - 25.37^2}\right]^2\right)} = 27.78 \text{ mm}$$

Following the calculation of r_{HPSTC} , the load angle and tip angle need to be computed as

$$\alpha_{HPSTC} = \cos^{-1}\left(\frac{r_{b,d}}{r_{HPSTC}}\right) = \cos^{-1}\left(\frac{25.37}{27.78}\right) = 24.04^\circ$$

$$\nu_d = \cos^{-1}\left(\frac{25.37}{30}\right) = 32.26^\circ$$

Next, the involute functions is determined as

$$\text{inv } \nu_d = \tan \nu_d - \nu_d = \tan(32.26^\circ) - \left(32.26^\circ \times \frac{\pi}{180}\right) = 0.0682$$

$$\text{inv } \nu_{HPSTC} = \tan \alpha_{HPSTC} - \alpha_{HPSTC} = \tan(24.04^\circ) - \left(24.04^\circ \times \frac{\pi}{180}\right) = 0.0265$$

Now, the parameter θ required for determining the load angle $\alpha_{Load,HPSTC}$ can be calculated as

$$\theta = \text{inv } \nu_d - \text{inv } \nu_{HPSTC} = 0.0682 - 0.0265 = 0.0417$$

$$\alpha_{Load,HPSTC} = \alpha_{HPSTC} - \theta = 24.04 - 0.0417 = 23.99 \approx 24^\circ$$

After applying the load angle on the HPSTC, the h_f of the $20^\circ/34^\circ$ configuration was found to be 3.245. Now, the form factor can be determined,

$$Y_{F,ISO} = \frac{6 (h_f m) \cos \alpha_{Load,HPSTC}}{(s_f)^2} - \frac{m \sin \alpha_{Load,HPSTC}}{s_f} = \frac{6 \times (3.245 \times 3) \times \cos(24^\circ)}{(6.332)^2} - \frac{3 \times \sin(24^\circ)}{6.332} = 1.14$$

To determine the stress correction factor, the parameters L , q_s , and a need to be calculated first,

$$L = \frac{s_f}{h_f} = \frac{6.332}{3.245} = 1.95$$

$$q_s = \frac{s_f}{2\rho_f} = \frac{6.332}{2 \times 1.14} = 2.78$$

$$a = \frac{1}{1.21 + \frac{2.3}{L}} = \frac{1}{1.21 + \frac{2.3}{1.95}} = 0.42$$

$$Y_{S,ISO} = (1.2 + 0.13 L) q_s^a = (1.2 + 0.13 \times 1.95) 2.78^{0.42} = 2.23$$

Then, the maximum bending stress for an applied torque of 1 Nm is,

$$\sigma_{ISO,max} = \frac{F_n}{bm} Y_{F,ISO} Y_{S,ISO} = \frac{T}{bmr_b} Y_{F,ISO} Y_{S,ISO} = \frac{1000}{4 \times 3 \times 25.37} \times 1.14 \times 2.23 = 8.35 \text{ MPa}$$

where $T = F_n \times r_b$.

4.1.4 Sample finite element method-based calculation

In metal-polymer pair of $20^\circ/34^\circ$ configuration subjected to 1 Nm, the maximum bending stress predicted using FEM ($\sigma_{F,FEM}$) was 8.78 MPa, and consequently, the length of the critical section (s_f) extracted from the FE model was 6.591 mm. Based on the contact position of the flanks, r_{HPSTC} was determined graphically to be 27.53. The $\alpha_{Load,HPSTC}$ needs to be calculated to determine the h_f .

$$\alpha_{HPSTC} = \cos^{-1} \left(\frac{r_{b,d}}{r_{HPSTC}} \right) = \cos^{-1} \left(\frac{25.37}{27.53} \right) = 22.85^\circ$$

$$\text{inv } \nu_{HPSTC} = \tan \alpha_{HPSTC} - \alpha_{HPSTC} = \tan(22.85^\circ) - \left(22.85^\circ \times \frac{\pi}{180} \right) = 0.0226$$

$$\theta = \text{inv } \nu_d - \text{inv } \nu_{HPSTC} = 0.0682 - 0.02254 = 0.0458$$

$$\alpha_{Load,HPSTC} = \alpha_{HPSTC} - \theta = 22.8 - 0.0458 = 22.8^\circ$$

For the calculated $\alpha_{Load,HPSTC}$, the corresponding h_f was found to be 3.191 mm. The form factor ($Y_{F,FEM}$) can be estimated by substituting the FEM-based bending moment arm and critical section thickness in the form factor expression,

$$Y_{F,FEM} = \frac{6 (h_f m) \cos \alpha_{Load,HPSTC}}{(s_f)^2} - \frac{m \sin \alpha_{Load,HPSTC}}{s_f} = \frac{6 (3.191 \times 3) \times \cos(22.8^\circ)}{(6.591)^2} - \frac{3 \times \sin(22.8^\circ)}{6.591} = 1.04$$

The stress correction factor ($Y_{S,FEM}$) must be calculated using the fillet stress factor ($\sigma_{F,FEM}$) and form factor ($Y_{F,FEM}$) values,

$$Y_{S,FEM} = \frac{\sigma_{F,FEM}}{Y_{F,FEM}} = \frac{\sigma_{FEM,max}}{\frac{F_n}{bm} \times Y_{F,FEM}} = \frac{8.78}{\frac{1000}{4 \times 3 \times 25.37} \times 1.04} = 2.57$$

4.1.5 Analytical method vs. Finite element method

The form factor, stress correction factor, and fillet stress factor calculated using the ISO method and FEM are represented in Figure 4.3. A comparison of the bending stresses of the steel-steel and steel-polymer pairs calculated using the ISO method and FEM is shown in Figure 4.4 (a). The bending stress distribution in metal – metal and metal – polymer gear pairs is shown in Figure 4.4 (b) – (g). A significant variation exists between the ISO and FEM results. In the metal – metal gear pair, the location of the critical section that alters the critical section parameters was determined solely by the angle of tangent. The load angle remained constant in the ISO method and FEM. However, for the metal - polymer pair, the low r_{HPSTC} caused by an early transition from the STC to the DTC zone reduced the $\alpha_{Load,HPSTC}$. Hence, the HPSTC and $\alpha_{Load,HPSTC}$ had significant influences over the location of the critical section. As the load position on the tooth flank moved towards the root, the location of the critical stresses on both the drive and coast side fillets moved away from the tip towards the end of the fillet (Andrews, 1991). Thus, the low r_{HPSTC} and $\alpha_{Load,HPSTC}$ values increased the critical section thickness. Consequently, $Y_{F,FEM}$ was smaller than $Y_{F,ISO}$, whereas $Y_{S,FEM}$ and $\sigma_{F,FEM}$ were larger than their ISO counterparts.

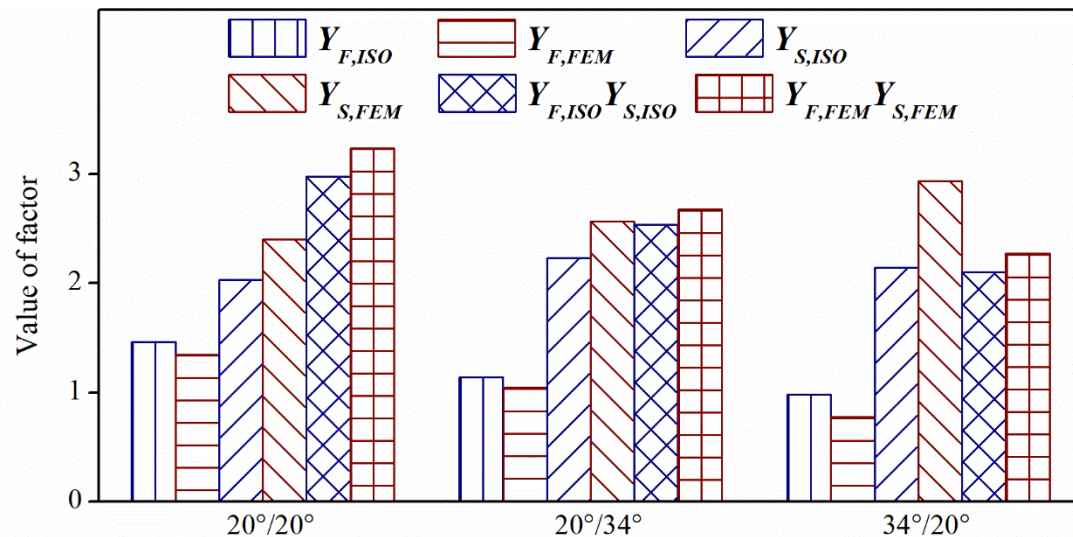


Fig. 4.3 ISO- and FEM-based values of form factor, stress correction factor, and fillet stress factor.

The variation of the fillet stress factor could be attributed to the difference in the stress magnitudes of the ISO method and FEM. The ISO method underestimated the bending stress because of the incorporation of the compressive stress component in the form factor expression. Lisle, Shaw and Frazer (2017) reported that a consideration of the radial component was one of the factors that caused the underestimation of the bending stress in the AGMA method. Thus, if the radial component was discounted, the fillet stress factor calculated by the ISO method would be higher than the FEM result. As evident from Figure 4.4 (a), the inclusion of compressive stress in ISO method B resulted in an underestimation of the bending stress. From a design perspective, underestimating the bending stress leads to a lower tooth strength. Hence, excluding the compressive stress when determining the bending stress could be useful for a conservative tooth design.

4.1.6 Symmetric vs. Asymmetric

In comparison to the symmetric configuration, the bending moment arm and critical section thickness were higher in the asymmetric configurations (Figure 4.2). The asymmetric configurations exhibited lower Y_F and higher Y_S values. The higher critical section thickness in asymmetric gear configurations decreased the form factor values. On the other hand, the reduced fillet length amplified the stress concentration in the asymmetric gears. These results are in agreement with the findings of Sekar and Muthuveerappan (2015). As evident from Figure 4.3, fillet stress factors ($Y_F Y_S$) of the 34°/20° and 20°/34° configurations are lower than that of the 20°/20° configuration. The fillet stress factors ($Y_F Y_S$) and bending stress results are concurrent. The fillet stress factor is lowest for the 34°/20° configuration and highest for the

20°/20° configuration. Despite the higher bending moment arm in the 34°/20° configuration, the bending stress was lower due to the higher critical section thickness. Cavdar, Karpas and Babalik (2005) observed that the $Y_F Y_S$ value of an asymmetric gear was lower than that of a symmetric gear. Furthermore, the $Y_F Y_S$ value decreased consistently with an increase in the drive side pressure angle of the asymmetric gear.

In the asymmetric configurations, the higher bending stress reduction obtained for the 34°/20° configuration as compared to the 20°/34° configuration was related to the dominating influence of the form factor. This was corroborated by the significant decrease in the form factor (29%) compared to the increase in the stress concentration factor (14%). The substantial form factor reduction was due to the higher compressive stress induced by the radial load component. From the form factor expression, it can be observed that a higher pressure angle decreases the tensile stress component (I) and increases the compressive stress component (II).

Compared to the 20°/34° configuration, the increase in compressive stress was 59%, and the decrease in tensile stress was 14%. Thus, it can be concluded that in asymmetric gears with a drive side pressure angle greater than the coast side pressure angle ($\alpha_d > \alpha_c$), high compressive stress aids in achieving a more significant bending stress reduction. This, in turn, will contribute to the higher fatigue life of the gear. Based on the maximum bending stresses exhibited by the symmetric and asymmetric configurations, it can be inferred that the asymmetric configuration with a higher drive side pressure angle will sustain a higher load and exhibit greater bending fatigue life compared to other configurations.

4.2 Bending fatigue life of symmetric and asymmetric gears

The test matrix comprised a total of 35 tests combining symmetric (20°/20°) and asymmetric (20°/34° and 34°/20°) gear configurations, with a test duration of more than 360 hours. The fatigue life distribution was in the high cycle fatigue regime for the applied load range. Figure 4.5 represents the load-bending fatigue life curves of the asymmetric and symmetric configurations in a semi-log plot. The respective markers indicate the fatigue life of the failed teeth, and arrows denote the instances of 'run-out.'

The bending fatigue life behaviors of the test gears are in agreement with the stress results of the FEM. The bending fatigue life of the baseline symmetric gear was drastically reduced in comparison to the asymmetric configurations. The reduction in the mean fatigue life varied in the range of 40-70% in comparison to the asymmetric gears. As previously stated, the primary

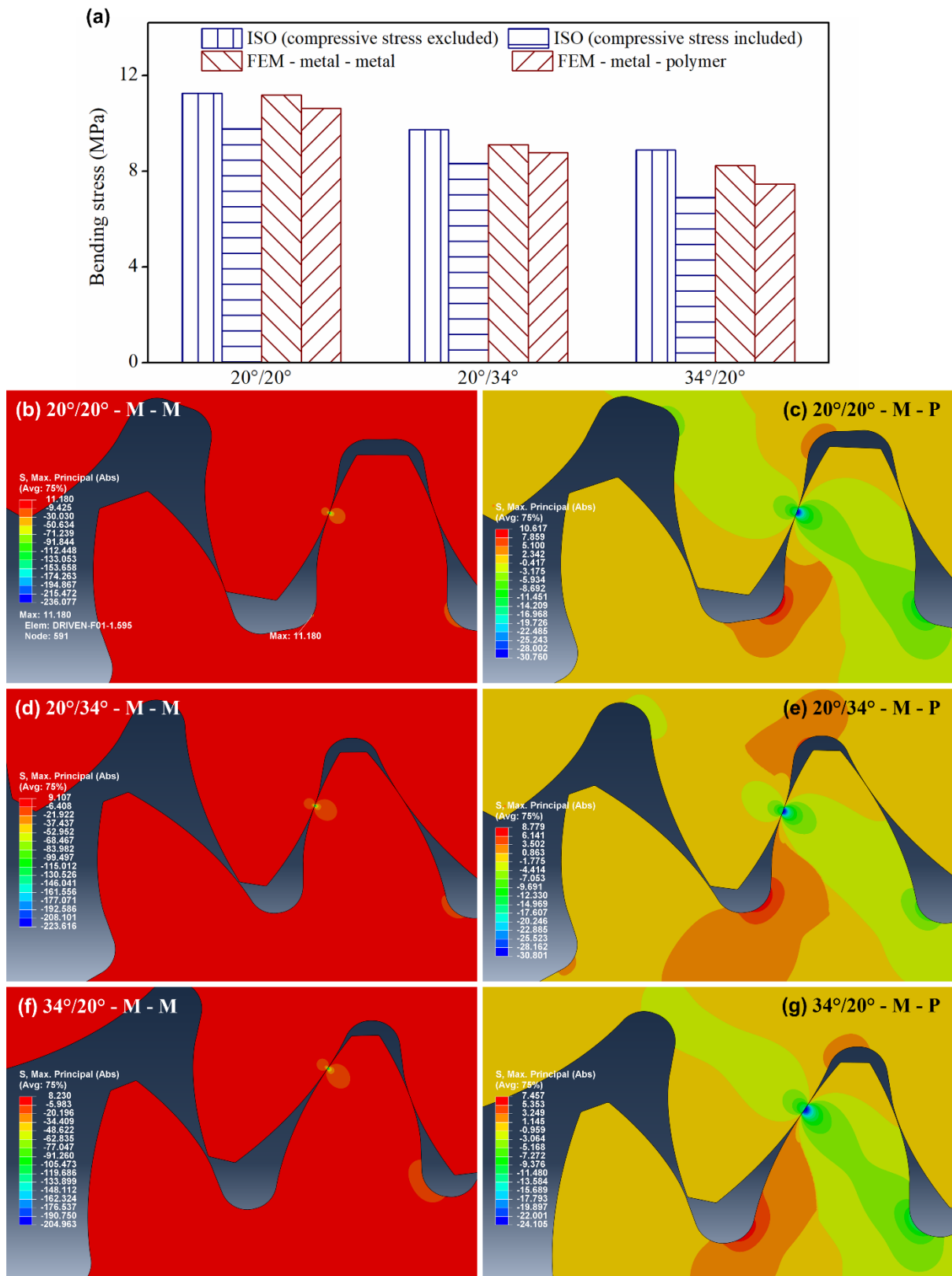


Fig. 4.4 (a) ISO- and FEM-based bending stresses of symmetric and asymmetric gears, (b, c) bending stress in symmetric gear, (d, e) bending stress in asymmetric configuration 20°/34°, and (f, g) bending stress in asymmetric configuration 34°/20°.

reason for the improved bending fatigue life of the asymmetric gears was the stress reduction due to the increased critical section thickness. The increase in the pressure angle shifted the location of the start of the active profile (SAP), thereby increasing the tooth thickness at the root and thus the critical section thickness. The reduction in the bending stress was enunciated by the lower form factors of the $34^\circ/20^\circ$ and $20^\circ/34^\circ$ configurations. The symmetric gear teeth failed in every instance, whereas in the asymmetric configurations, 'run-out' occurred. This demonstrated that the knee portion of the curve, which signifies the endurance limit, was higher for the asymmetric gear. The load corresponding to 'run-out' was higher for the $34^\circ/20^\circ$ configuration.

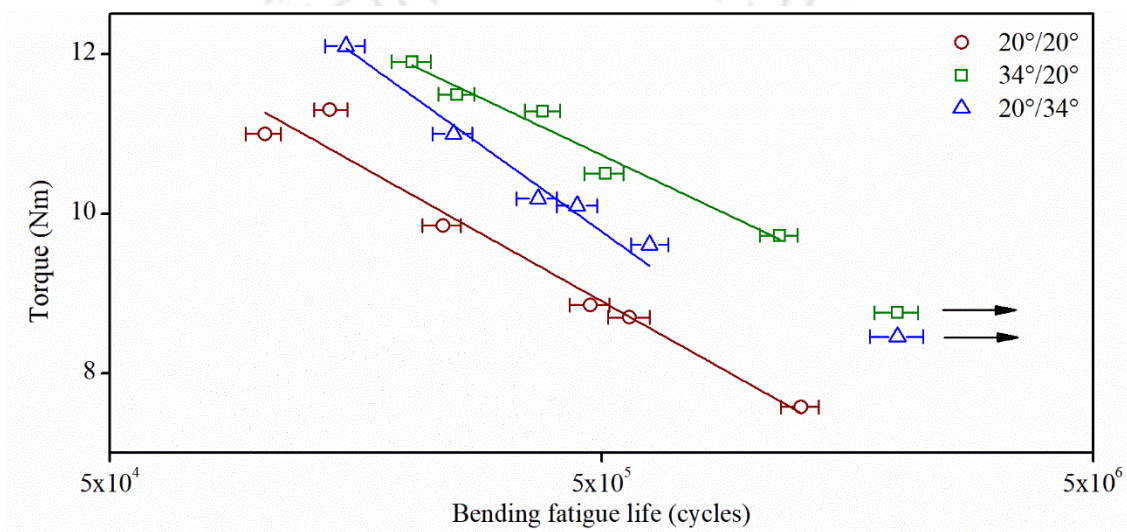


Fig. 4.5 Bending fatigue life distribution of symmetric and asymmetric gears.

Similarly, Brown *et al.* (2011) reported that an asymmetric gear configuration with a higher drive side pressure angle ($35^\circ/18^\circ$) achieved a 5.5% stress reduction compared to a baseline symmetric gear design ($25^\circ/25^\circ$) and exhibited a 16% higher mean endurance limit. Sanders *et al.* (2011) observed that the mean bending fatigue life of an asymmetric gear with a higher coast side pressure angle ($20^\circ/25^\circ$) was 3.5×10^5 , whereas the mean life of a symmetric gear ($20^\circ/20^\circ$) was 3.2×10^5 . The stress reduction for the $20^\circ/25^\circ$ configuration compared to the $20^\circ/20^\circ$ configuration was 7.6%. Contrary to our results, Mertens and Senthilvelan (2016) reported that the fatigue life of asymmetric gear ($34^\circ/20^\circ$) was lower than that of the symmetric gear ($20^\circ/20^\circ$). The inferior performance was attributed to the domination of contact fatigue over bending fatigue. This was confirmed by the presence of excessive tooth wear and the absence of root crack. In this study, the $34^\circ/20^\circ$ configuration exhibited a higher bending fatigue life than the $20^\circ/34^\circ$ configuration. The average fatigue life reduction for the $20^\circ/34^\circ$

configuration compared to the 34°/20° configuration was 20%. In the 34°/20° configuration, the combination of a lower bending moment arm (Figure 4.2 (f)) and higher compressive stress reduced the bending stress and enhanced the fatigue life. The trend lines displayed convergence at the top, indicating an improved bending fatigue life for the 20°/34° configuration at high loads. This improvement could be attributed to the bending stress alleviation caused by the deflection-induced load sharing.

4.2.1 Influence of load sharing on the bending fatigue strength

In general, the load sharing in gears depends on the contact ratio. Because the contact ratio of the 20°/34° configuration ($\epsilon_d = 1.53$) was greater than that of the 34°/20° configuration ($\epsilon_d = 1.25$), it exhibited higher load sharing. In addition, because of the considerable tooth deflection in polymer gears, the actual contact ratio was higher than the theoretical estimate. Consequently, the load shared by the STC region decreased with an increase in the applied load, resulting in lower bending stress. Thus, a tooth geometry with lower stiffness will undergo higher deflection and higher load sharing. Figure 4.6 illustrates the tooth deflections of the symmetric and asymmetric gears in the pitch region for low and high loads.

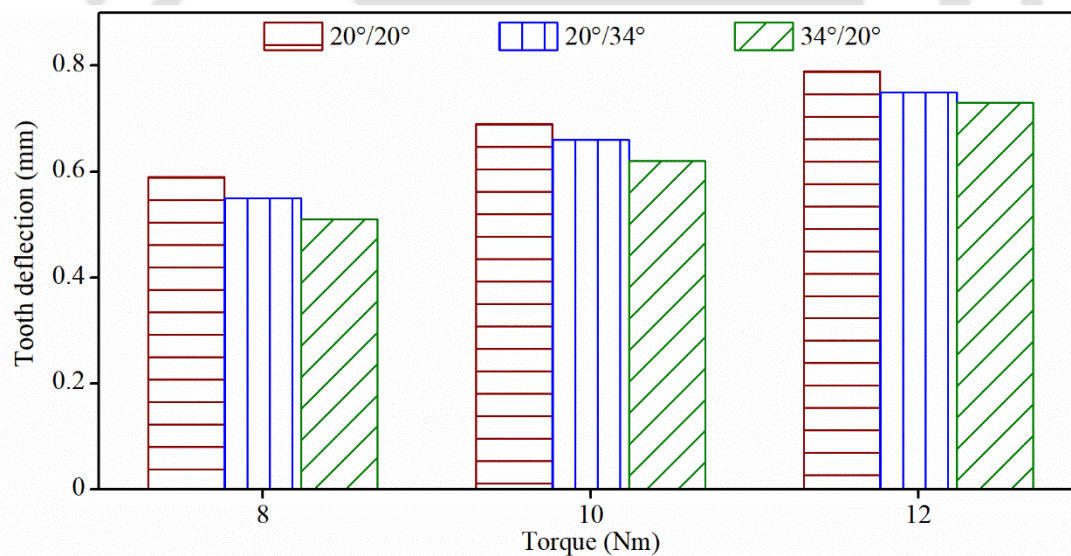


Fig. 4.6 Tooth deflections of symmetric and asymmetric gears.

As seen, the tooth deflection was largest in the symmetric gears, and the 34°/20° configuration exhibited the highest tooth stiffness among all the configurations. The trends indicate that the variation between the tooth deflections of the 34°/20° and 20°/34° configurations progressively decrease with an increase in load, with tooth deflection differences of 7% at 8 Nm and 3% at 12 Nm. This is due to the increased mesh stiffness of the 20°/34° configuration at high loads,

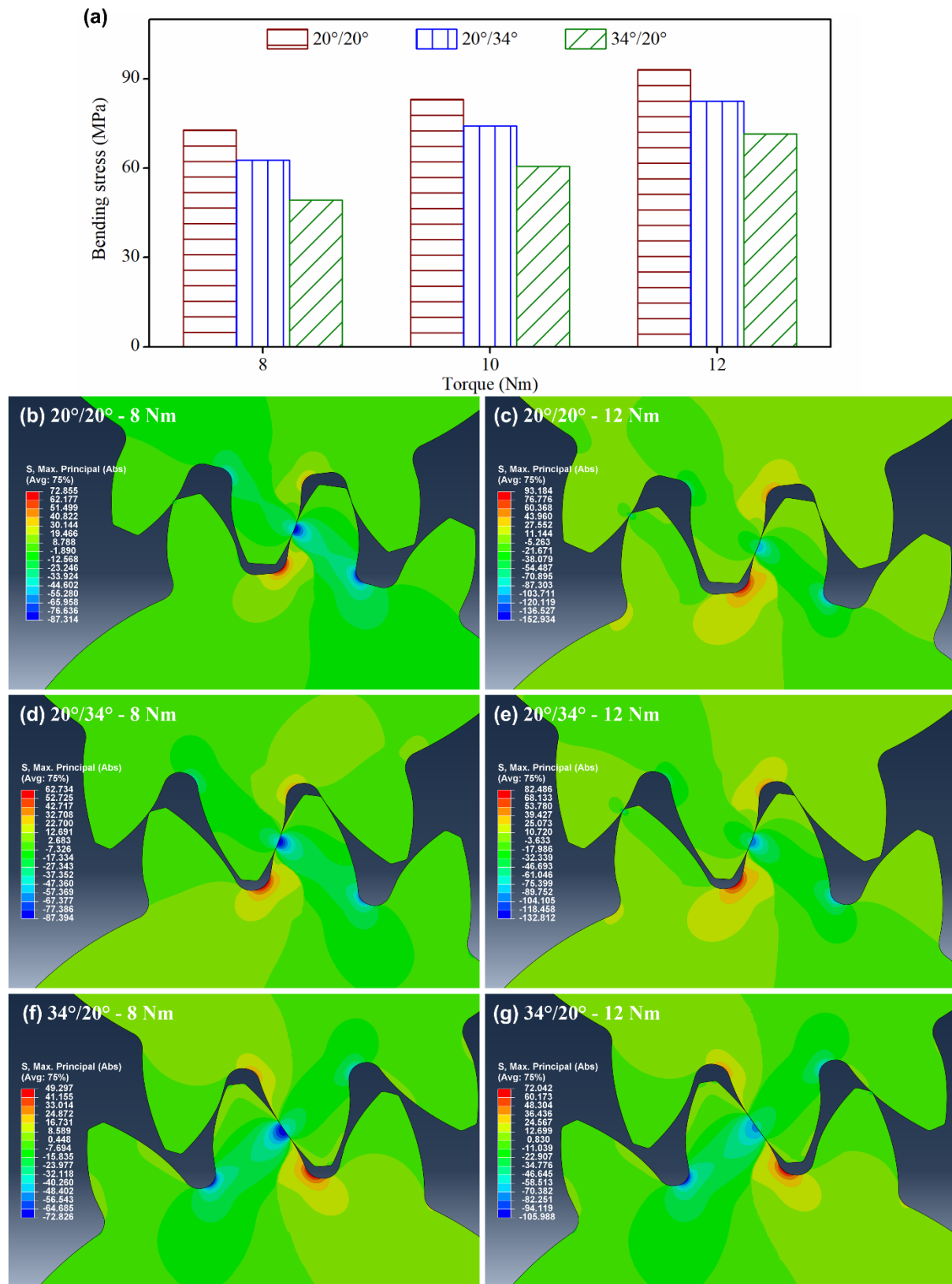


Fig. 4.7 (a) Maximum root bending stresses of symmetric and asymmetric gears, (b, c) bending stress distribution in symmetric gear, (d, e) bending stress distribution in asymmetric configuration 20°/34°, and (f, g) bending stress distribution in asymmetric configuration 34°/20°.

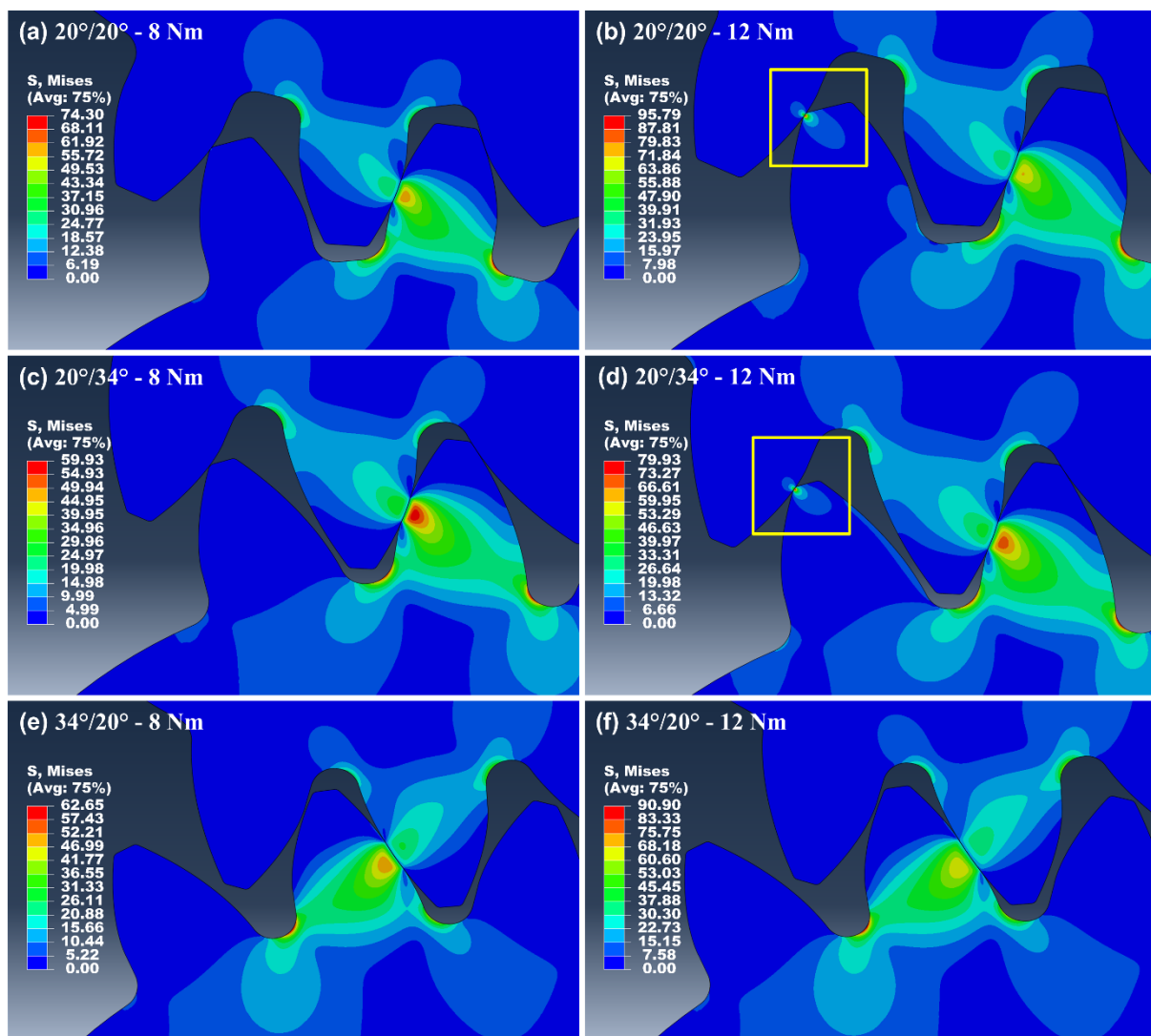


Fig. 4.8 von Mises stress distributions in symmetric and asymmetric gears subjected to 8 and 12 Nm: (a, b) 20°/20°, (c, d) 20°/34°, and (e, f) 34°/20° configurations.

promoted by the high load sharing. Correspondingly, the bending stress difference decreased from 21% at 8 Nm to 13% at 12 Nm (Figure 4.7 (a)). No load sharing occurred in the 34°/20° configuration because of the high tooth stiffness and low contact ratio. The von Mises stress distributions in the symmetric and asymmetric gears for 8 and 12 Nm are shown in Figure 4.8. The deflection-induced load sharing in the 20°/20° and 20°/34° configurations, along with the absence of load sharing in the 34°/20° configuration, are indicated. Mertens and Senthilvelan (2016) observed that, for a static bending load, the tooth deflection of the 34°/20° configuration was lower than that of the 20°/20° configuration. Similarly, Mohan and Senthilvelan (2014) compared the loads sustained by the symmetric and asymmetric gear teeth during displacement-controlled fatigue tests. For any specified displacement, asymmetric gears sustained a higher load than symmetric gears, confirming the higher stiffness of the asymmetric

tooth form. In addition, the load corresponding to the 34°/20° configuration was higher than that of the 20°/34° configuration, which implied the superior tooth stiffness of the 34°/20° configuration. These results consistently agree with our findings pertaining to tooth stiffness. Although deflection-induced load sharing has a beneficial influence on the bending strength, it leads to operation outside the theoretical line of contact. The premature and extended contact with the adjacent tooth causes interference, leading to accelerated wear failure. Hence, design modifications such as tip relief must be incorporated to address the increase in wear (Walton *et al.*, 1995).

4.3 Gear surface temperature

The surface temperature of gears increased during testing. The two major sources of heating in polymer gears are frictional heating and hysteresis heating. Frictional heating arises due to the interaction between the two sliding surfaces whereas hysteresis heating is caused by viscoelastic deformation. The frictional heating was infinitesimal in bending fatigue tests as the gears were subjected to bending loads only. Consequently, the primary source of heating was hysteresis, caused by cyclic straining. The hysteresis heating in polymer gears consists of two parts: contact hysteresis and bending hysteresis. Generally, the operating temperature of polymer gears under service conditions is substantially higher than the temperature rise caused by hysteretic heating during bending fatigue tests. This is due to the dominating effect of frictional heating on the thermal behavior.

Figure 4.9 (a) depicts the evolution of the surface temperature of the 34°/20° configuration gears subjected to 8.5 Nm. The temperature evolution was analogous to the typical temperature pattern observed in polymers subjected to fatigue – an initial phase of a rapid increase in temperature followed by a stable, quasi-isothermal phase. In Figure 4.9 (b) – (e), temperature evolution is illustrated by IR thermographs of 100, 1000, 5000, and 10000 s. The scale bar on the right side of IR images indicates the range of temperature variation in the area under study. The isothermal contours describe the temperature within the field of analysis.

The hysteresis heating is not uniform along the tooth profile and attains a maximum value near the root region (Mao, 1993). The gear tooth temperature at any location depends on the heat generated by hysteresis, and the heat dissipated due to convection. The material volume around the root zone is higher, which results in more significant heat generation and temperature. In the tip region, the volume of material is relatively lower, and heat dissipation to the environment is higher. As a result, the surface temperature at the tip is the lowest. The IR

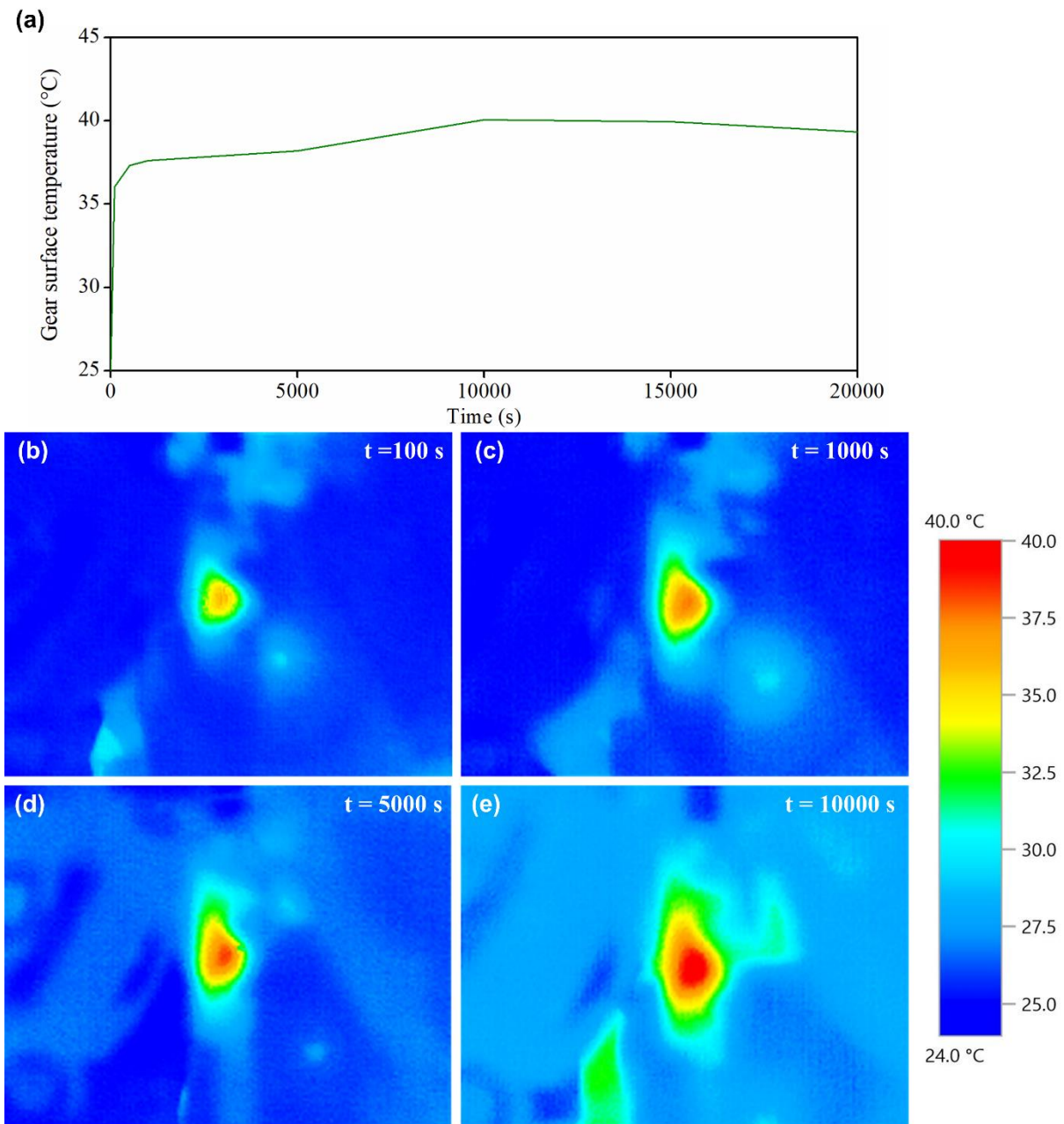


Fig. 4.9 Thermal behavior of 34°/20° configuration: (a) Typical surface temperature evolution during testing and (b, c, d, and e) IR thermographs of tooth at various stages.

images of the test gear teeth acquired during testing are in agreement with this pattern. The gear tooth surface temperature was greater near the root region, and the temperature decreased on either side of the maximum temperature contour. The initial rise in temperature constitutes a minute portion of the fatigue life. Since the steady-state phase persists for the major part of fatigue life, the impact of this phase on fatigue performance is substantial. Hence, it is appropriate to consider the average steady-state temperature for assessing the influence of temperature on fatigue life. Figure 4.10 (a) compares the average surface temperature of asym-

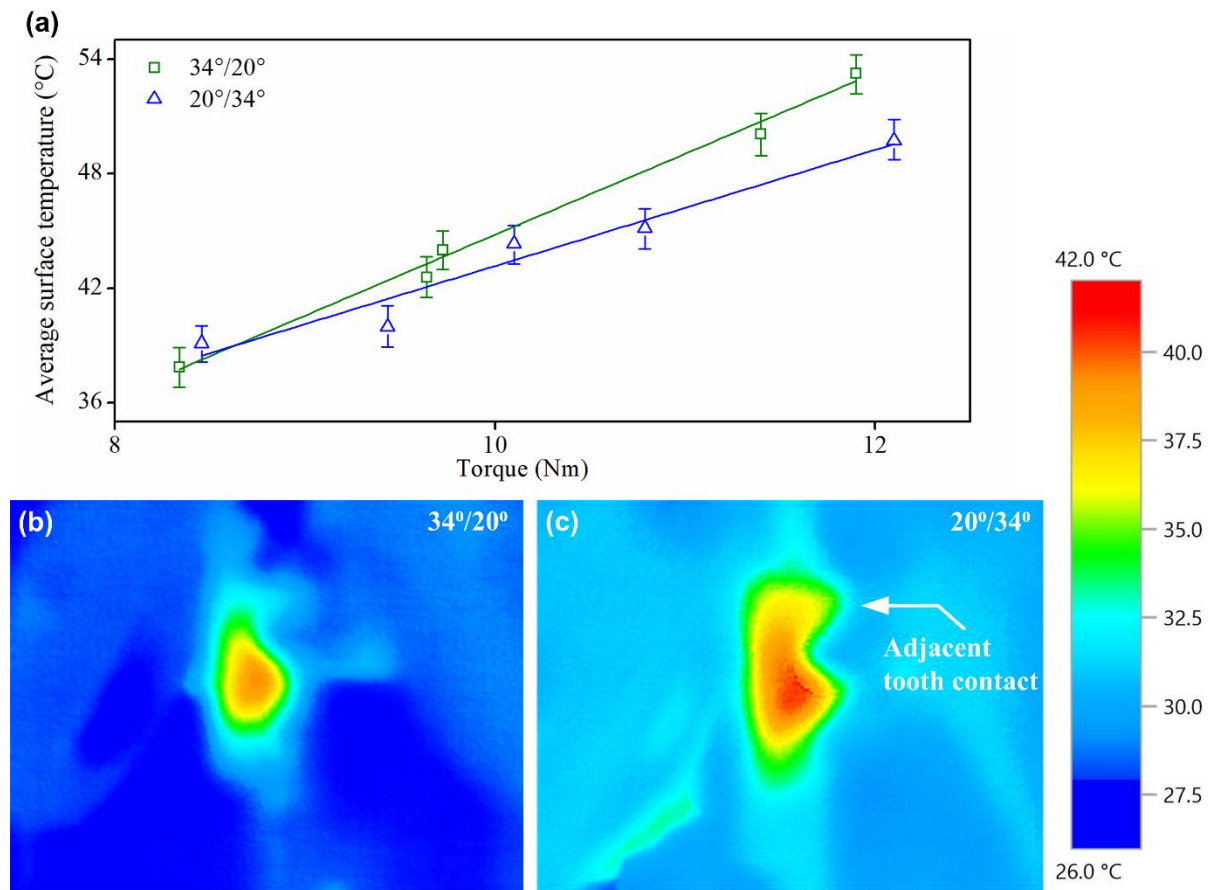


Fig. 4.10 (a) Average surface temperature during testing and (b, c) IR thermograph of 34°/20° and 20°/34° configurations at 20000 s.

-metric configurations subjected to various loads. It can be observed that the overall temperature rise with respect to the lab temperature was in the range of 20 - 25 °C. The difference between the average surface temperatures of 34°/20° and 20°/34° configurations varied with respect to load. Although the difference was greater at higher loads, the maximum variation was within 5 °C. Hence, it could be reasoned that the impact of operating temperature on the fatigue life was almost similar for each configuration. Therefore, the root bending stress could be the dominating factor determining the gear's bending fatigue life.

The analysis of failure morphology of the test gears (refer to Figure 4.11) showed no traces of molten material, implying the absence of thermal failure. The IR thermographs of 34°/20° and 20°/34° configurations at 20000 s, when subjected to 8.5 Nm, are shown in Figure 4.10 (b and c). The adjacent tooth contact caused by the lower drive side pressure angle in the 20°/34° configuration has been indicated. A detailed analysis of the thermal behavior of asymmetric polymer gears has been presented in the next chapter.

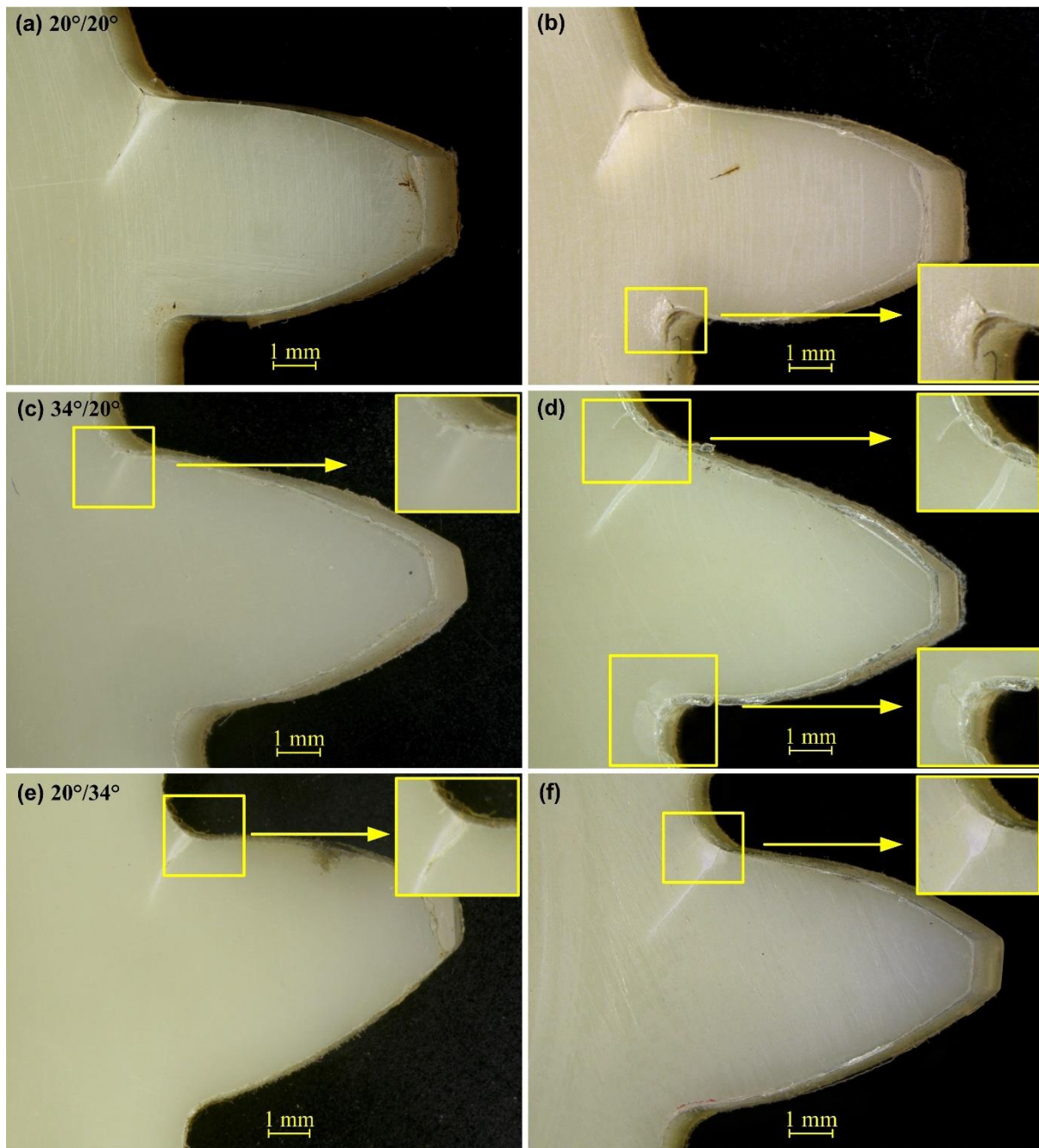


Fig. 4.11 Stereomicroscopic images of the bending fatigue failure in symmetric and asymmetric gear teeth: (a, b) 20°/20°, (c, d) 20°/34°, and (e, f) 34°/20° configurations. Multiple cracks on the drive side fillet and coast side cracks are indicated.

4.4 Failure modes under bending fatigue

Localized deformation zones originated in the fillet region and extended in the direction perpendicular to the stress. Figure 4.11 (a) – (f) and Figure 4.12 (a) – (f) show the stereomicroscopy and FESEM images of the symmetric and asymmetric teeth at low and high loads, respectively. The magnified view of selected regions (indicated in Figure 4.12 (a) – (f))

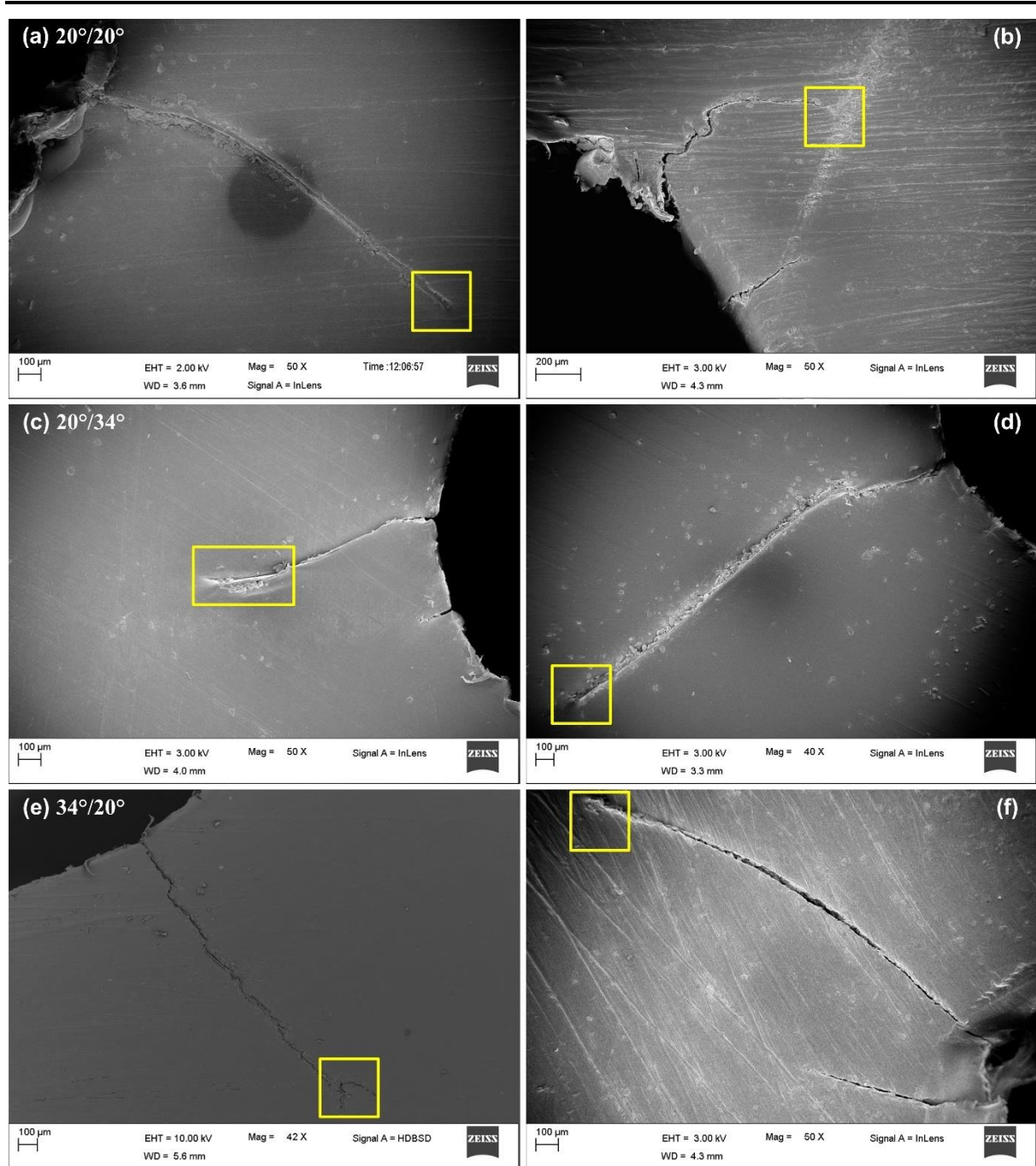


Fig. 4.12 FESEM images of symmetric and asymmetric gear teeth: (a, b) 20°/20°, (c, d) 20°/34°, and (e, f) 34°/20° configurations.

are shown in Figure 4.13 (a) – (f). The deformation zones resembled a wedge-shaped pattern of fine crazing, a characteristic feature observed in polymer failures. This pattern had a maximum width near the fillet and steadily decreased with an increase in the extent of the zone. The applied load and tooth stiffness influenced the extent of the crazing. High loads and high tooth deflection increased the crazing zone. Consequently, crazing was higher in the symmetric gears in comparison to the asymmetric gears as a result of the high tooth deflection. Crack

initiation and propagation followed the development of crazing. The crack propagation was along the boundary of the crazing zone. The crack path was curvilinear. The curvature of the crack path could be attributed to the significant tooth deflection of the polymer gears. Curvature was prominent in the symmetric gears. However, the crack path was virtually linear at all loads in the asymmetric gears. Multiple cracks occurred as a result of the existence of a high stress concentration in the fillet region.

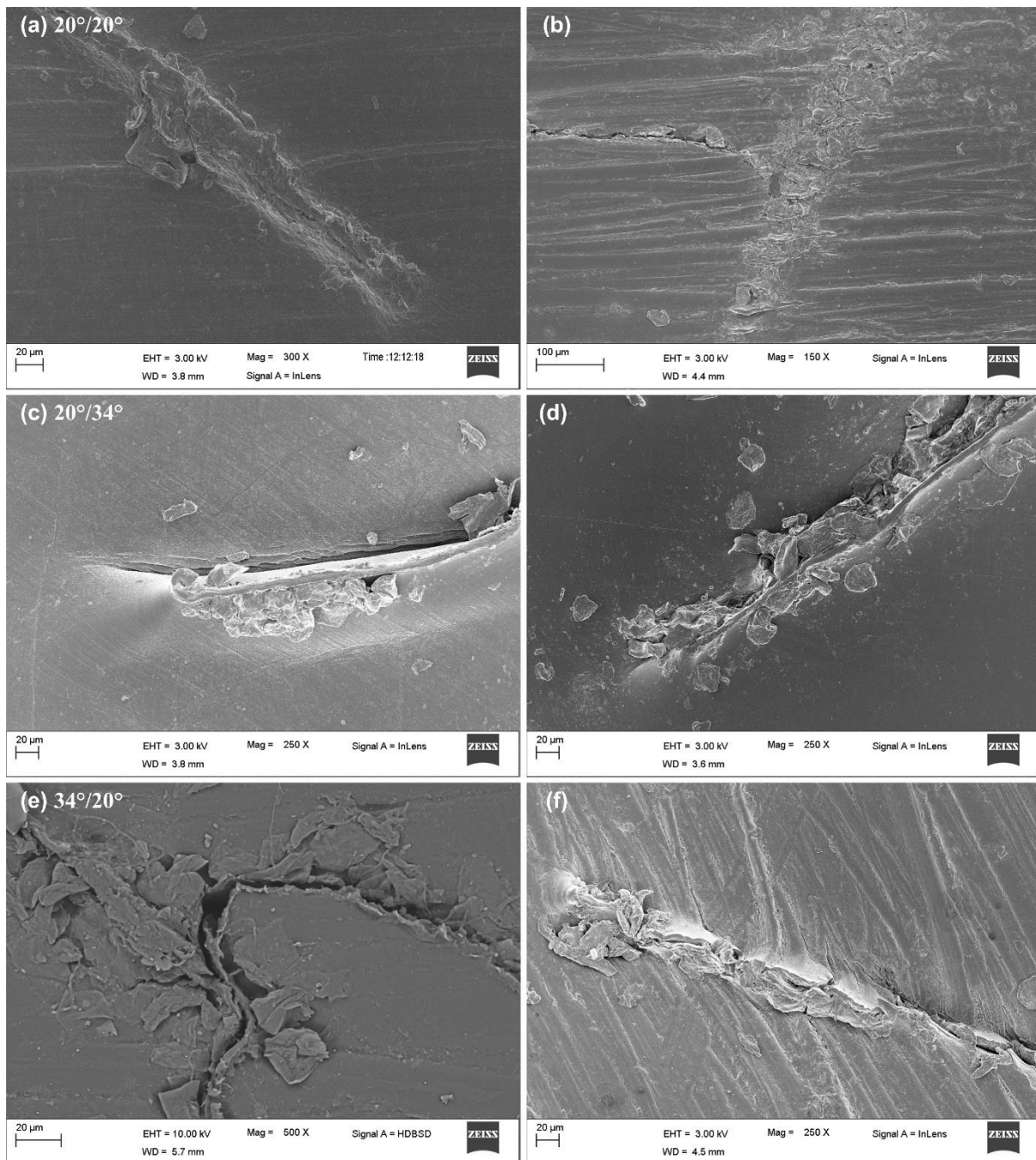


Fig. 4.13 Magnified view of crack tips of symmetric and asymmetric gear teeth: (a, b) 20°/20°, (c, d) 20°/34°, and (e, f) 34°/20° configurations.

In the asymmetric gears, multiple cracks were observed at both high and low loads. In contrast, the symmetric gears sustained multiple cracks only at high loads. This contradiction can be explained based on the different stress concentrations in the symmetric and asymmetric gears. As evident from the stress concentration factor (Y_S), the stress concentration in the asymmetric gears was higher than that in the symmetric gears. This caused the initiation of multiple cracks in the asymmetric gears, regardless of the load magnitude. At high loads, cracks initiated on the coast side fillet region in addition to the drive side fillets of the symmetric and asymmetric gears. Since the bending fatigue test is a non-rotational test, the amount of sliding that occurs due to the tooth deflection is limited. Owing to the infinitesimal amount of sliding, the tooth wear is very less in bending fatigue tests. Consequently, no wear measurement was carried out in this study. The visual examination of the tested teeth (Figure 4.11) indicated no significant change in the profile.

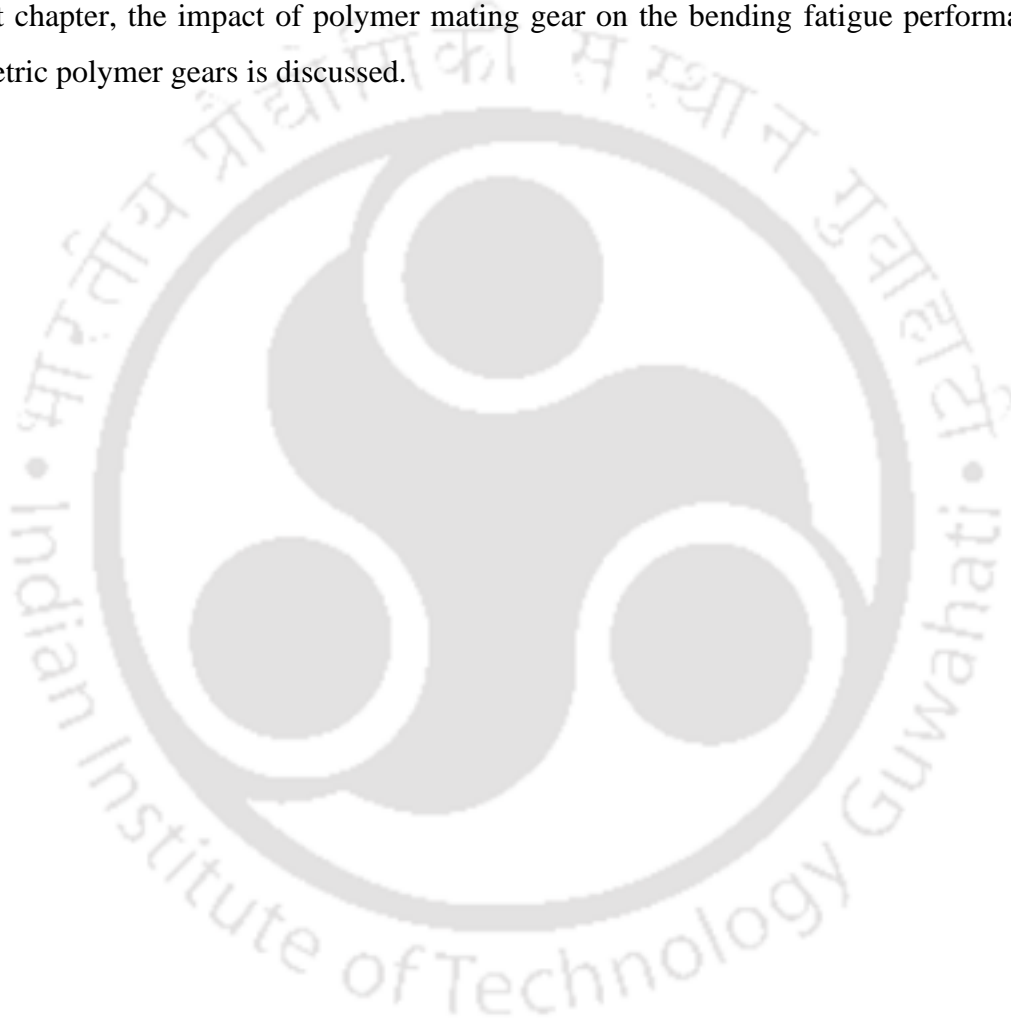
4.5 Summary

The bending fatigue performance of Nylon 66 symmetric and asymmetric spur gear configurations ($20^\circ/20^\circ$, $20^\circ/34^\circ$, and $34^\circ/20^\circ$) was evaluated numerically and experimentally. The nominal bending stresses in the fillets were determined by quasi-static stress analyses in ABAQUS. An adapted ISO framework was used for analytical calculations of the form and stress correction factors. Single tooth bending fatigue tests were conducted to experimentally determine the bending fatigue life. The major findings of the study are:

- The maximum bending stress reduction was found for the asymmetric configuration with a higher pressure angle on the drive side ($34^\circ/20^\circ$).
- Tooth asymmetry decreased the form factor by 20-40% and increased the stress correction factor by 5-20%.
- The form factor dominated the fillet stress factor and directly influenced the magnitude of the bending stress in the fillet.
- The asymmetric gear with a higher pressure angle on the drive side ($34^\circ/20^\circ$) exhibited the highest bending fatigue life among the tested configurations across low- and high-load regimes.
- The difference between the bending fatigue life of the two asymmetric configurations ($20^\circ/34^\circ$ and $34^\circ/20^\circ$) decreased with an increase in the load because the deflection-induced load sharing decreased the bending stress and increased the bending fatigue life of the $20^\circ/34^\circ$ configuration.

- The variation between the average surface temperatures of 34°/20° and 20°/34° configurations was dependent on the applied load. The influence of temperature on the bending fatigue life was almost similar for each configuration, as the maximum temperature difference was only 5 °C.
- Wedge-shaped craze zones were observed near the root fillet region along with multiple cracks.

The study confirmed that the asymmetric tooth form enhanced the bending fatigue strength. In the next chapter, the impact of polymer mating gear on the bending fatigue performance of asymmetric polymer gears is discussed.





Chapter 5

Effect of polymer mating gear on the bending fatigue performance of asymmetric polymer gears

The material of the mating gear has a definitive impact on the performance of polymer gear. The mating gear material has a considerable effect on the stiffness and thermal characteristics of the gear pair, affecting the fatigue strength. This chapter describes the bending fatigue characteristics of injection-molded Nylon 66 asymmetric gears ($34^\circ/20^\circ$ and $20^\circ/34^\circ$) mated with steel and injection-molded Nylon 66 gears. The study includes a detailed evaluation of the bending fatigue strength, load sharing behavior, thermal behavior, and failure morphology of metal – polymer (M-P) and polymer – polymer (P-P) gear pairs.

The first section compares the maximum nominal bending stress in the root region of metal-polymer and polymer-polymer gear pairs predicted using FEM. The influence of mating gear material on the load shared by the adjacent tooth and the attendant impact on the root bending stress is examined. The bending fatigue life of metal-polymer and polymer-polymer gear pairs, determined from experiments, has been described in the second section. The third section analyzes the variation in surface temperature caused by metal and polymer mating gears. The analysis also includes an assessment of the hysteresis behavior of the asymmetric gears. Finally, the results of failure analysis, entailing optical microscopy images and FESEM images of metal-polymer and polymer-polymer gear pairs, have been presented.

5.1 Root bending stress and load sharing behavior

The finite element analyses conducted as part of this study used ‘Gear pair model 2.’ The maximum principal stress on the drive side fillet was considered the maximum bending stress. The predicted bending stress corresponded to pitch point loading, as single tooth contact was absent for the considered load range. Similarly, Karimpour, Dearn and Walton (2010) observed that maximum bending stress occurred for pitch point contact in POM - POM gear pairs. The

bending stresses of symmetric and asymmetric gears of metal - polymer and polymer - polymer combinations are represented in Figure 5.1 (a). The distribution of principal stress in symmetric and asymmetric configurations of metal - polymer and polymer - polymer pairs is illustrated in Figures 5.1 (b) – (g). Similar to metal - polymer pairs, the bending stress of symmetric gear ($20^\circ/20^\circ$) was higher than that of asymmetric gear configurations ($20^\circ/34^\circ$ and $34^\circ/20^\circ$) of polymer - polymer pairs. In polymer - polymer pairs, the bending stresses of $20^\circ/20^\circ$ and $20^\circ/34^\circ$ configurations were significantly lower compared to the equivalent configurations of metal - polymer pairs. Compared to metal - polymer pairs, the bending stress of polymer - polymer pairs were lower by 13%. This drastic reduction in bending stress can be attributed to the higher load sharing in the polymer - polymer pairs, caused by the deflection-induced contact with the adjacent tooth.

The load sharing in metal - polymer and polymer - polymer gear pairs was compared using the load sharing ratio of the leading contact pair. The load sharing ratio was calculated based on the contact force data extracted from the simulation results. The formula for LSR was defined in equation 3.8. Figure 5.2 (a) shows the LSR of the symmetric and asymmetric configurations of metal - polymer and polymer - polymer gear pairs for 8, 10, and 12 Nm. In the polymer - polymer pairs of $20^\circ/20^\circ$ and $20^\circ/34^\circ$ configurations, the use of polymer driver gear increased the load shared by the trailing contact pair. The increased load sharing effectively reduced the load sustained by the leading contact pair, resulting in reduced stress levels. On the other hand, the polymer - polymer pair of $34^\circ/20^\circ$ configuration endured stress levels identical to the metal - polymer pair of $34^\circ/20^\circ$ configuration. This was caused by the lack of load sharing at 8 and 10 Nm and minimal load sharing at 12 Nm.

Unlike $20^\circ/20^\circ$ and $20^\circ/34^\circ$ configurations, the contact ratio of the $34^\circ/20^\circ$ configuration is inherently low due to the higher pressure angle. This increases the extent of the single tooth contact zone. Hence, the premature contact caused by higher tooth deflection was not present in the $34^\circ/20^\circ$ configuration. Consequently, deflection-induced load sharing was absent at lower loads and not prominent at higher loads. Figure 5.2 (b) – (g) compares the von Mises stress distribution in symmetric and asymmetric configurations of metal - polymer and polymer - polymer pairs for 8 Nm. In polymer - polymer pairs, the presence of load sharing in $20^\circ/20^\circ$ and $20^\circ/34^\circ$ configurations and the absence of load sharing in $34^\circ/20^\circ$ configuration can be observed. Yelle and Burns (1981) reported that the peak load of polymer - polymer pairs was lower compared to steel - polymer pairs of symmetric gears. In POM - POM and steel - POM pairs, the peak load as a proportion of the applied normal load was 57% and 75%, respectively.

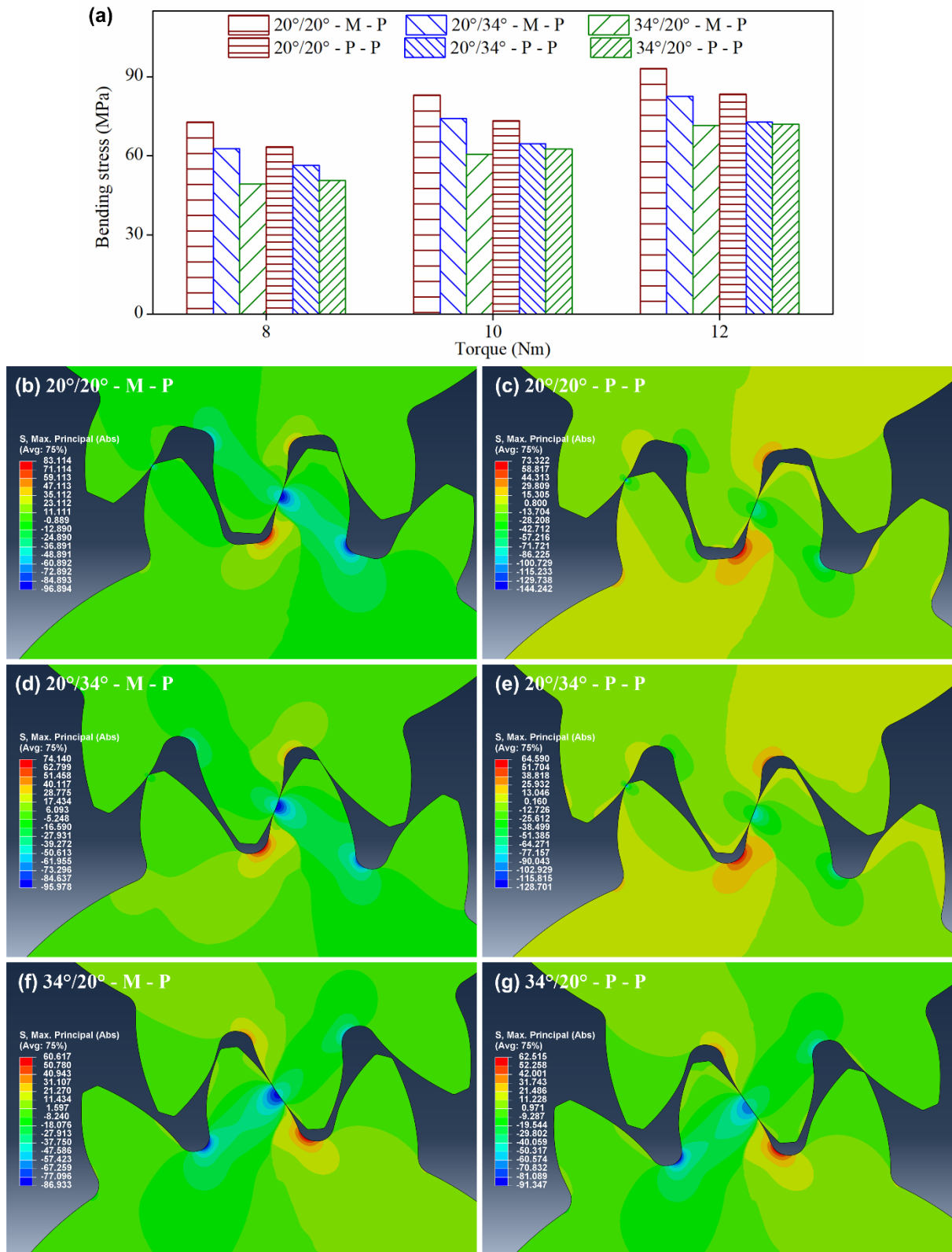


Fig. 5.1 Bending stress in metal - polymer (M-P) and polymer - polymer (P-P) pairs of symmetric and asymmetric configurations: (a) Maximum root bending stress, (b, c) Principal stress distribution in 20°/20° configuration, (d, e) Principal stress distribution in 20°/34° configuration, and (f, g) Principal stress distribution in 34°/20° configuration.

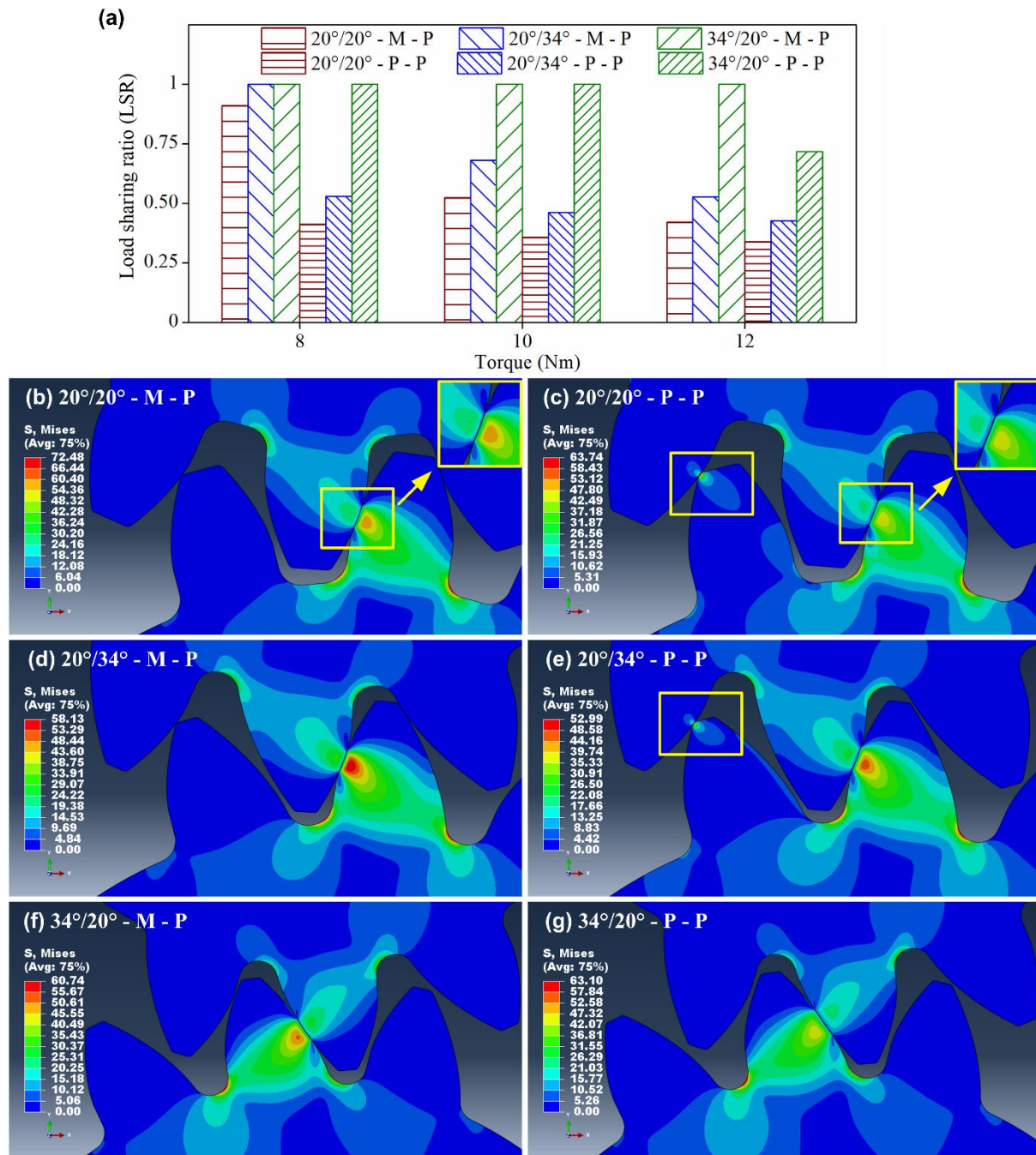


Fig. 5.2 Load sharing in metal - polymer (left) and polymer - polymer gear pairs (right): (a) LSR corresponding to 8, 10, and 12 Nm, (b, c) von Mises stress distribution in 20°/20° configuration subjected to 8 Nm, (d, e) von Mises stress distribution in 20°/34° configuration subjected to 8 Nm, and (f, g) von Mises stress distribution in 34°/20° configuration subjected to 8 Nm.

This was due to the higher actual contact ratio of polymer-polymer pairs. The dissimilar load sharing ratio of metal - polymer and polymer-polymer pairs was caused by the variation in the tooth deflection behavior. In metal - polymer pairs, only the driven gear tooth was subjected to deflection, whereas in polymer - polymer pairs, the deformation in the contact zone was shared

by the teeth of the driver and driven gears. This is evident from the surface profile of the contact zone in metal - polymer and polymer - polymer pairs (Figure 5.2 (b, c)). In metal - polymer pairs, the profile of the driven gear tooth conformed to the driver gear tooth. But, in polymer - polymer pairs, the profile of the contact zone was flat. In polymer - polymer pairs, the deflection of the driver gear tooth advanced the contact of the adjacent teeth. A similar contact zone deformation pattern was observed by Ziegltrum *et al.* (2020) in a pair of cylindrical disks under rolling contact. The deformation and contact area of the polymer - polymer pair were higher than the metal - polymer pair. In 20°/20° and 20°/34° configurations, the LSR decreased steadily with an increase in load, indicating a load-dependent behavior. This trend was absent in the 34°/20° configuration for all cases except the polymer - polymer pair loaded at 12 Nm, in which the LSR decreased due to the adjacent tooth contact.

Similarly, Karimpour, Dearn and Walton (2010) observed that the load sharing in the POM - POM gear pair increased with an increase in the applied torque. The higher tooth deflections increased the contact ratio and decreased the load sustained by the tooth. The load sharing ratio was below 1 in 20°/20° and 20°/34° configurations, indicating that the actual contact ratio surpassed 2 during operation. Thus, the gears functioned as High Contact Ratio (HCR) gears ($\varepsilon_\alpha > 2$) during operation albeit designed as Normal Contact Ratio (NCR) gears ($1 < \varepsilon_\alpha < 2$). Such transitional contact ratio operation can compensate for the inadequate flexural strength in polymer gears (Kapelevich, 2020). In the study by Yelle and Burns (1981), the load sharing ratio was below 1, and the actual contact ratio was higher than 2 for metal - polymer and polymer - polymer pairs. Similarly, in the work of Karimpour, Dearn and Walton (2010), the maximum load sharing ratio was 0.8.

5.2 Influence of mating gear material on the bending fatigue life

The bending fatigue life distribution of metal - polymer and polymer - polymer pairs of symmetric and asymmetric gear configurations are illustrated in Figure 5.3. The trials of 'run-out' are indicated by a pointed arrow. Similar to metal - polymer pairs, polymer - polymer pairs of asymmetric gears demonstrated higher fatigue life compared to polymer - polymer pairs of symmetric gears. The higher bending stress in symmetric gears reduced the fatigue strength. However, the load-carrying capacity of polymer-polymer gear pairs was reduced substantially compared to metal - polymer gear pairs. Previous studies available in the literature, in which rotational tests were conducted, reported similar findings. A study investigating the fatigue behavior of ABS and POM symmetric gears revealed that the fatigue life was higher for metal

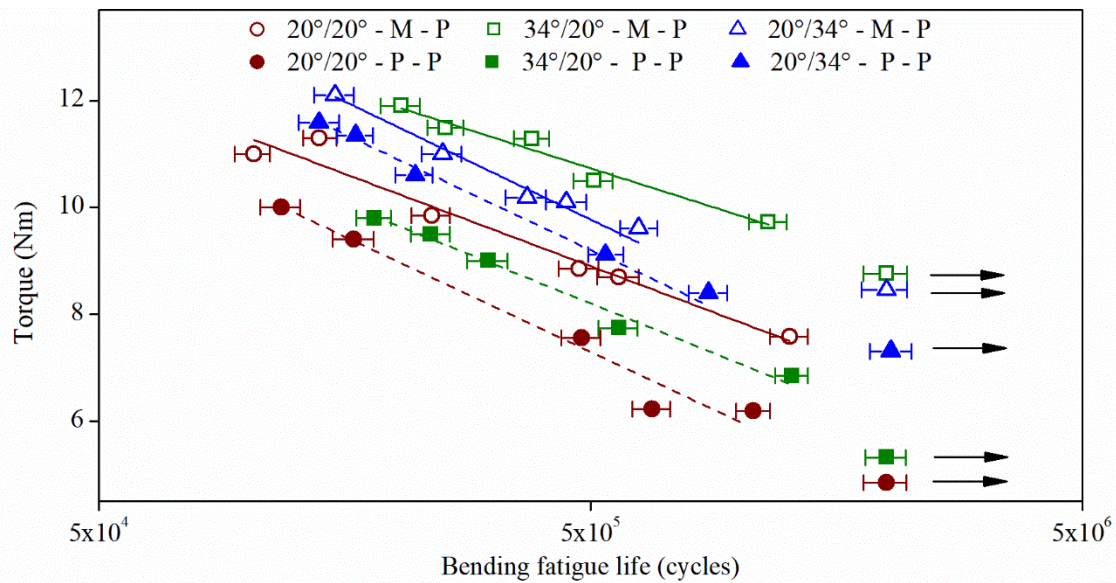


Fig. 5.3 Bending fatigue life of metal-polymer and polymer-polymer gear pairs.

- polymer pairs (Yamaguchi, 1990). In this study, the bending fatigue life of polymer - polymer pairs of $34^\circ/20^\circ$ configuration was lower than metal - polymer pairs of $34^\circ/20^\circ$ configuration despite enduring similar stress levels. In the case of the $20^\circ/34^\circ$ configuration, the load-carrying capacity of polymer - polymer pairs was not improved by the increased load sharing and lower bending stress. Then, the reduction in fatigue life of polymer - polymer pairs of asymmetric gears could be attributed to the thermal behavior of the gears during testing.

The average steady-state operating temperatures of metal - polymer and polymer - polymer pairs of asymmetric gears are illustrated in Figure 5.4 (a). The infrared thermal images of polymer-polymer pairs of $34^\circ/20^\circ$ and $20^\circ/34^\circ$ configurations subjected to 10 Nm are shown in Figure 5.4 (b, c). The operating temperature of polymer - polymer pairs was significantly higher than that of metal - polymer pairs at all loads. In semi-crystalline polymers, the mechanical properties deteriorate with an increase in temperature. Thus, the increase in operating temperature caused thermal softening and depleted the tooth strength. (Dearn, Hoskins, Petrov, *et al.*, 2013) observed that the surface temperature of the polymer - polymer gear pair of uncoated Nylon 66 was higher than that of the metal - polymer pair. Similarly, Koide *et al.* (2017) reported that the surface temperature of the POM - POM gear pair was higher than the steel - POM gear pair.

The surface temperature of gear is a measure of the thermal equilibrium between the heat generated and dissipated during operation. Due to the absence of external cooling, the principal mode of heat dissipation was conduction through the driver gear. The usage of Nylon 66 as the

driver gear reduced the capacity of the polymer - polymer gear pair to dissipate the heat generated during fatigue loading. As the thermal conductivity of Nylon 66 is lower than that of steel, the heat conducted in polymer-polymer pairs was lesser than that of metal - polymer pairs. In addition to the reduction in heat dissipation, an increase in hysteresis heat generation occurred concurrently.

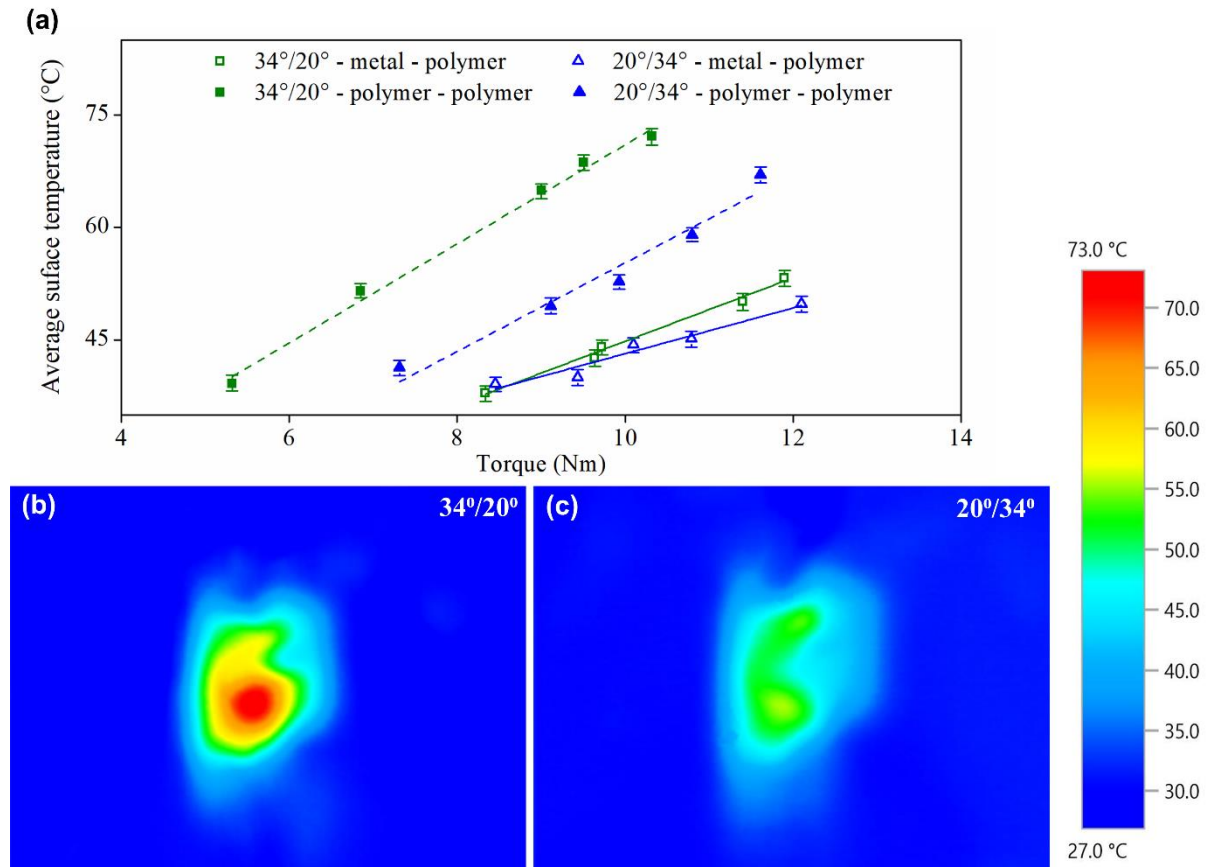


Fig. 5.4 Thermal behavior of gears: (a) Average surface temperatures of metal - polymer and polymer - polymer gear pairs and (b, c) Temperature distribution at cycle 10000 in 34°/20° and 20°/34° configurations subjected to 10 Nm.

The hysteresis heating depends on the volume of material undergoing strain. In metal - polymer pairs, the polymer driven gear was subjected to strain. On the contrary, in polymer - polymer gear pairs, the polymer driver gear increased the total volume of material undergoing strain. The Nylon 66 driver gear was subjected to considerable strain due to the lower tooth stiffness. The concerted effects of lower thermal conductivity and greater material volume increased the quantum of heat generated, and elevated the operating temperature. Consequently, the tooth strength of polymer - polymer gear pairs deteriorated considerably, resulting in lower fatigue life. Thus, in polymer - polymer gear pairs, the hysteresis heating superseded the effect of stress

and dominated the bending fatigue life. In asymmetric gears, the mating gear material determined the configuration with the highest bending fatigue strength. In metal - polymer pairs, the highest bending fatigue life was exhibited by the $34^{\circ}/20^{\circ}$ configuration. On the other hand, in polymer - polymer pairs, the $20^{\circ}/34^{\circ}$ configuration demonstrated higher bending fatigue strength compared to other configurations. The enhanced fatigue life of the $20^{\circ}/34^{\circ}$ configuration was partially attributable to the alleviation of bending stress due to higher extent of load shared by the adjacent tooth. In metal-polymer pairs, the bending stress of the $20^{\circ}/34^{\circ}$ configuration was greater than that of the $34^{\circ}/20^{\circ}$ configuration by 22%. But, in polymer - polymer pairs, the difference between the bending stresses was merely 5%. However, the primary cause of the reduction in the bending fatigue strength of the $34^{\circ}/20^{\circ}$ configuration was the higher hysteresis heat generation compared to the $20^{\circ}/34^{\circ}$ configuration.

In metal - polymer pairs, despite the higher operating temperature of the $34^{\circ}/20^{\circ}$ configuration, the bending fatigue life of the $34^{\circ}/20^{\circ}$ configuration was higher than that of the $20^{\circ}/34^{\circ}$ configuration. In that case, the temperature difference between $34^{\circ}/20^{\circ}$ and $20^{\circ}/34^{\circ}$ configurations was small, with a maximum variance of 5 °C. Hence, the detrimental effect of higher temperature on the tooth strength was minimal. However, the temperature difference between the configurations of polymer - polymer pairs was pronounced (up to 15 °C). The higher temperature adversely affected the tooth strength of the $34^{\circ}/20^{\circ}$ configuration more than the tooth strength of the $20^{\circ}/34^{\circ}$ configuration. Thus, the bending fatigue life of metal-polymer pairs was dominated by bending stress, whereas the operating temperature dominated the bending fatigue life of polymer - polymer pairs.

5.3 Analysis of deflection behavior

To determine the underlying cause behind the variable thermal response of asymmetric configurations, the hysteresis and thermal characteristics of the asymmetric polymer gears was investigated in detail. The disparity between the temperatures of $34^{\circ}/20^{\circ}$ and $20^{\circ}/34^{\circ}$ configurations can be explained by analyzing the tooth deflections at various points along the tooth height. The tooth deflection was predicted using quasi-static numerical analyses. The tooth deflection was extracted along the line that passed through the center of top land. The deflection of the loaded driven gear tooth was measured along this line from the top land up to the root. The tooth deflections of $34^{\circ}/20^{\circ}$ and $20^{\circ}/34^{\circ}$ configurations of metal - polymer and polymer - polymer gear pairs corresponding to applied torques of 8 and 12 Nm are shown in Figure 5.5 (a) and (b), respectively. Since the root of the tooth is constrained and the tip is

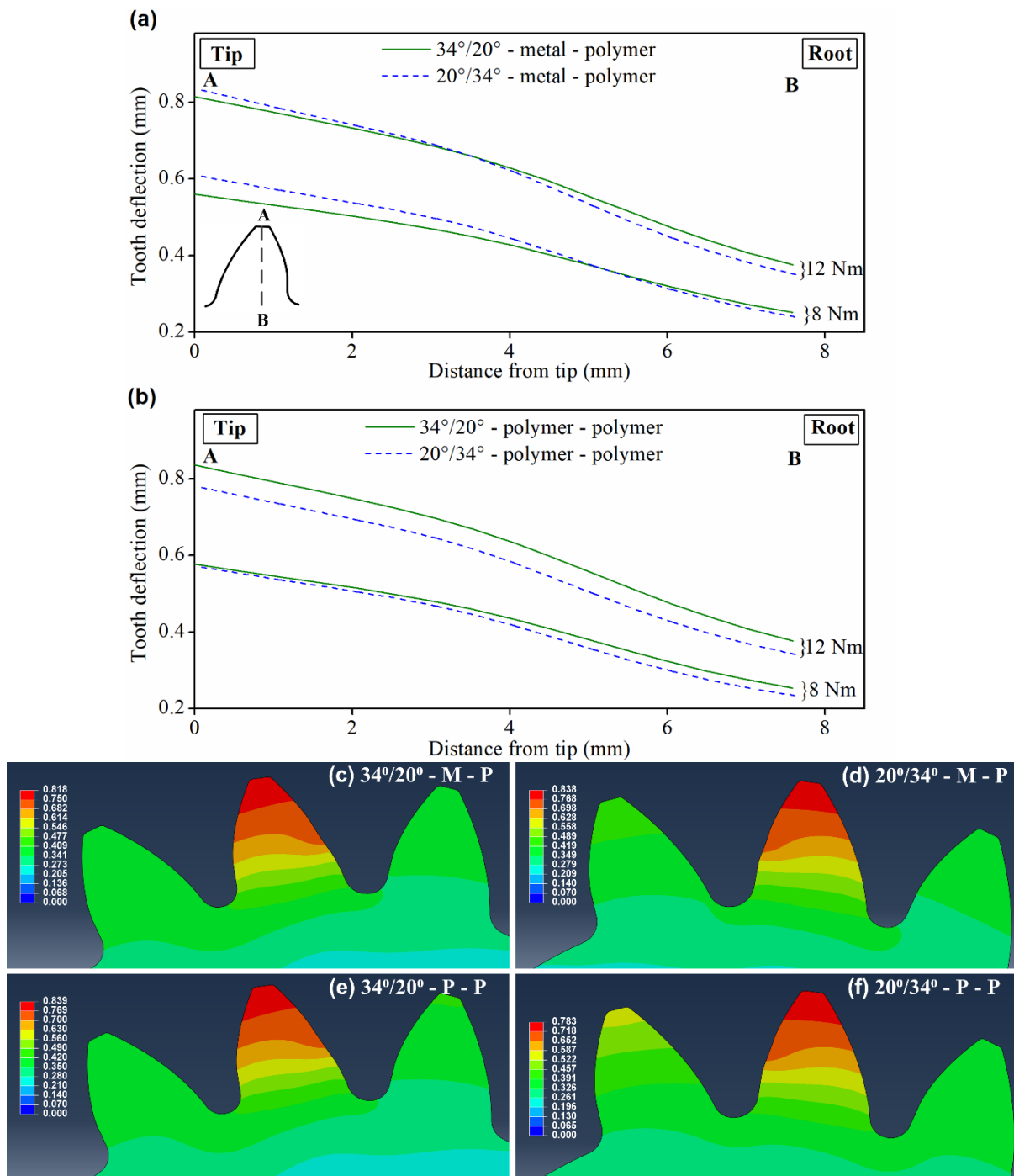


Fig. 5.5 Tooth deflections of asymmetric gear teeth subjected to 8 and 12 Nm: (a) Metal – Polymer pairs, (b) Polymer - Polymer asymmetric pairs, (c, d) Tooth deflection variation in metal - polymer pairs, and (e, f) Tooth deflection variation in polymer - polymer pairs.

freely suspended, the tooth deflection was higher on the tip and lower in the root region. The tooth deflection variation in each configuration can be observed in Figure 5.5 (c) – (f). For the 20°/34° configuration, tooth deflection of the polymer - polymer pair was lower than that of the metal - polymer pair. On the other hand, for the 34°/20° configuration, tooth deflection was

higher in the polymer - polymer pair. Generally, the stiffness of polymer - polymer pairs is lower than metal - polymer pairs and experience higher tooth deflection. But, the higher load sharing in the $20^\circ/34^\circ$ configuration impeded the deflection of the leading contact pair, resulting in lower deflection. However, the higher deflection of the polymer - polymer pair of $34^\circ/20^\circ$ configuration was due to inadequate load sharing. Regardless of the magnitude of tooth deflection, polymer - polymer pairs sustained higher operating temperatures compared to metal - polymer pairs.

Comparing the tooth deflections of metal - polymer pairs of $34^\circ/20^\circ$ and $20^\circ/34^\circ$ configurations, the deflection of the $20^\circ/34^\circ$ configuration was higher than that of the $34^\circ/20^\circ$ configuration near the tip region. However, a cross-over was observed between the trends of $34^\circ/20^\circ$ and $20^\circ/34^\circ$ configurations as the root was approached. Around the root region, the deflection of the $20^\circ/34^\circ$ configuration was less than that of the $34^\circ/20^\circ$ configuration. The cause for the cross-over between the deflection curves could be the stiffness mismatch between the materials of the driver and driven gear. The hysteresis heat generation is affected by this deflection behavior. As mentioned earlier, the hysteresis heat generation is high near the root, which results in the highest tooth temperature. The volume of material in the dedendum region is higher compared to the volume of material in the addendum region. Since hysteresis is volume-dependent, a higher strain in the root region will invariably lead to higher heat generation. Consequently, the higher tooth deflection of the $34^\circ/20^\circ$ configuration compared to the $20^\circ/34^\circ$ configuration in the dedendum region resulted in the higher operating temperature of the $34^\circ/20^\circ$ configuration.

The difference between the operating temperatures of $34^\circ/20^\circ$ and $20^\circ/34^\circ$ configurations was less at 8 Nm and increased linearly with an increase in the load. This increase in temperature difference was caused by the load-dependent increase in the volume of material in the $34^\circ/20^\circ$ configuration that was subjected to higher strain than the $20^\circ/34^\circ$ configuration. From Figure 5.5 (a), it is evident that at 12 Nm, the cross-over of the deflection curves of $34^\circ/20^\circ$ and $20^\circ/34^\circ$ configurations occurred earlier compared to 8 Nm. This indicates the increase in the volume of material in the $34^\circ/20^\circ$ configuration undergoing higher strain compared to the $20^\circ/34^\circ$ configuration. Accordingly, higher heat generation and a higher operating temperature were observed at 12 Nm. Thus, the convergence of bending fatigue life trend lines of $34^\circ/20^\circ$ and $20^\circ/34^\circ$ configurations in the high load region (Figure 5.3) was a consequence of two effects. The first one is the higher load sharing in the $20^\circ/34^\circ$ configuration, which decreased the bending stress. The second one is the higher hysteresis heat generation in the $34^\circ/20^\circ$

configuration, which reduced the tooth strength. Thus, the increase in applied load positively influenced the bending strength of the 20°/34° configuration and negatively influenced the bending fatigue strength of the 34°/20° configuration. Unlike the metal - polymer pairs, no cross-over between tooth deflection trends was observed in polymer - polymer pairs. The tooth deflection of the 34°/20° configuration was distinctly higher than the 20°/34° configuration from tip to root, without any cross-over. Therefore, the difference between the operating temperatures of 34°/20° and 20°/34° configurations was uniform across the load spectrum. Consequently, the trendlines of bending fatigue life of 34°/20° and 20°/34° configurations were parallel as well. As mentioned earlier, the polymer driver gear increased the volume of material subjected to hysteresis heating, causing higher operating temperature. Also, the higher tooth deflection of the 34°/20° configuration increased its operating temperature above that of the 20°/34° configuration.

5.4 Analysis of hysteresis behavior

The hysteresis loops of asymmetric gear configurations were determined experimentally and analyzed to complement the simulation results. The hysteresis loops were plotted using the values of applied torque and tooth deflection obtained from the torque sensor and rotary potentiometer, respectively. Parameters associated with the hysteresis loop, such as area, slope, and mean deflection are useful for analyzing the dissipation characteristics of the specimen. The area of the hysteresis loop represents the deformation energy dissipated during a cycle. The stiffness and creep behavior can be assessed using the slope and mean deflection values (Benaarbia, Chrysochoos and Robert, 2014). Hence, the comparison of loop parameters can provide experimental confirmation of the thermal behavior of metal - polymer and polymer - polymer gear pairs. For analysis, only a few hysteresis loops corresponding to selected cycles of metal - polymer and polymer - polymer pairs of 34°/20° and 20°/34° configurations were extracted and processed.

Figure 5.6 (a) shows the typical hysteresis curves of the metal - polymer pair of 34°/20° and 20°/34° configurations. The loops correspond to cycle 10000 of asymmetric gears subjected to a load of 12 Nm. The creep characteristics were examined by comparing the hysteresis loops at different intervals of time during testing of polymer - polymer pair of 34°/20° configuration at 12 Nm. Accordingly, the hysteresis loops of cycles 50, 500, 1500, and 5000 were studied (Figure 5.6 (b)). The hysteresis loops were not coincident, indicating that the mean tooth deflection of cycle increased over the course of life. This was caused by the 'cyclic creeping'

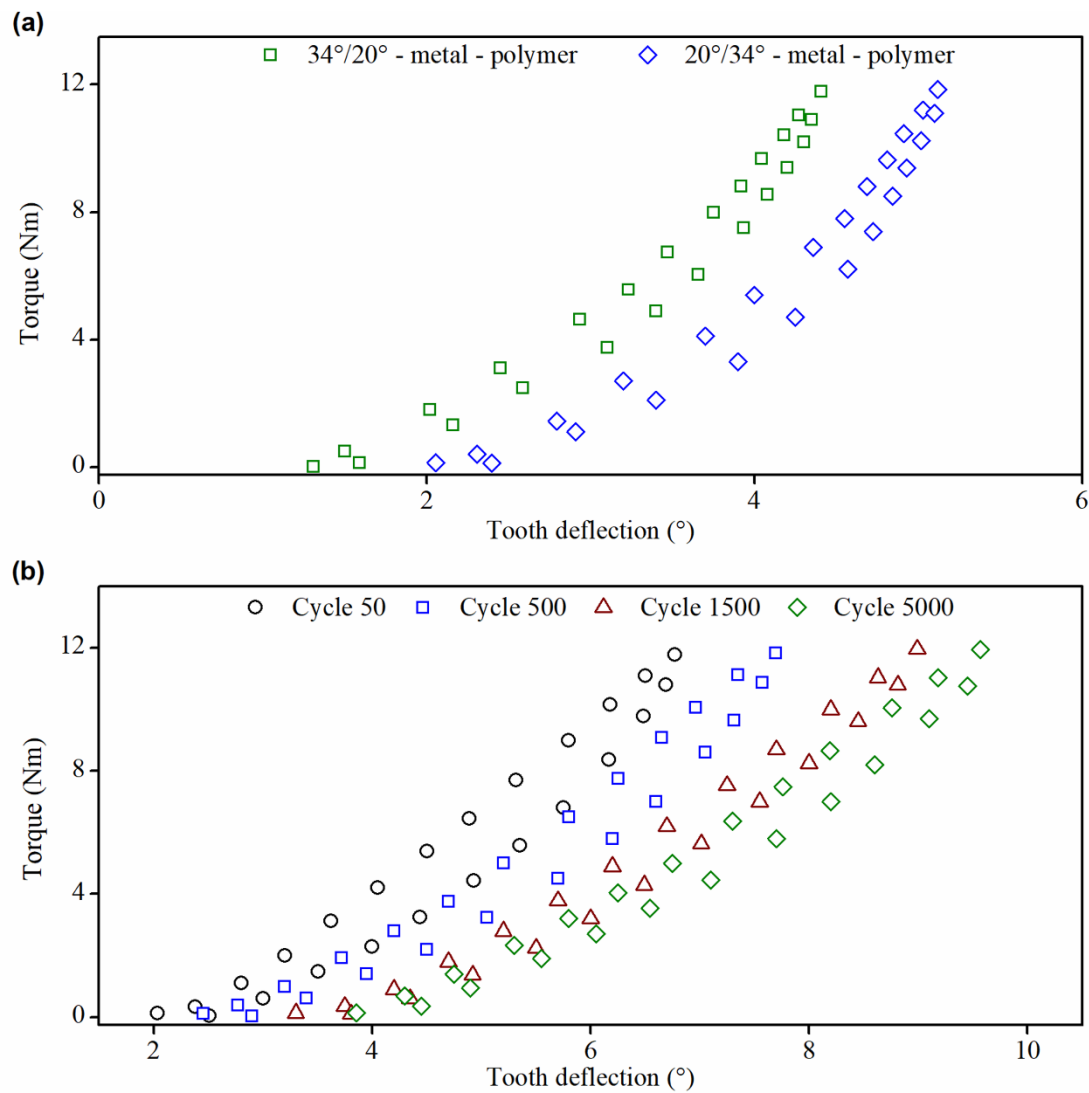


Fig. 5.6 Hysteresis loops of metal - polymer pairs corresponding to 12 Nm: (a) comparison of $34^\circ/20^\circ$ and $20^\circ/34^\circ$ configurations at cycle 10000 and (b) evolution of loops with progression of cycles.

or 'ratcheting.' Compared to cycle 50, the mean tooth deflection of cycles 500, 1500, and 5000 increased by 14%, 33%, and 42%, respectively. The same trend was observed in metal - polymer and polymer - polymer pairs of other configurations. The cyclic creeping was not affected by tooth asymmetry and driver gear material. The loop areas of metal - polymer and polymer - polymer pairs of $34^\circ/20^\circ$ and $20^\circ/34^\circ$ configurations were compared. The loop areas corresponding to cycle 10000 are represented in Figure 5.7 (b). The loop area of the $34^\circ/20^\circ$ configuration was greater than the $20^\circ/34^\circ$ configuration, indicating higher dissipated energy. In metal - polymer pairs, the loop area of $34^\circ/20^\circ$ configuration was higher by 18%, whereas in polymer - polymer pairs, the loop area was twice that of $20^\circ/34^\circ$ configuration. The higher dissipated energy of the $34^\circ/20^\circ$ configuration substantiates the higher surface temperature observed during testing. Similarly, the loop areas of polymer - polymer pairs were higher than

metal - polymer pairs. This is in agreement with the experimental temperature measurements. In $34^\circ/20^\circ$ configuration, loop area of the polymer - polymer pair was nearly two times (96%) that of the metal - polymer pair. However, in the case of the $20^\circ/34^\circ$ configuration, the increase in the loop area was merely 10%. The variation in loop areas of $34^\circ/20^\circ$ and $20^\circ/34^\circ$ configurations was a result of the different load sharing behavior. In the $20^\circ/34^\circ$ configuration, the higher load sharing observed in polymer - polymer pairs impeded the tooth deflection, resulting in a lower increase in the loop area. On the contrary, tooth deflection of the $34^\circ/20^\circ$ configuration was increased due to the lack of load sharing, leading to a higher loop area in polymer - polymer pairs. Figure 5.7 (a) compares the hysteresis loops of metal - polymer and polymer - polymer pairs of $34^\circ/20^\circ$ configuration corresponding to cycle 50. The higher tooth

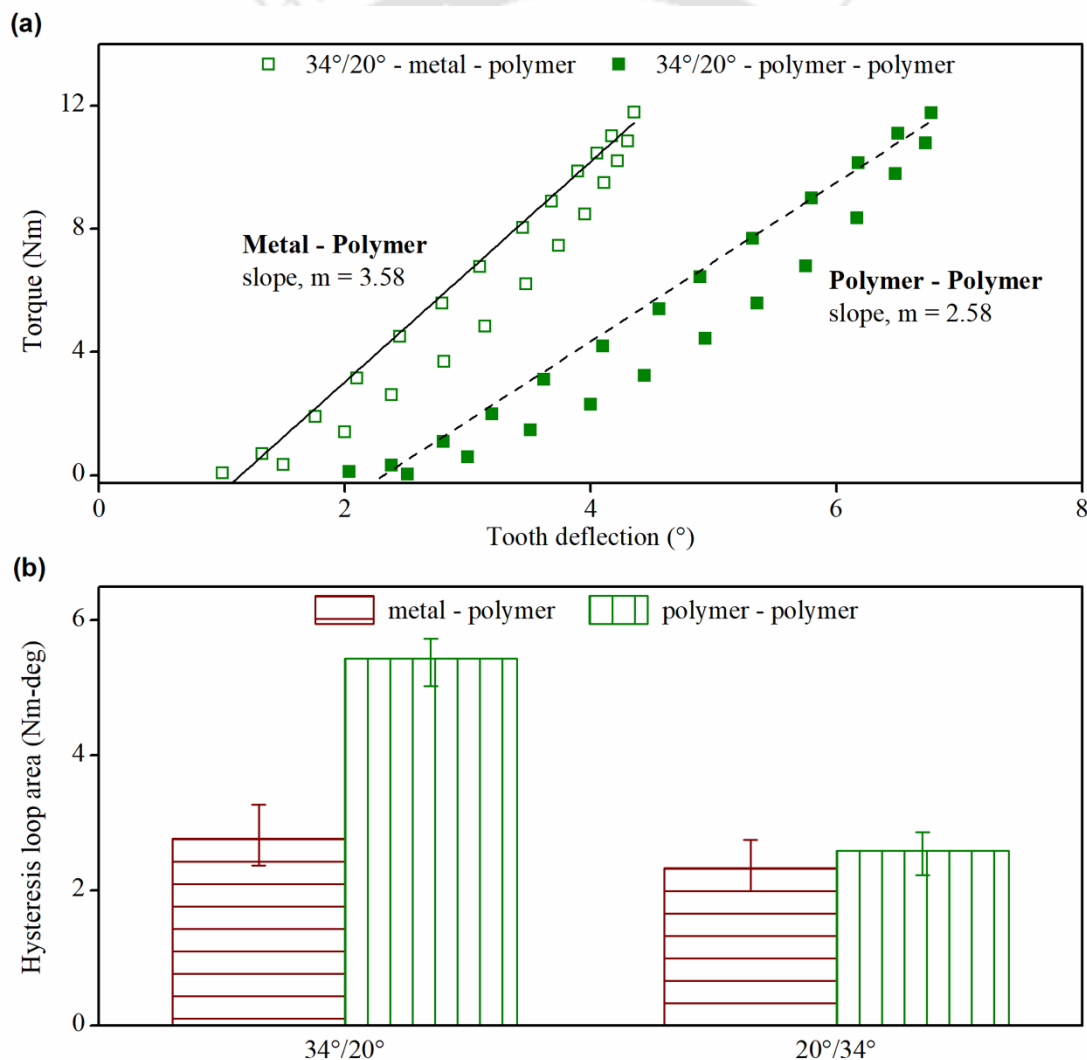


Fig. 5.7 Hysteresis behavior of metal - polymer and polymer - polymer pairs subjected to 12 Nm: (a) hysteresis loops of $34^\circ/20^\circ$ configuration at cycle 50 and (b) hysteresis loop areas of asymmetric configurations at cycle 10000.

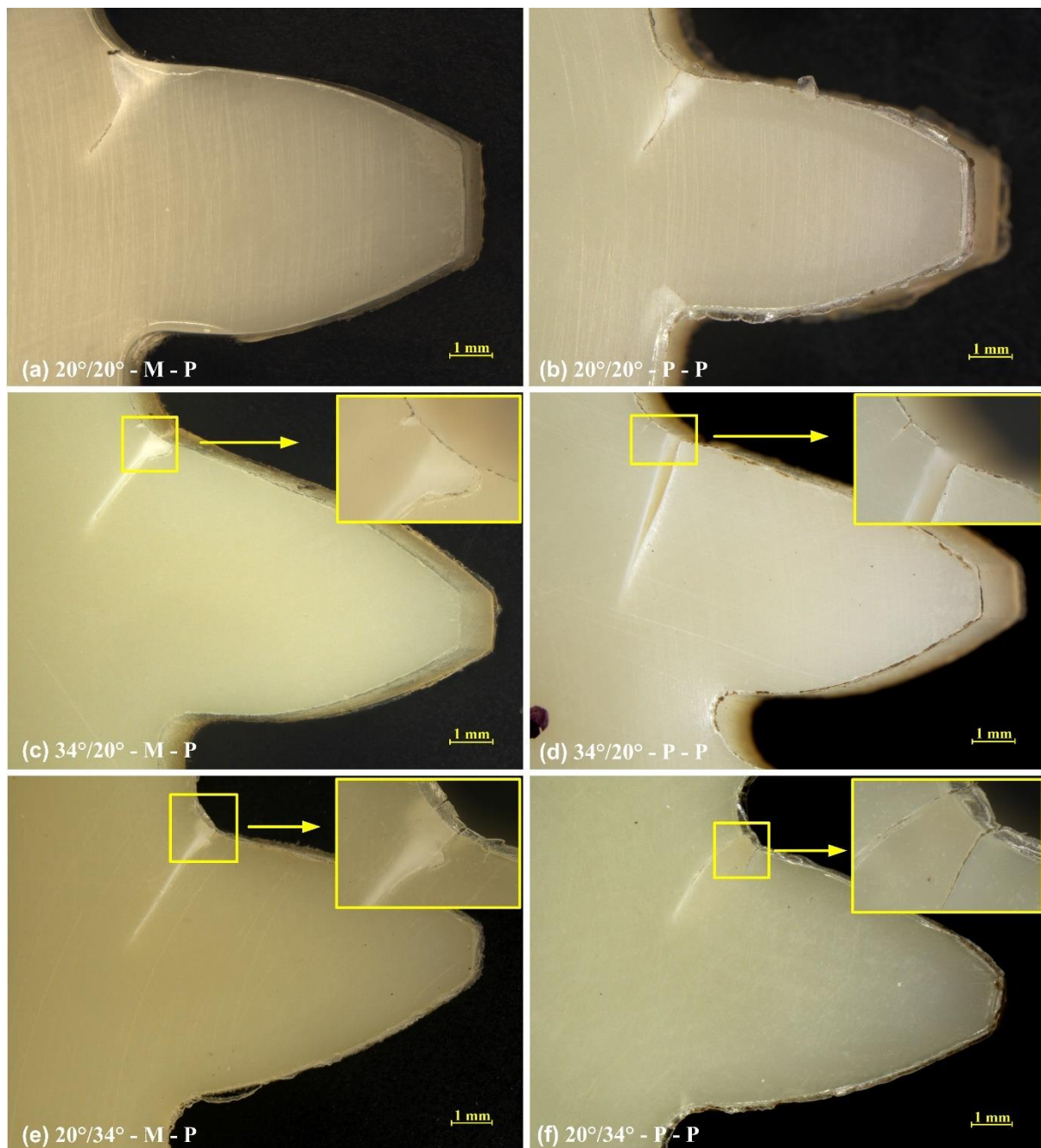


Fig. 5.8 Failed teeth of symmetric and asymmetric configurations: (a, c, e) metal-polymer pairs and (b, d, f) polymer-polymer pairs.

deflection of polymer - polymer gear pair can be observed. In addition, the inclination of the loop was higher in polymer - polymer pair, implying lower stiffness. To quantify the stiffness of metal - polymer and polymer - polymer pairs, slope of the loading curve was determined for each pair. Slope of the loading curve of metal - polymer pair ($m = 3.58$) was higher than that of polymer - polymer pair by 38%. The lesser slope value of polymer - polymer pair ($m = 2.58$) signified the lower stiffness of polymer - polymer pair. The same trend was observed during

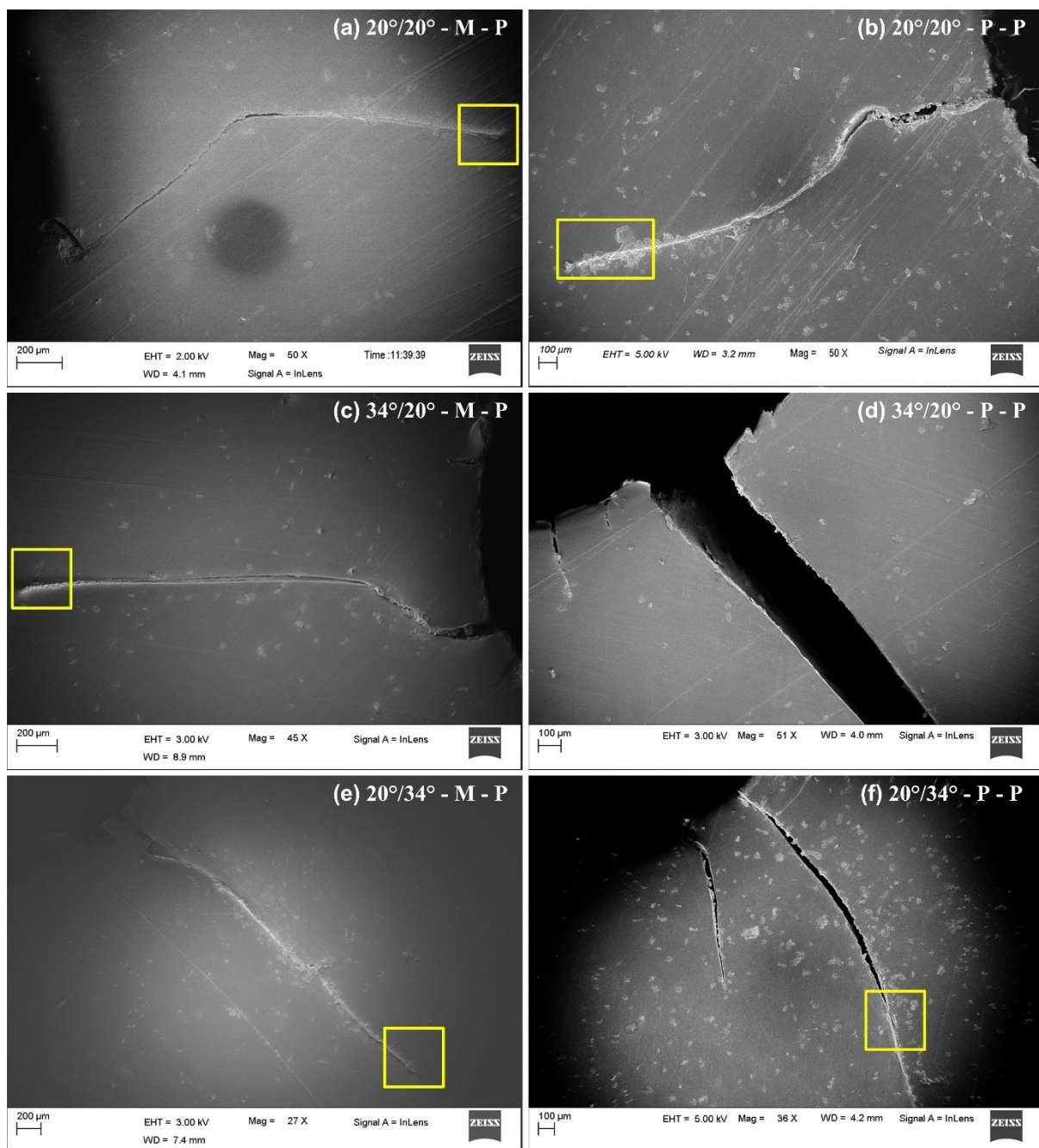


Fig. 5.9 FESEM images of 20°/20°, 34°/20° and 20°/34° test gears (top to bottom): (a, c, e) metal-polymer pairs and (b, d, f) polymer-polymer pairs.

the comparison of unloading curves. Also, mean tooth deflection of the polymer - polymer pair was higher than that of metal - polymer pair by 55%, confirming the lower stiffness.

5.5 Failure modes in metal - polymer and polymer - polymer pairs

In the previous chapter, bending fatigue failures in symmetric and asymmetric polymer gears mated with metal gears were compared. The emphasis was to analyze the effect of tooth asymmetry on the bending fatigue failure mode. However, in this chapter, the effect of mating

gear material on the bending fatigue failure mode has been discussed. The bending fatigue failure mode in polymer - polymer gear pairs was similar to the metal - polymer pairs. Although polymer - polymer gear pairs sustained higher temperatures than metal - polymer pairs, no significant difference was observed between the failure features. Figure 5.8 (a) – (f) shows the stereo microscopy images of the bending fatigue cracks of metal - polymer and polymer - polymer gear pairs. Figure 5.9 (a) – (f) depicts the FESEM images of the test gears.

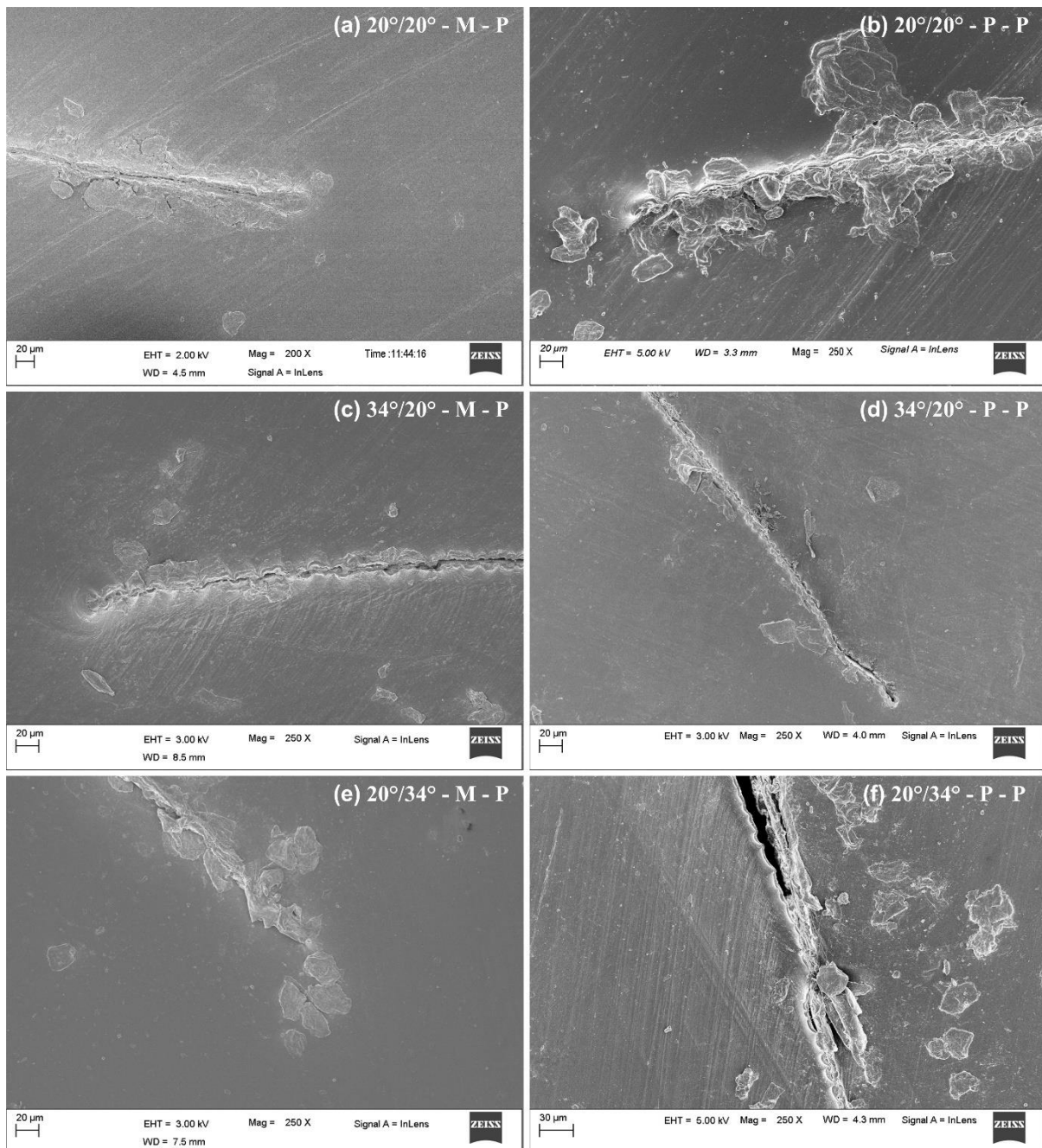


Fig. 5.10 Magnified view of crack tips of 20°/20°, 34°/20° and 20°/34° configurations (top to bottom): (a, c, e) metal-polymer pairs and (b, d, f) polymer-polymer pairs.

As anticipated, the teeth were not subjected to wear which was confirmed by the stereo microscopy images (Figure 5.8). The characteristic wedge-shaped deformation zone (stress-whitened zones) associated with polymers was present in the symmetric gears. The crack initiation and propagation were preceded by the occurrence of these stress-whitened deformation zones. In general, the size of the deformation zone in asymmetric gears was comparatively smaller. Also, the extent of the deformation zone in polymer - polymer pairs of asymmetric gears was marginally lower than that of metal - polymer pairs. This could be due to the lower bending stress in polymer - polymer gear pairs induced by higher load sharing.

The profile of the crack path was similar in both metal - polymer and polymer - polymer pairs. Multiple cracks originated in the fillet regions due to the high stress concentration. In symmetric gears, multiple cracks were observed only at high load cases of metal - polymer and polymer - polymer pairs. On the other hand, in asymmetric gears, multiple cracks were present at all loads throughout the applied load range in metal - polymer and polymer-polymer pairs. The close-up view of crack tips are shown in Figure 5.10 (a) – (f).

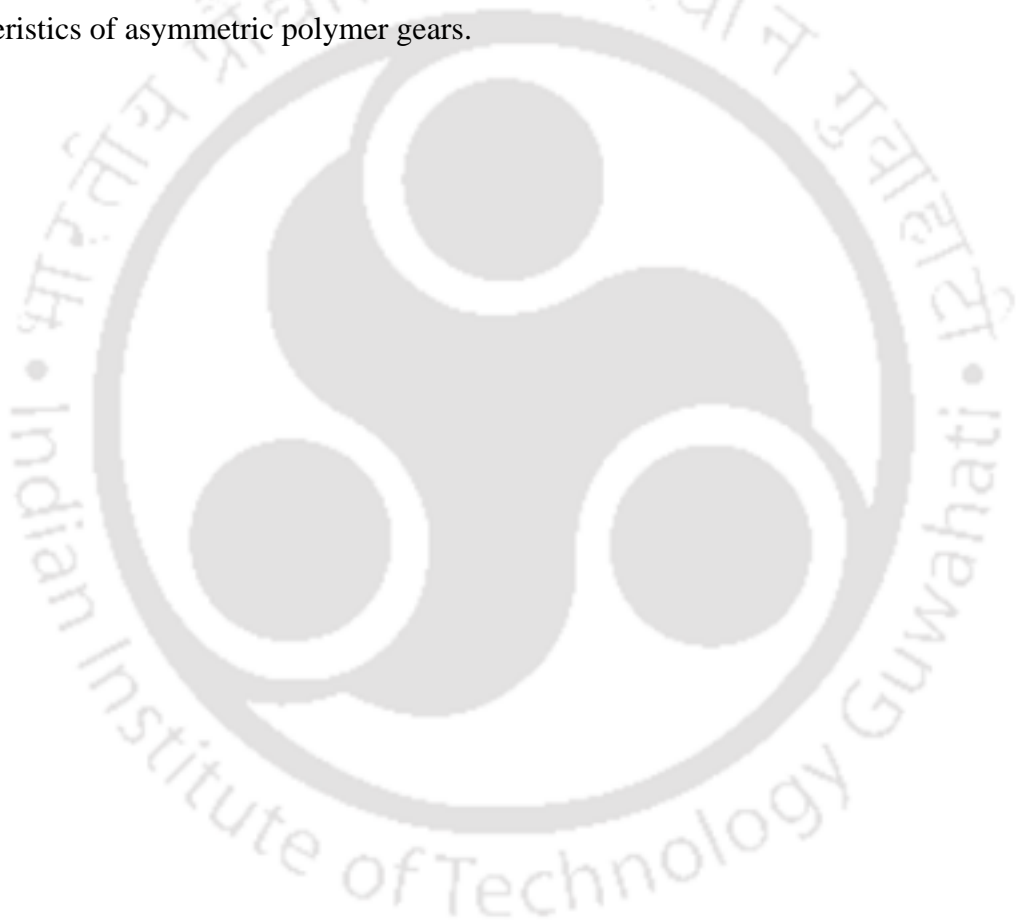
5.6 Summary

The effect of steel and Nylon 66 mating gears on the bending fatigue behavior of symmetric and asymmetric Nylon 66 gears was evaluated using numerical and experimental methods. The bending stress and load sharing behavior of metal-polymer and polymer-polymer pairs were predicted by ABAQUS simulations. Bending fatigue life was determined experimentally from bending fatigue tests conducted using a custom test rig. The findings of the investigation are given below:

- The load shared by the adjacent tooth increased markedly for polymer-polymer pairs of 20°/20° and 20°/34° configurations, which decreased the bending stress in the fillet. In the 34°/20° configuration, no bending stress reduction was achieved, as load sharing was minimal and observed only at high loads.
- The increased load sharing and decrease in bending stress were not beneficial for bending fatigue strength. The bending fatigue life of polymer-polymer pairs decreased considerably compared to metal-polymer pairs.
- The polymer driver gear increased the heat generation and decreased heat dissipation drastically. Consequently, the operating temperature of polymer-polymer pairs was greater than metal-polymer pairs, which decreased the bending fatigue strength.

- In asymmetric configurations, the deployment of polymer driver gear reduced the strength of the 34°/20° configuration more than that of the 20°/34° configuration due to the higher operating temperature of the 34°/20° configuration.
- The bending fatigue performance of polymer-polymer pairs depended on the operating temperature, whereas the maximum bending stress determined the bending fatigue performance of metal-polymer pairs in the fillet.

This study indicates that the drive side and coast side configuration that offers superior bending fatigue strength depends on the mating gear material. So far, the bending fatigue behavior of asymmetric polymer gears has been discussed. The next chapter discusses the deflection characteristics of asymmetric polymer gears.



Chapter 6

Tooth deflection characteristics of asymmetric polymer gears

The transmission error in polymer gears is significantly affected by the elastic deflection of meshing teeth. As transmission error dictates the dynamic behavior, optimum tooth deflection is vital for minimizing the transmission error and achieving acceptable dynamic behavior. This chapter describes the deflection characteristics of asymmetric Nylon 66 spur gears mated with steel and Nylon 66 gears which were evaluated using numerical simulations and experiments.

The results of numerical analyses have been presented initially, whereas the experimental results are presented at the end of the chapter. The first section describes the details and methods associated with numerical simulations. Following that, the mesh deflection characteristics such as phases in a mesh cycle, duration of mesh cycle, load sharing behavior, and variation within a cycle have been discussed. The third section examines the tooth deflection variation in each configuration.

After the overall analysis of mesh and tooth deflections, specific aspects such as peak deflection and amplitude of variation in a cycle have been analyzed. Then, the influence of asymmetric tooth and polymer mating gear on the path of contact is discussed. Finally, a comparison of the numerically predicted and experimentally determined mesh deflection values has been presented.

6.1 Details of numerical simulations

The gear pair model used in this study was 'Gear pair model 2.' The simulations were performed at multiple mesh positions along the path of contact. Each mesh position was separated by an interval of 2° roll angle. Two different load cases (1 and 1.5 Nm) were considered, and a total of 188 simulations were conducted as part of the study. The applied torque pattern and loading duration in simulations were similar to that during experiments. The experimental methodology has already been discussed in Chapter 3. The applied torque increased linearly from zero to the set value within 1 s and remained constant for the remaining duration.

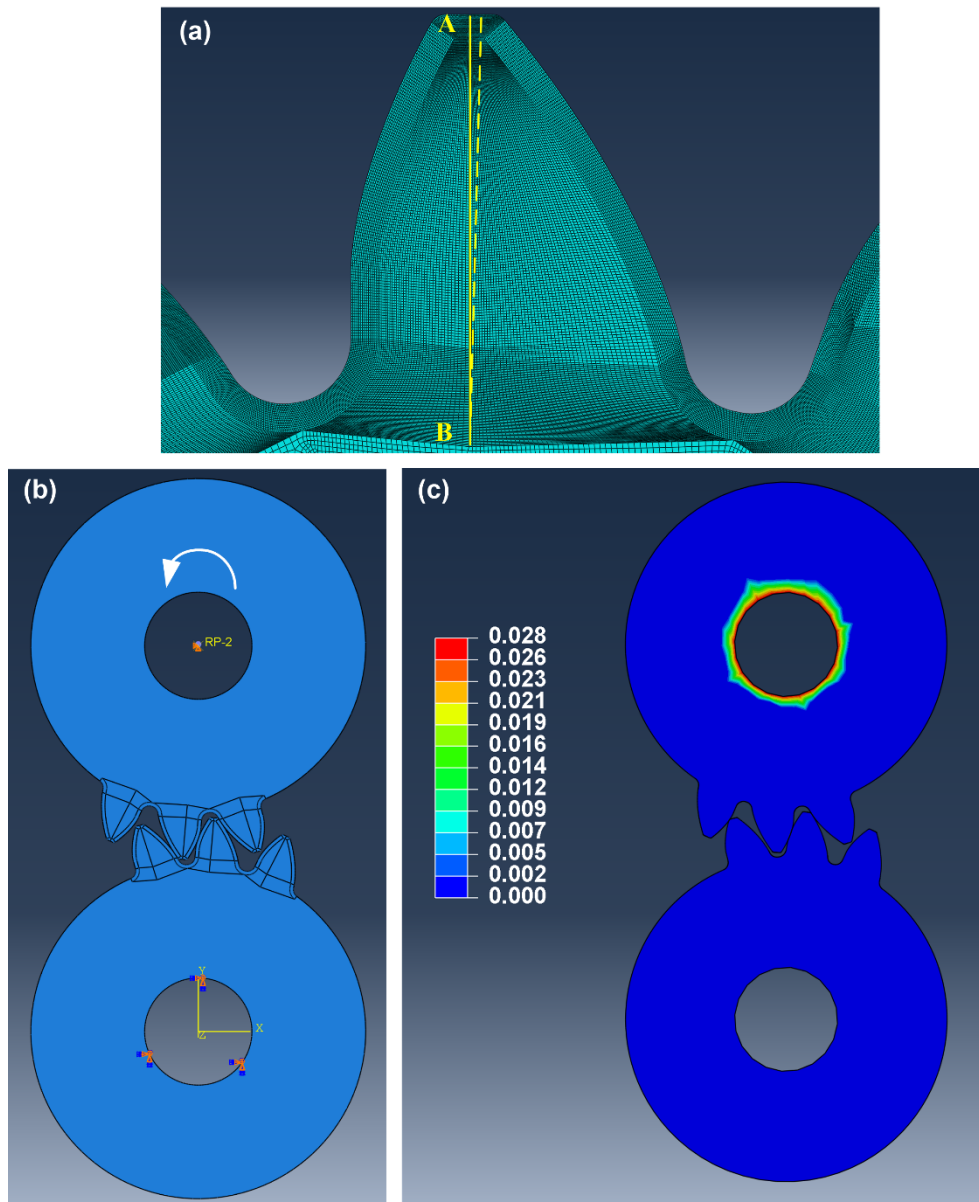


Fig. 6.1 (a) Path of measurement along the tooth depth, (b) Rotation of driver gear during loading, and (c) Typical driver gear rotation at the end of analysis.

In multiple numerical investigations, the driver gear rotation has been considered a measure of torsional mesh deflection (Tsai and Tsai, 1997; Wang and Howard, 2005). Hence, the rotation of the driver gear was acquired by extracting the rotation values of the node at the driver gear center axis (RP-2) (Figure 6.1 (b and c)). In addition to driver gear rotation, the deflection of driven teeth along the midline of the loaded tooth (AB) was extracted (Figure 6.1 (a)). The maximum deflection value, which corresponded to the tooth tip, was considered for analysis. Apart from deflections, the contact force on the drive side flank was extracted to determine the load sharing ratio using equation 3.8. The path of contact was charted by plotting the nodal coordinates in the contact patch corresponding to every mesh position.

6.2 Mesh deflection in symmetric and asymmetric gear pairs

6.2.1 Phases in a mesh cycle

A typical mesh deflection curve of a single mesh cycle constitutes three distinct regions: single tooth contact zone, double tooth contact zone, and 'Handover zones,' regions at the peripheries of double tooth contact zones. Figure 6.2 (a) and (b) presents a representative illustration of the single tooth contact and double tooth contact in gears. In a mesh cycle, the mesh stiffness in the DTC zones is higher than that in the STC zone, as load sharing in DTC zones decreases the tooth deflection. Theoretically, as contact transitions between the DTC zone and STC zone, the mesh stiffness varies abruptly. However, in service, the variation between the mesh stiffnesses of STC and DTC zones is gradual, owing to the material's flexibility. The regions of the DTC zone in which such variation occurs are called the 'Handover zones.' The existence of handover zones indicates contact outside the theoretical path of contact (Wang and Howard, 2005). The handover zones in a typical mesh cycle are shown in Figure 6.3.

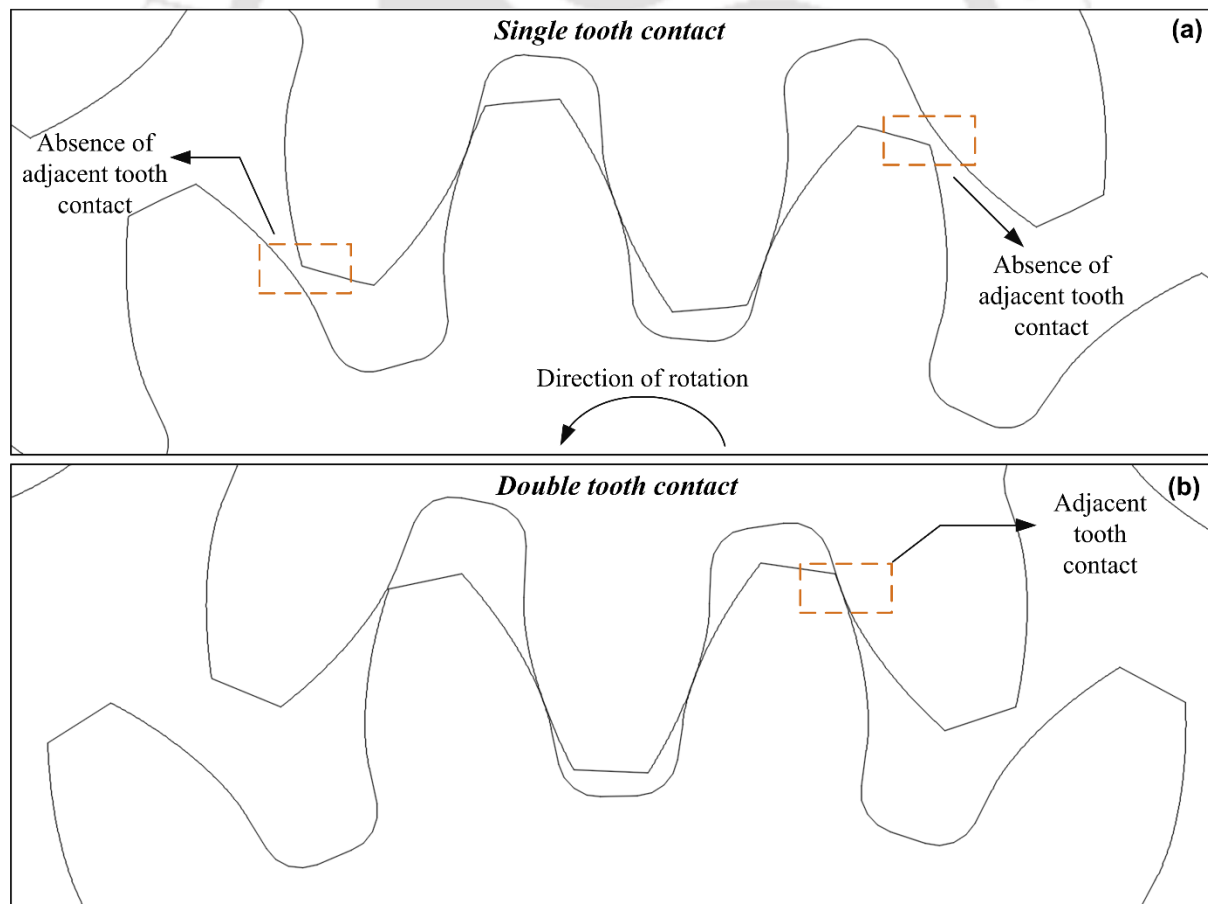


Fig. 6.2 (a) Single tooth contact and (b) double tooth contact.

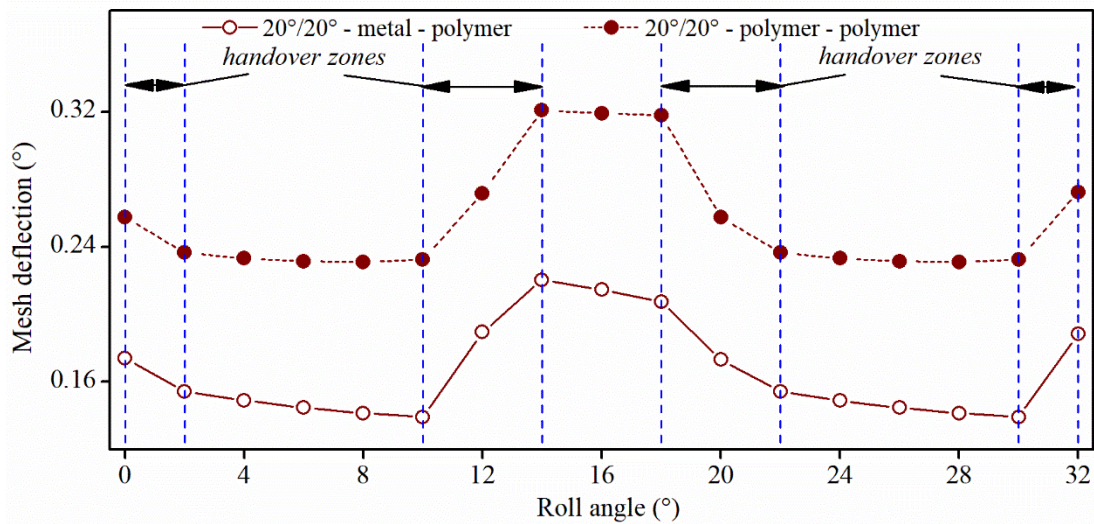


Fig. 6.3 Typical mesh deflection curves of symmetric gear pairs subjected to 1 Nm. The extents of handover zones are indicated.

As transition regions are clearly defined as 'handover zones,' hereafter in this chapter, the term 'DTC zone' has been used to refer to the region in the DTC zone, excluding the handover zones. Also, the references to 'addendum region' and 'dedendum region' imply the addendum and dedendum regions of the driven gear.

6.2.2 Mesh cycle duration

Figures 6.4 (a) and (b) depict the mesh deflections of symmetric and asymmetric configurations subjected to 1 and 1.5 Nm, respectively. The roll period – the total angular rotation of a gear pair between engagement and disengagement of a tooth – was used to measure the duration of the mesh cycle. The roll period was identical for 20°/20° and 20°/34° configurations (32°) whereas, it was 13% lesser (28°) for the 34°/20° configuration. The shorter contact duration in the 34°/20° configuration resulted from the larger pressure angle, which led to a delay in tooth engagement and advancement of tooth disengagement. Consequently, the STC zone widened, whereas the DTC zone contracted for the 34°/20° configuration. Besides the roll period, the periods of STC and DTC are influenced by the pressure angle on the loading flank. The STC period of 34°/20° configuration (8°) was twice that of STC periods of 20°/20° and 20°/34° configurations (4°). The DTC period of 34°/20° configuration (8°) was half of the DTC periods of 20°/20° and 20°/34° configurations (16°). The total period of handover zones in a mesh cycle was 12° for all configurations.

Thus, in 20°/20° and 20°/34° configurations, DTC was the dominant contact mode constituting 50% of the mesh cycle, whereas the proportions of STC and handover zone were ~13% and

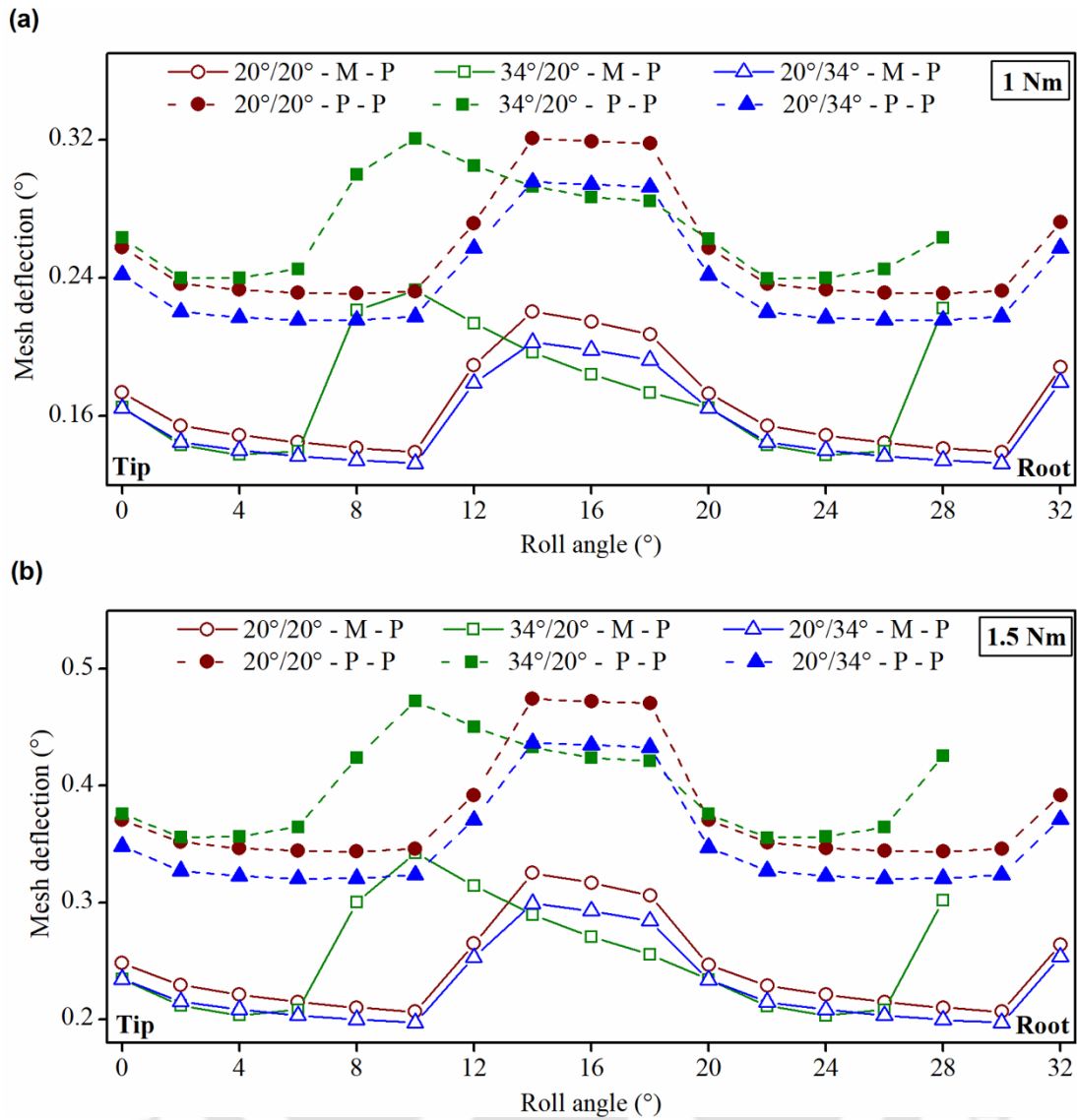


Fig. 6.4 Predicted mesh deflections of symmetric and asymmetric gear pairs during a cycle for: (a) 1 Nm and (b) 1.5 Nm.

~37%, respectively. However, in the 34°/20° configuration, the handover zone was the primary constituent (~43%), with the remainder evenly divided between STC (~29%) and DTC (~29%). In each configuration, the roll period and periods of STC, DTC and handover zones were the same for both metal - polymer (M-P) and polymer - polymer (P-P) engagements. They remained unchanged as the load was increased from 1 to 1.5 Nm.

6.2.3 Load sharing pattern

Before analyzing the tooth and mesh deflection characteristics of gears, studying the load sharing pattern in each gear configuration is essential. LSR of the leading pair of each configuration was determined. The LSR in STC and DTC zones of metal - polymer and

polymer - polymer pairs are shown in Figure 6.5. The minimum LSR in a cycle was observed at the start or end, depending on the configuration and mating gear material. In polymer - polymer pairs, the minimum LSR was at the end of the cycle in all three configurations. Similarly, in the metal - polymer pair of $20^\circ/34^\circ$ configuration, the minimum LSR was at the end of the cycle. However, in metal - polymer pairs of $20^\circ/20^\circ$ and $34^\circ/20^\circ$ configurations, the minimum LSR was at the beginning of the cycle (0°). The minimum LSR in a cycle was lowest in $34^\circ/20^\circ$ configuration and highest in $20^\circ/20^\circ$ configuration.

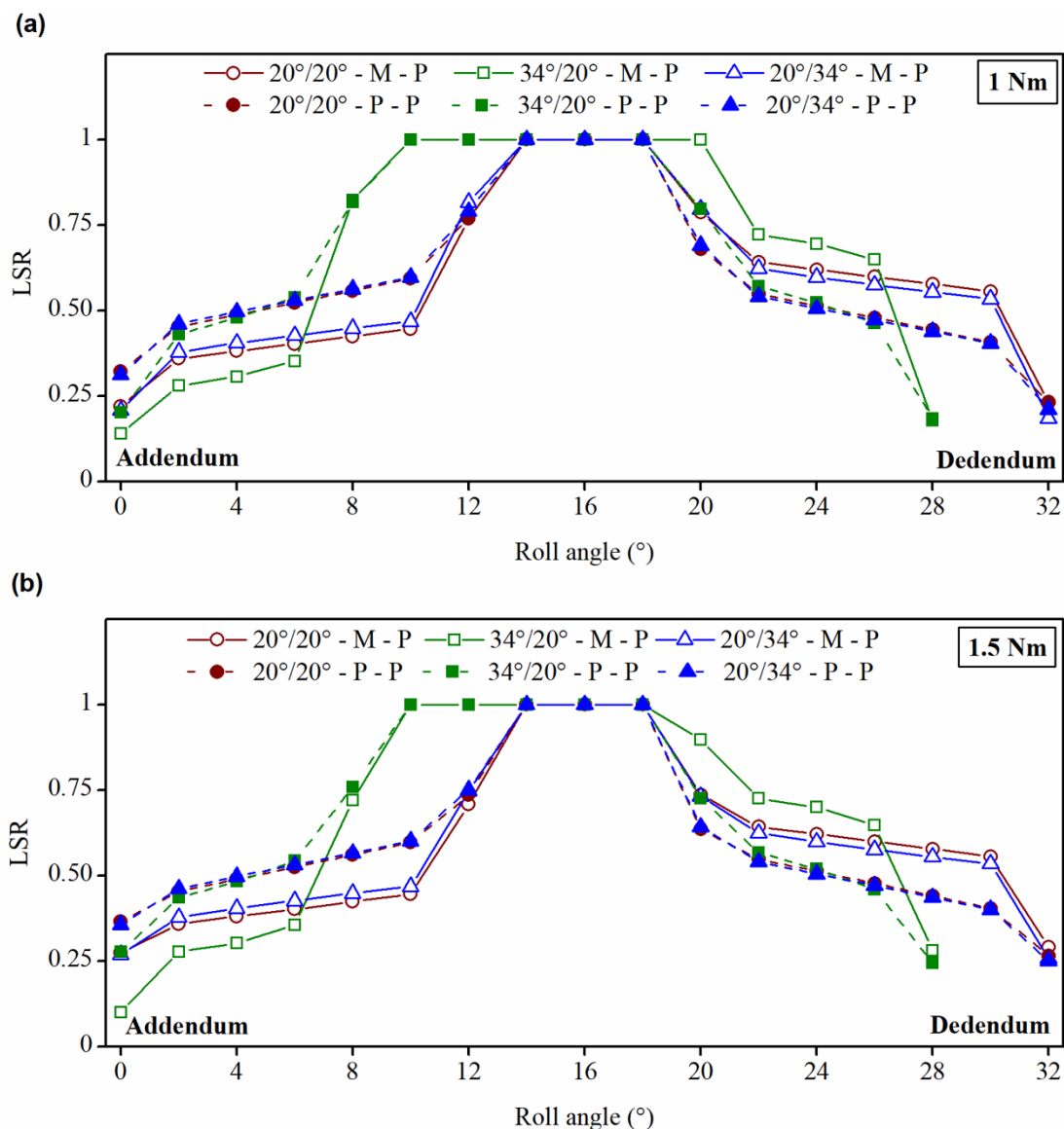


Fig. 6.5 Load sharing ratio of symmetric and asymmetric gears for: (a) 1 Nm and (b) 1.5 Nm.

In the addendum DTC zone, the LSR of the $34^\circ/20^\circ$ configuration was lower than that of $20^\circ/20^\circ$ and $20^\circ/34^\circ$ configurations by 12% – 63% and 17% – 63%, respectively. The LSR of $20^\circ/34^\circ$ was higher than other configurations in this region. The LSR in the dedendum DTC

zone was highest for $34^\circ/20^\circ$ configuration and lowest for $20^\circ/34^\circ$ configuration. The LSR of $20^\circ/20^\circ$ and $20^\circ/34^\circ$ configurations were almost the same as the pressure angle was identical. The deviation was less than 6% for metal - polymer pairs and below 3% when the mating gear material was polymer. Sekar and Muthuveerappan (2015) observed that the LSR in metal gear pairs of asymmetric configuration $30^\circ/20^\circ$ was lower compared to symmetric gear $20^\circ/20^\circ$ in DTC zones near the peripheries of the cycle. As the contact approached the STC zone, the LSR of asymmetric gear increased above the LSR of symmetric gear. Deng, Nakanishi and Inoue (2003) reported that the difference between LSR of asymmetric configuration $20^\circ/25^\circ$ and symmetric gear $20^\circ/20^\circ$ was insignificant as the variation in bending stiffness was uniform for each case.

The LSR curves in the metal - polymer pairs were unsymmetrical as LSR in the addendum DTC zone was lower than the LSR in the dedendum DTC zone. However, in polymer-polymer pairs, the LSR curves were rather symmetrical. Owing to this disparity, the LSR of polymer - polymer pairs was greater than that of metal - polymer pairs in the addendum DTC zone by 8% – 50%. On the other hand, the LSR of metal - polymer pairs was higher in the dedendum DTC zone by 15% – 39%. The literature has widely reported the skewed load sharing pattern in metal - polymer gear pairs (Tsukamoto, 1995; Van Melick, 2007; Kirupasankar, Gurnathan and Gnanamoorthy, 2012). Yelle and Burns (1981) observed that the load sustained by the addendum region was lower than the load sustained by the dedendum region of acetal gear in steel - acetal pairs. However, in acetal - acetal pairs, the load shared by the addendum and the dedendum regions were similar. The maximum load sustained during a cycle decreased in acetal gear pairs.

Generally, the load sharing is symmetrical about the pitch point in gear pair of identical geometry and material. The skewed LSR in metal - polymer pairs was a result of the substantial difference between the compliances of metal and polymer gears. Since the modulus of steel is very high, the compliance of steel gear is practically zero. As a result, the mesh compliance of the metal - polymer gear pair is dominated by the polymer gear tooth deflection. Generally, the tooth compliance is higher during contact in the addendum region and decreases as the contact moves toward the root (Arafa and Megahed, 1999). Thus, lower LSR in the addendum DTC zone of metal - polymer pairs could be a result of the higher compliance of the polymer gear tooth in the addendum, which increases the proportion of the load supported by the adjacent tooth. Conversely, both driver and driven gear teeth contribute to mesh compliance in polymer - polymer pairs, resulting in a symmetrical load sharing pattern. Meuleman *et al.* (2007)

reported that the deflection and mesh stiffness of steel - acetal pairs were dominated by the deflection of acetal gears, as the difference between stiffnesses of steel and acetal gears was large.

The increase in load altered the LSR across the cycle. At 1.5 Nm, LSR in the dedendum DTC zone increased, whereas LSR decreased in the addendum DTC region. However, the variation in LSR was significant only in the handover zones. The LSR decreased in the handover zones, indicating that a higher load increased the load carried by the adjacent tooth. This was accompanied by an increase in LSR in the handover zones at the start and the end of the cycle. As the load sustained by the leading tooth pair decreases in transition zones, the load endured by adjacent tooth pairs at the peripheries of the cycle increases. In the handover zones, the difference between LSR of 1 and 1.5 Nm was highest at the beginning and end of the mesh cycle. Among the configurations, the difference between LSR of 1 and 1.5 Nm was highest for the 34°/20° configuration and lowest for the 20°/20° configuration. The difference between LSR of 1 and 1.5 Nm was lesser in engagements of similar material.

6.2.4 Mesh deflection variation in a cycle

In general, the pattern of mesh deflection variation in a cycle was similar for all the configurations. In the STC zone, mesh deflection decreased as contact moved from the driven gear's highest point of single tooth contact to the lowest point of single tooth contact (LPSTC). In the addendum DTC region, mesh deflection declined steadily from the beginning of the cycle up to the start of the handover zone. The mesh deflection increased in the handover zone preceding the STC zone. Similarly, the mesh deflection decreased continuously up to the handover zone at the end of the cycle in the dedendum DTC region. These trends were observed in the metal - polymer pairs. The pattern of mesh deflection variation in 20°/20° and 20°/34° was identical in engagements of similar and dissimilar materials. In the polymer - polymer pair of 34°/20° configuration, the contact position in DTC zones at which the mesh deflection began to increase advanced by 2°.

The mating gear material affected the variation in mesh deflection within the DTC zones. From Figure 6.4, it can be observed that the magnitude of variation was lesser for the polymer - polymer pairs. The mismatch between the compliances of steel and Nylon 66 caused higher variation for the metal - polymer pairs (0.0034° – 0.0225°), as tooth deflection in steel gear was negligible. On the other hand, the use of similar material for driver and driven gears in polymer - polymer pairs decreased the mesh deflection variation (0.0025° – 0.0092°), as tooth

deflections in driver and driven gears complemented each other. The influence of material pairs on the shape of curves was reported by Meuleman *et al.* (2007). In the case of steel - acetal pairs, the shape of deflection, mesh stiffness, and TE curves were in the form of 'saw tooth' whereas, for acetal - acetal pairs, the curves were symmetrical.

The mesh deflection of the $20^\circ/34^\circ$ configuration was lesser than that of the $20^\circ/20^\circ$ configuration by 5% – 8% for similar engagement and by 4% – 8% for dissimilar engagement. However, the variation of mesh deflection of the $34^\circ/20^\circ$ configuration with respect to other configurations was not uniform across the cycle and was influenced by driver gear material. In metal - polymer pairs, the mesh deflection of the $34^\circ/20^\circ$ configuration was lower than that of $20^\circ/20^\circ$ and $20^\circ/34^\circ$ configurations in DTC zones and in the STC period 14° - 20° . The deviations between the mesh deflections of the $34^\circ/20^\circ$ configuration and the deflections of $20^\circ/20^\circ$ and $20^\circ/34^\circ$ configurations in the DTC zone were in the range of 3% – 8% and 2%, respectively. In the STC period 14° - 20° , the range of deviations was 5% – 17% and 3% – 10%, respectively.

However, in the period between 6° and 12° , the mesh deflection for the $34^\circ/20^\circ$ configuration was higher than that for $20^\circ/20^\circ$ (13% – 67%) and $20^\circ/34^\circ$ (2% – 76%) configurations, respectively. The higher mesh deflection in this period could be attributed to the greater bending moment arm, resulting from a longer STC period. In polymer - polymer pairs, the mesh deflection for the $34^\circ/20^\circ$ configuration was higher than that for the $20^\circ/20^\circ$ (1% – 38%) and $20^\circ/34^\circ$ (8% – 47%) configurations at every position, except the STC period 14° - 18° . Karpat *et al.* (2017) reported that the mesh stiffness of asymmetric gears was greater than that of the symmetric gears. The mesh stiffness was greater for configurations with a higher drive side pressure angle as well as higher coast side pressure angle. The increased mesh stiffness was attributed to the increased tooth thickness in the dedendum region.

The increase in load had no influence on the mesh deflection trend in metal - polymer and polymer - polymer pairs. However, at greater loads, premature and extended contacts shrink the duration of the single tooth contact zone and alter the shape of the mesh deflection curve. Meuleman *et al.* (2007) reported that the width of the single tooth contact zone in the transmission error curve decreased at higher loads. Also, the distinction between single tooth contact and double tooth contact disappears with the increase in load resulting in the transformation of the curve to a parabola. Parabolic load sharing curves were reported by Walton *et al.* (1994) and Karimpour, Dearn and Walton (2010). To understand the mesh

deflection trend in polymer - polymer pairs, the relation between load sharing behavior and tooth deflection and their impact on mesh deflection of each configuration must be analyzed in detail.

6.3 Tooth deflection variation in a cycle

Figure 6.6 shows the tooth deflection in metal - polymer and polymer - polymer pairs subjected to 1 and 1.5 Nm. The tooth deflection variation in driven gears of symmetric and asymmetric configurations is depicted in Figure 6.7. The polymer driving gear had no influence on the relationship between the tooth deflections of $20^\circ/20^\circ$ and $20^\circ/34^\circ$ configurations. The tooth deflection of the symmetric configuration was greater than that for the $20^\circ/34^\circ$ configuration throughout the mesh cycle, with deviations in the range of 7% – 15%. Although the LSR pattern was different for metal - polymer and polymer - polymer pairs, the relationship between the tooth deflections of $20^\circ/20^\circ$ and $20^\circ/34^\circ$ configurations remained the same. Consequently, the relationship between the mesh deflections followed the same trend.

In metal - polymer pairs, the tooth deflection of the $34^\circ/20^\circ$ configuration was lesser than that for the $20^\circ/20^\circ$ and $20^\circ/34^\circ$ configurations for the significant part of the mesh cycle involving the addendum DTC zone, and the region below pitch point ($15^\circ - 28^\circ$). The deviations with respect to the $20^\circ/20^\circ$ and $20^\circ/34^\circ$ configurations in the addendum DTC zone were in the range of 11% – 15% and 3% – 8%, respectively. In the period $15^\circ - 28^\circ$, the deviations ranged between 16% and 37% and 6% and 30%, respectively.

Despite the higher LSR in the dedendum DTC zone, the tooth deflection for the $34^\circ/20^\circ$ configuration was lower due to the lesser bending moment arm and higher tooth thickness in the dedendum region which increased the stiffness. The tooth deflection of the $34^\circ/20^\circ$ configuration was greater than that for the $20^\circ/20^\circ$ and $20^\circ/34^\circ$ configurations only in the handover zone preceding the STC zone ($7^\circ - 10^\circ$) and in the STC period between 10° and 13° . The higher tooth deflection in the handover zone could be attributed to the greater LSR of $34^\circ/20^\circ$ configuration in that region. The higher tooth deflection in the STC period ($10^\circ - 13^\circ$) was caused by a greater bending moment arm, resulting from the longer STC period in the $34^\circ/20^\circ$ configuration. The mesh deflection pattern for the $34^\circ/20^\circ$ configuration was similar to the tooth deflection pattern. Compared to $20^\circ/20^\circ$ and $20^\circ/34^\circ$ configurations, the mesh deflection was lesser in almost every region, except for handover zones.

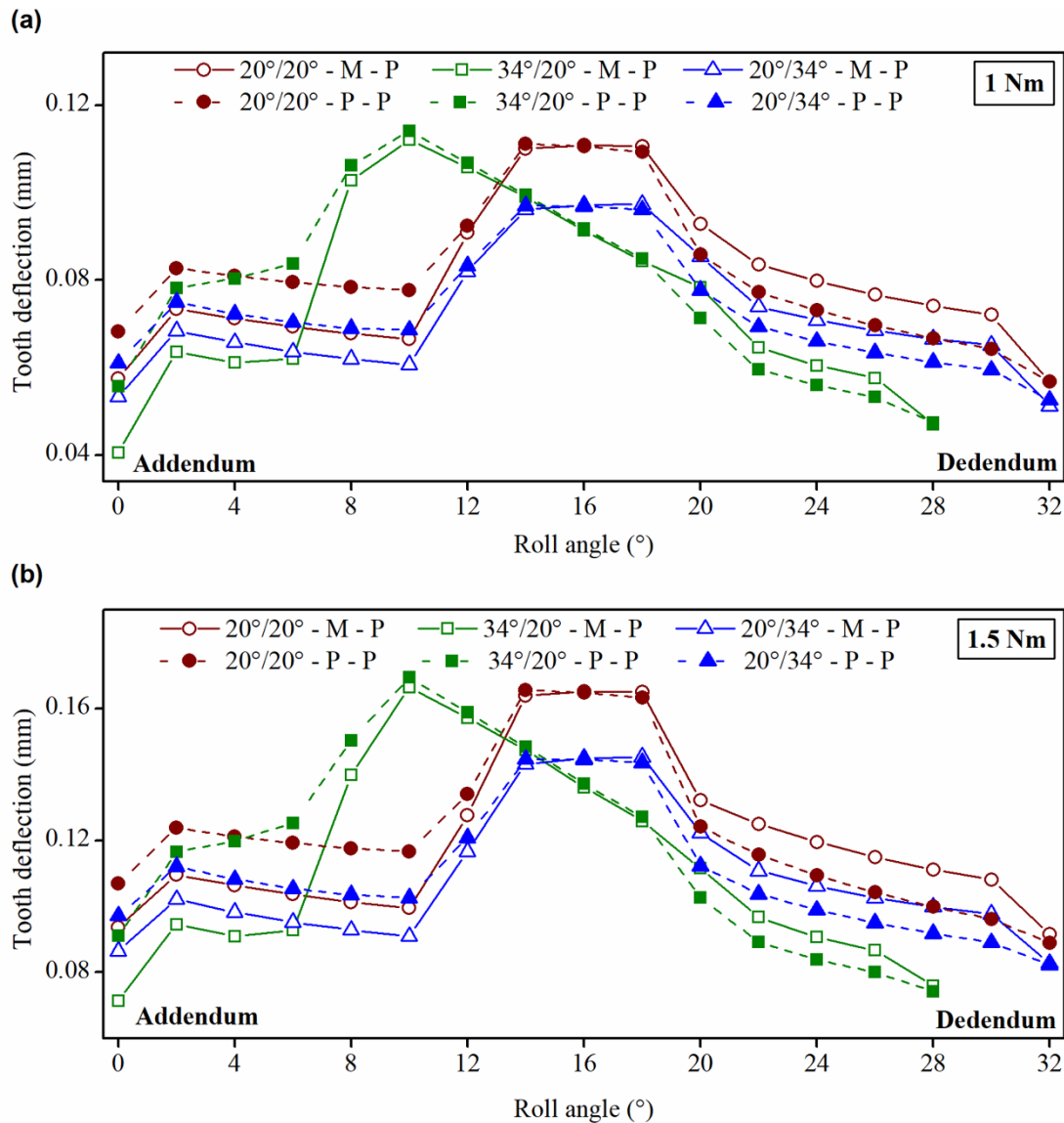


Fig. 6.6 Tooth deflection variation in a mesh cycle for: (a) 1 Nm and (b) 1.5 Nm.

The tooth deflections in metal - polymer pairs of 20°/20° and 20°/34° configurations were dissimilar in DTC zones, with deflections in the dedendum greater than the deflections in the addendum. This was a result of the unsymmetrical load sharing pattern observed in the metal - polymer pairs. However, despite the unsymmetrical load sharing pattern, the tooth deflections in DTC zones for the 34°/20° configuration were similar. The trend reversed in polymer - polymer pairs of 34°/20° configuration, as the tooth deflection in the dedendum DTC zone was significantly lesser than the tooth deflection in the addendum DTC zone. For 20°/20° and 20°/34° configurations, the tooth deflection decreased steadily in both DTC zones, and no disproportionate difference was observed between the tooth deflections in addendum and dedendum DTC zones. The symmetrical LSR pattern in polymer - polymer pairs was the cause behind the uniform variation in tooth deflections. But, the tooth deflection pattern for the

34°/20° configuration was unsymmetrical despite the symmetrical LSR pattern implying that the effect of polymer mating gear is different for gears with higher drive side pressure angle.

In polymer - polymer pairs of 34°/20° configuration, tooth deflection in the addendum DTC zone was greater than that of 20°/34° configuration (4% – 19%) but lesser than that of 20°/20° configuration (1% – 6%). The increase in LSR for the 34°/20° configuration was greater compared to other configurations in the addendum DTC zone leading to increased tooth deflection. In other regions, the trends observed were similar to the metal - polymer pairs, with tooth deflection lesser than that of 20°/20° and 20°/34° configurations in dedendum. The mismatch between the tooth deflection pattern in configurations with 20° pressure angle and configuration with 34° pressure angle affected the relationship between the mesh deflection for the 34°/20° configuration with respect to the other configurations.

The mesh deflection in the polymer - polymer pair of each configuration was greater than the mesh deflection of the corresponding metal - polymer pair at every position in the cycle. The range of deviations for the 20°/20°, 34°/20°, and 20°/34° configurations were 43% – 67%, 18% – 76%, and 43% – 64%, respectively. However, the relationship between tooth deflections of metal - polymer and polymer - polymer pairs of each configuration differed in addendum and dedendum. In each configuration, tooth deflection of the polymer - polymer pair was higher than that of the metal - polymer pair in the addendum region. In contrast, tooth deflection of the metal - polymer pair was higher in the dedendum region. This variation was a consequence of the unsymmetrical tooth deflection pattern in metal - polymer pairs of 20°/20° and 20°/34° configurations and polymer - polymer pairs of 34°/20° configuration.

The variance between mesh deflections of metal - polymer and polymer - polymer pairs in the addendum and dedendum DTC zones is affected by the differences between tooth deflections of metal - polymer and polymer - polymer pairs in the corresponding regions. As stated earlier, the mesh deflection in DTC zones of metal - polymer pairs was lowest for the 34°/20° configuration. But, among polymer - polymer pairs, the mesh deflection for the 34°/20° configuration was the highest in DTC zones. This divergence could be explained by the difference between the tooth deflections of metal - polymer and polymer - polymer pairs in addendum and dedendum DTC zones. Since mesh compliance at any position is the sum of compliances of meshing teeth at that position, the mesh deflection of a configuration in the DTC zone depends on the tooth deflections in addendum and dedendum regions.

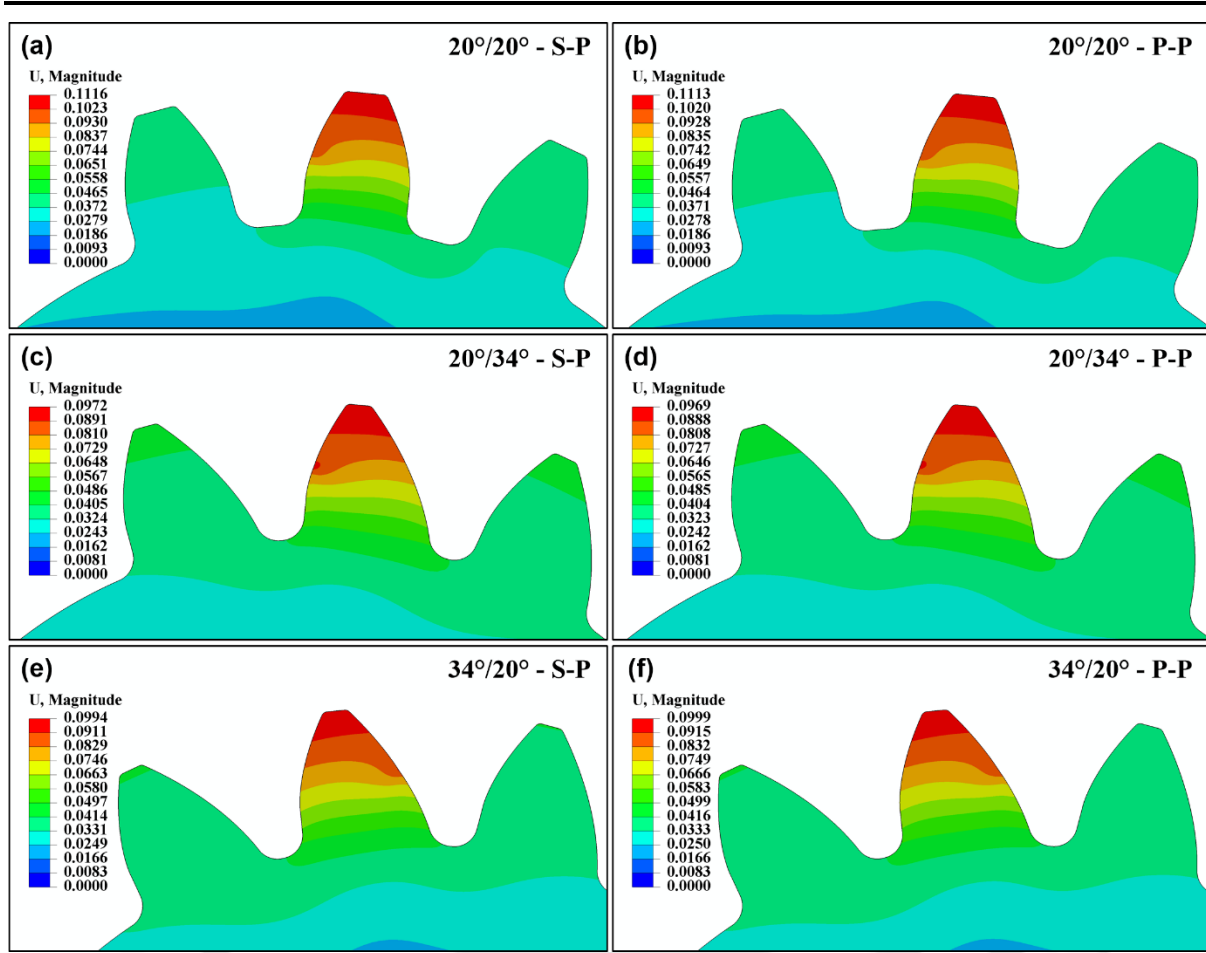


Fig. 6.7 Tooth deflection variation in driven gear subjected to 1 Nm at the pitch point: (a, b) 20°/20°, (c, d) 20°/34°, and (e, f) 34°/20° configuration.

In the addendum DTC zone, the tooth deflections in polymer - polymer pairs for the 20°/20°, 20°/34°, and 34°/20° configurations were greater than that of metal - polymer pairs by 15%, 11.5%, and 32%, respectively. On the other hand, in the dedendum DTC zone, the tooth deflections in polymer - polymer pairs of 20°/20°, 20°/34°, and 34°/20° configurations were lesser than that of metal - polymer pairs by 9%, 7.4%, and 7.5%, respectively. The decrease in tooth deflections in the dedendum DTC zone was similar for each configuration. But, the increase in tooth deflection in the addendum DTC zone was significantly higher for the 34°/20° configuration when compared to the 20°/20° and 20°/34° configurations. As a result, in polymer - polymer pairs, the mesh deflection for the 34°/20° configuration surpassed the mesh deflections of 20°/20° and 20°/34° configurations in the DTC zone.

6.4 Magnitude of mesh deflection

6.4.1 Peak mesh deflection in a cycle

The peak mesh deflection in a cycle corresponded to contact at HPSTC of the driven gear for symmetric and asymmetric configurations. Figure 6.8 shows the peak mesh deflection values of symmetric and asymmetric configurations. The position of HPSTC was 10° for $34^\circ/20^\circ$ configuration, and 14° for $20^\circ/20^\circ$ and $20^\circ/34^\circ$ configurations. Among the configurations, the peak mesh deflection in a cycle was highest for the $34^\circ/20^\circ$ configuration and lowest for the $20^\circ/34^\circ$ configuration. The peak deflection was highest in the asymmetric $34^\circ/20^\circ$ configuration despite the higher tooth thickness in the dedendum region. The higher drive side pressure angle prolonged the period of STC, increasing the bending moment arm. Conversely, the peak deflection in the $20^\circ/34^\circ$ configuration was the lowest, owing to the higher stiffness of asymmetric tooth form and an STC zone similar to symmetric gear.

As the load increased to 1.5 Nm, the peak mesh deflection of each configuration increased by an average of 47%. The peak values of polymer - polymer pairs were higher than that of metal - polymer pairs by 45% for $20^\circ/20^\circ$ and $20^\circ/34^\circ$ configurations, and 37% for the $34^\circ/20^\circ$ configuration. Since the difference between peak values of metal - polymer and polymer - polymer pairs (45%) was similar for $20^\circ/20^\circ$ and $20^\circ/34^\circ$ configurations, the difference between their peak mesh was 8% for both metal - polymer and polymer - polymer pairs. However, for the $34^\circ/20^\circ$ configuration, the variation between peak values of metal - polymer and polymer - polymer pairs was lesser (37%) than that for the $20^\circ/20^\circ$ and $20^\circ/34^\circ$ configurations.

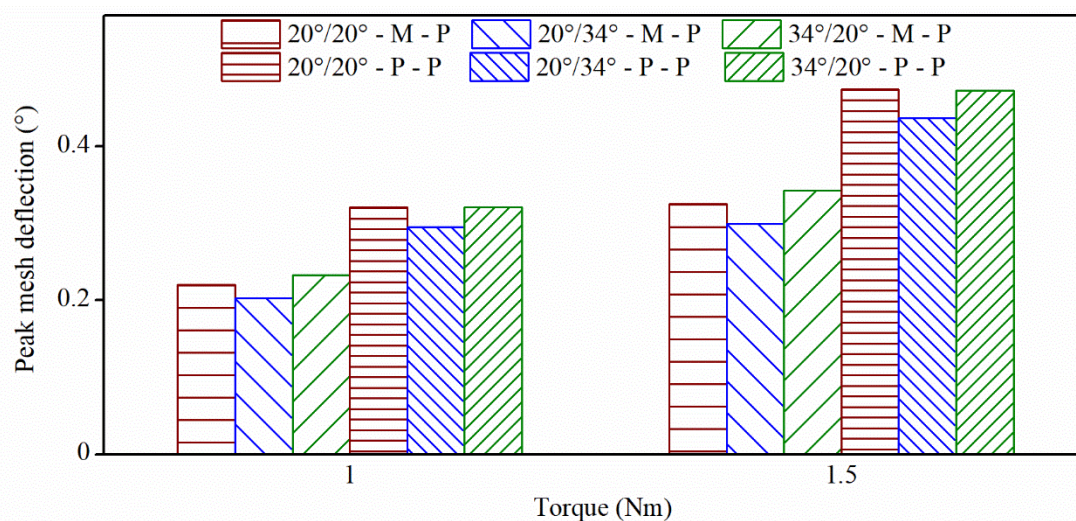


Fig. 6.8 Peak mesh deflection values of metal - polymer and polymer - polymer gear pairs.

This lower variation decreased the deviation between the peak mesh deflection of $34^\circ/20^\circ$ and peak mesh deflections of the other two configurations in polymer - polymer pairs. The deviation between peak values for $34^\circ/20^\circ$ and $20^\circ/34^\circ$ configurations was around 12% in metal - polymer pairs, whereas the difference was only 8% in polymer - polymer pairs. Similarly, the deviation between the peak values for the $34^\circ/20^\circ$ and $20^\circ/20^\circ$ configurations was reduced to less than 0.3% in polymer - polymer pairs, even though the deviation was 5% for metal - polymer pairs. In the study by Meuleman *et al.* (2007), mesh deflection of acetal - acetal pair was greater than that of steel - acetal pair.

6.4.2 Amplitude of mesh deflection in a cycle

The amplitude of mesh deflection represents the deviation between the peak and minimum mesh deflections in a cycle. Analyzing the peak-to-valley amplitude of a configuration is necessary to evaluate the extent of mesh stiffness variation in a cycle. Figure 6.9 represents the mesh deflection amplitude of each test configuration. The increase in load to 1.5 Nm increased the amplitude of each configuration by 45%. The amplitude was lowest for the $20^\circ/34^\circ$ configuration in metal - polymer and polymer - polymer pairs. This was anticipated as peak and minimum mesh deflection values for the $20^\circ/34^\circ$ configuration were the lowest. The highest amplitude was observed for the $34^\circ/20^\circ$ configuration among metal - polymer pairs. This could be attributed to the peak deflection, which was higher as compared to the other configurations. On the other hand, the $20^\circ/20^\circ$ configuration exhibited the highest amplitude among polymer - polymer pairs.

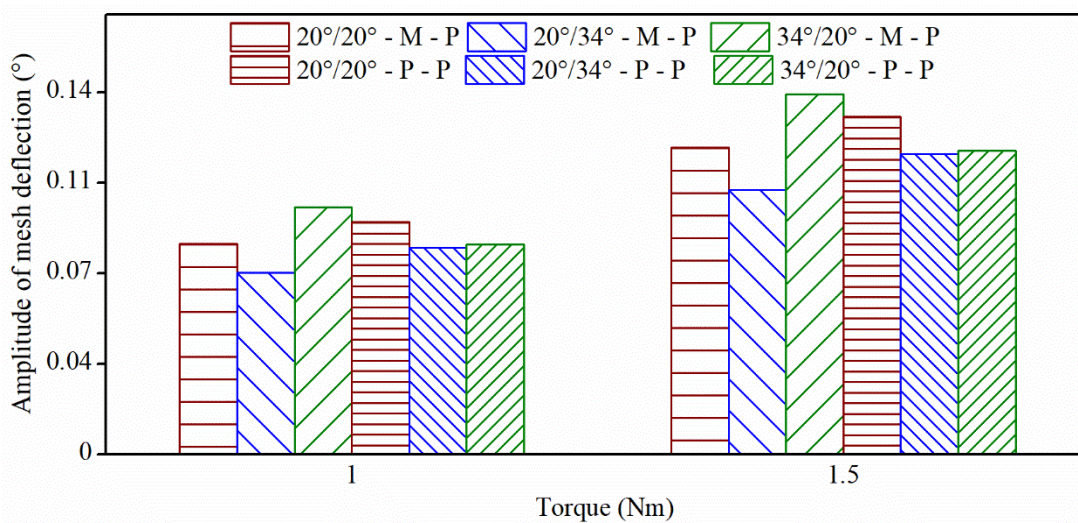


Fig. 6.9 Mesh deflection amplitude of symmetric and asymmetric configurations.

For the 20°/20° and 20°/34° configurations, the amplitude of polymer - polymer pairs was higher than that of metal - polymer pairs by 10% and 14%, respectively. But, in the polymer - polymer pair of 34°/20° configuration, the amplitude decreased by 15%. The minimum mesh deflection value increased to a greater extent for the 34°/20° configuration (74%) as compared to the 20°/20° (66%) and 20°/34° (62%) configurations in the polymer - polymer pair. Moreover, the increase in peak mesh deflection value for the 34°/20° configuration (37%) was lower compared to 20°/20° (45%) and 20°/34° (45%) configurations. Thus, for the polymer - polymer pair of 34°/20° configuration, the highest increase in the minimum mesh deflection and the lowest increase in the peak mesh deflection caused amplitude reduction.

6.5 Magnitude of tooth deflection in driven gears

6.5.1 Peak tooth deflection

The maximum tooth deflection for the 34°/20° configuration occurred for contact at the HPSTC (10°) in metal - polymer as well as the polymer - polymer pairs. In polymer - polymer pairs of 20°/20° and 20°/34° configurations, the peak tooth deflection corresponds to contact at the HPSTC (14°). In the metal - polymer pair of 20°/20° configuration, contact at pitch point (16°) resulted in maximum tooth deflection. In the metal - polymer pair of 20°/34° configuration, peak deflection was at the lowest point of single tooth contact (18°). The peak tooth deflection values of configurations are compared in Figure 6.10.

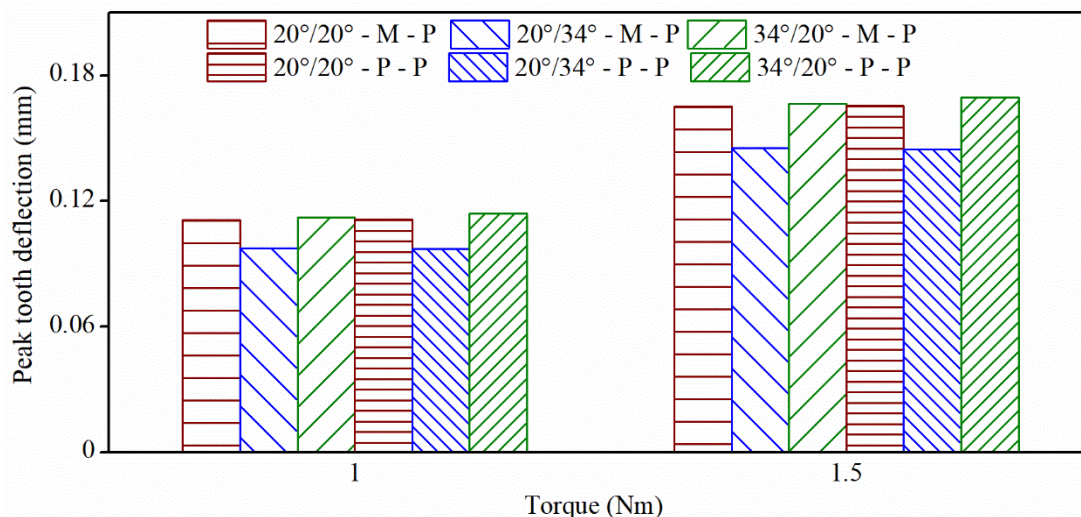


Fig. 6.10 Maximum tooth deflection values of symmetric and asymmetric configurations.

The maximum tooth deflection in a cycle was highest for the 34°/20° configuration and lowest for the 20°/34° configuration in metal - polymer and polymer - polymer pairs. The peak

deflection for the 34°/20° configuration was greater than the peak deflection for the 20°/34° configuration by 15% in metal - polymer pairs and 17% in polymer - polymer pairs. The peak deflection in polymer - polymer pairs was higher than that of the metal - polymer pair, except for the 20°/34° configuration. However, the difference between the peak deflections of metal - polymer and polymer - polymer pairs was insignificant. For the 20°/20° and 20°/34° configurations, the variation was less than 0.3%. For the 34°/20° configuration, the difference was 1.8%. The increase in load to 1.5 Nm increased the peak deflection by 48% in each configuration.

6.5.2 Amplitude of tooth deflection in a cycle

The peak-to-valley amplitude of tooth deflection (Figure 6.11) was analyzed to study the individual tooth stiffness variation in a cycle. The amplitude was highest for the 34°/20° configuration and lowest for the 20°/34° configuration. In metal - polymer pairs, the difference between the amplitudes of 34°/20° and 20°/34° configurations for 1 and 1.5 Nm were 55% and 52%, respectively. In polymer - polymer pairs, the difference was 50% for 1 Nm and 53% for 1.5 Nm. In each configuration, the amplitude of tooth deflection increased as the load was increased to 1.5 Nm. The increase in amplitude was 35% in metal - polymer pairs and 41% in polymer - polymer pairs.

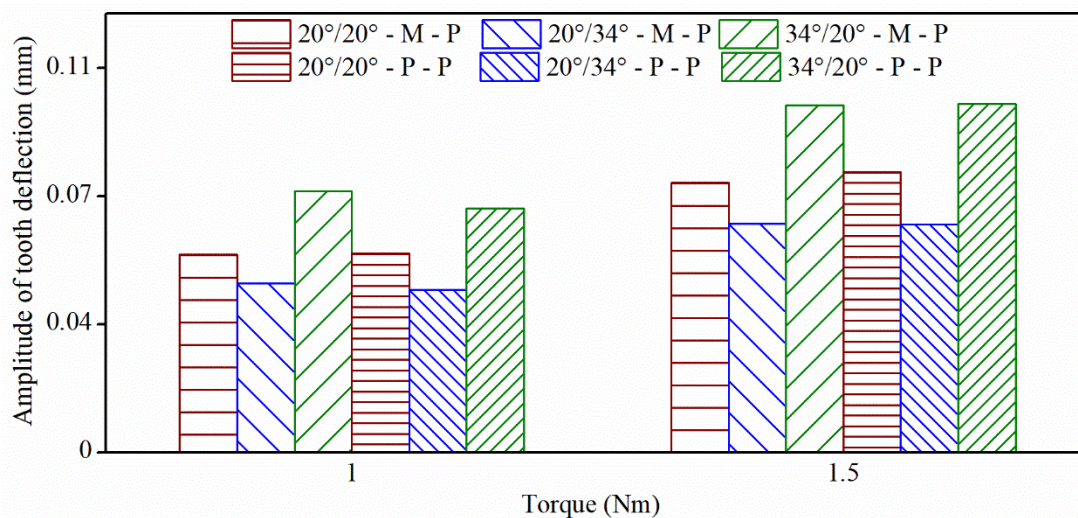


Fig. 6.11 Amplitude of tooth deflection in symmetric and asymmetric gears.

For the 20°/20° configuration, the increase in the amplitude of the polymer - polymer pair compared to the metal - polymer pair was 0.6% and 4.2% for 1 and 1.5 Nm, respectively. For the 20°/34° configuration, the amplitude of the polymer - polymer pair decreased by 3.8% and 0.4% for 1 and 1.5 Nm, respectively. For the 34°/20° configuration, the amplitude of the

polymer - polymer pair was lesser by 6.8% for 1 Nm but slightly greater (0.2%) for 1.5 Nm. Among the metal-polymer and polymer - polymer pairs of all configurations, the tooth deflection amplitude was lowest in the polymer - polymer pair of the 20°/34° configuration.

6.6 Path of contact

The path of contact is traced by the locus of contact points in a mesh cycle. The theoretical path of contact lies along the line of action, encompassed within addendum radii of the driver and driven gears (Figure 6.12). Due to excessive tooth deflection, the actual path of contact in polymer gears may deviate from the theoretical line. The simulated contact paths for the symmetric and asymmetric gears are shown in Figure 6.13. In this study, the actual contact path deviated significantly from the theoretical path at the peripheries of the cycle in each configuration, implying that premature and extended contacts occurred. As mentioned earlier, the presence of handover zones signified the existence of premature and extended contacts, which was further confirmed by the deviations in the path of contact. The deviated path extended along the addendum circles at the peripheries of the cycle. The deviation of the contact path along the addendum circles indicates that contact occurs in the involute portion of the tooth profile (Karimpour, Dearn and Walton, 2010).

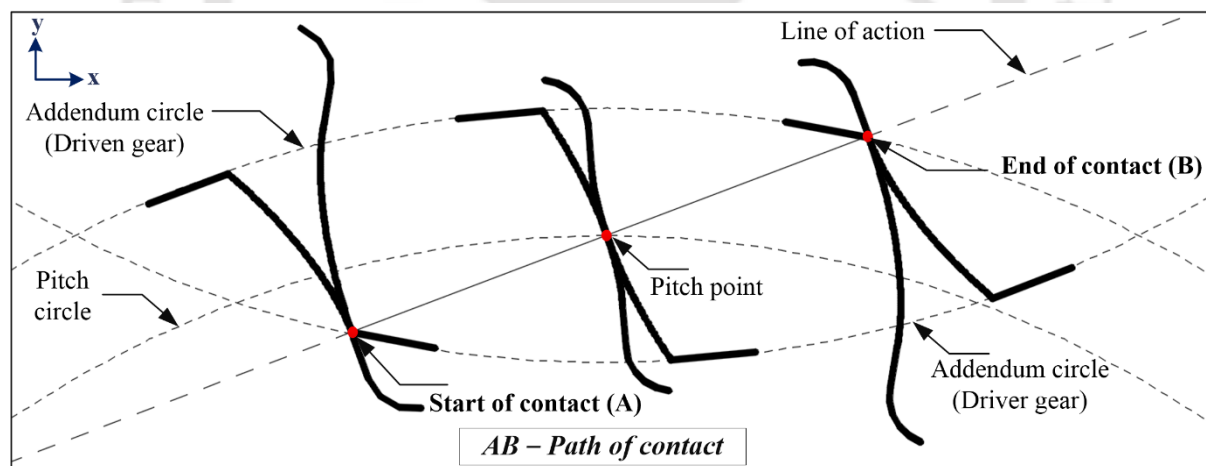


Fig. 6.12 Theoretical path of contact.

In other regions of the path, the deviation with respect to the theoretical path was within 0.5%. The lower deviation suggests that the kinematic behavior was appropriate for the loads applied. At the peripheries, the deviations were within 4%. Among the configurations, the deviations from the theoretical path were higher for the 34°/20° configuration (2.6% – 3.7%). The deviations in the extended contact zone (end of cycle) were higher than those in the premature contact region (start of cycle). The trend was identical in both similar and dissimilar material

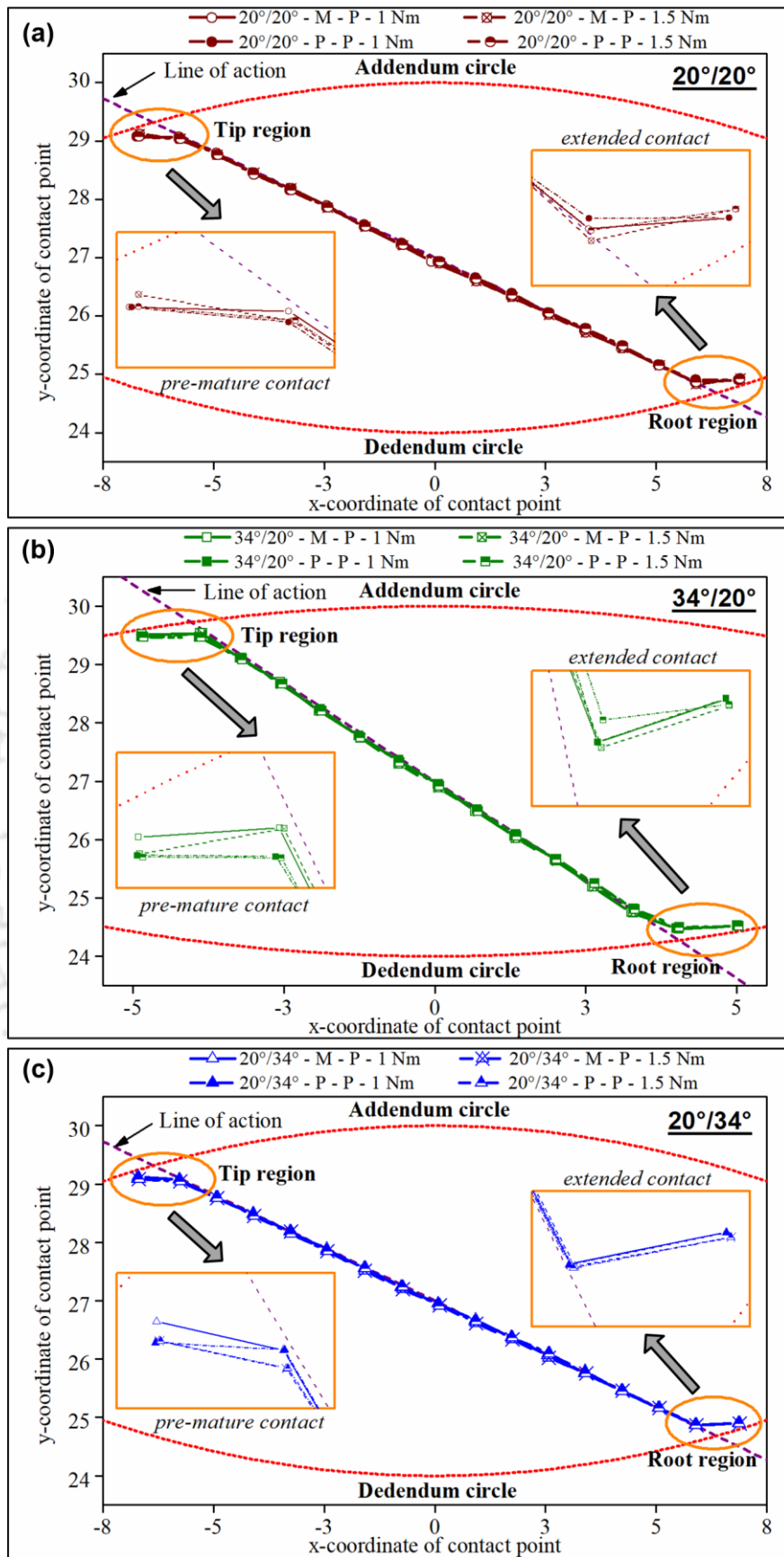


Fig. 6.13 Predicted contact path of metal - polymer and polymer - polymer gear pairs subjected to 1 and 1.5 Nm: (a) 20°/20°, (b) 34°/20°, and (c) 20°/34°.

pairs. The variations in the path of contact induced by the increase in load were minimal, as the applied torque was lesser in magnitude. Generally, an increase in load increases the contact path, characterized by an extended roll period. Karimpour, Dearn and Walton (2010) reported that the premature contact occurred in advance, and extended contact persisted for a longer period in acetal gears for higher applied torque values.

6.7 Comparison of experimental and simulation values

Figure 6.14 (a) and (b) indicates the mesh deflection values obtained from experiments. The mesh deflection trends obtained from experiments were similar to that predicted from the simulations. Similarly, the roll period and position of peak deflection were the same in experiments and simulations. In the experimental traces, the STC zones are distinguishable. However, the handover zones are not distinctly identifiable as they merged with the DTC zones. The viscoelastic material model grossly under-predicted the mesh deflection values, as experimentally determined values were substantially higher than the simulation values. Figure 6.15 indicates the specific error corresponding to each roll angle position in symmetric and asymmetric configurations.

In metal - polymer pairs of $20^\circ/20^\circ$, $34^\circ/20^\circ$, and $20^\circ/34^\circ$ configurations loaded at 1 Nm, the experimental values were greater than that of simulation values by 45% – 56%, 25% – 51%, and 43% – 55%, respectively. For the same load, in polymer - polymer pairs of $20^\circ/20^\circ$, $34^\circ/20^\circ$, and $20^\circ/34^\circ$ configurations, the experimental values were higher than that of simulation values by 47% – 63%, 52% – 56%, and 53% – 59%, respectively. As evident, the deviation between experimental and simulation values was higher for engagements with polymer driver gear. Similarly, the difference between simulation and experimental values increased as the load increased to 1.5 Nm. At 1.5 Nm, the deviations between experimental and simulation values of metal - polymer pairs of $20^\circ/20^\circ$, $34^\circ/20^\circ$, and $20^\circ/34^\circ$ configurations were 48% – 60%, 37% – 52%, and 47% – 58%, respectively. In polymer – polymer pairs of $20^\circ/20^\circ$, $34^\circ/20^\circ$, and $20^\circ/34^\circ$ configurations, the deviations were in the range of 55% – 65%, 54% – 61%, and 57% – 65%, respectively. Only a simple viscoelastic model was employed to predict the deflection, so an appreciable deviation between experimental and simulation values was observed. The following issues caused the variation between simulation and experimental values:

- Material behavior – The linear viscoelastic model calibrated using limited characterization tests was inadequate to predict the material behavior accurately. Hence, a custom-defined,

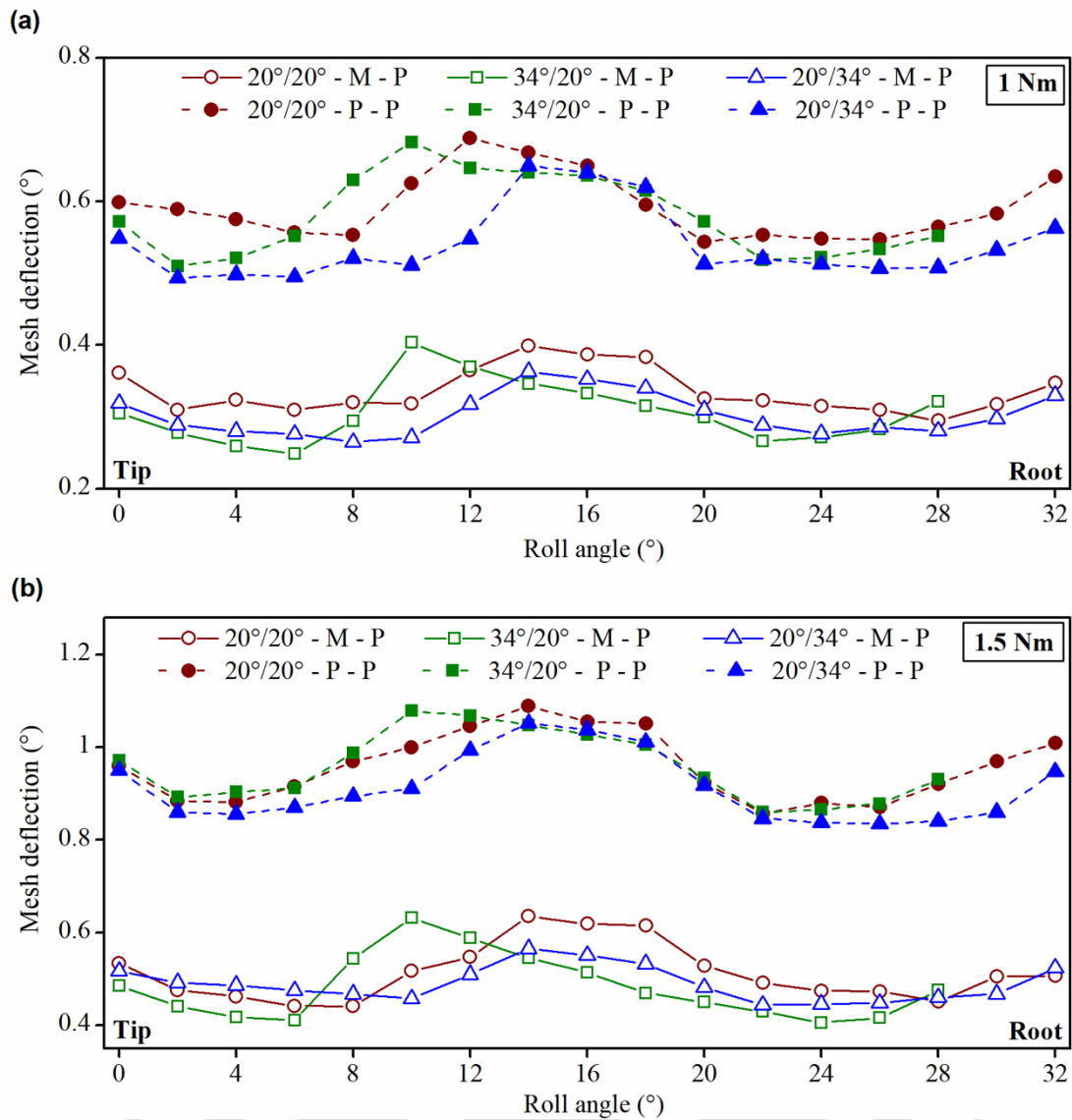


Fig. 6.14 Mesh deflection values determined from experiments: (a) 1 Nm and (b) 1.5 Nm.

non-linear constitutive model must be defined and calibrated using extensive material characterization tests for precise simulation of the material behavior.

- Geometric accuracy – The gear teeth in the FE model were geometrically perfect without any profile or lead errors. The accuracy of actual gear tooth geometry was inferior, which affects the contact pattern between meshing gear teeth.
- Backlash – The backlash between meshing teeth alters the contact position, affecting the magnitude of mesh deflection obtained in experiments. The backlash between meshing teeth was not incorporated in the FE model.
- Human error – The contact between teeth at each position was established manually by precisely rotating the driver gear to the required roll angle position. Although the roll

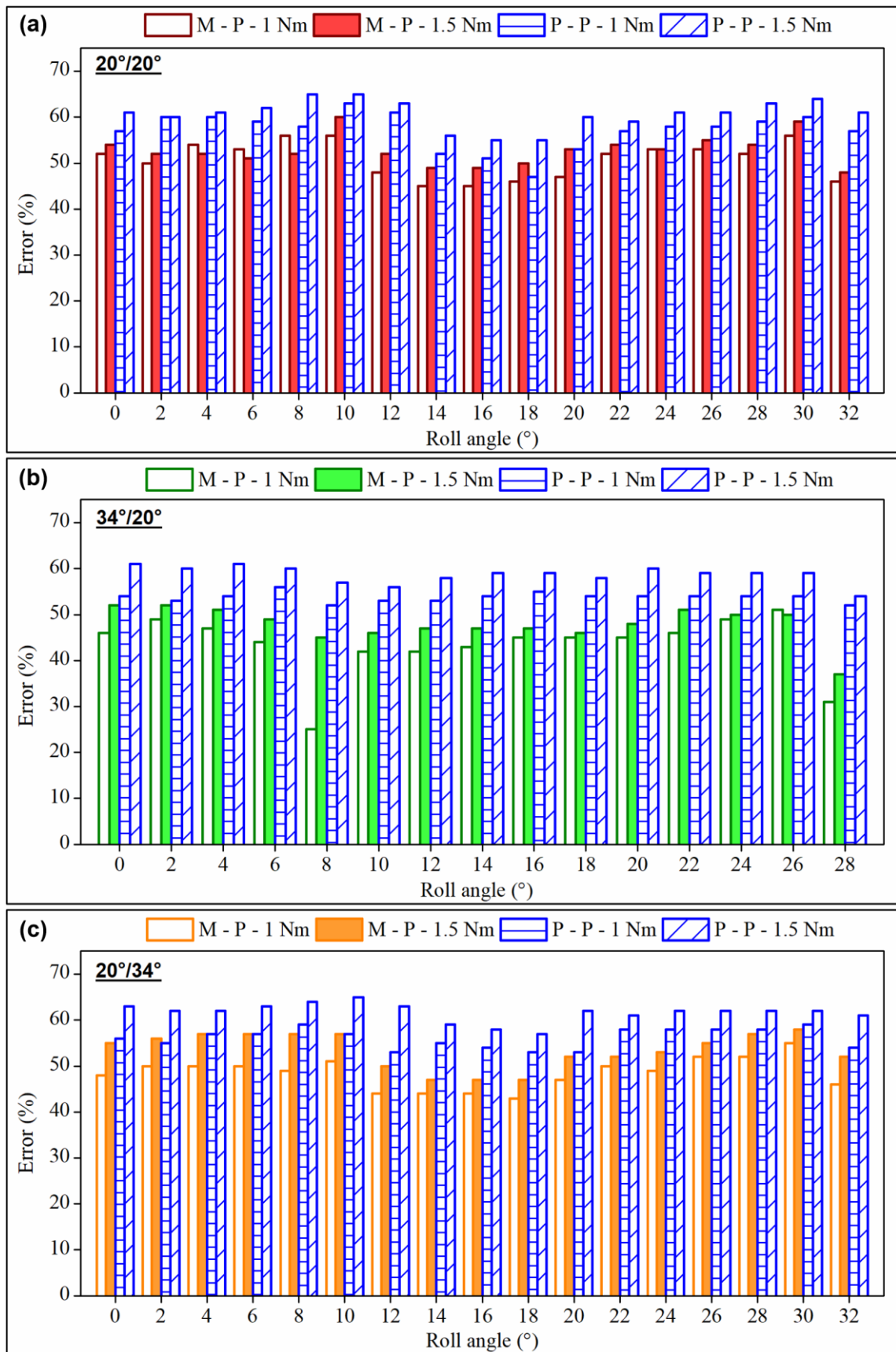


Fig. 6.15 Deviations between experimental and simulation values: (a) 20°/20°, (b) 34°/20°, and (c) 20°/34° configuration.

duration was monitored carefully using the potentiometer readings, the prevalence of human error is unavoidable in experiments.

In spite of the shortcomings, the similarity between experimental and numerical trends confirms the ability of the current FE model to predict the general mesh deflection characteristics. The measurement of mesh deflection using simple static experiments assists the designer in verifying of the utility of the proposed FE model immediately. In addition, experimental measurements provide an estimate of the actual range of deflection in a particular gear design. This simple experimental approach can be followed in the early stages of design. In advanced stages of design, a sophisticated FE model that incorporates the elements of actual experimental conditions must be employed to obtain accurate predictions.

6.8 Design implications

6.8.1 Tooth asymmetry

The peak mesh deflection for the symmetric gears was greater than that for the $20^\circ/34^\circ$ configuration by 8% (Table 6.1). However, the peak mesh deflection for the $34^\circ/20^\circ$ configuration exceeded that for the symmetric gears by 5% in metal - polymer pairs. In polymer - polymer pairs, mesh deflection for the symmetric gear was slightly higher (0.3%) than that for the $34^\circ/20^\circ$ configuration at 1.5 Nm. Similar to peak mesh deflection, mesh deflection amplitude for the symmetric gear was lesser than that for the $34^\circ/20^\circ$ configuration in metal - polymer pairs by 14%. However, in polymer - polymer pairs, the amplitude for the symmetric gear was higher by 10%. Compared to the $20^\circ/34^\circ$ configuration, amplitude for symmetric gear was higher by 16% and 12% in metal - polymer and polymer - polymer pairs, respectively.

The asymmetric tooth form confers greater tooth thickness in the dedendum region compared to the symmetric tooth. However, the influence of tooth asymmetry on the deflection behavior was not the same for $34^\circ/20^\circ$ and $20^\circ/34^\circ$ configurations. The relation between the stiffnesses of $34^\circ/20^\circ$ configuration and symmetric gear depends on the mating gear material and applied load. Conversely, the $20^\circ/34^\circ$ configuration exhibited lesser peak deflection and peak-to-valley amplitude compared to the symmetric gear for different material engagements and applied load. Hence, asymmetric tooth form with a lower drive side pressure angle ($20^\circ/34^\circ$) could be considered in place of symmetric tooth form.

Table 6.1 Mesh deflection parameters of symmetric and asymmetric configurations.

<i>Configuration</i> <i>Parameter</i>	Symmetric 20°/20°	Asymmetric 34°/20°	Asymmetric 20°/34°
Peak mesh deflection			
<u>Metal-Polymer pair</u>			
1 Nm	0.2205	0.2329	0.2027
1.5 Nm	0.3252	0.3423	0.2991
<u>Polymer-Polymer pair</u>			
1 Nm	0.3206	0.3207	0.2955
1.5 Nm	0.4743	0.4728	0.4367
Amplitude of mesh deflection			
<u>Metal-Polymer pair:</u>			
1 Nm	0.0814	0.0954	0.0701
1.5 Nm	0.1186	0.1391	0.1022
<u>Polymer-Polymer pair:</u>			
1 Nm	0.0897	0.0801	0.0799
1.5 Nm	0.1306	0.1173	0.1162

6.8.2 Mating gear material

The peak mesh deflection was lower in metal - polymer pairs, as the deflection of steel gear tooth was insignificant. Since the polymer gear tooth deflection dominated mesh deflection, the load sharing pattern was unsymmetrical in DTC zones. The polymer mating gear amplified the magnitude of peak mesh deflection. However, the load sharing pattern was symmetrical due to the considerable tooth deflection in the driver gear tooth.

The drive side pressure angle of a configuration determined the impact of polymer driver gear on specific parameters. The mesh deflection variation within DTC zones decreased in 20°/20° and 20°/34° configurations. In the configuration with a larger pressure angle on the loading flank (34°/20°), the mesh deflection variation within the DTC zone increased in polymer - polymer pairs. Similarly, the peak-to-valley amplitude of mesh deflection increased in polymer - polymer pairs of 20°/20° and 20°/34° configurations whereas, a decline in amplitude was observed in the 34°/20° configuration. The metal - polymer pairs exhibited higher mesh stiffness for the considered tooth configurations and applied load. As mesh stiffness of polymer - polymer pairs was lesser, tooth dimensions could be modified to minimize the deflection within the desired levels.

6.9 Summary

The mesh deflection of Nylon 66 spur gears was predicted by quasi-static simulations and measured experimentally using static deflection tests. The influence of tooth asymmetry and mating gear material was studied by evaluating metal - polymer and polymer - polymer engagements of asymmetric tooth configurations $34^\circ/20^\circ$ and $20^\circ/34^\circ$. The principal results from the study are given as follows:

- The peak mesh deflection for asymmetric configuration $20^\circ/34^\circ$ was found to be lesser than that for symmetric gear by 8% – 12%. The peak mesh deflection for the other asymmetric configuration $34^\circ/20^\circ$ was greater than that for symmetric gear by 0.3% – 5%.
- The load sharing in dissimilar material pairs was unsymmetrical, with the LSR in the dedendum region of driven gear significantly greater compared to the LSR in the addendum region. The load sharing pattern in polymer - polymer pairs was symmetrical as the compliances of the driver and driven gear teeth are similar.
- The peak mesh deflections for polymer-polymer pairs were greater than that for metal - polymer pairs. The mesh deflections for $20^\circ/20^\circ$ and $20^\circ/34^\circ$ configurations increased to a greater extent (45%) than the mesh deflection for the $34^\circ/20^\circ$ configuration (37%).
- The polymer driver gear increased the mesh deflection amplitude in configurations with a drive side pressure angle of 20° (10% – 14%) and decreased the mesh deflection amplitude in configuration with the drive side pressure angle 34° (15%).
- Although premature and extended contacts occurred in symmetric and asymmetric configurations, the periods of STC and DTC in each configuration remained the same for 1 and 1.5 Nm.

This study indicates that the asymmetric tooth form generally decreases the tooth deflection and increases the mesh stiffness, which can reduce the deflection component of the transmission error. The use of materials with similar stiffness increases the mesh deflection but balances the mesh stiffness in the addendum and dedendum regions. This chapter concludes the discussion on the performance of asymmetric polymer gears. The following chapters (Chapters 7 and 8) discuss the bending fatigue performance of polymer gears built using the selective laser sintering process.



Chapter 7

Bending fatigue performance of selective laser sintered polymer gears built in ‘flat’ configuration

Additive manufacturing processes such as selective laser sintering are witnessing greater attention from designers owing to the design freedom and economical manufacturing in lesser volumes. This chapter describes the bending fatigue behavior of selective laser sintered Nylon 12 gears built in a ‘flat’ configuration. The material processing in layered manufacturing processes differs from injection molding, which is the incumbent method for polymer gear fabrication. This has significant consequences for material properties and component performance.

The first section discusses the single tooth bending fatigue strength of selective laser sintered Nylon 12 gears built in a ‘flat’ configuration and injection-molded Nylon 66 gears. The influence of the manufacturing process on the heat generated during the testing phase has been examined in the second section. In general, the bending fatigue strength of gears may vary with respect to the duration of loading. Accordingly, the bending fatigue strength and thermal behavior of the selective laser sintered gears under low cycle fatigue and high cycle fatigue conditions have been discussed. The final section describes the post-failure investigation conducted to study the effect of layered manufacturing on the failure modes of gears. In this chapter, the term ‘SLS gears’ refers to the selective laser sintered gears built in ‘flat’ configuration.

7.1 Bending fatigue life of selective laser sintered gears

The bending fatigue tests on SLS and IM gears were conducted without the adjacent teeth. The nominal bending stress in the root region was determined analytically using the expressions of ISO 6336-3 Method B (Eq. 3.2 – 3.7). The critical section parameters used in bending stress calculation – determined graphically using the 30° tangent method – have been described in

Chapter 4. Table 7.1 shows the critical section parameters and geometry factors used in the calculation. For the considered test loads, the nominal bending stress in the fillet was in the range of 57.29 – 90 MPa. The ‘run-out’ trials are marked by an arrow adjoining the datapoint. The tests were conducted at three stress levels. In summary, the experimental campaign comprised 24 tests (including both SLS and IM gears), entailing 461 hours of test duration. The Stress-life curves of SLS and IM gears were generated by plotting the bending fatigue life corresponding to the applied bending stress in a semi-logarithmic plot. Figure 7.1 depicts the S-N curves of the test gears.

Table 7.1 Critical section parameters and geometry factors of the test gear.

h_f	s_f	Y_F	Y_S
3.082	5.481	1.795	2.031

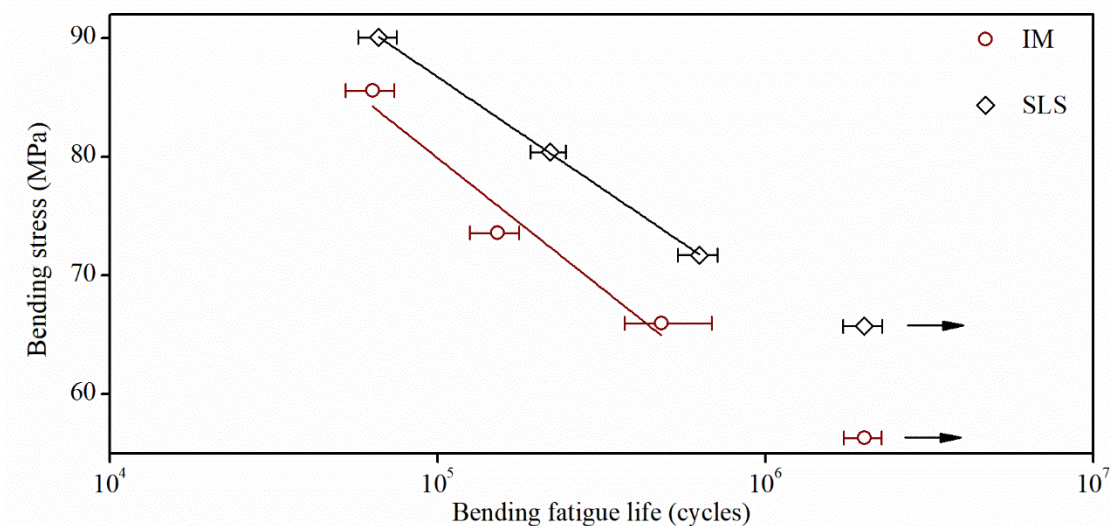


Fig. 7.1 Stress-life curves of injection-molded and selective laser sintered gears.

The SLS gears exhibited higher fatigue life than IM gears across the low cycle and high cycle fatigue regimes. However, the trendlines were not parallel and displayed a tendency to converge in the low cycle fatigue region, corresponding to the higher end of the applied load spectrum. This convergence of trendlines indicates the degradation of the SLS gears' fatigue properties at higher stress levels, which resulted in the decline of fatigue performance. The minimum stress endured by the test gears during run-out trials was 57 MPa. During the run-out trials, the SLS gear sustained 15% higher stress compared to the IM gear. The current study differs from Zhang, Pursell, *et al.* (2020) in the additive manufacturing process (SLS and FDM) and testing mode (bending fatigue test and dynamic test). However, the relative fatigue

performance of AM and IM gears observed in this work was similar to that of Zhang, Pursell, *et al.* (2020). The fatigue performance of AM gears with respect to IM gears in the LCF regime deteriorated in both studies. Van Hooreweder *et al.* (2013) reported that SLS and IM specimens subjected to tension-compression fatigue loading demonstrated similar fatigue strength without any significant difference. Thus, the variable fatigue behavior observed during the component level study was absent in studies investigating fatigue performance at the specimen level.

The monotonic properties of the material influence the fatigue strength of a component. Studies conducted to compare the responses of SLS and IM specimens to monotonic loading indicated that the tensile and flexural properties of SLS specimens were superior to that of IM specimens. Athreya, Kalaitzidou and Das (2011) reported that the flexural and tensile modulus of Nylon 12 SLS specimens were higher than IM specimens by 25% and 35%, respectively. Similar behavior was observed in the study by Van Hooreweder *et al.* (2013), wherein the Nylon 12 SLS specimens exhibited better tensile modulus than IM specimens. Zhu *et al.* (2015) compared the tensile performance of IM and SLS PP and noticed that the tensile strength and modulus of SLS specimens were better than the IM specimens. Dupin *et al.* (2012) noted that the flexural modulus of Nylon specimens prepared by SLS was higher than the specimens fabricated by IM. Hence, the enhanced bending fatigue performance of the SLS gears observed in this study could be ascribed to the superior tensile and bending strengths conferred by the SLS process.

During service, the mechanical properties of gears undergo variation owing to the influence of operational and environmental factors. The gear operating temperature is one such variable that crucially influences the operating performance and fatigue life. However, the effect of operating temperature on the relative performance of FDM and IM gears was not discussed. Hence, in this study, the thermal responses of IM and SLS gears were compared to determine the effect of temperature on fatigue life.

7.2 Thermal behavior of gears during testing

The bending fatigue life of gears is dependent on the maximum bending stress at the root region, which causes crack initiation and propagation, leading to tooth fracture. However, in the case of polymer gears, in addition to mechanical stress, the gear temperature during operation prominently influences the gear strength and, consequently, the gear life. In bending fatigue tests, heat generated by hysteresis significantly reduces the gear strength (Kodeeswaran *et al.*, 2019). Figure 7.2 shows the average surface temperature of SLS and IM gears at various

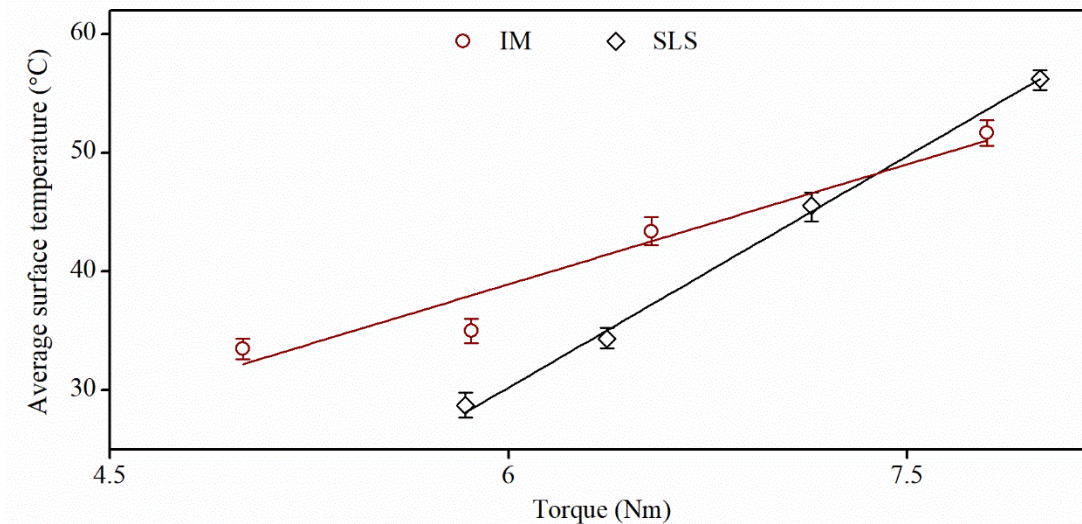


Fig. 7.2 Average surface temperature of the test gears at various loads.

test loads. Infrared thermal images of the test gear teeth during testing at torques of 6 and 8 Nm are shown in Figure 7.3. In the high cycle fatigue regime, SLS gears experienced lower temperatures compared to IM gears. The lower temperatures of SLS gears can be attributed to the brittleness, which moderated the material deformation and diminished the hysteresis heat generation. The lack of ductility in SLS components has been reported in several works (Dupin *et al.*, 2012; Van Hooreweder *et al.*, 2013; Zhu *et al.*, 2015; Arai *et al.*, 2017). Monotonic tensile and flexural tests indicated that the elongation at break of SLS specimens was substantially lower than IM specimens.

The factor which induces brittleness is the higher degree of crystallinity of SLS parts compared to IM parts. This was substantiated by the findings of Dupin *et al.* (2012), wherein for Nylon 12 specimens, an increase in the elongation at break was observed with a reduction in the crystallinity. In that work, the crystallinity of SLS specimens ranged between 29 and 34%, whereas it was 26% for IM parts. The cooling rate of the SLS process is extremely low compared to the IM process, which increases the thermal mobility of molecules during the crystallization process, resulting in a higher fraction of crystalline structure and crystal size (Zhu *et al.*, 2015). The typical cooling duration of injection molded and selective laser sintered Nylon 12 specimens reported in the literature are 30 s and 12 h, respectively (Van Hooreweder *et al.*, 2013).

In this study, the test gears exhibited a variable thermal behavior similar to the fatigue behavior. The average surface temperature of the test gears increased linearly for an increase in the applied load. However, the rates of temperature rise of SLS and IM gears were unequal and

resulted in a convergence of trends at higher loads. The surface temperature differential between IM and SLS gears was greater at lower loads and decreased steadily as the applied load increased, culminating in an inversion of trends around 7.5 Nm. This precipitous increase in the temperature of SLS gears indicates the increased hysteresis heat generation at higher loads, which stems from the reduction of material strength. Thus, the variable fatigue behavior of the test gears is a consequence of the variable thermal behavior.

The superior fatigue life of SLS gears in the HCF regime was due to the lower surface temperature. On the other hand, the increase in temperature at higher loads reduced the strength of the SLS gears in the LCF regime. Figure 7.4 is a semi-log plot illustrating the evolution of the surface temperature of SLS and IM gears with respect to fatigue cycles at 6 and 8 Nm. The load-based behavior is visible, with IM and SLS gears exhibiting higher surface temperatures at 6 Nm and 8 Nm, respectively. The temperature profile consisted of an initial, linear increase in temperature followed by a plateau phase, where a quasi-isothermal condition was experienced. In instances of gear failure, the plateau phase was followed by a sharp rise in temperature until the failure of the tooth. However, in cases of non-failure, such as the SLS gear loaded at 6 Nm, the quasi-isothermal condition persisted till the end of the trial.

Based on the temperature profile of the gears subjected to loads of 6 and 8 Nm, it can be argued that, for load values where the surface temperature stabilizes during the plateau phase, the life of the gear increases substantially. Conversely, in load cases where the temperature continues to increase beyond the plateau phase, the thermal softening precipitates the failure of the gear tooth. Van Hooreweder *et al.* (2013) reported that the SLS and IM samples subjected to uniaxial cyclic fatigue failed due to thermomechanical effects. The surface temperature of the specimens increased linearly up to a temperature of 34 °C, followed by a sudden rise till failure. Also, when specimens were loaded at stress lesser than the endurance limit, a quasi-isothermal state ensued, resulting in higher fatigue life.

Thus, the SLS and IM gears subjected to fatigue undergo thermomechanical failure. Accordingly, the thermal behavior at different loads is a significant factor in determining the fatigue performance of SLS gears with respect to the IM gears. The next chapter offers further discussion on the thermal behavior of selective laser sintered gears. To understand the underlying cause behind the fatigue response, it is necessary to investigate the modes of failure as well. At the foremost, the role of the layered structure of SLS gears on the crack propagation must be assessed.

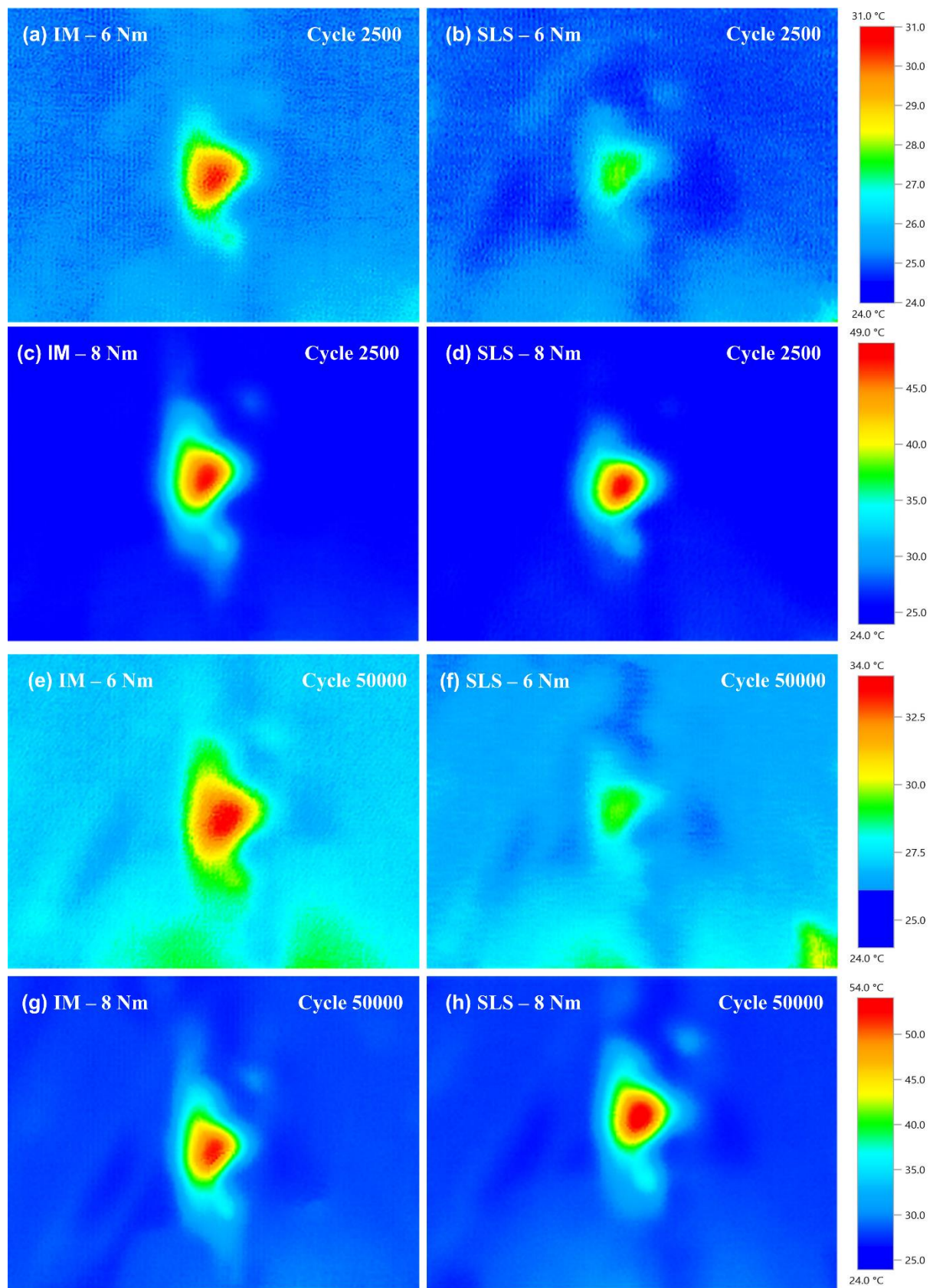


Fig. 7.3 IR thermal images of injection-molded (left) and selective laser sintered (right) gears subjected to 6 and 8 Nm: (a - d) 2500 cycle and (e - h) 50000 cycle.

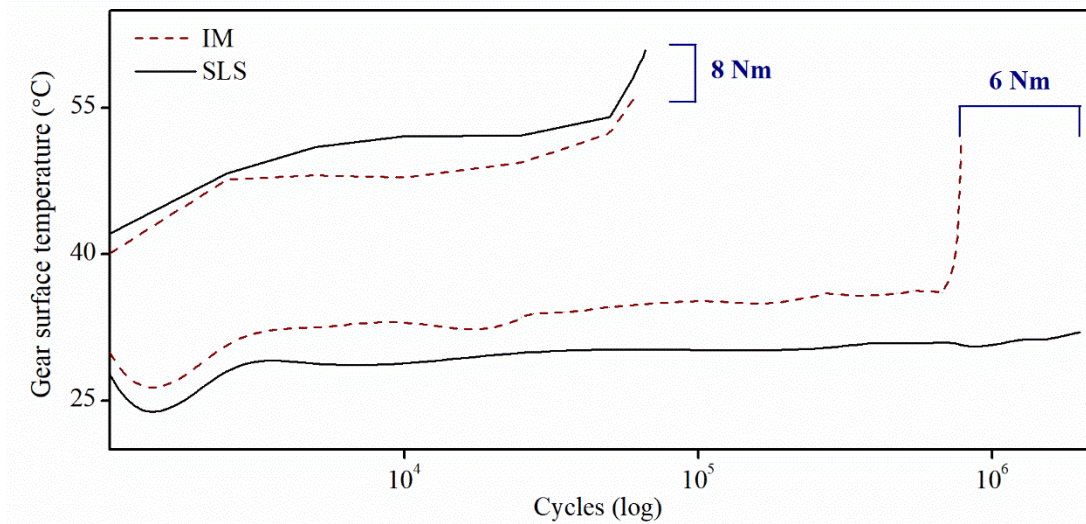


Fig. 7.4 Surface temperature evolution in selective laser sintered and injection-molded gears subjected to 6 and 8 Nm.

7.3 Investigation of failure mode

7.3.1 Crack propagation in additively manufactured parts

In additively manufactured parts, the multi-layered structure influences the crack propagation behavior significantly and determines the failure life of the component. The rate of crack propagation depends on the layer orientation, which in turn is determined by the build configuration. The crack propagation mode in AM parts can be classified into two: cross-laminar and inter-laminar propagation. The crack propagates across multiple layers during cross-laminar propagation, whereas in inter-laminar propagation, the crack propagates along the interface between consecutive layers. In certain instances, the mode of crack propagation is mixed, wherein both cross-laminar and inter-laminar propagation occurs for different extents of duration, depending on the layer orientation.

The resistance to crack propagation is determined by the energy required per unit volume of the material to extend the crack during loading. The fracture toughness is directly proportional to the energy absorbed by the material during propagation. Thus, greater energy absorption during loading retards the crack propagation rate, increasing the fatigue life. The cross-laminar mode of propagation absorbs a higher amount of energy resulting in slower crack propagation. On the other hand, in the inter-laminar mode, the layer interface zone acts as a preferential pathway and accelerates crack propagation (Hart and Wetzel, 2017). The inferior strength of the interface region could be attributed to the insufficient adhesion between the layers resulting from the presence of pores and residual particles (Leigh, 2012; Czelusniak and Amorim, 2020).

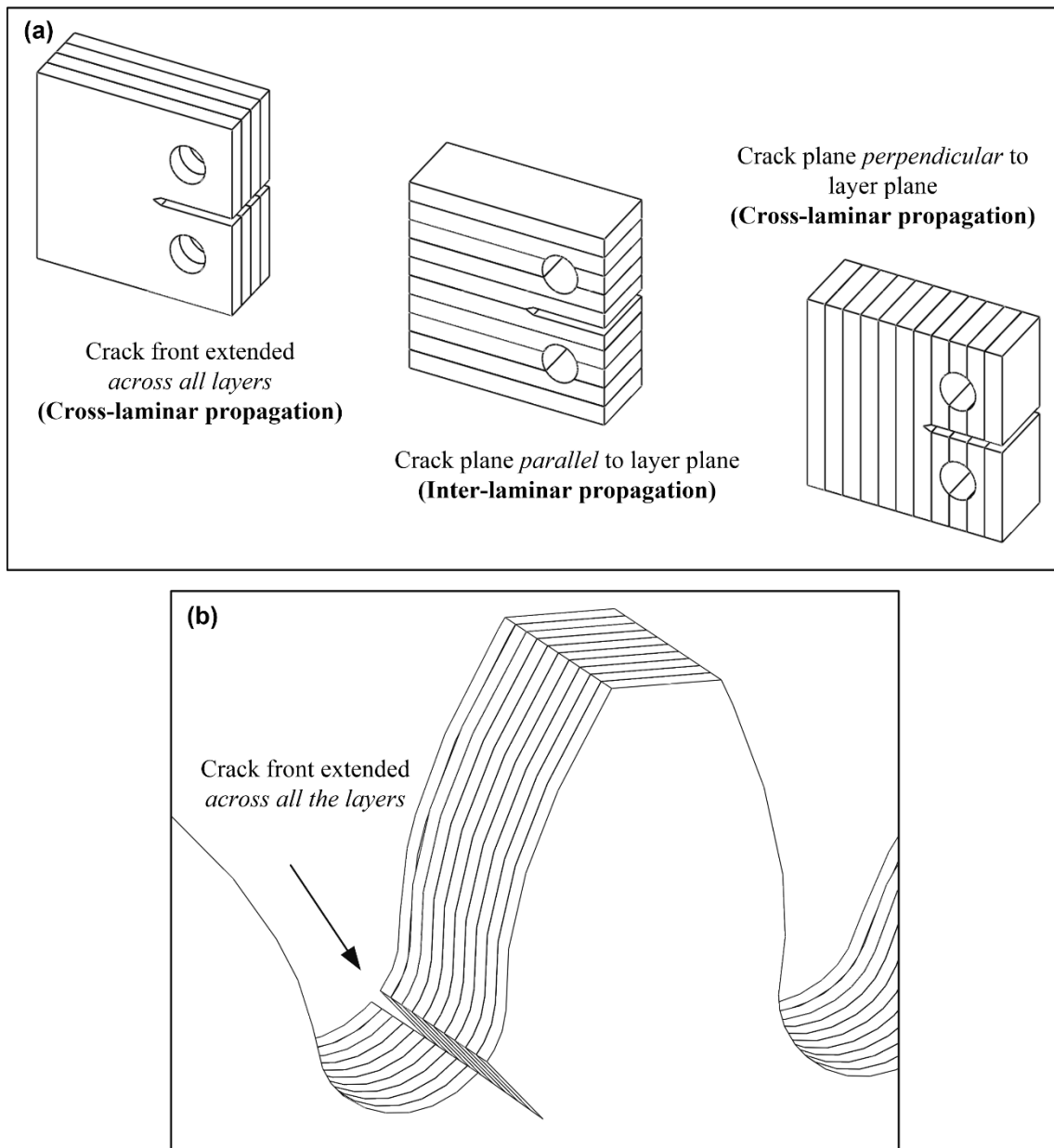


Fig. 7.5 (a) The three standard build configurations of additively manufactured compact tension specimens and (b) Bending fatigue crack in selective laser sintered gear built in ‘flat’ configuration.

Cano, Salazar and Rodríguez (2018) compared the fracture behavior of SLS Nylon 12 compact tension specimens built in two different orientations: layer orientation parallel to the loading direction (PARA) and the layer direction perpendicular to the loading direction (PERP). The peak load sustained by the specimen was higher for the PARA specimens in which the crack propagated perpendicular to the layer orientation. The cross-laminar crack propagation could be classified further into two types based on the location of the initial crack plane. In the first case, the crack initiates in a single layer and propagates across other layers in a sequential manner. In the second case, the crack plane is encompassed by all layers during initiation and

extends across all layers simultaneously. Brugo *et al.* (2016) evaluated the fracture toughness of SLS PA 2200 CT specimens built in three configurations. Among the specimens of the three different configurations, the resistance to crack propagation was higher for the specimen in which all the layers included a portion of the crack plane during initiation. Figure 7.5 (a) illustrates the three different types of the orientation of the crack plane with respect to the layers in additively manufactured CT specimens. Figure 7.5 (b) represents the orientation of the crack plane in the SLS 'flat' gears.

7.3.2 Failure morphology of selective laser sintered and injection-molded gears

The test gears failed by bending fatigue crack initiation and propagation. Figure 7.6 (a) and (b) shows the failed teeth of test gears loaded at 8 Nm as observed under a stereomicroscope. Figure 7.6 (c) and (d) depict the broad view of the failed teeth as observed under the FESEM. The magnified view of different locations in the crack is shown in Figure 7.6 (e) – (h). The difference between the surface evenness of IM and SLS gears was conspicuous in the FESEM images. The surface of IM gear was smooth and devoid of porosity. However, the surface of SLS gear was rugged and consisted of multiple voids. The presence of voids is inevitable in parts made of the SLS process owing to the absence of external pressure during the coalescence of powder particles. The material stock is melted and packed densely into the mold cavity by applying pressure during injection molding. However, the coalescence of powder particles in the selective laser sintering process is caused by the internal surface tension, which is insufficient to pack particles densely (Zhu *et al.*, 2015).

The location of the crack mouth was approximately identical for both the SLS as well as IM gears. The crack trajectory was virtually straight and perpendicular to the root fillet. In the SLS gears, the crack faces were separated distinctly due to the brittleness of the material. On the contrary, the ductile nature of the IM gears resulted in the closure of the crack faces. The nature of crack propagation was tortuous in SLS gears and smooth in IM gears (Figure 7.6 (c) and (d)). The higher fatigue life of SLS gears compared to the IM gears could be partly attributed to the higher resistance to crack propagation in SLS gears. Due to the 'flat' build configuration, the initial crack plane extended across all the layers along the face width. The crack propagated in cross-laminar mode, and the crack front traversed along all the layers simultaneously. This mode of propagation required a higher amount of energy to advance the crack front and resulted in higher fatigue life. However, the crack propagation was not impeded in the IM gears, resulting in a smoother crack path and lower fatigue life. The damage zone around the crack is

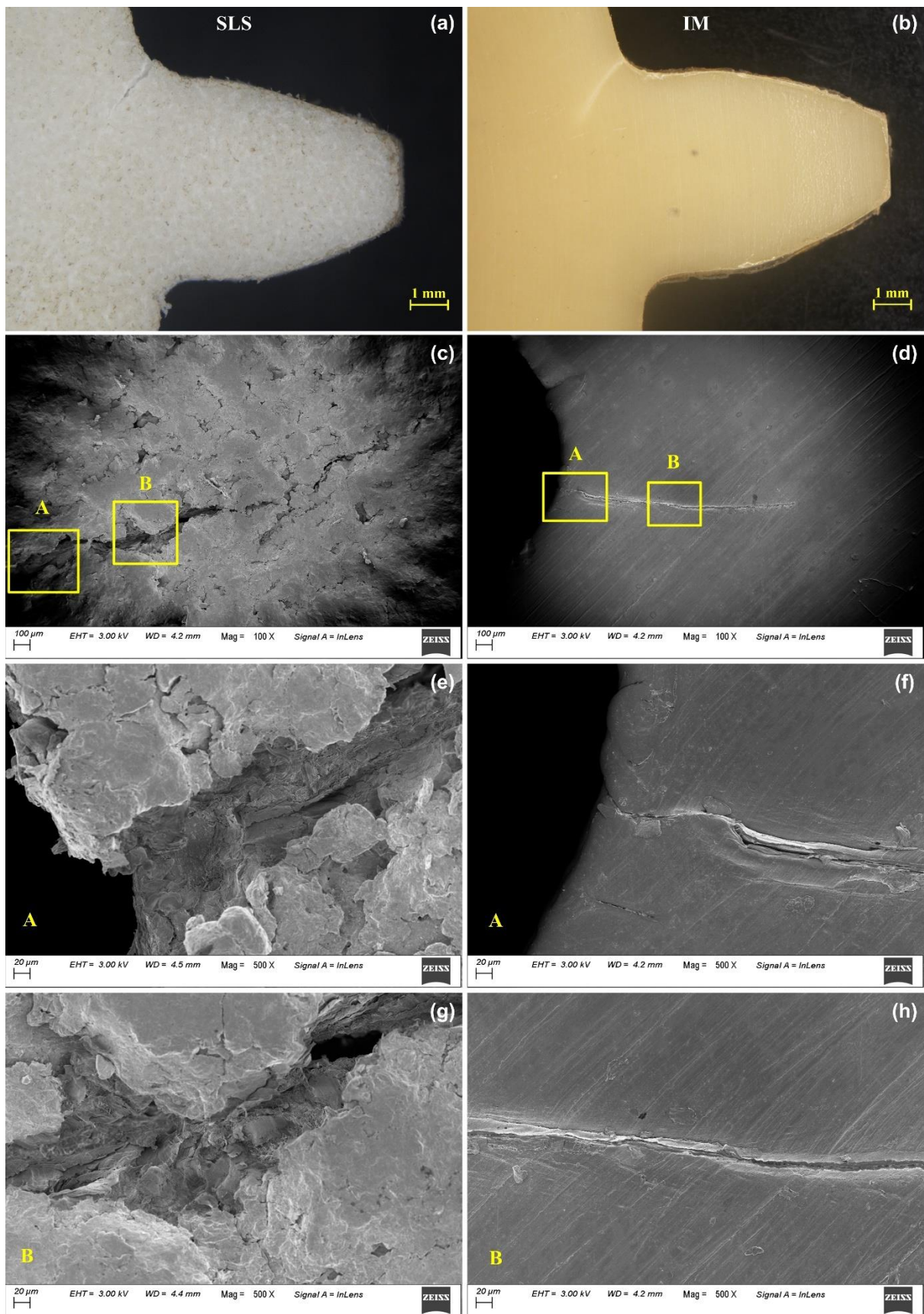


Fig. 7.6 Failure zone images of test gears loaded at 8 Nm: (a, c, e, g) selective laser sintered gear built in ‘flat’ configuration and (b, d, f, h) injection-molded gear.

another indicator of the energy consumed during the crack propagation. The extent of the damage zone was broader in SLS gears and narrow in IM gears. This corroborates the higher fatigue life of SLS gears compared to IM gears. Thus, the analysis of thermal behavior and failure morphology of SLS and IM gears reveals that the higher bending fatigue life exhibited by the SLS gears could be attributed to the gear operating temperature at that particular load and the general increase in resistance to crack propagation provided by the 'flat' build configuration.

7.4 Summary

In the present chapter, the bending fatigue performances of selective laser sintered Nylon 12 gears built in a 'flat' configuration and injection-molded Nylon 66 gears were evaluated experimentally. Single tooth bending fatigue tests were conducted in an in-house, custom-built test setup. The major findings of the study are as follows:

- The SLS gears exhibited superior bending fatigue performance compared to IM gears. The variation between the bending fatigue strengths of SLS and IM gears was different in LCF and HCF regimes.
- The different fatigue behavior of SLS gear in the LCF and HCF regimes was induced by the change in thermal behavior. The surface temperature of SLS gears was lower than IM gears in the HCF regime and higher than IM gears in the LCF regime.
- The multi-layered structure of SLS gears caused a tortuous crack path. The crack path in IM gears was smooth as the material structure was homogeneous.
- The 'flat' build configuration of SLS gears augmented the resistance to crack propagation as the cross-laminar crack propagation increased the energy required to advance the crack.

This investigation demonstrates that the selective laser sintered gears built in a 'flat' configuration could sustain a greater number of bending fatigue cycles compared to injection molded gears. This study also highlights the advantages offered by layered manufacturing in terms of the enhanced resistance to crack propagation. The next chapter discusses the bending fatigue performance of selective laser sintered gears built in the 'on-edge' configuration.



Chapter 8

Effect of ‘on-edge’ build configuration on the bending fatigue behavior of selective laser sintered polymer gears

The build configuration and the attendant layer orientation in selective laser sintered parts determine the strength of the part. The build configuration of the part influences the time required for building the part as well. The injection molding is well-suited for serial manufacturing of polymer gears due to its higher production rate. Hence, for additive manufacturing of polymer gears, the selection of build configuration that can deliver a greater number of parts in a single pass is desirable for orders requiring the fabrication of more than one unit. The ‘on-edge’ configuration can accommodate a greater number of units on the build platform. This chapter describes the bending fatigue behavior of selective laser sintered Nylon 12 gears built in an ‘on-edge’ configuration.

The influence of layer orientation on the single tooth bending fatigue strength of each SLS gear tooth configuration has been discussed in the first section. The second section compares the stress-life curves of the SLS gear tooth configurations with the highest and lowest bending fatigue strengths with that of the injection-molded gears. The thermal behavior of the selective laser sintered gear configurations, encompassing the average surface temperature and temperature evolution, has been analyzed in the third section. The final section discusses the morphology of the failure zone on the gear tooth surface and examines the fracture surfaces of the selective laser sintered and injection-molded gears. In this chapter, the term ‘SLS gears’ refers to selective laser sintered gears built in the ‘on-edge’ configuration. SLS ‘flat’ gears are mentioned explicitly.

8.1 Effect of layer orientation on the bending fatigue strength

Figure 8.1 depicts the bending fatigue life of each test configuration corresponding to a load of 5 Nm. Considering the 0° configuration as the reference, fatigue life increased with an increase

in the layer orientation angle. The peak fatigue life was observed for the 40° configuration, whereas the 160° configuration exhibited the lowest fatigue life. Thus, 40° and 160° were considered for further testing at different stress levels. The 40° configuration was the transition point beyond which the bending fatigue strength started to decrease.

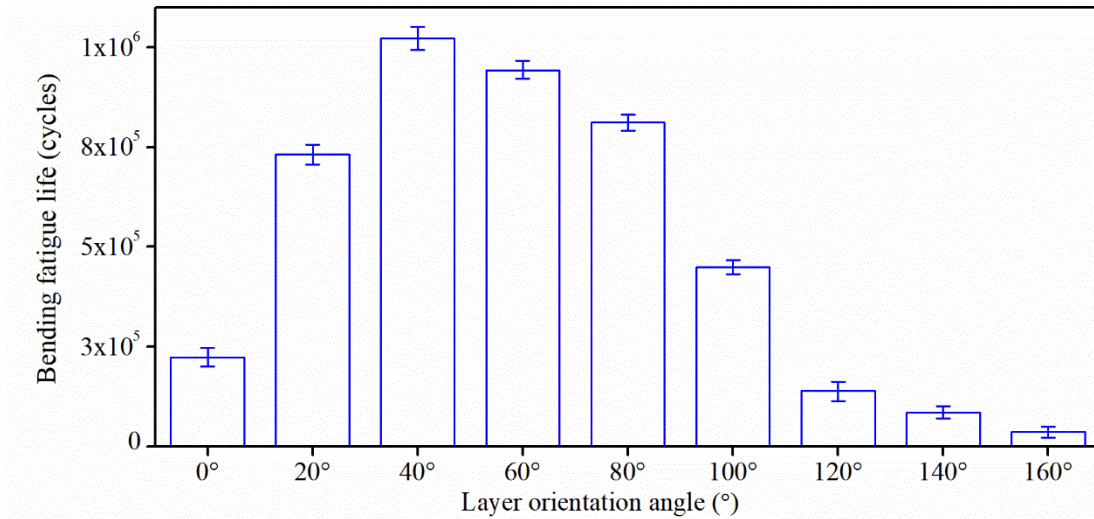


Fig. 8.1 Bending fatigue life of selective laser sintered gear teeth subjected to 5 Nm.

The variation of bending fatigue strength among the test configurations was similar to the one observed by Jain, Pandey and Rao (2009). In that, tensile specimens with six orientations ranging between 0° and 90° at an interval of 15° were tested. The tensile strength increased from the 0° orientation and started to decline beyond the peak of the 60° orientation. In our study, the bending fatigue life of the 40° tooth exceeded the life of the 160° tooth by a factor of 28. This substantial difference between the bending fatigue strengths of the strongest and weakest configurations poses significant implications for the gear performance during operation. Since the bending fatigue strength of the 160° configuration was the lowest, it must be regarded as the strength of the gear.

8.2 S-N curves of injection-molded and selective laser sintered gears

The stress-life curves were plotted in a semi-log scale, and trendlines were fitted using the linear regression technique. Among laser sintered specimens, differences in the porosity level and quality of sintering between layers affect the mechanical properties (Khudiakova *et al.*, 2020), which can cause variations in experimental data. The maximum nominal bending stress values were in the range of 43 – 85 MPa. Similar to the previous chapter (Chapter 7), the ISO 6336-3 Method B equations (3.2 – 3.7) defined in Chapter 3 were used for bending stress calculations. The parameters used in bending stress calculation are indicated in Table 7.1 of

Chapter 7. Figure 8.2 shows the stress-life curves of IM and SLS configurations. As mentioned earlier, the bending strength of IM gears was lesser than that of the SLS gears built in the ‘flat’ configuration. However, the IM gears exhibited greater bending fatigue life than the SLS gears built in the ‘on-edge’ configuration. In the SLS gear configurations, the 40° configuration exhibited considerably greater fatigue than the 160° configuration. Unlike the SLS configurations, which failed during the 5 Nm trials, a similar load trial in IM gear resulted in a ‘run-out.’ This indicates that the knee portion of the S-N curve was around that region. IM and SLS 160° configuration trendlines were parallel, indicating uniform fatigue behavior throughout the applied load range. However, the trendlines of IM and SLS 40° configuration were not parallel and tended to diverge with an increase in the bending stress. A similar trend was observed between the bending fatigue life of IM gears and SLS gears built in the ‘flat’ configuration. This divergence implies a load-specific fatigue behavior, which demands further investigation.

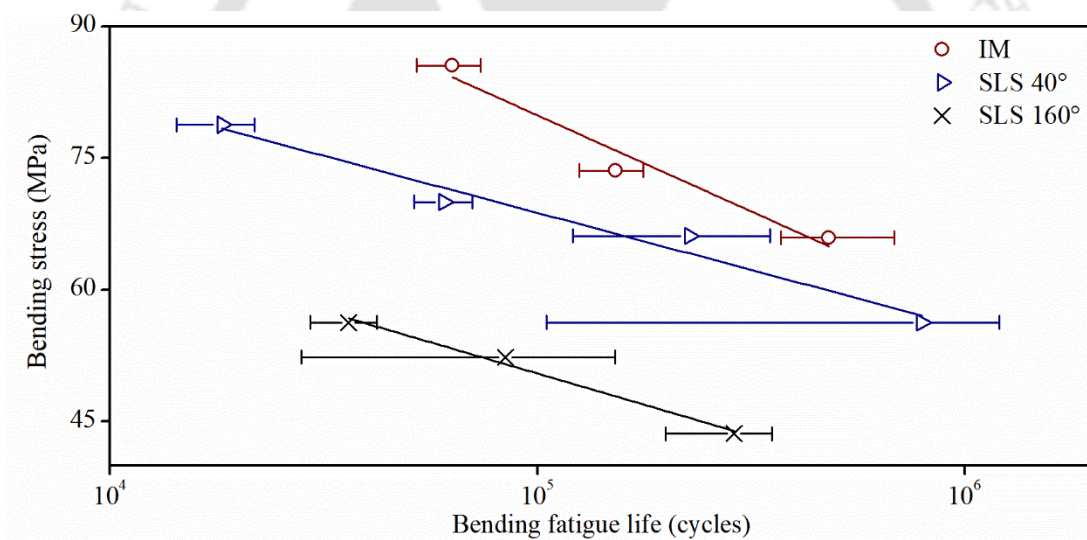


Fig. 8.2 S-N curves of injection-molded and selective laser sintered gears.

The anisotropy between IM and SLS gears could be ascribed to the factors related to material processing. In IM, the entire feedstock is subjected to melting, followed by extrusion and rapid cooling to ambient conditions. On the contrary, in SLS, the fusion between particles is attained by localized melting. The end product remains in the pre-heated powder bed for a considerable time resulting in a low cooling rate. The crystallization characteristics are altered by the heating and cooling rate of the process. Accordingly, the variations in the heating and cooling processes during injection molding and selective laser sintering cause different microstructures and properties.

The anisotropy between the SLS configurations 40° and 160° was due to the layer orientation. In multi-layered structures prepared by SLS, the anisotropy in mechanical properties is a function of intralayer and interlayer strengths. The particle-particle bonding along a sintering vector and adhesion between adjacent sintering vectors in a layer constitute the intralayer strength. The interlayer strength is the layer-layer bonding between adjacent layers along the build direction. Due to the time lag between the sintering of consecutive vectors in each layer, the initial vector undergoes cooling, which reduces the bonding with the subsequent vector. Similarly, at the interlayer level, time lag and deposition of a fresh layer of powder over the sintered layer induce cooling, which weakens the bond with the subsequent layer (Ajoku *et al.*, 2006). Thus, the intralayer and interlayer strengths of SLS specimens depend on the degree of sintering in the bonding regions and are susceptible to inconsistency. This inconsistency in bond strength at the interlayer and intralayer regions could be a source of the anisotropic fatigue behavior.

Munguia and Dalgarno (2015) observed substantial overlap among the fatigue behavior of SLS Nylon 12 rotating bending and reversed bending specimens built in flat, on-edge, and upright configurations. The anisotropy caused by the different build configurations was insignificant. Similarly, Van Hooreweder *et al.* (2013) observed minimum variations between the fatigue life of SLS Nylon 12 tensile specimens of on-edge and upright configurations. In the same study, the fatigue life of IM specimens was comparable to that of SLS specimens. This implies that the change in the material processing method caused no meaningful anisotropy in the fatigue properties. Conversely, in the current study, the trendlines of the IM and SLS gears were distinct, and no overlap was observed. The anisotropy in the bending fatigue strength was significant.

To gain further insights, the impact of gear operating temperature on the fatigue life must be investigated as the mechanical properties of polymers are sensitive to temperature. In addition to temperature, the bending fatigue life of gear is affected by the resistance to crack propagation. Hence, the influence of the material processing method and tooth layer orientation on the resistance to crack propagation must be evaluated. The thermal and failure analysis of the test gears are presented in the consequent sections.

8.3 Surface temperature of gears

The gear surface temperature increased rapidly from the ambient temperature ($23 - 27^\circ\text{C}$) during loading and attained a stable, quasi-isothermal condition. Following the commencement

of failure, the temperature climbed sharply from the steady-state condition and reached the peak temperature. For the applied load range, the maximum rise in temperature for IM, SLS 40°, and SLS 160° configurations were 17 °C, 18 °C, and 12 °C, respectively. The 40° configuration and IM exhibited similar temperature rises. The surface temperature evolution of the test gear configurations was analyzed at three stages of fatigue life: 50, 75, and 100%. Figure 8.3 presents the IR images of the IM and SLS gears corresponding to a load of 6 Nm. The temperature variation in gear tooth at various stages of life (50, 75, and 100%) is shown.

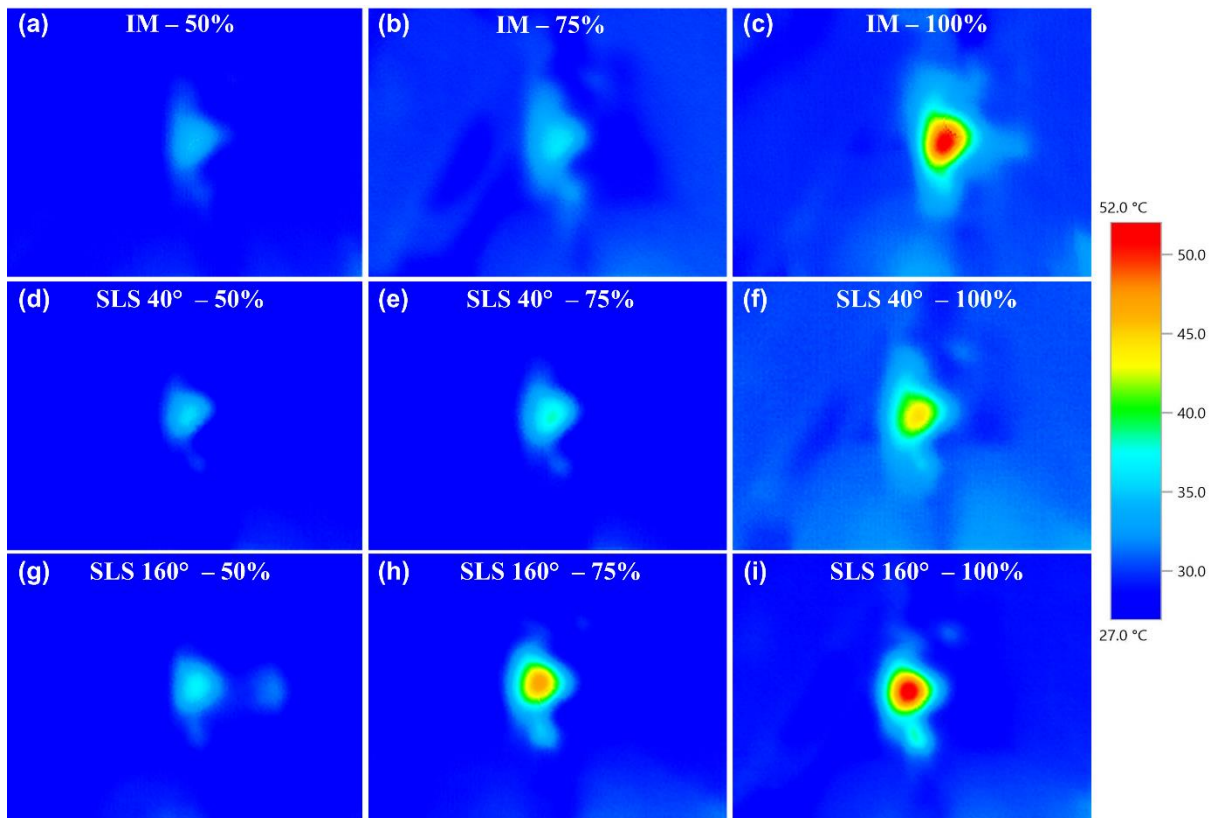


Fig. 8.3 Infrared thermal images at 50, 75, and 100% of the lifetime corresponding to the load of 6 Nm: (a, b, c) injection-molded gear, (d, e, f) selective laser sintered gear 40° configuration, and (g, h, i) selective laser sintered gear 160° configuration.

For an applied load of 6 Nm, the 160° configuration experienced the highest surface temperature at each stage of the fatigue life. The surface temperature of IM gears was slightly lesser than that of the SLS 40° configuration in the intermediate stages (50 and 75%). However, the surface temperature of the IM gears exceeded that of the SLS 40° configuration near the end of fatigue life (100%). At 50% of fatigue life, the variation among the surface temperatures of IM and SLS gears was minimal. The surface temperatures of 40° and 160° configurations increased considerably at each stage. However, the surface temperature of IM gears increased

significantly only at the end of the fatigue life (100%). The isothermal contours of 40° and 160° configurations evolve steadily in each stage, although the temperature of the 40° configuration was lower than that of the 160° configuration. In IM gear, the IR image of 100% life was markedly different from that of 50% and 75% life. The sharp temperature rise at the end of life could be due to the onset of failure in these gears. Figure 8.4 depicts the average steady-state surface temperature of the IM and SLS gear configurations. At 5 Nm, the SLS 160° configuration exhibited the highest average surface temperature. The average surface temperature was the lowest for the IM gears. The surface temperature was similar for SLS 40° configuration and IM gears. However, the trendline slope was higher for the SLS 40° configuration, leading to divergence of the trendlines. Thus, the difference between the surface temperatures of IM and the 40° configuration expanded as the applied load increased. This unequal increase in the surface temperature of the SLS 40° configuration could be a cause for the lower fatigue life at higher stress levels. The divergence of fatigue trendlines of 40° configuration and IM gears in the LCF region confirmed this. As reported in the previous chapter, this load-specific variable thermal behavior was observed in SLS gears built in the ‘flat’ configuration as well.

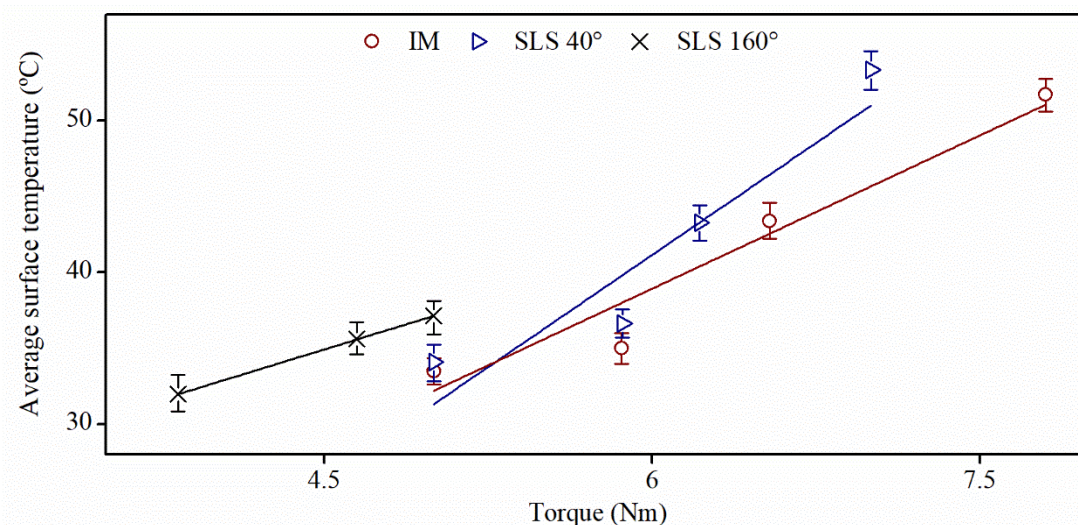


Fig. 8.4 Average surface temperature of test gears as a function of the applied torque.

As mentioned earlier, hysteresis is the primary source of heat generation in gear bending fatigue tests, as frictional heating caused by sliding is minimal. The material viscoelastic deformation governs hysteresis behavior during loading. In the study by Van Hooreweder *et al.* (2013), the thermal responses of SLS and IM Nylon 12 tensile specimens were similar when subjected to uniaxial fatigue. No appreciable variation in temperature was observed between the two

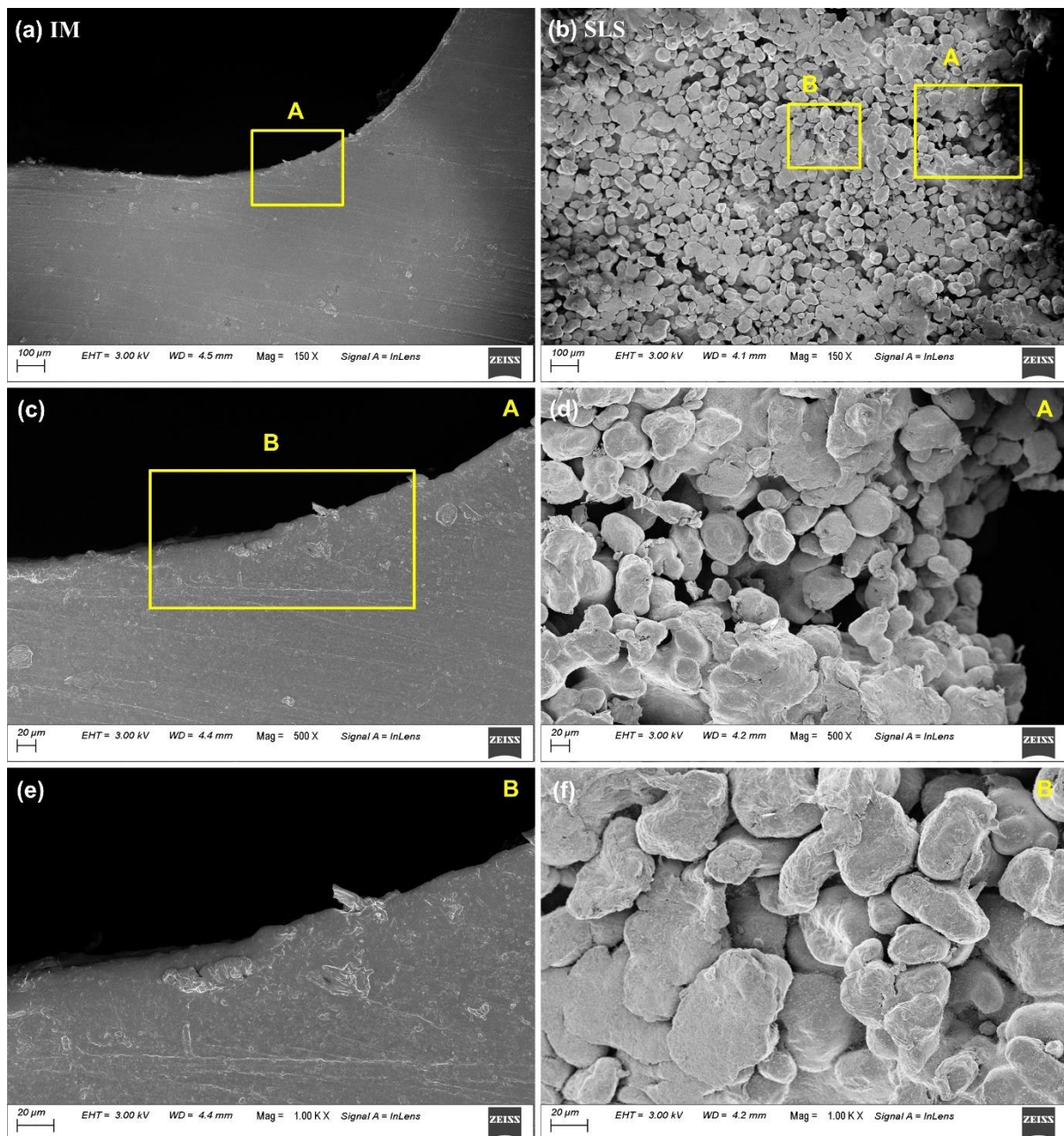


Fig. 8.5 Surfaces of injection-molded gear tooth (a, c, e) and selective laser sintered gear tooth (b, d, f) in the fillet region. Broad and close-up views of the surfaces are presented.

specimens. However, in this investigation, the IM gears exhibited lesser surface temperature than that of the SLS gears built in the 'on-edge' configuration. Then, in addition to hysteresis, some other source of heat generation could be present in gears prepared by the powder bed fusion process. Generally, the injection molded parts are homogeneous as the entire feedstock of material is melted and cooled in a single step. However, the SLS process generates an inhomogeneous part with voids as the powder particles are fused progressively. The FESEM images of the test gear surfaces (Figure 8.5) corroborate the differences in the material morpho-

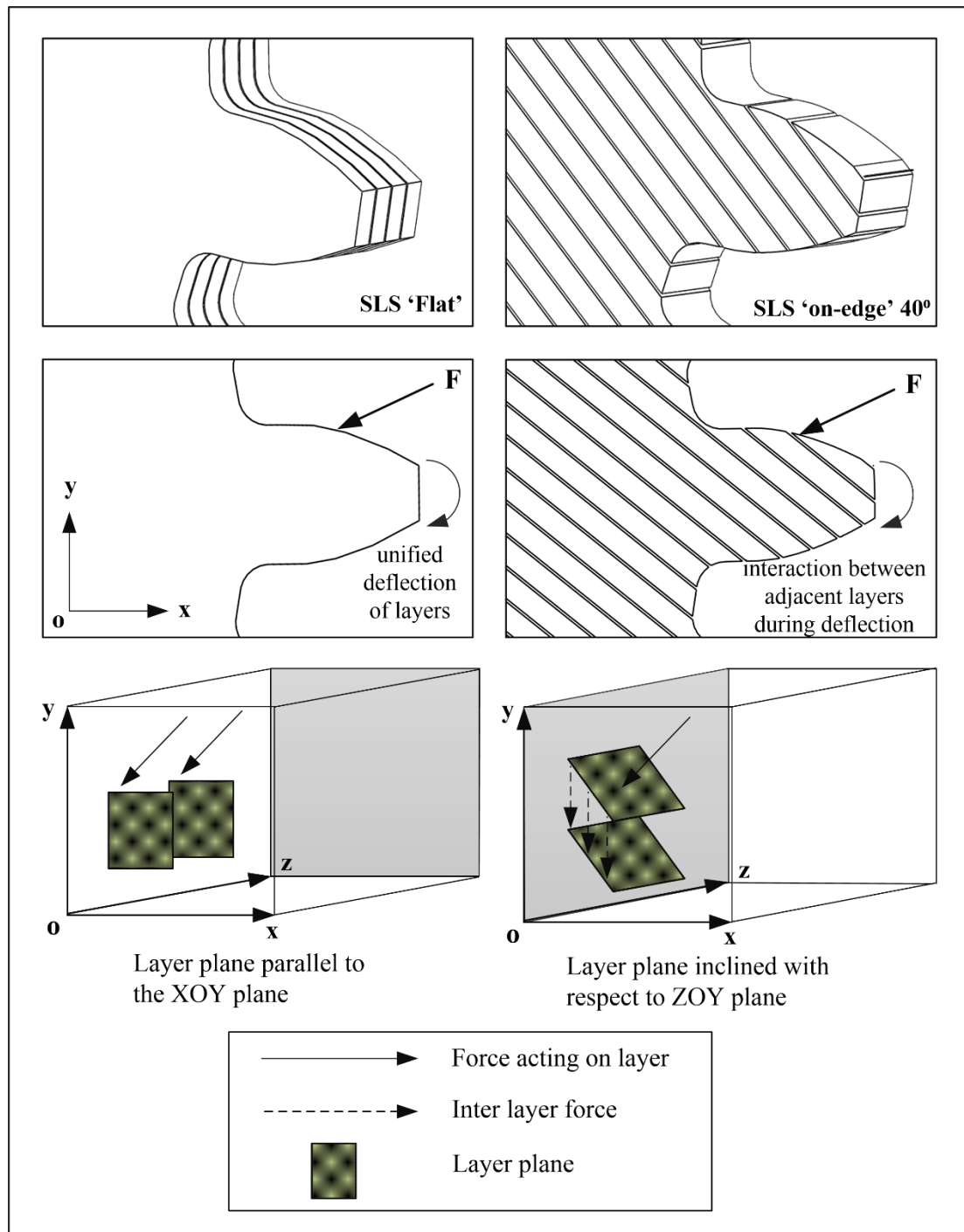


Fig. 8.6 Orientation of layer planes in selective laser sintered gears.

-logy. Due to the inhomogeneity of SLS parts, interactions may occur between the surfaces of powder particles at the interlayer and intralayer level during cyclic loading. Consequently, this friction between the surfaces of powder particles could act as a heat source, increasing the gear temperature. Since the tooth deflection increases with an increase in the applied load, the interactions among the powder particles could intensify, leading to greater frictional heat. Then, the load-specific thermal behavior in selective laser sintered gears could be a result of the

increased particle interactions at higher loads. Although powder particles are present in both SLS 'flat' and 'on-edge' gears, each configuration's thermal behavior was not the same. In SLS gears built in the 'flat' configuration, the surface temperature was lesser than that of IM gears in the HCF regime. The surface temperature of IM gears was surpassed by SLS 'flat' gears only when subjected to high loads. This difference between the thermal behaviors of SLS 'flat' and 'on-edge' gears suggests that the build configuration of the gears may affect the heat generation during loading. The orientation of the layer plane differs in 'flat' and 'on-edge' gear configurations. This variation affects the extent of powder particle interactions at the interlayer and intralayer regions during tooth deflection. Figure 8.6 illustrates the orientation of tooth layer planes in a three-dimensional space.

In SLS 'flat' gears, the applied load acts on all layers of the tooth simultaneously as the layers are stacked along the facewidth. This results in the deflection of all tooth layers in a unified manner during loading. Consequently, the relative displacement of one layer with respect to the adjacent layer is minimal or non-existent, decreasing the interactions between particles in interlayer regions. Nevertheless, particles in sintering vectors on each layer plane could interact among each other during tooth deflection. Accordingly, this intralayer shearing could be the source of heat generation in SLS 'flat' gears.

In SLS 'flat' gears, the layer plane is parallel to the orthogonal coordinate plane XOY. But, the layer planes in SLS 'on-edge' gear teeth are not parallel to any orthogonal plane except the 0° configuration, which is parallel to the XOZ plane. The layer planes of other configurations are inclined with respect to the ZOY plane. Due to the inclined layer plane, the tooth load is not shared by each layer equally as in the case of SLS 'flat' gears. Consequently, the tooth deflection causes relative displacement of each layer with respect to adjacent layers. Depending on the layer orientation, a layer could press against the adjacent layer or slide with respect to the adjacent layer during tooth deflection. In either case, considerable powder particle interactions occur at the interlayer level, along with the intralayer interactions caused by layer deflection. Thus, the extent of interlayer interactions during loading could be the cause of the dissimilar thermal behavior of 'flat' and 'on-edge' gears. More investigation is necessary to comprehensively understand the tooth deflection and the consequent heat generation in selective laser sintered gears.

The temperature rise in semi-crystalline polymers is accompanied by the softening of amorphous chains. This leads to the re-orientation of the chains, causing a reduction in the

stiffness of the material (Amel *et al.*, 2016). Consequently, the material undergoes a higher magnitude of deformation at the same stress level, resulting in localized stress concentration at the sites of inclusions. This is followed by the initiation of micro-cracks, crack coalescence, and propagation. The chain softening and stiffness reduction is hastened when the material temperature increases above the glass transition temperature. In Nylon 12, the glass transition occurs in the range of 23.5 °C – 55 °C (Van Hooreweder *et al.*, 2010). As the operating temperature of the SLS gears remained within this range, it could be inferred that material stiffness reduction occurred during testing.

The acceptable range of temperature rise during fatigue testing of additively manufactured components is 10 °C (Terekhina *et al.*, 2020). In SLS 160° configuration gears, the average surface temperature was in the range of 32 – 37 °C for the considered loads. In IM and SLS 40° configuration gears, the average surface temperature ranged between 32 °C and 53 °C. The temperature exceeded 40 °C when the applied load was greater than 6 Nm. Hence, the influence of temperature on fatigue performance could be significant when loaded at higher stress levels, causing thermomechanical failure. Since the maximum temperature rise in 160° configuration gears was 12 °C only, the impact of temperature on the fatigue life could not be substantial. Then, the cause of failure in 160° configuration gears could be entirely mechanical.

8.4 Crack propagation in gears

The fatigue life of a component comprises initiation life and propagation life. In spur gears, bending fatigue failures are characterized by cracks propagating perpendicular to the fillet. Gears subjected to bending fatigue fail by mixed-mode fracture (Mode I and II). However, the crack propagation is dominated by Mode I (Lewicki and Ballarini, 1997). Accordingly, the propagation life is a function of Mode I fracture toughness (K_{IC}) of the gear material. As mentioned earlier, the cross-laminar fracture mode involves higher resistance to crack propagation as crack extends across multiple layers, absorbing a higher amount of energy. On the other hand, in the inter-laminar fracture mode – the crack plane is parallel to the layer plane – the resistance is lower due to crack propagation along the interface region. In the study by Brugo *et al.* (2016), the K_{IC} of SLS Nylon 12 was higher for CT specimens with layer orientation perpendicular to the direction of crack propagation compared to CT specimens with layer orientation parallel to the direction of crack propagation. The preferential pathway offered by the interlayer region was identified as the cause for the lower resistance to fracture. Therefore, the variation in the bending fatigue life of SLS gear configurations could be a result

of the difference in resistance to crack propagation. To confirm this, the crack path and fracture surfaces should be analyzed in detail.

8.4.1 Examination of failure zone morphology

The stereomicroscope images of IM and SLS (40° and 160° configurations) gear teeth subjected to 6 Nm are shown in Figure 8.7 (a, c and e). The detection of bending fatigue crack in IM gear was effortless as the crack was distinctly visible during testing and idle conditions.

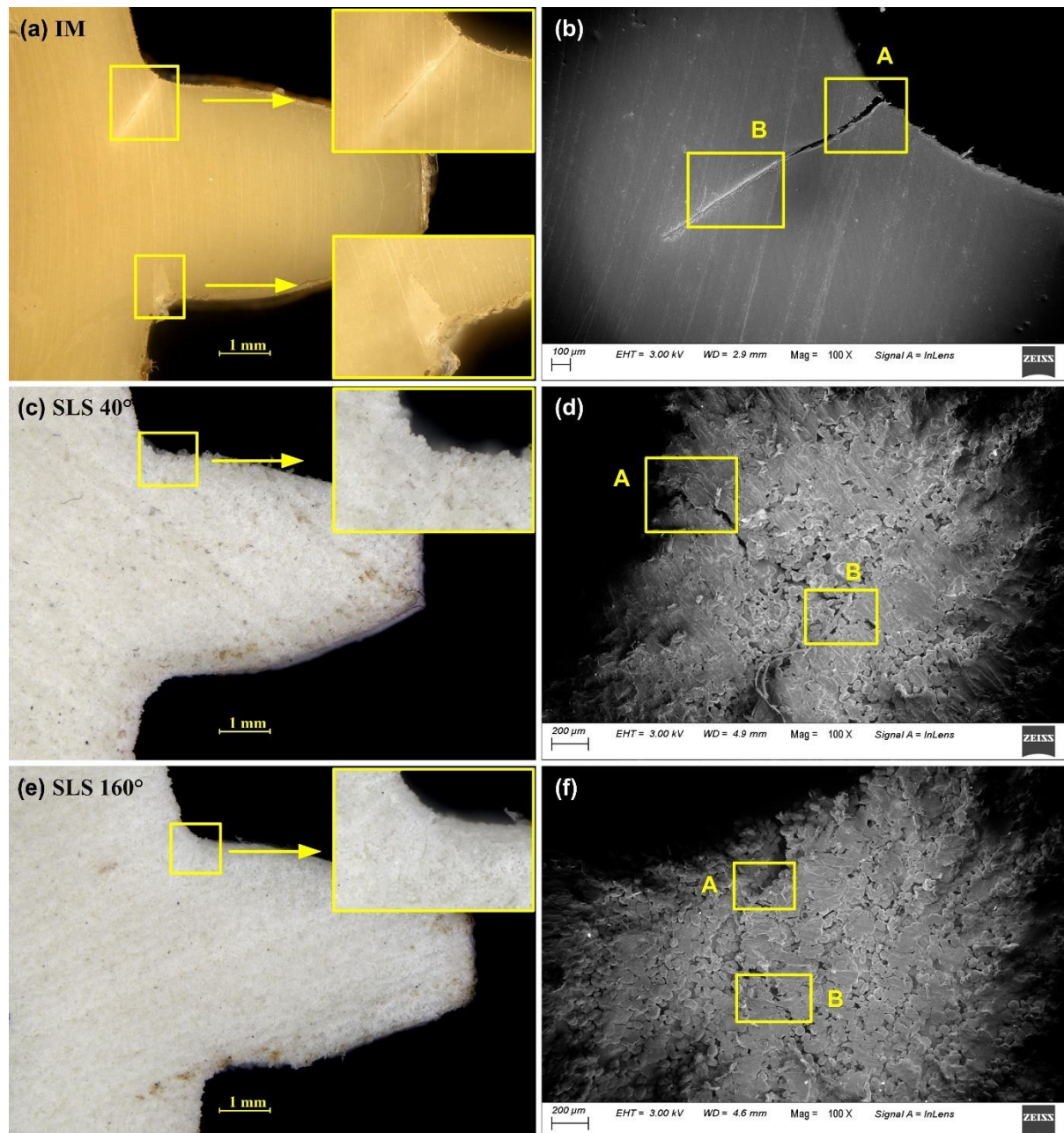


Fig. 8.7 Bending fatigue cracks in test gears observed under stereomicroscope (a, c, e) and FESEM (b, d, f). (a, b) Injection-molded gear, (c, d) Selective laser sintered gear tooth 40° configuration and (e, f) Selective laser sintered gear tooth 160° configuration.

However, in SLS gears, crack detection during the idle time was difficult. The visibility of crack on the gear surface was affected by the surface attributes such as evenness and color, which are dependent on the processing method. The surface of IM gear was even, whereas the layered manufacturing of SLS gear resulted in an uneven surface. The crack merged with the surface undulations, which affected the identification. Moreover, a craze (stress-whitened zone) existed around the crack in IM gears, which aided crack identification. Crazeing occurs

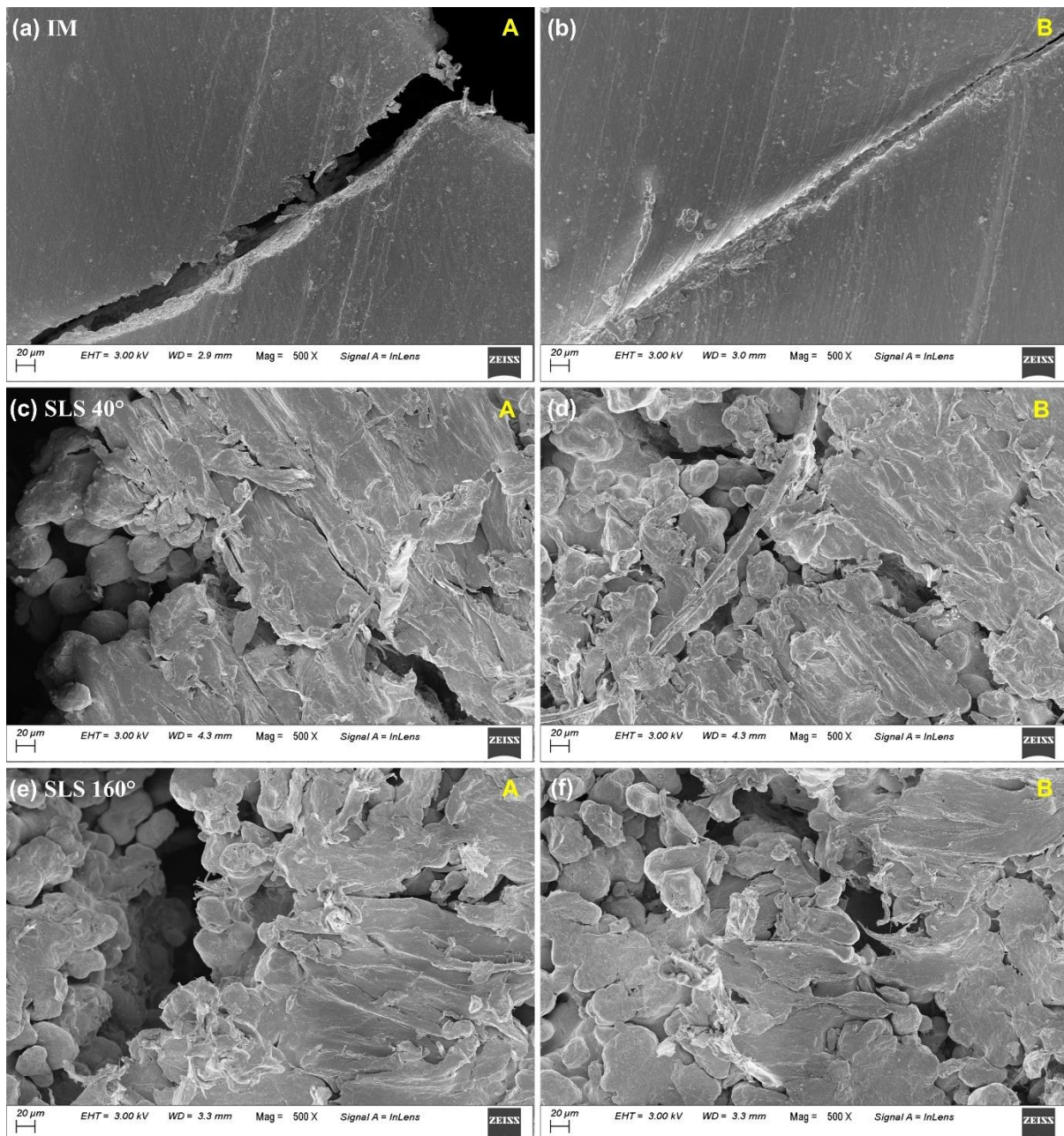


Fig. 8.8 Magnified view of the bending fatigue cracks as observed under FESEM: (a, b) Injection-molded gear, (c, d) Selective laser sintered gear tooth 40° configuration and (e, f) Selective laser sintered gear tooth 160° configuration.

due to the elongation of a microscopic void in a region of stress concentration. In SLS gears, the craze zone was not visible in the teeth. The issue with crack identification was overcome by viewing the failed teeth under the FESEM, which revealed the crack path of both IM and SLS gears. Figure 8.7 (b, d, and f) illustrate the FESEM images of the failure zones shown in Figure 8.7 (a, c and e). Figure 8.8 shows the magnified views of regions indicated in Figure 8.7. Although regions with well-combined and fully molten material could be observed, contours of partially molten spherical powder particles were noticed as well. This indicates that the coalescence of particles was not uniform in all regions across the surface. The crack path was generally straight in all the test gears. In SLS gears, the layered structure deflected the crack path, resulting in a tortuous path. On the other hand, the trajectory of crack propagation was quite steady in IM gears as the material structure was uniform and continuous. From Figure 8.7 (c), it could be observed that the layer orientation of the SLS 40° configuration was oblique with respect to the direction of crack propagation, and the crack propagated in a cross-laminar mode (Figure 8.7 (d)).

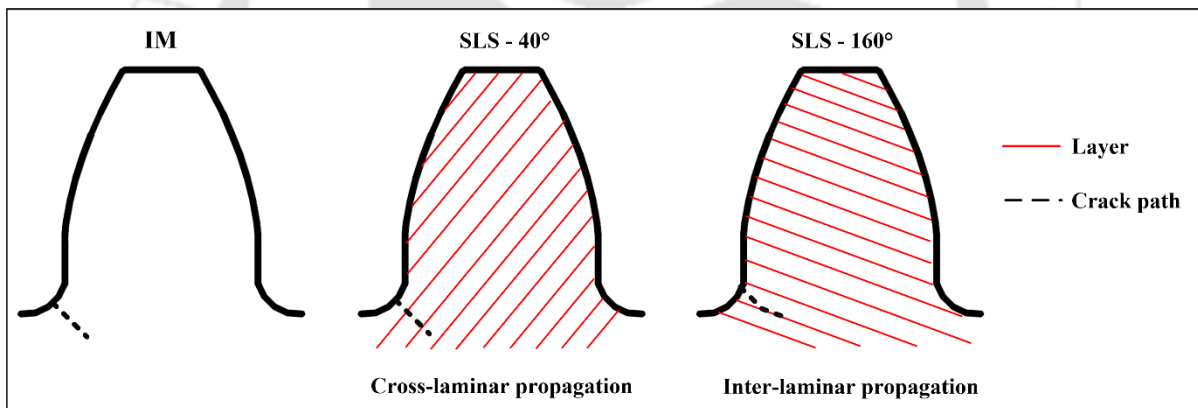


Fig. 8.9 Crack propagation in injection-molded and selective laser sintered gear teeth.

However, in the SLS 160° configuration (Figure 8.7 (e)), the crack propagated in a mixed-mode that was predominantly inter-laminar. Although the layer orientation was closely aligned with the general direction of bending fatigue crack propagation, the crack path was not linear (Figure 8.7 (f)). After initiation, the crack propagated along a layer briefly and then switched to the cross-laminar mode. The crack propagated in the cross-laminar mode for a short distance, in which the crack jumped across a few layers. Following that, the crack propagation occurred in the inter-laminar mode till the end of the experiment. Figure 8.9 illustrates the direction of crack propagation with respect to the layer orientation in SLS 40° and SLS 160° teeth. Since the SLS 160° configuration sustained a predominantly inter-laminar mode of crack propagation, the resistance to propagation was lesser than that of the SLS 40° configuration.

Therefore, the higher bending fatigue life of the 40° configuration could be a result of the greater resistance offered to crack propagation.

8.4.2 Fractography

Figure 8.10 (a - f) shows the fracture surfaces of IM and SLS gears tested at 6 Nm. The appearance of each fracture surface was distinctly different from other surfaces. The fracture surface of IM gear was homogeneous and bereft of any voids (Figure 8.10 (a, b)). Strands of polymer chains undergo plastic deformation and rupture during cyclic loading due to the repeated extension and contraction. The presence of crazes in the fillet region (Figure 8.7 (a)) implies the occurrence of plastic deformation in the IM gear. This was substantiated by the presence of hemispherical, crater-like features on the fracture surface caused by the rupturing of craze fibrils. The incidence of crazing followed by steady crack propagation implies that the failure was ductile in IM gears.

In the case of SLS gears, the fracture surfaces were highly inhomogeneous, comprising multiple voids. The fracture surface of the 160° configuration (Figure 8.10 (e, f)) encompassed fully and partially melted powder particles similar to the surface in the fillet region. The voids were small and limited in number. In addition to intact particles, particles that were subjected to tearing were observed. These features are consistent with the inter-laminar mode of fracture in which the crack propagates by rupturing the bonds between particles of two adjacent layers. In contrast to the 160° configuration, the surface of the 40° configuration (Figure 8.10 (b, c)) was extremely uneven and marked by bigger voids resulting from the detachment of powder particles. The detachment of material could be attributed to the weaker bonding between adjoining particles. In 160° configuration, the preferential path provided to the crack propagation by the interlayer region confined the damage to that region. Conversely, in the 40° configuration, the cross-laminar crack propagation resulted in extensive damage. This was confirmed by the absence of powder particles on the fracture surface. Since the extent of material damage is an indicator of the energy absorbed during crack propagation, it is evident that the 40° configuration absorbed higher energy compared to the 160° configuration.

The analysis of failure morphology ascertained that the processing method affects the failure mode in polymer gears. In SLS gears built in the ‘on-edge’ configuration, the layer orientation oblique to crack propagation direction increased the energy absorbed during the failure, resulting in improved fatigue strength. Nonetheless, the bending fatigue life was greater for the IM gears, implying that the energy absorbed by SLS gears (‘on-edge’ configuration) for crack

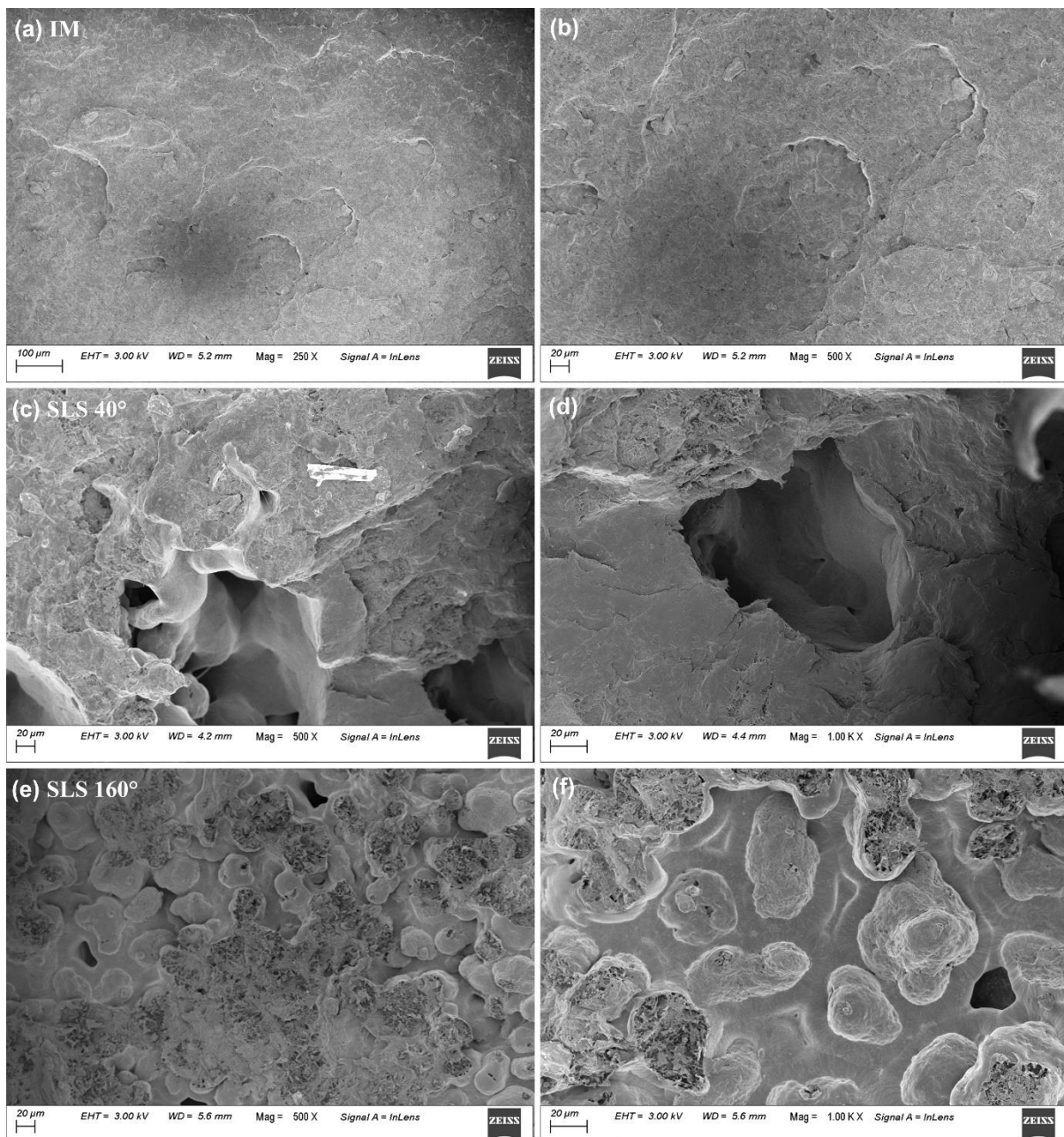


Fig. 8.10 Fracture surfaces of test gears viewed under FESEM. (a, b) Injection-molded gear, (c, d) Selective laser sintered gear tooth 40° configuration and (e, f) Selective laser sintered gear tooth 160° configuration.

propagation was lower than that of IM gears. On the other hand, in SLS gears built in the 'flat' configuration, energy absorption during crack propagation was greater, resulting in higher bending fatigue strength compared to IM gears. As already demonstrated by Brugo *et al.* (2016) using the compact tension specimens, the crack propagation resistance is greater when the crack front is encompassed by all the layers, as in the case of SLS gears built in the 'flat' configuration.

8.5 Summary

The bending fatigue performance of selective laser sintered Nylon 12 gears built in an ‘on-edge’ configuration was evaluated and compared with injection-molded gears. The gears were submitted to constant frequency single tooth bending fatigue tests in a custom-designed gear test rig to evaluate the influence of layered manufacturing on the thermal behavior and failure morphology. The principal findings are:

- The anisotropy in bending strength of SLS gears, induced by the deviation in tooth layer orientation, was significant. The bending fatigue life of the 40° configuration was 28 times greater than that of the 160° configuration.
- The bending fatigue strength of IM gears was greater than that of SLS gears in LCF and HCF regions. However, the difference between the strengths of SLS 40° configuration and IM gear was lesser in the HCF regime.
- The superior strength of IM gears was attributed to the lower operating temperature. The difference between the surface temperatures of SLS 40° configuration and IM gear increased progressively as the applied load increased.
- In SLS gears, the influence of layered structure on the crack propagation behavior depends on the tooth layer orientation. Conversely, the crack propagation behavior in IM gears was uniform across all teeth as the material morphology was homogeneous.
- Cross-laminar crack propagation occurred in the SLS 40° configuration as the layer orientation was oblique with respect to the crack plane. In SLS 160° configuration, the layer orientation provided the interlayer zone as a preferential pathway for crack propagation. As a result, the layered structure hindered the crack propagation in the 40° configuration whereas, in the 160° configuration, crack propagation was accelerated.

This investigation reveals that the bending fatigue strength of SLS Nylon 12 gears built in the ‘on-edge’ configuration is inadequate in comparison to injection molded Nylon 66 gears. Also, the variation in tooth layer orientation imparts significant anisotropy in terms of bending strength, surface temperature, and failure modes. On account of these shortcomings, it is preferable not to employ SLS gears built in ‘on-edge’ configuration for power transmission applications in place of injection-molded gears. Instead, selective laser sintered gears built in the ‘flat’ configuration could be considered, as the bending fatigue strength was greater than that of injection molded gears and remained uniform for all teeth.

Chapter 9

Conclusion and Scope for future work

This work has made an attempt to study the impact of asymmetric tooth profile and mating gear material on the bending fatigue strength and deflection behavior of injection-molded polymer spur gears. Moreover, this work has endeavored to understand the influence of the selective laser sintering manufacturing process and build configuration during the SLS process on the bending fatigue performance of polymer gears. To this end, the bending fatigue performances of symmetric ($20^\circ/20^\circ$) and asymmetric ($34^\circ/20^\circ$ and $20^\circ/34^\circ$) Nylon 66 gears were evaluated under metal – polymer (AISI SS 316/Nylon 66) and polymer – polymer engagements (Nylon 66/Nylon 66). The static deflections of metal – polymer and polymer – polymer pairs of symmetric and asymmetric injection-molded gears were estimated. Following that, the bending fatigue performances of selective laser sintered Nylon 12 symmetric gears built in ‘flat’ and ‘on-edge’ configurations were assessed and compared with the bending fatigue performance of injection-molded Nylon 66 gears. Both experimental and numerical techniques were adopted as part of the study to evaluate the performance parameters.

The experimental evaluation of bending fatigue performance entailed the determination of bending fatigue life and surface temperature of gears by bending fatigue tests in an in-house developed test rig. Post-failure microscopic analyses were conducted to examine the morphology of the failed gear teeth. Numerical analysis was performed to complement the experimental study involving injection-molded gears. Multi-pair contact models of symmetric and asymmetric gear pairs were developed in ABAQUS[®]. The stress distribution in the teeth was studied by predicting the principal stress and von Mises stress. The load sharing behavior of each tooth configuration was evaluated by calculating the load share ratio using the contact forces sustained by the leading and trailing contact pairs. The tooth and mesh deflections of injection-molded gear pairs of each configuration were predicted to evaluate the deflection behavior. The experimental determination of mesh deflections was accomplished using static tooth deflection tests in an in-house built setup.

The major conclusions derived from the work are listed in the following section. The final section outlines a few possible directions in which the current work can be extended.

9.1 Conclusions

The major conclusions from the present study are:

- Asymmetric tooth profile decreases bending stress and improves the bending fatigue life. The bending fatigue strength of metal – polymer pairs of asymmetric gears depends on the bending stress, whereas in polymer – polymer pairs, operating temperature determines the bending fatigue life of asymmetric gears.
- The asymmetric configuration with a greater pressure angle on the drive side ($34^\circ/20^\circ$) causes maximum bending stress reduction, whereas the asymmetric configuration with a lower drive side pressure angle ($20^\circ/34^\circ$) minimizes the hysteresis heat generation.
- A greater pressure angle on the coast side flank ($20^\circ/34^\circ$) decreases the peak mesh deflection in the cycle, whereas a greater drive side pressure angle ($34^\circ/20^\circ$) increases the amplitude of variation in the cycle.
- Metal mating gear enhances the mesh stiffness of the gear pair, whereas polymer mating gear balances the mesh stiffness in the addendum and dedendum region.
- Selective laser sintering of polymer gears in the 'flat' build configuration confers greater resistance to crack propagation, resulting in superior bending fatigue strength compared to injection-molded polymer gears.
- The varying layer orientation in the teeth of SLS 'on-edge' gears induces significant anisotropy in the bending fatigue strength and crack propagation behavior, resulting in an inferior performance with respect to injection-molded gears.

9.2 Limitations and Scope for further research

- This work evaluated the fatigue behavior of asymmetric Nylon 66 gears under bending load. The fatigue behavior of asymmetric Nylon 66 gears in actual service conditions can be assessed by conducting dynamic rotational tests which encompass bending and contact fatigue.
- In this work, the material behavior was simulated using linear elasticity and linear viscoelasticity. In future works, a non-linear viscoelastic model may be employed to predict the material behavior with greater accuracy.
- This work evaluated the deflection characteristics of asymmetric gears under quasi-static conditions. Future works can determine the tooth deflection and dynamic transmission error of asymmetric polymer gears using low-speed rotational tests.

- In this work, only two standard build configurations were considered for selective laser sintered gears. Additive manufacturing of gears with layer orientation in alignment with the tooth profile can be explored.





References

1. **AGMA 946-A21** (2021) *Test methods for plastic gears*. Alexandria, Virginia.
2. **Ajoku, U., Saleh, N., Hopkinson, N., Hague, R. and Erasenthiran, P.** (2006) 'Investigating mechanical anisotropy and end-of-vector effect in laser-sintered nylon parts', *Proceedings of the Institution of Mechanical Engineers, Part B: Journal of Engineering Manufacture*, 220(7), pp. 1077–1086.
3. **Amel, H., Rongong, J., Moztarzadeh, H. and Hopkinson, N.** (2016) 'Effect of section thickness on fatigue performance of laser sintered nylon 12', *Polymer Testing*, 53, pp. 204–210.
4. **Andrews, J.D.** (1991) 'A finite element analysis of bending stresses induced in external and internal involute spur gears', *The Journal of Strain Analysis for Engineering Design*, 26(3), pp. 153–163.
5. **ANSI/AGMA 1010-F14** (2014) *Appearance of gear teeth - Terminology of wear and failure*. Alexandria, Virginia.
6. **ANSI/AGMA 2101-D04** (2004) *Fundamental rating factors and calculation methods for involute spur and helical gear teeth*. Alexandria, Virginia.
7. **Arafa, M.H. and Megahed, M.M.** (1999) 'Evaluation of spur gear mesh compliance using the finite element method', *Proceedings of the Institution of Mechanical Engineers, Part C: Journal of Mechanical Engineering Science*, 213(6), pp. 569–579.
8. **Arai, S., Tsunoda, S., Kawamura, R., Kuboyama, K. and Ougizawa, T.** (2017) 'Comparison of crystallization characteristics and mechanical properties of poly(butylene terephthalate) processed by laser sintering and injection molding', *Materials and Design*, 113, pp. 214–222.

9. **ASTM D4065-20** (2020) *Standard practice for plastics: Dynamic mechanical properties: Determination and report of procedures*. West Conshohocken, Pennsylvania: ASTM International.
10. **ASTM D638-14** (2014) *Standard test method for tensile properties of plastics*. West Conshohocken, Pennsylvania: ASTM International.
11. **Athreya, S.R., Kalaitzidou, K. and Das, S.** (2011) 'Mechanical and microstructural properties of Nylon-12/carbon black composites: Selective laser sintering versus melt compounding and injection molding', *Composites Science and Technology*, 71(4), pp. 506–510.
12. **Benaarbia, A., Chrysochoos, A. and Robert, G.** (2014) 'Influence of relative humidity and loading frequency on the PA6.6 cyclic thermomechanical behavior: Part I. mechanical and thermal aspects', *Polymer Testing*, 40, pp. 290–298.
13. **Berger, U. and Mäule, B.** (2009) 'Rapid manufacturing of high reduction polymer gears by use of stereolithography', *IEEE/ASME International conference on Advanced Intelligent Mechatronics, 14-17 July, Singapore*, pp. 613–617.
14. **Blattmeier, M., Witt, G., Wortberg, J., Eggert, J. and Toepker, J.** (2012) 'Influence of surface characteristics on fatigue behaviour of laser sintered plastics', *Rapid Prototyping Journal*, 18(2), pp. 161–171.
15. **Brown, F.W., Davidson, S.R., Hanes, D.B., Weirles, D.J. and Kapelevich, A.** (2011) 'Analysis and testing of gears with asymmetric involute tooth form and optimized fillet form for potential application in helicopter main drives', *Gear Technology*, 28(4), pp. 46–55.
16. **Brugo, T., Palazzetti, R., Ciric-Kostic, S., Yan, X.T., Minak, G. and Zucchelli, A.** (2016) 'Fracture mechanics of laser sintered cracked polyamide for a new method to induce cracks by additive manufacturing', *Polymer Testing*, 50, pp. 301–308.
17. **Cano, A.J., Salazar, A. and Rodríguez, J.** (2018) 'Effect of temperature on the

fracture behavior of polyamide 12 and glass-filled polyamide 12 processed by selective laser sintering', *Engineering Fracture Mechanics*, 203, pp. 66–80.

18. **Cano, A.J., Salazar, A. and Rodríguez, J.** (2019) 'Effect of the orientation on the fatigue crack growth of polyamide 12 manufactured by selective laser sintering', *Rapid Prototyping Journal*, 25(5), pp. 820–829.
19. **Carneiro, O.S., Silva, A.F. and Gomes, R.** (2015) 'Fused deposition modeling with polypropylene', *Materials and Design*, 83, pp. 768–776.
20. **Cathelin, J., Letzelter, E., Guingand, M., de Vaujany, J. P., and Chazeau, L.** (2013) 'Experimental and numerical study of a loaded cylindrical PA66 gear', *Journal of Mechanical design*, 135(4), 41007, pp. 1–9.
21. **Caulfield, B., McHugh, P.E. and Lohfeld, S.** (2007) 'Dependence of mechanical properties of polyamide components on build parameters in the SLS process', *Journal of Materials Processing Technology*, 182(1–3), pp. 477–488.
22. **Cavdar, K., Karpát, F. and Babalik, F.C.** (2005) 'Computer aided analysis of bending strength of involute spur gears with asymmetric profile', *Journal of Mechanical Design*, 127(3), pp. 477–484.
23. **Chakrour, A.E., Hammami, C., Hammami, A., De-Juan, A., Chaari, F., Fernandez, A., Viadero, F. and Haddar, M.** (2021) 'Quasi-static study of gear mesh stiffness of a polymer-metallic spur gear system', in *Advances in Materials, Mechanics and Manufacturing II*. Cham: Springer, pp. 301–307.
24. **Costopoulos, T. and Spitas, V.** (2009) 'Reduction of gear fillet stresses by using one-sided involute asymmetric teeth', *Mechanism and Machine Theory*, 44(8), pp. 1524–1534.
25. **Czelusniak, T. and Amorim, F.L.** (2020) 'Influence of energy density on selective laser sintering of carbon fiber-reinforced PA12', *International Journal of Advanced Manufacturing Technology*, 111(7–8), pp. 2361–2376.

26. **Dearn, K.D., Hoskins, T.J., Petrov, D.G., Reynolds, S.C. and Banks, R.** (2013) ‘Applications of dry film lubricants for polymer gears’, *Wear*, 298-299, pp. 99–108.
27. **Dearn, K.D., Hoskins, T.J., Andrei, L. and Walton, D.** (2013) ‘Lubrication regimes in high-performance polymer spur gears’, *Advances in Tribology*, 2013, pp. 1–9.
28. **Demet, S.M. and Ersoyoğlu, A.S.** (2021) ‘An analysis of the effect of pressure angle change on bending fatigue performance in asymmetrical spur gears’, *Proceedings of the Institution of Mechanical Engineers, Part L: Journal of Materials: Design and Applications*, 235(9), pp. 2142–2150.
29. **Deng, G., Nakanishi, T. and Inoue, K.** (2003) ‘Bending load capacity enhancement using an asymmetric tooth profile (1st report, influences of pressure angle on tooth root stress and bending stiffness)’, *JSME International Journal Series C Mechanical Systems, Machine Elements and Manufacturing*, 46(3), pp. 1171–1177.
30. **Deng, X., Hua, L. and Han, X.** (2015) ‘Research on the design and modification of asymmetric spur gear’, *Mathematical Problems in Engineering*, 2015, pp. 1–13.
31. **DIN 3990:1987-12** (1987) *Calculation of load capacity of cylindrical gears - Introduction and general influence factors*. Berlin: Beuth Verlag.
32. **Doğan, O. and Karpaz, F.** (2019) ‘Crack detection for spur gears with asymmetric teeth based on the dynamic transmission error’, *Mechanism and Machine Theory*, 133, pp. 417–431.
33. **Du, S., Randall, R.B. and Kelly, D.W.** (1998) ‘Modelling of spur gear mesh stiffness and static transmission error’, *Proceedings of the Institution of Mechanical Engineers, Part C: Journal of Mechanical Engineering Science*, 212(4), pp. 287–297.
34. **Dudley, D.W. and Radzevich, S.P.** (2012) ‘Appendix A: Evolution of Gear Art’, in *Dudley’s handbook of practical gear design and manufacture*. Second. Boca Raton: CRC press, pp. 671–715.

35. **Duncan, J.** (2008) 'Principles and applications of mechanical thermal analysis', in Gabbott, P. (ed.) *Principles and Applications of Thermal Analysis*. Hoboken, New Jersey: Blackwell Publishing, pp. 119–163.
36. **Dupin, S., Lame, O., Barrès, C., and Charneau, J.Y.** (2012) 'Microstructural origin of physical and mechanical properties of polyamide 12 processed by laser sintering', *European Polymer Journal*, 48(9), pp. 1611–1621.
37. **Durakbasa, N.M., Demircioglu, P., Bauer, J., Bogrekci, I., Bas, G., Bodur, O., and Poszvek, G.** (2019) 'Additive miniaturized-manufactured gear parts validated by various measuring methods', in *International conference on Measurement and Quality Control-Cyber Physical Issue, 4-7 June, Belgrade, Serbia*. Springer, pp. 276–290.
38. **Fekete, G.** (2021) 'Numerical wear analysis of a PLA-made spur gear pair as a function of friction coefficient and temperature', *Coatings*, 11(4), 409, pp. 1–11.
39. **Fernandes, P.J.L.** (1996) 'Tooth bending fatigue failures in gears', *Engineering Failure Analysis*, 3(3), pp. 219–225.
40. **Fink, B., Weidig, R., Ferfecki, F. J., Whitehead, T., and Salisbury, J.** (2019) 'Engine NVH performance improvements with polymer gears', in *Automotive Acoustics Conference 2015*. Springer Vieweg Verlag, pp. 240–254.
41. **Fuentes, A., Gonzalez-Perez, I., Sanchez-Marin, F. T., and Hayasaka, K.** (2013) 'On the behavior of asymmetric cylindrical gears in gear transmissions', in *Proceedings of the FISITA 2012 World Automotive Congress*. Berlin, Heidelberg: Springer, pp. 143–150.
42. **Fürstenberger, M.** (2013) *Betriebsverahlten verlustoptimierter Kunststoffzahnräder*. Ph.D. Thesis, Technische Universität München/FZG, München.
43. **García-García, R. and González-Palacios, M.A.** (2018) 'Method for the geometric modeling and rapid prototyping of involute bevel gears', *The International Journal of Advanced Manufacturing Technology*, 98(1), pp. 645–656.

44. **Gbadeyan, O.J., Mohan, T.P. and Kanny, K.** (2020) 'Processing and characterization of 3D-printed nanoclay/acrylonitrile butadiene styrene (abs) nanocomposite gear', *The International Journal of Advanced Manufacturing Technology*, 109(3), pp. 619–627.
45. **Gibson, I. and Shi, D.** (1997) 'Material properties and fabrication parameters in selective laser sintering process', *Rapid Prototyping Journal*, 3(4), pp. 129–136.
46. **Goodridge, R.D., Tuck, C.J. and Hague, R.J.M.** (2012) 'Laser sintering of polyamides and other polymers', *Progress in Materials Science*, 57(2), pp. 229–267.
47. **Götz, J. and Stahl, K.** (2019) 'On the future of gears in electrified drive trains', *International Journal of Powertrains*, 8(4), pp. 327–342.
48. **Hart, K.R. and Wetzell, E.D.** (2017) 'Fracture behavior of additively manufactured acrylonitrile butadiene styrene (ABS) materials', *Engineering Fracture Mechanics*, 177, pp. 1–13.
49. **Hasl, C., Liu, H., Oster, P., Tobie, T. and Stahl, K.** (2017) 'Method for calculating the tooth root stress of plastic spur gears meshing with steel gears under consideration of deflection-induced load sharing', *Mechanism and Machine Theory*, 111, pp. 152–163.
50. **Hasl, C., Illenberger, C., Oster, P., Tobie, T. and Stahl, K.** (2018) 'Potential of oil-lubricated cylindrical plastic gears', *Journal of Advanced Mechanical Design, Systems and Manufacturing*, 12(1), pp. 1–9.
51. **Van Hooreweder, B., De Coninck, F., Moens, D., Boonen, R. and Sas, P.** (2010) 'Microstructural characterization of SLS-PA12 specimens under dynamic tension/compression excitation', *Polymer Testing*, 29(3), pp. 319–326.
52. **Van Hooreweder, B., Moens, D., Boonen, R., Kruth, J.P. and Sas, P.** (2013) 'On the difference in material structure and fatigue properties of nylon specimens produced by injection molding and selective laser sintering', *Polymer Testing*, 32(5), pp. 972–981.

53. **Van Hooreweder, B. and Kruth, J.P.** (2014) 'High cycle fatigue properties of selective laser sintered parts in polyamide 12', *CIRP Annals - Manufacturing Technology*, 63(1), pp. 241–244.
54. **ISO/ASTM 52921** (2013) *Standard terminology for additive manufacturing-coordinate systems and test methodologies*. West Conshohocken, Pennsylvania: ASTM International.
55. **ISO 6336-3** (2006) *Calculation of load capacity Microstructural characterization of SLS-PA12 specimens under dynamic tension/compression excitation'of spur and helical gears - Part 3: Calculation of tooth bending strength*. Geneva: ISO.
56. **Jain, P.K., Pandey, P.M. and Rao, P.V.M.** (2008) 'Experimental investigations for improving part strength in selective laser sintering', *Virtual and Physical Prototyping*, 3(3), pp. 177–188.
57. **Jain, P.K., Pandey, P.M. and Rao, P.V.M.** (2009) 'Effect of delay time on part strength in selective laser sintering', *The International Journal of Advanced Manufacturing Technology*, 43, pp. 117–126.
58. **Kalin, M. and Kupec, A.** (2017) 'The dominant effect of temperature on the fatigue behaviour of polymer gears', *Wear*, 376–377, pp. 1339–1346.
59. **Kapelevich, A.** (2000) 'Geometry and design of involute spur gears with asymmetric teeth', *Mechanism and Machine Theory*, 35(1), pp. 117–130.
60. **Kapelevich, A.** (2020) 'Optimal polymer gear design: Metal-to-plastic conversion', *Gear Technology*, 37(3), pp. 40–45.
61. **Kapelevich, A.L.** (2013) 'Historical Overview', in *Direct gear design*. Boca Raton: CRC Press, pp. 1–15.
62. **Kapelevich, A.L.** (2019a) 'Asymmetric gear applications', in *Asymmetric gearing*. Boca Raton: CRC Press, pp. 229–249.

63. **Kapelevich, A.L.** (2019b) 'Plastic gear design specifics', in *Asymmetric gearing*. Boca Raton: CRC Press, pp. 157–178.
64. **Kapelevich, A.L. and Shekhtman, Y. V.** (2009) 'Tooth fillet profile optimization for gears with symmetric and asymmetric teeth', *Gear Technology*, 26(7), pp. 73–79.
65. **Karimpour, M., Dearn, K.D. and Walton, D.** (2010) 'A kinematic analysis of meshing polymer gear teeth', *Proceedings of the Institution of Mechanical Engineers, Part L: Journal of Materials: Design and Applications*, 224(3), pp. 101–115.
66. **Karpát, F., Ekwaro-Osire, S., Cavdar, K. and Babalik, F.C.** (2008) 'Dynamic analysis of involute spur gears with asymmetric teeth', *International Journal of Mechanical Sciences*, 50(12), pp. 1598–1610.
67. **Karpát, F., Dogan, O., Yuce, C. and Ekwaro-Osire, S.** (2017) 'An improved numerical method for the mesh stiffness calculation of spur gears with asymmetric teeth on dynamic load analysis', *Advances in Mechanical Engineering*, 9(8), 1687814017721856, pp. 1–12.
68. **Karpát, F., Yuce, C. and Doğan, O.** (2020) 'Experimental measurement and numerical validation of single tooth stiffness for involute spur gears', *Measurement*, 150, 107043, pp. 1–9.
69. **Khudiakova, A., Berer, M., Niedermair, S., Plank, B., Truszkiewicz, E., Meier, G., Stepanovsky, H., Wolfahrt, M., Pinter, G. and Lackner, J.** (2020) 'Systematic analysis of the mechanical anisotropy of fibre-reinforced polymer specimens produced by laser sintering', *Additive Manufacturing*, 36, 101671, pp. 1–14.
70. **Kirupasankar, S., Gurunathan, C. and Gnanamoorthy, R.** (2012) 'Transmission efficiency of polyamide nanocomposite spur gears', *Materials and Design*, 39, pp. 338–343.
71. **Kodeeswaran, M., Verma, A., Suresh, R. and Senthilvelan, S.** (2016) 'Bi-directional and uni-directional bending fatigue performance of unreinforced and carbon fiber

reinforced polyamide 66 spur gears’, *International Journal of Precision Engineering and Manufacturing*, 17(8), pp. 1025–1033.

72. **Kodeeswaran, M., Verma, A., Suresh, R. and Senthilvelan, S.** (2019) ‘Effects of frequency on hysteretic heating and fatigue life of unreinforced injection molded polyamide 66 spur gears’, *Proceedings of the Institution of Mechanical Engineers, Part L: Journal of Materials: Design and Applications*, 233(5), pp. 781–789.
73. **Kodeeswaran, M., Suresh, R. and Senthilvelan, S.** (2016) ‘Transmission characteristics of injection moulded polymer spur gears: experimental and numerical evaluation’, *International Journal of Powertrains*, 5(3), pp. 246–263.
74. **Kodeeswaran, M., Suresh, R. and Senthilvelan, S.** (2019) ‘Effect of strain rate on bending and transmission characteristics of injection molded polyamide 66 spur gears’, *Proceedings of the Institution of Mechanical Engineers, Part L: Journal of Materials: Design and Applications*, 233(6), pp. 1145–1155.
75. **Koide, T., Yukawa, T., Takami, S., Ueda, A., Moriwaki, I., Tamura, A. and Hongu, J.** (2017) ‘Tooth surface temperature and power transmission efficiency of plastic sine-curve gear’, *Journal of Advanced Mechanical Design, Systems and Manufacturing*, 11(6), pp. 1–7.
76. **Kumar, P., Kommogi, R.K. and Senthilvelan, S.** (2009) ‘Injection molded asymmetric spur gear — development and preliminary performance evaluation’, *International Journal of Plastics Technology*, 13(2), pp. 186–192.
77. **Leigh, D.K.** (2012) ‘A comparison of polyamide 11 mechanical properties between laser sintering and traditional molding’, in *Proceedings of the 24th solid freeform fabrication symposium, The University of Texas at Austin, Austin, TX, USA*.
78. **Letzelter, E., de Vaujany, J.P., Chazeau, L and Guingand, M.** (2009) ‘Quasi-static load sharing model in the case of Nylon 6/6 cylindrical gears’, *Materials & Design*, 30(10), pp. 4360–4368.

79. **Lewicki, D.G. and Ballarini, R.** (1997) 'Effect of rim thickness on gear crack propagation path', *Journal of Mechanical Design, Transactions of the ASME*, 119(1), pp. 88–95.
80. **Li, Z. and Mao, K.** (2013) 'Frictional effects on gear tooth contact analysis', *Advances in Tribology*, 2013, pp. 1–9.
81. **Lieh, J., Wang, B. and Badiru, O.** (2017) 'The accuracy and surface roughness of spur gears processed by fused deposition modeling additive manufacturing', in *Additive Manufacturing Handbook*. CRC Press, pp. 519–530.
82. **Lisle, T.J., Shaw, B.A. and Frazer, R.C.** (2017) 'External spur gear root bending stress: A comparison of ISO 6336:2006, AGMA 2101-D04, ANSYS finite element analysis and strain gauge techniques', *Mechanism and Machine Theory*, 111, pp. 1–9.
83. **Litvin, F.L., Lian, Q. and Kapelevich, A.L.** (2000) 'Asymmetric modified spur gear drives: reduction of noise, localization of contact, simulation of meshing and stress analysis', *Computer Methods in Applied Mechanics and Engineering*, 188(1–3), pp. 363–390.
84. **Maitra, G.M.** (1994) 'Fundamentals of toothed gearing', in *Handbook of gear design*. Second. New Delhi: Tata McGraw-Hill Education, pp. 1–27.
85. **Majewski, C. and Hopkinson, N.** (2011) 'Effect of section thickness and build orientation on tensile properties and material characteristics of laser sintered nylon-12 parts', *Rapid Prototyping Journal*, 17(3), pp. 176–180.
86. **Mao, K.** (1993) *The performance of dry running non-metallic Gears*. Ph.D. Thesis, University of Birmingham, Birmingham, UK.
87. **Mao, K., Li, W., Hooke, C.J. and Walton, D.** (2009) 'Friction and wear behaviour of acetal and nylon gears', *Wear*, 267(1–4), pp. 639–645.
88. **Mao, K., Greenwood, D., Ramakrishnan, R., Goodship, V., Shroufi, C., Chetwynd,**

- D. and Langlois, P.** (2019) ‘The wear resistance improvement of fibre reinforced polymer composite gears’, *Wear*, 426, pp. 1033–1039.
89. **Marimuthu, P. and Muthuveerappan, G.** (2016a) ‘Design of asymmetric normal contact ratio spur gear drive through direct design to enhance the load carrying capacity’, *Mechanism and Machine Theory*, 95, pp. 22–34.
90. **Marimuthu, P. and Muthuveerappan, G.** (2016b) ‘Investigation of load carrying capacity of asymmetric high contact ratio spur gear based on load sharing using direct gear design approach’, *Mechanism and Machine Theory*, 96, pp. 52–74.
91. **Mašović, R., Jagarčec, V., Miler, D., Domitran, Z., Bojčetić, N. and Žeželj, D.** (2019) ‘Analysis of printing direction impact on dimensional accuracy of spur gears’, in *IFTOMM World Congress on Mechanism and Machine Science*. Springer, pp. 1111–1120.
92. **Masuyama, T. and Miyazaki, N.** (2016) ‘Evaluation of load capacity of gears with an asymmetric tooth profile’, *International Journal of Mechanical and Materials Engineering*, 11(1), pp. 1–9.
93. **Van Melick, H.G.H.** (2007) ‘Tooth bending effects in plastic spur gears’, *Gear Technology*, 24(7), pp. 58–66.
94. **Mertens, A.J., Kumar, P. and Senthilvelan, S.** (2016) ‘The effect of the mating gear surface over the durability of injection-molded polypropylene spur gears’, *Proceedings of the Institution of Mechanical Engineers, Part J: Journal of Engineering Tribology*, 230(12), pp. 1401–1414.
95. **Mertens, A.J. and Senthilvelan, S.** (2016) ‘Durability of injection moulded asymmetric involute polymer spur gears’, *International Journal of Powertrains*, 5(3), pp. 264–280.
96. **Meuleman, P.K., Walton, D., Dearn, K.D., Weale, D.J. and Driessen, I.** (2007) ‘Minimization of transmission errors in highly loaded plastic gear trains’, *Proceedings*

of the Institution of Mechanical Engineers, Part C: Journal of Mechanical Engineering Science, 221(9), pp. 1117–1129.

97. **Mo, S., Ma, S. and Jin, G.** (2019) ‘Research on composite bending stress of asymmetric gear in consideration of friction’, *Proceedings of the Institution of Mechanical Engineers, Part C: Journal of Mechanical Engineering Science*, 233(399), pp. 2939–2955.
98. **Mohan, N.A. and Senthilvelan, S.** (2014) ‘Preliminary bending fatigue performance evaluation of asymmetric composite gears’, *Mechanism and Machine Theory*, 78, pp. 92–104.
99. **Moya, J.L., Machado, A.S., Velásquez, J.A., Goytisoló, R., Hernández, A.E., Fernández, J.E. and Sierra, J.M.** (2010) ‘A study in asymmetric plastic spur gears’, *Gear solutions*, 8(84), pp. 34–41.
100. **Munguia, J. and Dalgarno, K.** (2014) ‘Fatigue behaviour of laser-sintered PA12 specimens under four-point rotating bending’, *Rapid Prototyping Journal*, 20(4), pp. 291–300.
101. **Munguia, J. and Dalgarno, K.** (2015) ‘Fatigue behaviour of laser sintered Nylon 12 in rotating and reversed bending tests’, *Materials Science and Technology*, 31(8), pp. 904–911.
102. **Muni, D. V, Kumar, V.S. and Muthuveerappan, G.** (2007) ‘Optimization of asymmetric spur gear drives for maximum bending strength using direct gear design method’, *Mechanics Based Design of Structures and Machines*, 35(2), pp. 127–145.
103. **Pedersen, N.L.** (2010) ‘Improving bending stress in spur gears using asymmetric gears and shape optimization’, *Mechanism and Machine Theory*, 45(11), pp. 1707–1720.
104. **Pedrero, J.I., Rueda, A. and Fuentes, A.** (1999) ‘Determination of the ISO tooth form factor for involute spur and helical gears’, *Mechanism and Machine Theory*, 34(1), pp. 89–103.

105. **Pisula, J., Budzik, G., Turek, P., and Cieplak, M.** (2021) ‘An analysis of polymer gear wear in a spur gear train made using FDM and FFF methods based on tooth surface topography assessment’, *Polymers*, 13(10), 1649, pp. 1–20.
106. **Pogačnik, A. and Tavčar, J.** (2015) ‘An accelerated multilevel test and design procedure for polymer gears’, *Materials and Design*, 65, pp. 961–973.
107. **Rosato, M.G., Rosato, Donald V and Rosato, Dominick V.** (2001) ‘Design influencing factor’, in *Plastics design handbook*. New York: Springer Science & Business Media, pp. 37–85.
108. **SAE J1619** (2017) *Single tooth gear bending fatigue test*. Warrendale, Pennsylvania: SAE.
109. **Sanders, A., Houser, D.R., Kahraman, A., Harianto, J. and Shon, S.** (2011) ‘An experimental investigation of the effect of tooth asymmetry and tooth root shape on root stresses and single tooth bending fatigue life of gear teeth’, in *Proceedings of the ASME 2011 International Design Engineering Technical Conferences and Computers and Information in Engineering Conference*. Washington, USA, pp. 297–305.
110. **Sekar, R.P. and Muthuveerappan, G.** (2015) ‘Estimation of tooth form factor for normal contact ratio asymmetric spur gear tooth’, *Mechanism and Machine Theory*, 90, pp. 187–218.
111. **Sekar, R.P.** (2019) ‘Performance enhancement of spur gear formed through asymmetric tooth’, *Proceedings of the Institution of Mechanical Engineers, Part J: Journal of Engineering Tribology*, 233(9), pp. 1361–1378.
112. **Senthilvelan, S. and Gnanamoorthy, R.** (2006) ‘Effect of gear tooth fillet radius on the performance of injection molded Nylon 6/6 gears’, *Materials and Design*, 27(8), pp. 632–639.
113. **Simulia** (2014) ‘Linear viscoelasticity’, in *ABAQUS 6.14. Analysis User’s Guide. Volume III: Materials*. Providence, Rhode Island: Dassault Systèmes, pp. 22.7.1–

22.7.2.

114. **Smith, J.D.** (2003) 'Causes of noise', in *Gear Noise and Vibration*. Second. Boca Raton: CRC Press, pp. 1–11.
115. **Smith, Z. and Ulrich, A.** (2012) 'Exploiting the potential of plastic gears', *Gear solutions*, pp. 40–47.
116. **Sobolak, M., Polowniak, P., Cieplak, M., Oleksy, M. and Bulanda, K.** (2020) 'Application of polymeric materials for obtaining gears with involute and sinusoidal profile', *Polimery*, 65(7–8), pp. 563–567.
117. **Sobolak, M. and Budzik, G.** (2008) 'Experimental method of tooth contact analysis (TCA) with rapid prototyping (RP) use', *Rapid Prototyping Journal*, 14(4), pp. 197–201.
118. **Sobolak, M. and Jagielowicz, P.E.** (2012) 'Rapid prototyping techniques for prototyping and research of polymer gear transmissions', *Acta Mechanica Slovaca*, 16(3), pp. 68–73.
119. **Soudmand, B.H. and Shelesh-Nezhad, K.** (2020) 'Failure and wear analysis of poly(butylene terephthalate) nanocomposite spur gears', *Tribology International*, 151, 106439. pp. 1–15.
120. **Starr, T.L., Gornet, T.J. and Usher, J.S.** (2011) 'The effect of process conditions on mechanical properties of laser-sintered nylon', *Rapid Prototyping Journal*, 17(6), pp. 418–423.
121. **Stichel, T., Frick, T., Laumer, T., Tenner, F., Hausotte, T., Merklein, M. and Schmidt, M.** (2017) 'A round robin study for selective laser sintering of polyamide 12: Microstructural origin of the mechanical properties', *Optics & Laser Technology*, 89, pp. 31–40.
122. **Terekhina, S., Tarasova, T., Egorov, S., Guillaumat, L. and Hattali, M.L.** (2020) 'On the difference in material structure and fatigue properties of polyamide specimens

produced by fused filament fabrication and selective laser sintering’, *The International Journal of Advanced Manufacturing Technology*, 111(1), pp. 93–107.

123. **Thirumurugan, R. and Muthuveerappan, G.** (2010) ‘Maximum fillet stress analysis based on load sharing in normal contact ratio spur gear drives’, *Mechanics based Design of Structures and Machines*, 38(2), pp. 204–226.
124. **Thirumurugan, R. and Muthuveerappan, G.** (2011) ‘Critical loading points for maximum fillet and contact stresses in normal and high contact ratio spur gears based on load sharing ratio’, *Mechanics based Design of Structures and Machines*, 39(1), pp. 118–141.
125. **Thomas, B., Sankaranarayanan, K., Ramachandra, S. and Suresh Kumar, S.P.** (2018) ‘Search method applied for gear tooth bending stress prediction in normal contact ratio asymmetric spur gears’, *Proceedings of the Institution of Mechanical Engineers, Part C: Journal of Mechanical Engineering Science*, 232(24), pp. 4647–4663.
126. **Trobentar, B., Hriberšek, M., Kulovec, S., Glodež, S. and Belšak, A.** (2022) ‘Noise evaluation of S-polymer gears’, *Polymers*, 14(3), 438. pp. 1–16.
127. **Trobentar, S., Glodež, S. and Zafošnik, B.** (2015) ‘Deflection analysis of spur polymer gear teeth’, *Journal of Multidisciplinary Engineering Science and Technology*, 2(4), pp. 847–853.
128. **Tsai, M.H. and Tsai, Y.C.** (1997) ‘A method for calculating static transmission errors of plastic spur gears using FEM evaluation’, *Finite Elements in Analysis and Design*, 27(4), pp. 345–357.
129. **Tsukamoto, N.** (1995) ‘Argument on plastic gears for power transmission’, *JSME international journal. Ser. C, Dynamics, control, robotics, design and manufacturing*, 38(1), pp. 1–8.
130. **VDI 2736 Blatt 2:2014-06** (2014) *Thermoplastic gear wheels - Cylindrical gears -*

Calculation of the load-carrying capacity. Berlin: Beuth Verlag.

131. **Walton, D., Tessema, A.A., Hooke, C.J. and Shippen, J.M.** (1994) 'Load sharing in metallic and non-metallic gears', *Proceedings of the Institution of Mechanical Engineers, Part C: Journal of Mechanical Engineering Science*, 208(2), pp. 81–87.
132. **Walton, D., Tessema, A.A., Hooke, C.J. and Shippen, J.M.** (1995) 'A note on tip relief and backlash allowances in non-metallic gears', *Proceedings of the Institution of Mechanical Engineers, Part C: Journal of Mechanical Engineering Science*, 209(6), pp. 383–388.
133. **Walton, D., Cropper, A.B., Weale, D.J. and Meuleman, P.K.** (2002) 'The efficiency and friction of plastic cylindrical gears. Part 1: Influence of materials', *Proceedings of the Institution of Mechanical Engineers, Part J: Journal of Engineering Tribology*, 216(2), pp. 75–92.
134. **Wang, J. and Howard, I.** (2005) 'Finite element analysis of high contact ratio spur gears in mesh', *Journal of Tribology*, 127(3), pp. 469–483.
135. **Wood, A.K., Williams, V. and Weidig, R.** (2012) 'The relative performance of spur gears manufactured from steel and PEEK', *Gear Technology*, 29(2), pp. 58–65.
136. **Wörz, A., Wudy, K., Drummer, D., Wegner, A. and Witt, G.** (2018) 'Comparison of long-term properties of laser sintered and injection molded polyamide 12 parts', *Journal of Polymer Engineering*, 38(6), pp. 573–582.
137. **Yamaguchi, Y.** (1990) 'Gears', in *Tribology of plastic materials: their characteristics and applications to sliding components*. Amsterdam, Netherlands: Elsevier, pp. 294–332.
138. **Yelle, H. and Burns, D.J.** (1981) 'Calculation of contact ratios for plastic/plastic or plastic/steel spur gear pairs', *Journal of Mechanical Design*, 103, pp. 528–542.
139. **Zhang, Y., Mao, K., Leigh, S., Shah, A., Chao, Z. and Ma, G.** (2020) 'A parametric

study of 3D printed polymer gears’, *The International Journal of Advanced Manufacturing Technology*, 107(11), pp. 4481–4492.

140. **Zhang, Y., Pursell, C., Mao, K. and Leigh, S.** (2020) ‘A physical investigation of wear and thermal characteristics of 3D printed nylon spur gears’, *Tribology International*, 141, 105953, pp. 1–10.
141. **Zhu, W., Yan, C., Shi, Y., Shifeng, W., Liu, J. and Shi, Y.** (2015) ‘Investigation into mechanical and microstructural properties of polypropylene manufactured by selective laser sintering in comparison with injection molding counterparts’, *Materials and Design*, 82, pp. 37–45.
142. **Ziegler, A., Maier, E., Lohner, T. and Stahl, K.** (2020) ‘A numerical study on thermal elastohydrodynamic lubrication of coated polymers’, *Tribology Letters*, 68(2), pp. 1–13.
143. **Zorko, D., Kulovec, S., Tavčar, J. and Duhovnik, J.** (2017) ‘Different teeth profile shapes of polymer gears and comparison of their performance’, *Journal of Advanced Mechanical Design, Systems and Manufacturing*, 11(6), pp. 1–10.
144. **Zorko, D.** (2021) ‘Investigation on the high-cycle tooth bending fatigue and thermo-mechanical behavior of polymer gears with a progressive curved path of contact’, *International Journal of Fatigue*, 151, 106394, pp. 1–15.

Publications based on the research work

1. **A. Karthik Pandian, S.S. Gautam and S. Senthilvelan**, Experimental and numerical investigation of the bending fatigue performance of symmetric and asymmetric polymer gears, *Proceedings of the Institution of Mechanical Engineers, Part L: Journal of Materials: Design and Applications*, **234**(6), 2020, 819–834.
2. **A. Karthik Pandian, S.S. Gautam and S. Senthilvelan**, Effect of metal and polymer mating gears on the bending fatigue performance of asymmetric polymer gears, *Proceedings of the Institution of Mechanical Engineers, Part L: Journal of Materials: Design and Applications*, **235**(10), 2021, 2324–2339.
3. **A. Karthik Pandian, S.S. Gautam and S. Senthilvelan**, Comparison of the bending fatigue performances of selective laser sintered and injection moulded nylon spur gears, *Proceedings of the Institution of Mechanical Engineers, Part L: Journal of Materials: Design and Applications*. **236**(3), 2022, 513-523.
4. **A. Karthik Pandian, S.S. Gautam and S. Senthilvelan**, Effect of layer orientation on the single tooth bending fatigue strength of polymer gears manufactured by selective laser sintering, *Proceedings of the Institution of Mechanical Engineers, Part L: Journal of Materials: Design and Applications*. **236**(8), 2022, 1557-1573.
5. **A. Karthik Pandian, S.S. Gautam and S. Senthilvelan**, Influence of tooth asymmetry and mating gear material on the tooth deflection characteristics of polymer gears. *Proceedings of the Institution of Mechanical Engineers, Part C: Journal of Mechanical Engineering Science*. 09544062221124835. 2022.

Presentation at International conferences

1. **A. Karthik Pandian, S.S. Gautam and S. Senthilvelan**, Comparison of bending fatigue performances of selective laser sintered and injection-molded polyamide spur gears, 3rd *International Conference on Materials, Design and Applications (MDA2020)*, University of Porto, Porto, Portugal. November 5-6, 2020.



Curriculum Vitae

1. Name : **A. Karthik Pandian**
2. Date of birth : 23 August 1993
3. E-mail : a.karthik.corres@gmail.com
4. Educational qualifications
 - 2011 – 2015** : **Bachelor of Engineering**
 - Institution : Dr. Mahalingam College of Engineering and Technology,
Pollachi – 642003,
Tamil Nadu, India.
 - Specialization : *Automobile Engineering*
 - 2016 – 2022** : **Doctor of Philosophy**
 - Institution : Indian Institute of Technology Guwahati,
Guwahati – 781039,
Assam, India.
 - Specialization : *Mechanical Engineering*
 - Date of registration : 5 January 2016
 - Date of thesis submission : 13 June 2022
 - Date of viva-voce : 12 November 2022

Doctoral Committee

Supervisors

Dr. S. Senthilvelan

Professor

Department of Mechanical Engineering

Indian Institute of Technology Guwahati

Dr. Sachin Singh Gautam

Associate Professor

Department of Mechanical Engineering

Indian Institute of Technology Guwahati

Chairperson

Dr. Uday S. Dixit

Professor

Department of Mechanical Engineering

Indian Institute of Technology Guwahati

Members

Dr. S. Kanagaraj

Professor

Department of Mechanical Engineering

Indian Institute of Technology Guwahati

Dr. Hemant B. Kaushik

Professor

Department of Civil Engineering

Indian Institute of Technology Guwahati